Study of Glass-Steel Interface for Corrosion Resistant Applications

A

Thesis

Submitted for the award of degree of

DOCTOR OF PHILOSOPHY

By

Bhupinder Kaur
(Regd. No. 900812001)

Under the supervision of

Dr. O.P. Pandey
(Senior Professor)

Dr. Kulvir Singh
(Professor)

School of Physics & Materials Science
Thapar University
Patiala-147004
June 2013

CERTIFICATE

This is to certify that the thesis entitled "**Study of Glass-Steel Interface for Corrosion Resistant Applications**" which is being submitted by Ms. Bhupinder Kaur to School of Physics and Materials Science, Thapar University, Patiala in fulfillment of the requirements for the award of the degree of Doctor of Philosophy, is a record of candidate's own work carried out by her under our guidance and supervision. The matter presented in this thesis has not been submitted in part or full for the award of any degree in any other University or Institute.

Date: 21/06/2013

Place: Patiala

Dr. O.P. Pandey
Senior Professor
School of Physics and Materials Science
Thapar University
Patiala–147004 (India)

Dr. Kulvir Singh
Professor & Head
School of Physics and Materials Science
Thapar University
Patiala–147004 (India)

CERTIFICATE

This is to certify that the thesis entitled "**Study of Glass-Steel Interface for Corrosion Resistant Applications"** which is being submitted by Ms. Bhupinder Kaur to School of Physics and Materials Science, Thapar University, Patiala in fulfillment of the requirements for the award of the degree of Doctor of Philosophy, is a record of candidate's own work carried out by her under our guidance and supervision. The matter presented in this thesis has not been submitted in part or full for the award of any degree in any other University or Institute.

Date: 21/06/2013
Place: Patiala

Dr. O.P. Pandey
Senior Professor
School of Physics and Materials Science
Thapar University
Patiala–147004 (India)

Dr. Kulvir Singh
Professor & Head
School of Physics and Materials Science
Thapar University
Patiala–147004 (India)

ACKNOWLEDGEMENTS

This dissertation would not have been possible without the guidance and help of several individuals who in one way or another contributed and extended their valuable assistance in the preparation and completion of this study. First and foremost, my utmost gratitude to my supervisors ***Dr. O.P. Pandey*** *(Senior Professor) and* ***Dr. Kulvir Singh*** *(Professor & Head) School of Physics and Materials Science, Thapar University, Patiala for his unflinching encouragement and support throughout the course of this research effort, which exceptionally inspire and enrich my growth as a student and researcher.*

I would like to thanks ***Dr. K.K. Raina****, Distinguish Prof. and Deputy Director, Thapar University, Patiala for his constant encouragement and moral supports during various stages of the work. I am also very thankful to* ***Dr. B.N. Chudasama****, Assistant Professor for his whole-hearted support and blessings.*

I would like to acknowledge the financial assistance from the projects ***(11-112/2008(BSR) and 39-510/2010 (SR))*** *of University Grants Commission, Govt. of India.*

My sincere thanks to ***Mrs. Sushila Pandey*** *and* ***Mrs. K. Singh*** *for their affirmative approaches and believes in me which motivated me to work harder. I would also like to acknowledge* ***Dr. C.P. Khatter*** *for providing all possible technical help during my initial course of investigation.*

My sincere thanks are due to ***Mr. Purushotam*** *for his help in characterization. I would like to acknowledge* ***Mr. Jant Singh, Mrs. Praveen, Mr. Vijay*** *and* ***Mr. Indermani*** *for their needful help during various stages of laboratory setup and administrative formalities.*

I would like to thank ***Dr. Vishal Kumar*** *and* ***Dr. Kamalpreet Kaur Waraich*** *for their valuable help during the initial stage of my work. Very special thanks to friends and research scholars* ***Dr. Akshay Kumar, Dr. Manoj Sharma, Dr. Neeraj, Dr. Jasmeet Kaur Gill, Dr. Gurbinder Kaur, Dr. Ravi Shukla, Mr. Kapil Sood, Mr. Harjinder Singh, Mr. Ranvir Panwar, Mr. Ishvdeep Singh, Ms. Samita, Ms. Mani Mahajan, Mr. Gaurav, Mr. Paramjyot Jha, Ms. Chandni, Mr. Rishi, Mr. Gurmeet Singh Lottey, Ms. Jagdeep Kaur, Mr. Satwinder Singh, Ms. Sakshi*** *and* ***Ms. Pooja Singla*** *for their help and support at all the time. I take this opportunity to express my respect and*

thankfulness to all my well-wishers, colleagues of School of Physics and Materials Science for their encouragement and support.

*My husband **S. Sharanjeet Singh Sidhu** and **my family** deserve the special thanks and great appreciation for their patience, persistent moral support and capability to rejuvenate me during the course of the Ph.D. work at each step. Their faith made me confident at every time.*

*Words are inadequate in expressing my sincere thanks to my grandmother **Sardarni Harjeet Kaur** for her support and prayers in every moment of difficulty. Last but not least, my parents, father **S. Davinder Singh Gill** and mother **Mrs. Gurjeet Kaur** deserve special mention for their inseparable support and prayers. Thanks to my younger brother **S. Avtar Singh** and my sister-in-law **Mrs. Arvinder Kaur** for being supportive and caring sibling. Above all, hidden force by **Almighty God** for blessing and steering me in the right direction to achieve the goal.*

*I am also thankful to my son **Sardar Manraj Singh Sidhu** who enjoyed my work and allowed me to write this thesis while playing with computer and also with my papers.*

(Bhupinder Kaur)

List of publications

Published

1. **B. Kaur**, K. Singh, O. P. Pandey, Microstructural study of Crofer 22 APU-glass interface for SOFC application, **International Journal of Hydrogen Energy** 37 (2012) 3839-3847.
2. **B. Kaur**, K. Singh, O. P. Pandey, Microstructural Analysis of Glass-steel Interface, **Surface and Coatings Technology** 217 (2013) 156-161.
3. **B. Kaur**, K. Singh, O. P. Pandey, Corrosion study of SiO_2-CaO-Al_2O_3-Na_2O-TiO_2 glass coating on the low carbon steel, **Surface Engineering**, 29 (2013) 479-483.

Under revision

1. **B. Kaur**, K. Singh, O. P. Pandey, Influence of modifier on dielectric and ferroelectric properties of aluminosilicate glass, **Journal of Non-Crystalline Solids** (under review).
2. **B. Kaur**, K. Singh, O. P. Pandey, Structural, thermal and optical properties of SiO_2-CaO-Al_2O_3-Na_2O-TiO_2 glasses, **Indian Journal of Applied and Pure Physics** (under review).

List of papers presented in conference (International/National)

1. **B. Kaur**, K. Singh and O.P. Pandey, "Bonding characteristic of SiO_2-CaO-Al_2O_3-Na_2O-TiO_2 glass with dual phase steel", in proceedings of School on Glass Formers and Glasses held at JNCAR, Jakkur (Bangalore) during 4 – 20th Jan'10.
2. **B. Kaur**, K. Singh and O.P. Pandey, "Microstructural investigation of Crofer 22 APU-glass interfaces for SOFC application." in proceedings of International Conference on Renewable Energy (ICRE 2011) held at University of Rajasthan (Jaipur) during 17 – 21st Jan'11.
3. **B. Kaur**, K. Singh and O.P. Pandey, "A Study of Interaction between Glasses and Steels." in proceedings of 22nd Annual General Meeting of MRSI held at AMPRI, Bhopal (MP)during 14 –16th Feb'11.

TABLE OF CONTENTS

LIST OF FIGURES

LIST OF TABLES

PREFACE

Glass is an amorphous (non-crystalline) solid material. Glasses are typically brittle and optically transparent. The most familiar type of glass used since centuries in windows and drinking vessels is soda-lime glass. Glass and glass-ceramics are assuming increasing importance in different industries including the medical, dental, chemical, communications, aerospace, and nuclear fields. However, if coated on metallic substances they can provide good corrosion resistance with support of metallic core provided the coating is stable. One of the major applications of these coating could be for the components used in underwater pathway. The resistance offered by glass surface in different corrosive environment particularly in aqueous solution is of great practical significance. Thus, it is essential to know the surface chemistry of different glasses in order to optimize their performance. In general terms the durability of glass may be defined as resistance of the glass surface to corrosion, i.e., chemical or physical changes caused by interaction with the environment. Consequently, durability of glass is a function of glass composition and surface state as well as the corrosive conditions of the environment. Stability of glasses depends upon various factors that include specifications of physical state, shape, surface condition as well as their physicochemical data in different corroding media which depends upon the mode of corrosion, and method of their evaluation. These are the primary objectives for choosing a glass–ceramic coating against all other types of available coating materials.

Glass coating on metallic substance may be useful to manufacturing industries as it may lead to development of heat and corrosion resistant material. A strong joining of two materials depends on chemical and physical factors of the interfaces. The combination of transparency and hardness at room temperature along with sufficient strength and excellent corrosion resistant to different environments make glass indispensable. The high chemical resistance offered by glass coating may provide good corrosion resistant and higher life to steel. Generally passive films, conversion coatings, metallic and organic coatings confer corrosion protection via a variety of mechanisms, including formation of barriers to the penetration of corrodants, high ionic resistivity in surface layers to minimize electrochemical reactions under the coating at the metal–coating interface and presence of active corrosion inhibitiors. As glasses are chemically inert inorganic

substances, the coating of glasses can provide better corrosion protection at the interface.

The present work deals with the synthesis, characterization and compatibility of (60-x) SiO_2 -10 Al_2O_3-5 TiO_2-15 CaO- (10+x) Na_2O (x= 0, 5, 10 and 15) glasses with crofer, duplex, HSLA and stainless steel (SS). The entire work in this thesis is presented in **five chapters**.

Chapter 1 gives description about glasses, their classification based on constituents used and various structural models for different glasses. Further the application of glass as a promising candidate for coating application on steel has been discussed. Detail description of corrosion, particularly in marine environment for both steel structures and glasses has been discussed. The various ways of corrosion protection of steels have been described. It also elaborates the reason for selecting glass as a coating material on steel over others materials as a corrosion resistant coat.

Chapter 2 describes the literature details on glass corrosion, steel corrosion and glass-steel interaction study. Corrosion of glasses in different environment leads to development of different product. These have also been reviewed with aim to correlate it with the present work. The corrosion behavior of glasses at glass-steel interface is influenced by type of steel used as a substrate. The role of different glass formers, modifiers and additives which provide good interfacial bonding is also described as these influence the glass transition temperature, viscosity and diffusivity for having good wettability. The literature work of those categories of papers which are relevant to present study is presented here.

Chapter 3 describes the experimental procedures followed to prepare glasses of different compositions, the specifications of different steels used and procedure adopted to prepare diffusion couple from these materials. Further the preparation of working electrode, cell and testing solution for corrosion testing is also documented. The characterization procedures along with instrument's details, working and operating conditions have been given.

Chapter 4 describes the results into three sections. First section contains the results of glasses obtained by Differential Thermal Analysis (DTA), Thermal Dilatometric Analysis (TDA), X-Ray Diffraction (XRD), Scanning Electron Microscopy (SEM) with Energy Dispersive Spectroscopy (EDS), Fourier Transform Infrared Spectroscopy (FTIR), UV-Visible and dielectric measurement of the glass samples are analyzed and discussed. The

entire work has been done to achieve the properties of glasses which can make it suitable as glass coating material on steel. The properties which are required for making the glass suitable for coating are glass transition temperature (T_g), crystallization temperature (T_c) and thermal expansion coefficient (TEC).

The second section gives information on important aspect of glass interaction with steels. The interaction study of glasses with crofer, duplex, HSLA and SS is described. For this study, glass powder of N-series and commercial glasses was coated by slurry method on steel and heated at 900 °C and 700 °C for 1 h, respectively. The top glass surface as well as the interface was analyzed under scanning electron microscope with EDS.

The third section presents the corrosion study of glasses, steels and diffusion couples. Corrosion studies of N-series glasses followed by their characterization using XRD, FTIR and ICP methods. The electrochemical testing of N-series glasses is described as it is a critical study to check the dissolution characteristic of glasses in varieties of aqueous solution. Corrosion study of steels is essential to know the nature of corrosion including pitting that takes place in present experimental set-up. Though data on steels are available but not for the acquired laboratory set-up where all materials are tested under similar environment. The electrochemical study of, best diffusion couples is investigated for varied time period of short to long time. These diffusion couples are characterized by SEM with EDS after corrosion to have a better understanding from industrial point of view.

Chapter 5 presents the overall conclusion of entire work and suggestion for future work.

Chapter 1

INTRODUCTION

Overview

This chapter describes about glasses, their classification based on constituents used and various structural models for different glasses. Further the application of glass as a promising candidate for coating application on steel is discussed. Additionally, the chapter also deals with corrosion, particularly in marine environment for both steel structures and glasses. The various ways of corrosion protection of steels have been described. This chapter also elaborates the reason for selecting glass as a coating material on steel over other materials for corrosion protection.

1.1. Glasses

Glass is an amorphous (non-crystalline) solid material. Glasses are typically brittle and optically transparent. The most familiar type of glass used since centuries in windows and drinking vessels is soda-lime glass [1]. In science, the term glass is usually defined as solid possessing non-crystalline (i.e., amorphous) structure that exhibits a glass transformation region when heated towards the liquid state. Glasses are made of quite different class of materials: metallic alloys, ionic melts, aqueous solutions, molecular liquids and polymers. For many applications (bottles, eyewear) polymer glasses (acrylic glass, polycarbonate, polyethylene terephthalate) are a lighter alternative to traditional silica glasses.

1.1.1. Glass formation

Glasses are usually formed by solidification from the melt. It exhibits an atomic structure close to that observed in the supercooled liquid phase but displays all the mechanical properties of a solid. The structure of glasses can be clearly distinguished from that of liquids, since glass structure is effectively independent of temperature. This can best be understood by observing the variation in specific volume of the crystal, liquid and glass as a function of temperature (Fig. 1.1). On cooling the liquid, there is a discontinuous change in volume at the melting point if the liquid crystalizes. However, if no crystallization occurs, the volume of the liquid decreases at the same rate as above the melting point until there is a decrease in the expansion coefficient at a range of temperature called the glass transformation range. Below this range, the glass structure does not relax at the cooling rate used. The expansion coefficient for the glassy state is usually about the same as that for the crystalline solid. If slower cooling rates are used so that the time available for the structure to relax is increased, the supercooled liquid persists to a lower temperature and higher density glass results. Similarly, by heating the glassy material in the annealing range, in which slow relaxation can occur, the glass structure in time approaches an equilibrium density corresponding to the supercooled liquid at this temperature [2].

A concept useful in discussing the properties of glasses is the glass transition temperature T_g, which corresponds to the temperature of the intersection between the curve for the glassy state and that the supercooled liquid (Fig. 1.1). Different cooling rates, corresponding to different relaxation times, give rise to a different configuration in the glassy state equivalent to different points along the curve for the supercooled liquid.

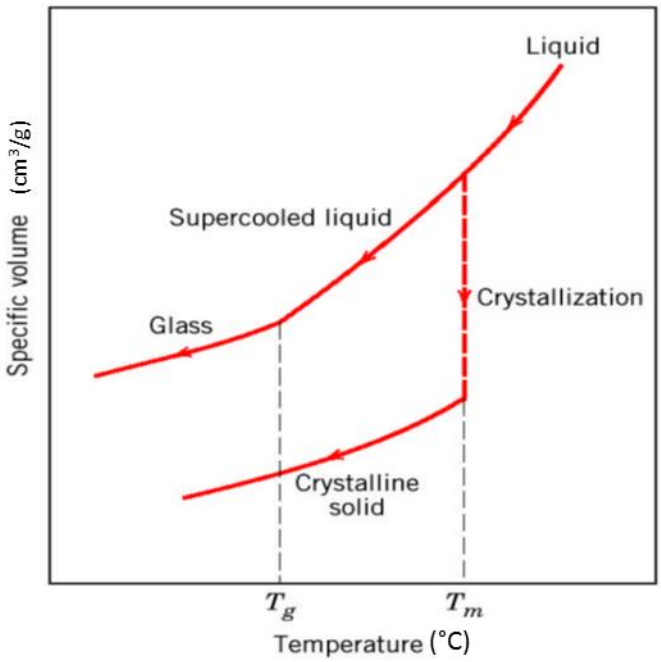

Fig. 1.1: Schematic specific volume-temperature relations for liquid, glass and crystal [2].

As the liquid is cooled from high temperature without crystallizing, a region of temperature is reached in which a bend appears in the volume-temperature relation. In this region, the viscosity of the material has increased to a sufficiently high value, typically about 10^{12} to 10^{13} P, so that the sample exhibits solid like behavior. On the scale of atomic structure, the distinguishing structural characteristic of glasses, like the liquids from which many are derived, is the absence of atomic periodicity or long-range order. Such a lack of periodicity does not imply the absence of short-range order, on a scale of a few angstroms. This short-range order which characterizes a particular glass or liquid may be described in terms of an atom-centered coordinate system and is frequently represented in terms of radial distribution functions.

1.1.2. Models of glass structure

1.1.2.1. Crystallite model

X-ray diffraction patterns from glasses generally exhibit broad peaks centered in the range where strong peaks are also seen in the diffraction patterns of the corresponding crystals. Such observation led to the suggestion that glasses are composed of assemblages of very small crystals, termed crystallite, with the observed breadth of the glass diffraction pattern resulting from particle-size broadening. It is well established that measurable broadening of X-ray diffraction peaks occur for particle sizes or grain sizes smaller than about 0.1 micron. The broadening increases linearly with

decreasing particle size. This model was applied to both single-component and multicomponent glasses.

1.1.2.2. Random-network model

According to this model, glasses are viewed as three-dimensional network or arrays, lacking symmetry and periodicity, in which no unit of the structure is repeated at regular intervals. In the case of oxide glasses, these networks are composed of oxygen polyhedral.

Adopting the hypothesis that a glass should have energy content similar to that of the corresponding crystal, Zachariasen [3] considered the conditions for constructing a random network such as shown in Fig. 1.2 and suggested four empirical rules for the formation of an oxide glass:

(i) Each oxygen ion should be linked to not more than two cations.

(ii) The coordination number of oxygen ions about the central cation must be small i.e. 4 or less.

(iii) Oxygen polyhedral share corners, not edges or faces.

(iv) At least three corners of each polyhedron should be shared.

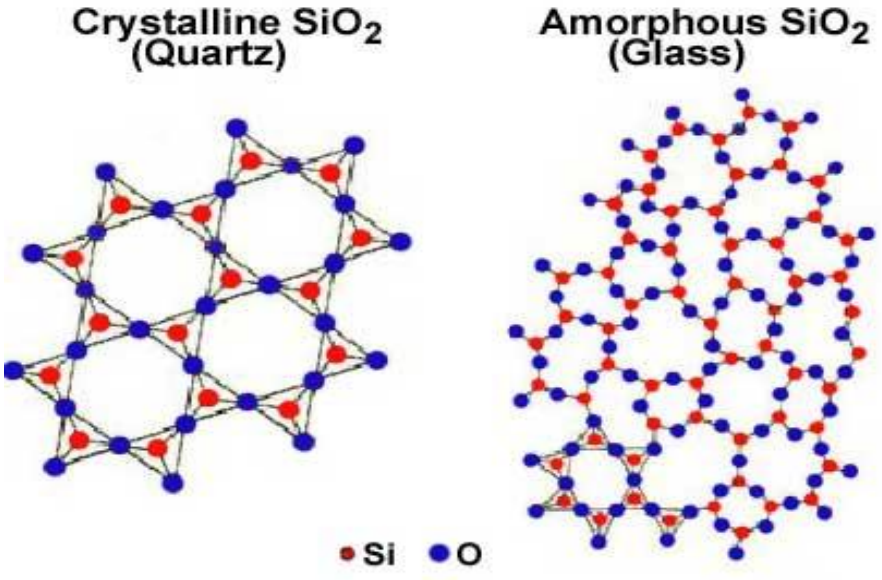

Fig. 1.2: Schematic representation of ordered crystalline form and random-network glassy form of the same composition [3].

In practice, the glass-forming oxygen polyhedra are triangles and tetrahedra, and cations forming such coordination polyhedra have been termed network formers. Alkali silicates form glass easily, and the alkali ions are supposed to occupy random positions distributed through the structure, located to provide local charge neutrality as shown in Fig. 1.3. Since their major function is viewed as providing additional oxygen ions which modify the network structure, they are called network

modifiers. Cations of higher valence and lower coordination number than the alkalis and alkaline earth metals may contribute in part to the network structure and are referred as intermediates.

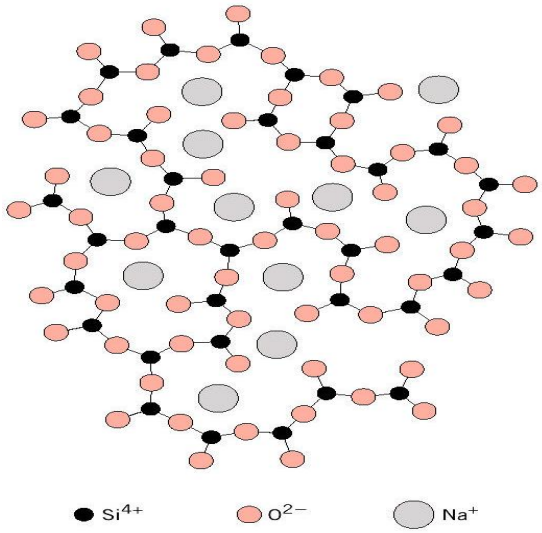

Fig. 1.3: Schematic representation of the structure of a sodium silicate glass [4].

The random-network model was originally proposed to account for glass formation as resulting from the similarity of structure and internal energy between crystalline and glassy oxides where the kinetic considerations preventing crystallization during cooling are important. The model remains as the best general picture of many silicate glasses and may be generalized as a random-array model in which the structural elements are randomly arranged where no unit of the structure is repeated at regular intervals in three dimensions.

In addition to above discussed models, several other models have also been suggested to represent the structures of glasses. One of these termed as the pentagonal dodecahedron model, views silicate glasses as composed of pentagonal rings of SiO_4 tetrahedra [5-6]. From a given tetrahedron, the rings extend in six directions to include the six edges and form twelve-sided dodecahedral cavities. Because of their five-fold symmetry, these dodecahedral cages cannot be extended in three dimensions without accompanying strain which ultimately prevents maintenance of the silicon-oxygen bonds. Although pentagonal rings of SiO_4 tetrahedra may indeed exist in the structure of glasses such as fused silica, but the reason for the existence of glassy structure is not known.

1.1.3. Structure of oxide glasses

There are three classes of components for oxide glasses: network formers, intermediates, and modifiers. The network formers (silicon, boron, germanium, phosphorus, etc.) form a highly cross-linked network of chemical bonds. The intermediates (titanium, aluminium, zirconium, beryllium, magnesium, zinc etc.) can act as network former and modifier both depending upon glass

composition. The modifiers (calcium, lead, lithium, sodium, potassium etc.) alter the network structure. These are usually present as ions, compensated by nearby non-bridging oxygen atoms, bound by one covalent bond to the glass network and holding one negative charge to compensate for the positive ion nearby. Some elements can play multiple roles; e.g. lead can act both as a network former (Pb^{4+} replacing Si^{4+}), or as a modifier. The presence of non-bridging oxygens lower the relative number of strong bonds in the material and disrupt the network, thus decreasing the viscosity of the melt and lowering the melting temperature and other transition temperatures. The alkali metal ions are small and mobile. Their presence in glass allows a degree of electrical conductivity, especially in molten state or at high temperature. Their mobility, however, decreases the chemical resistance of the glass, allowing leaching by water and facilitating corrosion. Alkaline earth ions, with their two positive charges require two non-bridging oxygen ions to compensate for their charge. These ions are less mobile and also hinder diffusion of other ions, especially the alkalis. The most common commercial glasses contain both alkali and alkaline earth ions (usually sodium and calcium), for easier processing and satisfying corrosion resistance [7]. Corrosion resistance of glass can be achieved by dealkalization and removal of the alkali ions from the glass surface by reaction with other cations e.g. sulfur or fluorine compounds. Presence of alkaline metal ions has other detrimental effect like loss tangent of the glass at different frequencies leading to variation in their electrical resistance.

1.1.3.1.Silicate glasses

One of the most important glass formers is silica (SiO_2). Pure crystalline silica melts at 1,710 °C. In pure form, silica glass exhibits such properties as low thermal expansion, high softening temperatures and excellent chemical and electrical resistance. In pure form it is relatively transparent over a wide range of wavelengths to visible and ultraviolet light and to ultrasonic waves. The addition of alkali or alkaline earth oxides to SiO_2 increases the ratio of oxygen to silicon to a value greater than 2 and breaks up the three-dimensional network with the formation of singly bonded oxygens which do not participate in the network [8]. The high viscosity (Fig. 1.4) and melting temperature of silica glass are affected by the presence or absence of alkali and alkaline earth cations. In structure, the modifying cations are located in the vicinity of the singly bonded oxygens to accompanying local charge neutrality [9].

Introduction of Al_2O_3 into soda lime silicate glass leads to formation of AlO_4 tetrahedral units when the amount of Al_2O_3 is less than sodium oxide. AlO_4 unit has a negative unit charge, and an equal amount of non-bridging oxygen is reduced. Therefore, Na/Al ratio gives a measure of the negative

charge distribution on the glass network. In other words, it is for site distribution of alkali ions in alkali aluminosilicate glass system. Glass Na/Al>1, where almost half of Na^+ ions interact with non-bridging oxygens (NBO), and the other half are located near AlO_4 tetrahedral units. Hereafter, Na^+ ion site to which an NBO contributes is called NBO-site while the other Na^+ site to which AlO_4 contributes is called charge compensation-site (CC-site). In Glass Na/Al=1, this means that all Na^+ ions are in CC-sites in this glass and all oxygen atoms are arranged as bridging oxygens [10].

1.1.3.2. Borate glasses

Addition of alkali or alkaline earth oxides to B_2O_3 results in the formation of BO_4 tetrahedra where each of the oxygens added with the alkali oxide ions converts two triangles to tetrahedra. Upto alkali oxide concentrations of about 30 mole %, nearly all the modifier oxides have the effect of converting BO_3 triangles to BO_4 tetrahedra. The singly bonded oxygens are presumably associated with BO_3 triangles rather than BO_4 tetrahedra, since the requirements for local charge compensation by the modifying cations is simpler in the case of the triangular arrangements [11].

1.1.3.3. Germanate and phosphate glasses

Glassy GeO_2 is composed of GeO_4 tetrahedra, with a mean germanium-oxygen-germanium bond angle of 138°. The structural model of a random network of oxygen tetrahedra seems reasonable for this material. In contrast to fused silica, the distribution of intertetrahedral angles for vitreous Germania is quite sharp. Measurements of physical properties such as density suggest that the addition of alkali oxide to GeO_2 may result in the formation of GeO_6 octahedra upto 15 to 30 wt. % alkali oxide. Information on the structure of phosphate glasses has been determined largely from chromatographic studies. Like silicate and most germanate glasses, phosphate glasses are composed of oxygen tetrahedra; but unlike the silicate and germanate analogs, a PO_4 tetrahedron can be bonded to at most three other similar tetrahedra. The most familiar structural units in phosphate glasses are rings or chains of PO_4 tetrahedra. The results of the chromatographic studies have elucidated the change in average length of chains as the P_2O_5 concentration of phosphate glasses is varied. With other additions, such as alumina, it is possible to simulate the characteristics of network-based silicate or germanate glasses [12].

1.1.4. Viscosity-temperature relation

The viscosity of amorphous materials depends on chemical composition, for example, in silicate systems viscosity attains the highest value for vitreous silica as shown in Fig. 1.4.

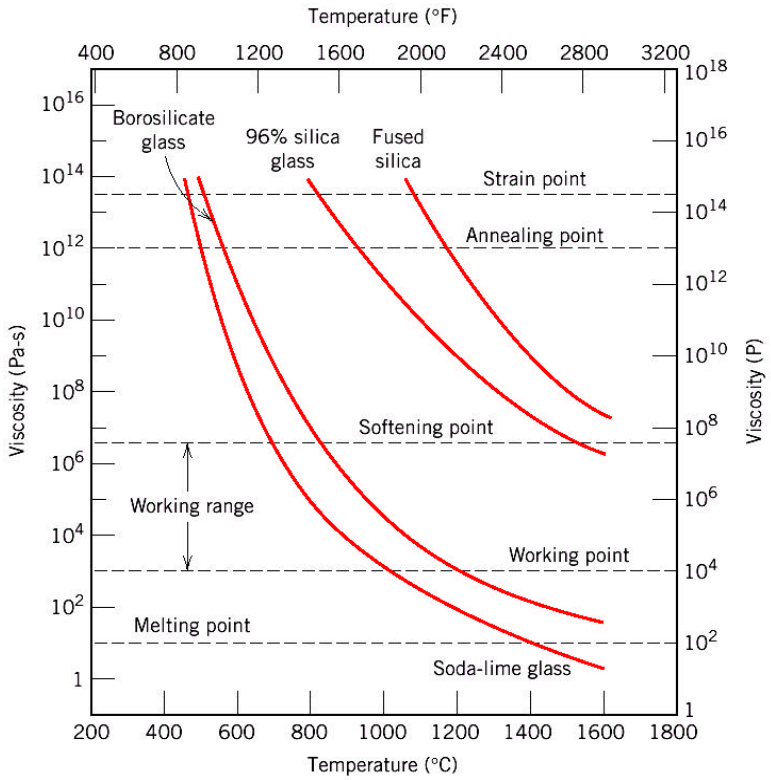

Fig.1.4: Viscosity of amorphous silicates and important technological points in glass manufacture industry [13].

1.2. Glass Coating

Glass coating (also known as Vitreous Enamel) is simply a thin layer of glass fused at high temperature on to the surface of a metal. It has many excellent properties: it is smooth, hard, chemically resistant, durable, scratch resistant, long-lasting color fastness, easy-to-clean and fire resistant. Moreover, it does not fade with UV light. It is a material made by fusing powdered glass onto substrate by firing, usually between 750 and 850 °C. The powder melts, flows, and then hardens to a smooth, durable vitreous coating on metal, or on glass or ceramics. Fired enamelware is an integrated layered composite of glass and metal. The glass frit is applied to the steel sheet surface either as water-based slurry or as a dry, electrostatically-applied powder [14].

There are two basic types of coatings. One is applied as a two-coat system, a ground coat plus a cover coat. The ground coat is applied to the steel sheet to promote adhesion of the cover coat. Ground-coat frits contain oxides that help to promote adhesion between the steel surface and the enamel coating. The other type of coating is called a one-coat system. As the name implies, this is a single-coat achieved by single-fire coating. This method of coating requires the use of more selectively processed steels. Steels that are used for coating need to have specialized properties in order to be coated successfully and obtain good adhesion between the glass and steel surface [15].

1.3. Corrosion

Corrosion is a natural impact of atmospheric environments like marine, industrial, urban and rural and affects the structural stability of the components. The annual loss due to corrosion can be compared with that of other natural calamities like earthquakes and cyclones, however, its impact is indirect. Loss due to corrosion has been reported to account for more failures in terms of cost and tonnage than any other environment. The overall loss due to corrosion alone amounts to at least 2 to 4 percent of GNP and at least 25 percent of this could be avoided by using appropriate corrosion-control technology [16].

1.3.1. Marine corrosion

Seawater is a conductive electrolyte, containing dissolved salts, gases, suspended organic and inorganic matters and live organisms. Apart from these, huge number of additional variables like temperature, pressure, hydrodynamic conditions and oxygen concentration are also involved. It is very difficult to understand thorough understanding of all possible marine conditions. However, an all-embracing and comprehensively applicable single model would be the ideal.

Steel is still the most common constructional material used in marine conditions. Steel for ships, drilling platforms, offshore structure, underwater pipelines or cables, is an attractive material because of its excellent mechanical properties and weldability. Moreover, it is abundant and cheaper to produce relatively at low cost compared to other materials. However, its corrosion resistance is certainly not ideal especially in a corrosive medium such as seawater which contains 3 - 3.5% sodium chloride [17].

A large part of the dissolved components of seawater is present as ion pairs, or in complexes, rather than as simple ions. While the major cations are largely uncomplexed, the anions, other than chloride are of varying degrees that one present in the form of complexes. About 13% of the magnesium and 9% of the calcium in ocean waters exist as magnesium sulfate and calcium sulfate, respectively. More than 90% of the carbonate, 50% of the sulfate, and 30% of the bicarbonate exist as complexes. Many minor or trace components occur primarily as complexed ions at the pH and the redox potential of seawater. Boron, silicon, vanadium, germanium, and iron form hydroxide complexes. Surface seawater characteristically has pH values higher than 8 owing to the combined effects of air-sea exchange and photosynthesis. The carbonate ion concentration is consequently relatively high in surface waters. In fact, surface waters are almost supersaturated with respect to the calcium carbonate phases, calcite and aragonite. The introduction of molecular carbon dioxide into subsurface waters

during the decomposition of organic matter decreases the saturation state with respect to carbonates. The opposite is true of deeper waters that are often under saturated in carbonates [18].

Chlorinity, conductivity and salinity are three terms which helps to measure the degree of corrosive seawater [19]. Salinity is roughly the number for grams of dissolved matter per kilogram of seawater. Generally, salinity of seawater lies between 33 to 37 parts per thousand. Local conditions may affect the value of salinity. Conductivity of sea water depends strongly on temperature, somewhat less strongly on salinity and very weakly on pressure. If the temperature is measured, then conductivity can be used to determine the salinity. Salinity as computed through conductivity and appears to be more closely related to the actual dissolved constituents. Therefore, temperature is measured at the same time as conductivity, to remove the temperature effect and obtain salinity. Chlorinity is defined as the weight in grams of the chloride ion content per 1000 grams of water. It refers to the sample of seawater titrated with silver nitrate, to precipitate bromides, iodides and chlorides. To calculate chlorinity the total content of halogen is taken as being chloride.

1.3.2. Glass corrosion

Glass is much more resistant to corrosion than most materials and considered as corrosion-proof. Glass windows after several years exposure to atmosphere remain clear and apparently unaffected. Glass bottles hold a wide range of liquids that would dissolve other materials. In the laboratory, reactions are carried out in glass beakers and flasks without damage to the beakers or contamination of the solutions reacting. But, in spite of these indications that glass is indestructible by chemical attack, under certain conditions it will corrode, even dissolve. In these cases, it is important to choose the right type of glass, since some are more corrosion resistant than others. Only a few chemicals aggressively attack glass i.e. hydrofluoric acid, concentrated phosphoric acid (when hot, or when it contains fluorides), hot concentrated alkali solutions and superheated water. Hydrofluoric acid is the most powerful of this group; it attacks any type of silicate glass. Other acids attack only slightly; the degree of attack can be measured in laboratory tests but such corrosion is rarely significant in service for acids other than hydrofluoric and phosphoric [20].

Acids and alkali solutions attack glass in different ways. Alkalis attack the silica directly while acids attack the alkali in the glass. When an alkali solution attacks a glass surface, the surface simply dissolves. This process continuously exposes a fresh surface, which in turn is dissolved. As long as the supply of alkali is sufficient, this type of corrosion proceeds at a uniform rate.

Acid corrosion behaves quite differently. By dissolving the alkali in the glass composition, a porous surface is left that consists of the silica network with holes where the alkali has been removed by the

acid. This porous surface slows the rate of attack since the acid must penetrate this surface layer to find alkali to dissolve.

Corrosion by water is similar to acid corrosion where alkali is removed from the glass surface. Water corrosion acts at a much slower rate. At high temperatures, however, water corrosion can become significant e.g. gauge glasses for steam boilers. These products must be protected from the superheated water by a sheet of mica or replaced on a schedule that insures that they will not be seriously weakened. Of the glasses studied, fused (silica) glass had the greatest corrosion resistance, followed by the low-alkali aluminosilicate and borosilicate glasses. Sodium seemed to be detrimental to the stress corrosion resistance of glass [21].

1.3.2.1. Mechanism of glass corrosion

1.3.2.1.1. Aqueous medium:

Reaction between aqueous solution and glass leads to surface deterioration of glass as a function of glass composition. Various factors such as solution pH, temperature, content of salts, complexing agents, impurities, etc. also affect the corrosion mechanism of glass. A variety of physicochemical and optical methods was used to analyze the leached components. In an extremely simplified version, the corrosion mechanism of alkali silicate or alkali-alkaline earth silicate glasses can be represented by the following model [22]:

(a)

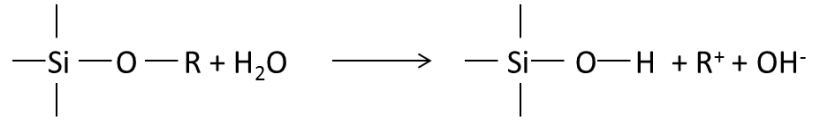

Step (a) illustrates a typical hydrolysis reaction. An oxygen alkali bond near the interface is broken by the migration of R^+ ion and the oxygen atom dissociates a water molecule to satisfy its force field with hydrogen ion. Free hydroxyl ion is formed in this process leading to dissociation of glass.

(b)

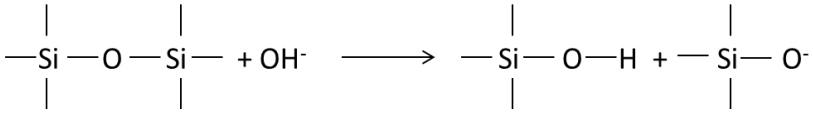

In step (b), which can proceed only if the first step has already been taken, the very strong Si-O-Si bond is broken such that one end of the broken radical becomes of a Silanol end by proton transfer or hydroxyl ion attachment and the other produces an end structure capable of dissociating water molecule as shown in step (c).

(c)

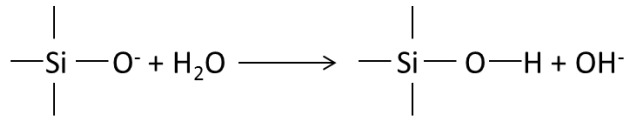

Silanol groups may either go into solution or form a film on the glass surface.

1.3.2.1.2. Atmosphere

Corrosion of glass by atmosphere has been classified into two types, dynamic and static, depending on the conditions of exposure of the glass surface to condensed moisture. During dynamic weathering, water from atmosphere adhere to the surface of the glass and extract alkali ion according to reaction (a), but replenished continuously before the pH rise into high alkaline range.

Under static weathering conditions, a small volume of water remain in contact on a large glass surface area for a long duration and when pH attains the value of > 8.5 alkaline attack according to reaction (b) causes severe structural surface damage.

Many laboratory tests have been devised for testing corrosion resistance. Some of them aim at accelerating rate of corrosion by employing high temperatures or by grinding the glass to a specified grain size to expose more surface area to the corroding solution [23]. After treatment for the specified time and at the specified temperature, the weight loss of the glass is measured or the amount of alkali extracted can be determined. Many factors influence the rate of corrosion and no laboratory test to date is capable of predicting service behavior under all conditions. Concentration and rate of agitation of the corroding solution are important factors. As corrosion progresses, the test solution becomes contaminated with components extracted from the glass which may increase or decrease the corrosion rate. Some glass products have a silica-rich skin, so the surface will show a different corrosion rate from the interior [24].

1.4. Corrosion protection

1.4.1. Coating of glasses

Plating, painting, and the application of enamel are the most common anti-corrosion treatments. They work by providing a barrier of corrosion-resistant material between the damaging environment and the structural material. Platings usually fail only in small sections, and if the plating is nobler than the substrate like chromium on steel, a galvanic couple cause any exposed area to corrode much more rapidly than an unplated surface. Painted coatings are relatively easy to apply and have fast drying. Although temperature plays important role, but humidity may cause variation in life times of the coating. Enamel coating (glass coating) is extremely corrosion resistance which permanently protects the steel surfaces [25].

1.4.2. Improvement of glass durability

Glass durability is improved by an ion-implantation process on the surface layer of glass with certain thickness. A practical example of technical importance is the incorporation of tin oxide in the bottom

surface of float glass. The resulting higher durability of the bottom surface can be explained simply by dealkalization. However, excessive tin concentration in the surface layer may lead to structural changes which may lower the acid durability of the glass [26]. Ion-exchange reactions method is another method to improve glass durability. It involves replacement of alkali ions, commonly Na^+, by other monovalent cations such as H^+, Ag^+, Cu^+. In other words, ions diffusion is blocking the mechanism for alkali migration from the interior to the surface. Thus, the reaction of surface is minimized during aqueous solution attack.

1.5. Corrosion testing

All corrosion is an electrochemical process of oxidation and reduction reactions. As corrosion occurs, electrons are released by the metal (oxidation) and gained by elements (reduction) in the corroding solution. Because there is a flow of electrons (current) in the corrosion reaction, it can be measured and controlled electronically [27]. Therefore, controlled electrochemical experimental methods can be used to characterize the corrosion properties of metals and metal components in combination with various electrolyte solutions. The corrosion characteristics are unique to each metal/solution system.

References

1. Mewburn, Glass windows in Alnwich Castle, Notes and Queries, Volumes I-XII, Issue 304, 25 (1855) 147.
2. C. A. Angell, Chem. Rev. 90 (1990) 523–542.
3. W.H. Zachariasen, J. Amer. Chem. Soc. 54 (1932) 3841-3851.
4. G.N. Greaves, W. Smith, E. Giulotto, E. Pantos, J. Non-Cryst. Solids 222 (1997) 13-24.
5. S.J. Gurman, J. Non-Cryst. Solids 125 (1990) 151-160.
6. R. Hosemann, M.P. Hentschel, U. Schmeisser, R. Brückner, J. Non-Cryst. Solids 83 (1986) 223-234.
7. S. Das, S. Datta, D. Basu, G. C. Das, Ceram. Int. 35 (2009) 1403–1406.
8. H.A. Robinson, J. Phys. Chem. Solids 26 (1965) 209-222.
9. A. C. Hannon, B. Vessal, J. M. Parker, J. Non-Cryst. Solids 150 (1992) 97-102.
10. L. Cormier, D.R. Neuville, Chem. Geol. 213 (2004) 103– 113.
11. K.P. Mueller, Glastechnische Berichte 42 (1969) 83-89.
12. H. Verweij, J.H.J.M. Buster, J. Non-Cryst. Solids 34 (1979) 81-99.
13. J.E. Shelby, Introduction to glass science and technology, The Royal Society of Chemistry, UK, 2005.
14. L. Bragina, O. Shalygina, N. Kuryakin, V. Annenkov, N. Guzenko, K. Kupriyanenko, V. Hudyakov, A. Landik, IOP Conference Series: Materials Science and Engineering 25 (2011), Article number012012.
15. A. Zhang, Z. Jian, S. Jiao, D. Wei, Int. J. Surf. Sci. Eng. 5 (2011) 5-6.
16. X. Wang, Mater. Sci. 5 (2005) 91.
17. H. Meng, X. Hu, A. Neville, Wear 263 (2007) 355-362.
18. R.E. Melchers, Corrosion 61(2005) 237-245.
19. P. R. Roberge, Handbook of Corrosion Engineering, McGraw-Hill, New York, 2000.
20. C. Cailleteau, Insight into silicate-glass corrosion mechanisms, Nature (2008).
21. M. Hock, E. Schäffer, W. Döll, G. Kleer, Surf. Coat. Tech. 163-164 (2003) 689-694.
22. B.C. Bunker, J. Non-Cryst. Solids 179 (1994) 300-308.
23. T.A Wassick, R.H. Doremus, W.A. Lanford, C. Burman, J. Non-Cryst. Solids 54 (1983) 139-151.
24. N. Pandya, D.W. Muenow, S.K. Sharma, B. L. Sherriff, J. Non-Cryst. Solids 176 (1994) 140-146.
25. F. Tang, G. Chen, J.S. Volz, R.K. Brow, M. Koenigstein, Constr. Build. Mater. 35 (2012) 376–384.
26. L.L. Hench, J. Non-Cryst. Solids 19 (1975) 27-39.
27. S.F. Rudy, Plat. Surf. Finish. 90 (2003) 28-29.

Chapter 2

LITERATURE REVIEW

Overview

In this chapter the literature review on glass corrosion, steel corrosion and interfacial reactions between glass-steel has been presented. Corrosion of glasses in different environment leads to formation of different crystalline phases. These have also been reviewed with aim to correlate it with the present work done in this thesis. The corrosion behavior of glasses at glass-steel interface is influenced by type of steel used as a substrate. The role of different glass formers, modifiers and additives which provide good interfacial bonding is also described as these influence the glass transition temperature, viscosity and diffusivity for having good wettability.

2.1. Surface properties of Glasses

Glass and glass-ceramics are typical class of material with increasing importance in different industries including the medical, dental, chemical, communications, aerospace, and nuclear fields. The resistance offered by glass surface in different corrosive environment particularly in aqueous solution is of great practical significance [1]. Thus it is essential to know the surface chemistry of different glasses in order to optimize their performance [2, 3]. Durability of glass may be defined in general terms as resistance of the glass surface to corrosion, i.e., to chemical or physical changes caused by interaction with the environment. Consequently, durability of glass is a function of glass composition and surface state as well as the corrosive conditions of the environment. Stability of glasses depends upon various factors that include specifications of physical state, shape, surface condition as well as their physicochemical data in different corroding media which depends upon the mode of corrosion, and method of their evaluation [4].

Schott and Forester [5-6] through their systematic experiments have concluded that the first step in the attack on glass surfaces is by water that enters into the body of the glass. This is known as the hypothesis of an actual miscibility between water and silicate glasses. This has been confirmed by many subsequent workers. Barus [7] found that glass heated under pressure with water at 185 °C has swelled and became white and turbid. While at 210 °C, solution became a clear liquid. But at low temperature, the only single process responsible is decomposition of glass. As described in chapter 1, there are three general classes of reactions that occur between glass and aqueous solutions. These are (1) hydration, in which molecular water enters the glass as an intact solvent; (2) hydrolysis, in which water reacts with metal-oxygen bonds in the glass to form hydroxyl groups; and (3) ion-exchange reactions, in which modifier cations such as sodium are replaced by protons (or other cations). For complex glasses, all three reactions occur simultaneously. Each reaction influences the kinetics and mechanisms of the other reactions. However, before the dissolution behavior of different glass compositions are discussed, the features governing each reaction type are discussed independently [8].

The dominant mechanism for water penetration into glass depends on the relative rates for the two pathways. The rate of the molecular diffusion pathway is primarily controlled by steric constraints imposed by the size of the voids present in the glass network. For silicates, the void size is determined by the distribution of rings in the structure consisting of interconnected silicate tetrahedra. For complex glasses, modifier cations such as Na^+ can fill or partially block such voids. The effect of ring size on diffusion has been determined for crystalline aluminosilicate zeolites. When the structure contains voids which are large (> 0.7 nm) relative to the kinetic

diameter of the water molecule (0.28 nm), the molecule can diffuse through silicates as rapidly as it can through liquid water ($D=3\times10^{-5}$ cm^2/s). For puckered rings containing six silicate tetrahedra where the ring opening (0.24 nm) is comparable in size with the water molecule such as zeolites diffusion is much slower ($D = 2\times10^{-13}$ cm^2/s). If smaller rings are present, molecular water cannot penetrate the voids. The only way for water to penetrate such structures is to break open the rings via hydrolysis.

2.1.1. Silica glasses

2.1.1.1. Silica-water reactions

Silica has the simplest structure for analysis of glass-water reactions where modifier cations capable of ion-exchange reactions are not present. All oxygens are bridging oxygens and all Si tetrahedral sites are Q_4 sites (no. of bridging oxygens on a particular tetrahedral Si sites) predicted to be resistant to hydrolysis. The Q_4 sites interconnect to form rings. Rings containing five or more Q_4 units can pucker to produce relatively strain-free configurations which are spectroscopically indistinguishable [9-10]. However, rings containing four, three and two tetrahedra contain enough internal strain to change the frequencies associated with vibrational modes as detected via Raman or infrared spectroscopies. Significant concentrations of three- and four-fold rings are detected in fused silica. The distribution of larger rings is difficult to determine. However, comparisons involving He and Ne diffusion into silica glass and into zeolites suggest that four-, five- and six-membered rings are most common and that there are few interconnected voids involving larger rings [11]. In the absence of ring opening via hydrolysis, hydration of silica is predicted to be negligible.

Experimental results on both the dissolution and hydration of silica indicate that it is highly resistant to attack by water as expected on the basis of glass structure. Below pH 8 at room temperature, silica glass dissolves at a rate of around 10^{-16} mol/cm^2 s, or of the order of 10 nm/y. As the solution pH is increased from 8 to 14, the dissolution rate increases to as high as 10^{-12} mol/cm^2 s as expected due to both the increase in the concentration of OH^- and the enhanced solubility of silica at higher pH due to the formation of silicate anions. In aqueous solutions, hydrated layers are not produced on silica surfaces because the silica dissolves via network hydrolysis before it can be hydrated. When silica is exposed to steam atmospheres, hydrated layers can form because the reaction products of network hydrolysis do not have a solution phase to dissolve into glass. Isotopic labeling experiments clearly show that steam hydration of silica glass involves 'reversible' network hydrolysis leading to extensive exchange of oxygen between the water and the glass. The activation energies (ranging from 17 to 20 kcal /mol) and absolute

rates for steam hydration and network hydrolysis leading to dissolution are similar, which is also consistent with a hydrolysis mechanism for steam hydration.

While silica is not susceptible to aqueous corrosion (except in strong base), silica glass is highly susceptible to environmentally assisted crack growth, or stress corrosion cracking. In stress corrosion, water can greatly accelerate the rate at which cracks in silica grow from surface flaws under an applied load, leading to catastrophic failure. The mechanism for stress corrosion involves the rapid hydrolysis of local Si-O bonds which are deformed via applied stress. The kinetics of silica hydrolysis as a function of local strain energy have been modeled by studying the rate of hydrolysis of strained bonds in silicate rings containing three or two tetrahedral units [6]. The latter edge-shared tetrahedra, found in the surfaces of dehydroxylated silica, react over one million times faster than normal unstrained rings, illustrating the nature of local deformations that can influence the reactivity of silica. Although the level of strain is lower in three- and four-fold rings, the presence of such rings and other strained bonding configurations accounts for the enhanced dissolution of fused silica relative to quartz. The one outstanding feature is the superiority of silica glass over all others that the chemical resistivity of a glass is proportional to its silica content. However, the addition of other substances is necessary to lower the temperature of the melt or other desirable qualities.

2.1.2. Alkali Silicate Glasses

Soda and potash, the alkalis, are commonly introduced into silica glass to increase fusibility. Alkali silicate glasses are of particular interest due to the mixed alkali effect; as one alkali is substituted for another, there is a highly non-linear change in the physical properties involving cation motion. The most widely accepted description of the structure of oxide glasses is given by the Zachariasen- Warren model [12]. In this model, the structure of vitreous SiO_2 is a continuous random network of corner-sharing $SiO_{4/2}$ tetrahedra. The bond lengths and bond angles within the tetrahedra are well defined, and the random nature of the structure arises from the distributions of both the Si-O-Si and dihedral angles between the tetrahedra. This model is extended to alkali silicate glasses by regarding the alkali cations as network modifiers. In the modified random network (MRN) model [13], the addition of one network modifier unit M_2O causes one bridging oxygen (BO) atom between two connected tetrahedra to be replaced by two non-bridging oxygen (NBO) atoms, one in each tetrahedron.

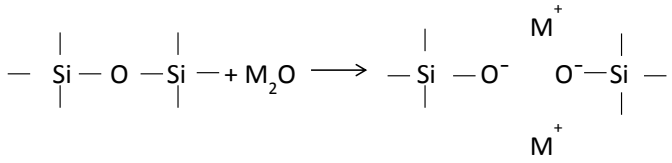

The negative charge on the singly charged NBOs is balanced by near positively charged M^+ cations.

2.1.2.1. Leaching of alkali silicate glasses

Hydration, hydrolysis, and ion-exchange reactions all occur on the surfaces of alkali silicate glasses exposed to water. By contrast with silica, network hydrolysis is not the only factor contributing to the rate of surface hydration. As alkali cations are removed from the surface via ion exchange, voids which were occupied by the alkali ions can be replaced by water, facilitating diffusion of water into the surface. Except in highly basic solutions, the silicate network dissolves at a rate slower than the rate of water penetration. As a result, thick hydrated, alkali depleted surface layers can form on alkali silicates even at room temperature [14]. The alkali-nonbridging oxygen-silicon linkage in the structure of silicate glasses readily form peroxides and superoxides which react vigorously with CO_2 to form carbonates and with H_2O to form hydroxides. Similarly, when silicate glass fractures the newly created surfaces are exposed to air and water [15]**.**

2.1.2.2. Composition dependence

Simple alkali silicate glasses contain charge compensated ion pairs such as Si-O-Na^+, introducing Q_3 and Q_2 groups into the Q_4 network [16]. Therefore, the alkali silicates are more susceptible to network hydrolysis than is silica. The total number of non-bridging oxygens increases with the modifier content of the glass (e.g., from 0.5 to 0.67 to 1.0 in the series Na_2O-$4SiO_2$ to Na_2O- $3SiO_2$ to Na_2O-$2SiO_2$) [17]. For a given modifier, the reactivity of the alkali silicate glasses increases with the non-bridging oxygen content. However, glasses containing the same modifier content but different modifier cations (e.g., Na^+ versus K^+) do not react with water at the same rate. In general, the lower the charge-to-ionic radius ratio of the modifier cation, the glass will be more reactive. Addition of CaO to soda-lime glass greatly enhances the corrosion resistance relative to a simple sodium silicate glass. Two factors appear to contribute to the above trends. First, exchange of large cations such as K^+ leaves behind larger voids in the network than does leaching of smaller cations such as Na^+, providing larger openings into which water can diffuse. Second, the distribution of non-bridging oxygens among the different Q species is different depending upon the modifier used. Smaller, more highly charged modifiers

such as Li^+ and Ca^{2+} can promote clustering of non-bridging oxygens via reactions such as $2Q_3 \rightarrow Q_2 + Q_4$ [13]. The above clustering can lead to phase separation, in which reactive Q_2 regions are surrounded by silica-like Q_4 regions that are more resistant to both hydrolysis and hydration. However, even in the absence of phase separation; increase in the mole fraction of Q_4 appears to improve leaching resistance. For the alkali silicate dissolution another structural known as the Q distribution is required to predict accurately the glass dissolution behavior. Hydration, network hydrolysis, and ion-exchange reactions can all lead to degradation of silicate glasses exposed to water. The relative rates of the three reactions and the observed dissolution mode (selective leaching versus uniform dissolution) are critically dependent on the distribution and reactivity of specific sites and presence of functional groups within the glass structure. Each site type exhibits different reactivity patterns as a function of environmental parameters such as solution pH. Different bond types in glass are hydrolyzed via different mechanisms with different rates. Charge distributions at different sites, such as non-bridging oxygens and tetrahedral borate or aluminate sites, exhibit different local charge distributions and ion-exchange characteristics. Therefore, detailed information concerning the local structure of glass and the variation of structure with composition and preparation conditions is essential for predicting dissolution behavior [18].

2.1.2.3. Environmental dependence

The environmental dependence for both ion exchange and network hydrolysis are categorized on the basis of the acid-base properties of the silanol group and the hydrolysis characteristics of Q units in silicate networks in glasses. Surface silanol groups have an effective pH of nearly 10, which correspond to the transition pH between extensive ion-exchange (leading to selective alkali leaching) and little exchange. Measurements of the extraction of alkali versus pH are consistent with the exchange behavior of silanol groups. Below pH 9, alkali leaching is extensive, and exhibits little pH dependence. The rate of alkali extraction drops sharply between pH 9 and 11, and in highly basic solutions is almost as slow as the rate of network dissolution. Above pH 9, where silicate anions become stable and nucleophilic attack by OH^- is promoted. The dissolution rate of the silicate network increases for all alkali silicates. The pH dependence for network dissolution is similar to that observed for silica [19]. The one environmental factor which does not influence leaching as predicted is the Na^+ concentration in solution. While leaching can be retarded by as much as a factor of five in NaCl brine solutions, leach rates in more dilute solutions are almost independent of Na^+ [11].

2.1.3. Alkali aluminosilicate glasses

When Day and Rindone [20] substituted Al_2O_3 for Na_2O in a binary sodium silicate glass, they succeeded in eliminating the non-bridging oxygen ions. This was due to the fact that $A1_2O_3$ by itself does not introduce enough oxygen ions into the network so that the aluminum ion can be coordinated by four oxygen ions. As a result, non-bridging oxygen ions are utilized to satisfy the requirements.

All the factors discussed above regarding the hydration, hydrolysis and ion-exchange of alkali silicate glasses also apply to alkali aluminosilicate glasses. However, to understand the relative rates at which the glass alteration reaction occurs, the structural differences between alkali silicates and glasses such as aluminosilicates need to be taken into account. In simple alkali silicate glasses, all modifier cations are charge-compensated by non-bridging oxygens. Creation of non-bridging oxygens lowers the effective crosslink density of the glass, creates Q_3 and Q_2 sites which are more prone to network hydrolysis and allows formation of silanol groups via ion-exchange and promote structural alterations within the leached layer. In alkali aluminosilicate glasses, modifier cations can be charge compensated by AlO_4^- sites in addition to non-bridging oxygens. Such sites modify both the inherent reactivity and extended structure of the glass. Anionic tetrahedral sites such as AlO_4^- are approximately five orders of magnitude more resistant to ion-exchange by protons than are nonbridging oxygens. Selective leaching from such sites does not occur above pH 5 (compared with pH 10) for non-bridging oxygen sites. In neutral pH solutions, the fraction of Na^+ associated with non-bridging oxygens are selectively leached leaving the fraction associated with AlO_4^- sites untouched. It is difficult to exchange modifier cations from Al sites without selectively leaching the Al [21].

A combination of infrared, Raman, and magic angle spinning nuclear magnetic resonance (MAS-NMR) spectroscopy is used to study molecular versus OH within synthetic alkali silicate glasses. These glasses were hydrated over a period of about 6 years at ambient conditions. The lithium glass was found to be the least hydrated. The sodium glass contained ~5.2 wt. % H_2O whereas the potassium glass was essentially a gel with approximately 32 wt. % H_2O. The lithium glass was estimated to contain less than 0.01 wt. % H_2O [22].

Glass reacts with atmospheric water to produce an alkali-hydroxide layer and a high resistivity inter-diffusion layer. The level of electrode polarization was shown to be correlated with the amount of hydroxyl groups on the glass surface. The structure of the glass surface was characterized by the dielectric measurements and a space-charge model. As an example, the resistivity and thickness of the inter-diffusion layer of 25 mol% Na_2O-SiO_2 glass were estimated.

The space-charge model leads to a reasonable interpretation of dielectric measurements in glass [23].

2.2 Steels

The most abundant corrosive electrolyte on the earth is sea water. The sea or ocean is used for transportation, construction of ports, platforms for petro carbon exploitation, generation of power, intake structures etc. Different types of ocean structural systems comprising of materials like steel, composites, alloys of aluminium, brass and stainless steels are used [24]. The word 'steel' means that iron constitutes the bulk of the material, while the use of the adjective 'stainless' implies absence of staining, rusting in pure and dry air where normal steels are highly susceptible [25]. Uniform and pitting corrosions are generally observed on stainless steels used in the construction of the majority of ships including naval vessels [26]. In the present work discussions have been confined to only for those steels which have been used in this work.

2.2.1. Ferritic stainless steel

The various types of rotating components like impeller blades, pumps, dredging systems, propellers, heat exchangers, and deacerates are used in marine industry. Thus in more aggressive environments, mild steel cannot work sufficiently. High strength, nonmagnetic, cold worked ferritic stainless steels have found applications as construction materials [27]. The excellent corrosion resistance, good mechanical properties with reasonable cost are the contributing factors for their application as outstanding material. When the sea water under pressure comes in contact with rotating components, the components undergoes corrosion fatigue, stress corrosion cracking. If the formation of the oxide film layer on the component is disturbed by impact which results in erosion-corrosion [28].

In seawater process industries, 316-type alloys have been formidable material for construction of evaporators, distiller pipes, pumps valves and condensers. These alloys are the most dependable structural materials under dynamic or flow conditions and virtually show no corrosion even after very long exposures. However, these alloys are subject to localized corrosion in the presence of chloride ions and under static or stagnant conditions. The pitting of 316 L stainless steel is often encountered in desalination plant and appears to be the most effective factor responsible for corrosion failure in plants. The pits also provide active crevices for a formidable corrosion attack. In most cases, pitting is a precursor of crevice corrosion, and there are obvious similarities between crevice and pitting corrosion mechanisms [29]. The great difference in carbon solubility between γ- and α-iron leads normally to the rejection of carbon from the α-phase. The transformation of $\gamma \rightarrow \alpha$ occurs via a eutectoid reaction that plays a dominant role in

heat treatment. The eutectoid temperature is 723 °C and the eutectoid composition is about 0.8 wt. % carbon. On slowly cooling alloys containing less than 0.80 wt.% C, proeutectoid ferrite is formed from austenite in the range 910–723 °C with enrichment of the residual austenite in carbon. At 723 °C, the remaining austenite, containing 0.8 wt. % carbon, transforms to pearlite, a lamellar mixture of ferrite and iron carbide (cementite). In austenite with 0.80–2.06 wt. % carbon, on slow cooling in the temperature interval from 1147 to 723 °C, cementite first forms progressively depleting the austenite in carbon. At 723 °C, the austenite, containing 0.8 wt. % carbon, transforms to pearlite. Ferrite, cementite, and pearlite are thus the principle constituents of the microstructure of plain carbon steels as they are subjected to relatively slow cooling rates to avoid the formation of metastable phases such as martensite and bainite [30].

Mechanism of corrosion occurs by the acceleration of the mass transfer from the metal to the flowing water. The rate of corrosion depends on the rate of dissolution of Fe $(OH)_2$ from the boundary layer and replenished from the base metal. The atmospheric corrosion of carbon steel exposed in Wanning area, which is located in the south part of China with tropic marine environment characters, was studied at different exposure periods (up to 2 years). The weight loss test indicated that the corrosion rate of carbon steel sharply increased during 6 months' exposure and gradually reduced after longer exposure. The results of rust analysis revealed that the underlying corrosion performance of the carbon steel was dependent on the inherent properties of the rust layers formed under different conditions such as composition and structure. Among all the iron oxide, β-FeOOH exerted significant influence. The presence of a monolayer of the rust as well as β-FeOOH accelerated the corrosion process during the initial exposure stage and transformed to γ-Fe_2O_3 in the wet-dry cycle, which was beneficial to protect the substrate and reduced the corrosion rate [31]. The corrosion fatigue initiation and short crack growth behavior of different wrought low-carbon and stabilized ferritic stainless steels was characterized under simulated boiling water reactor and pressurized water reactor [32]. The Si- and Al-bearing steel exhibited excellent corrosion resistance in the exposure test as compared with carbon steel [33].

Guo [34] investigated the corrosion behavior of steels with different carbon content by a salt fog test and an outdoor test. The results indicate that homogenous microstructures, proper amounts of carbon content and fine carbon- rich phases that are produced by appropriate processes are beneficial for the corrosion resistance of steels. Eliyan et al. [35] evaluated the electrochemical corrosion aspects of 13-Cr ferritic stainless steel in bicarbonate solutions. They prepared chloride free and 3 wt.% chloride containing solutions of bicarbonate at 20, 40, and 60 °C. The behavior

exhibited a cathodic dependence on bicarbonate and temperature where the corrosion rates consequently increased. In the presence of chloride, cathodic dependence was temperature dependent [35]. The impact corrosion and abrasion behavior of steels used in the liner of wet-grinding machine in metallurgical industry has been investigated [36]. It was found that under the same simulated conditions, the impact corrosion and abrasion property of the low carbon steel is better than the high manganese steel and the medium carbon alloy steel.

Case hardening by carburization has long been recognized to produce wear-resistant surfaces in steels. Historically, case hardening has not been applicable to chromium-containing alloys such as stainless steels, due to chromium carbide formation that significantly degraded corrosion performance. As a result, the availability of case-hardened alloys for applications in corrosive environments was extremely limited. A new low-temperature (450°–500 °C) para equilibrium carburization technique has been developed for introducing carbon into stainless steel surfaces without formation of carbides. This surface modification technique has been termed Low-Temperature Colossal Supersaturation (LTCSS). Para equilibrium refers to the concept that the diffusion of substitutional solutes (metal atoms) is slower than the diffusion of interstitial solutes (carbon atoms). Substitutional solutes are effectively immobile under LTCSS treatment conditions, whereas carbon can diffuse considerable distances into the alloy. These interstitially hardened surfaces constitute a new branch of engineered materials, in which improved corrosion resistance is attained alongside improvements in wear and fatigue resistance [37]. Also the nano-crystallization of stainless steel greatly improved the corrosion resistance in 0.5M Na_2SO_4 (pH 2) solution [38].

2.2.2. Duplex stainless steel

Duplex stainless steels are a family of grades combining good corrosion resistance with high strength and ease of fabrication. They provide significantly greater strength than the austenite grades while exhibiting good ductility and toughness [39]. The high corrosion resistance and excellent mechanical properties with attractive appearance are the result of chemical composition and uniform microstructure. Due to presence of both austenitic and ferritic phase, the duplex stainless steel shows attractive properties than ferritic stainless steels such as high tensile strength and fatigue strength, good toughness at low temperatures, adequate formability and weldability and excellent resistance to stress corrosion cracking, pitting and general corrosion [40-42].

DSS find an increasing use as an substitute to austenitic stainless steels, mainly where chloride or sulphide stress corrosion cracking are of concern, e.g., in the oil and gas, pulp and paper,

petrochemical industries [43-45]. In general, the DSS with 45% ferrite in matrix exhibits much higher mechanical strength and similar corrosion resistance as compared to standard 304 stainless steels [46]. The dissolution of σ phase to ferrite in DSS at high temperature range strongly depends on the initial distribution and the morphology of σ phase [47-48].

Generally duplex stainless steels with composition (22-26) % Cr – (5-7) %Ni – (0.15-0.25) % N, have yield strengths two to three times higher than those of austenitic stainless steels and also exhibit greater resistance to stress corrosion cracking in chloride environments than does 316 stainless steel [49]. Nitrogen addition in stainless steel raises the UTS, yield strength and produce a variety of markable properties like high ductility and resistance to stress corrosion cracking [40, 50].

Choi et al. [51] analyzed the corrosion behavior of the steels with small amount of Cr, Cu, Ni and Ca in synthetic tap water. It revealed that corrosion rates of all specimens are quite low, especially, Cu, Ni and Ca containing specimens. The lowest corrosion rate observed was due to the formation of insoluble rust layer at the initial stage of corrosion.

In order to clarify some features of atmospheric corrosion mechanisms, two kinds of steels (1 and 4%Ni-bearing steels) were investigated in 0.3%NaCl solution under wet/dry cyclic corrosion tests to simulate the coastal environment. The cross-section of rusted steels was analyzed by ESEM after 100 wet/dry cycles. The results showed that the addition of Ni improved the corrosion protection [52].

Ezuber et al. [53] studied the pitting corrosion characteristics of duplex stainless steel types SAF 2205 and 3RE60 duplex stainless steels in artificial seawater at various test temperatures (25, 50 and 80 °C) . The results clearly indicated that the presence of nitrogen and relatively higher chromium content in the 2205 alloy is an advantage for seawater pitting corrosion resistance. The corrosion resistance of steel in environments of 1 M NaCl solutions saturated in CO_2 was investigated in the absence and presence of different concentrations of thiosulfate at 22 and 50 °C [54]. The corrosion tests revealed remarkable increase in the chloride corrosion rate in the presence of dissolved CO_2 species and corrosion rate increased with increasing thiosulfate concentration. The corrosion testing of steels for 180 days in the Gulf in Kuwait revealed that the corrosion behavior of the materials tends to vary as a function of the rate formation of the marine bio-film on the surface of tested materials [55].

2.2.3. High strength low alloy (HSLA) steel

HSLA grade steels are Cu bearing low carbon steels which were developed by the US navy in the mid-1980's [56-57]. Quenched and tempered microalloyed steels HSLA-80 are alternative

materials to HY-80. These steels offer better weldability due to their extra-low C content. Copper precipitation is one of the main hardening mechanisms available in the HSLA-80 steel which leads to formation of a bainitic microstructure with low C content. The HSLA-80 steel developed maximum hardness during a 600 °C age hardening. These showed a significant hardness decrease during the 700 °C age hardening that was probably due to over aging and tempering effects [58]. Higher strength value obtained at a faster cooling rate of 35 °C/s is due to highly dislocated acicular ferrite structure along with fine precipitation of microalloying carbides and carbonitrides [59]. The observations demonstrate that water-quenched steel has finer multiphase constituents of lath martensite, bainite and twined martensite, whereas air-cooling has resulted in a mixture of bainitic ferrite, retained austenite. When the steel is cooled in sand, the maximum volume fraction of polygonal ferrite was produced [60]. Newer designs of this steel has reduced carbon content upto 0.006 wt.% for better weldability and corrosion resistance [61].

A single scan and multi-scan test was done for low alloy steels in 3.5% NaCl and in seawater. The results obtained in 3.5% NaCl are in good agreement with the results obtained by an immersion corrosion test carried out in sea water [62]. The corrosion behavior of alloy steels was investigated in synthetic potable water. Results showed that all specimens exhibited active corrosion behavior and corrosion rate tended to decrease as a result of adding alloying elements than that of carbon steel and alloying elements existed in protective compounds in the rust layer [63]. Corrosion of the alloy steels was suppressed by insoluble compound formed near the surface [64]. Itagaki et al. [65] also worked on this low carbon steel covered with the ion-exchange membrane to discuss the effect of the ion transfer inside the rust film. The resistance of the rust films of Fe–3% Ni, Fe–1%W and Fe–0.6% Mo was large value, indicating that the low ion permeability rate inside the rust film contributed in decreasing the corrosion rate of low-alloy steel. The corrosion behaviors of the as-quenched Fe–30 wt.%Mn–7 wt.%Al–*x* wt.%Cr–1 wt.%C alloys (*x*=0, 3, 6 and 9) in 3.5% NaCl have been investigated. Passivation could be observed for all the alloys except for the alloy without Cr content. Also the decrease of corrosion rates of the alloy containing 9 wt.% Cr was due to the formation of $(FeMnCr)_7C_3$ carbides in the austenite matrix and on the grain boundaries [66].

2.3. Glass coating

During 70s and 80s, the future of electroplating seemed gloomy but with increasing demand in electronics, space, defense and other engineering industries, the commercial applications of deposition processes increased manifold. About 45% of total share of surface modification is done by industrial painting. Thus, glass and glass–ceramic coatings are not only new generation

of coatings but also versatile engineering materials which increases the service life of different types of metallic substrates. However, corrosion is a major problem for both aerospace and the marine environment. Thus, the prevention of corrosion is very important. To date, there is certain progress towards the implementation of different procedures to reduce corrosion losses. Vitreous (enamel) coatings are glossy inorganic compositions which adhere to metals by fusion and protect them against corrosive conditions to increase the service life of enamelled equipment [67]. The glass ceramic enamels have greater corrosion resistance, resistance to abrasive wear and are widely used in chemical equipment construction [68].

Among various coating systems for industrial and engineering applications, glass and glass–ceramic coatings have advantages of chemical inertness, high temperature stability and superior mechanical properties such as abrasion, impact etc. as compared to other coating materials [69].

Table 2.1. Physico-chemical properties of different coating materials [69].

Properties	Glass–ceramic coating	Stainless steel	Plastic	Anodized aluminium	Stoving paint
Colour performance	Very good	Poor	Good	Poor	Good
Cleanliness	Excellent	Very good	Fair	Fair	Fair
Resistance to heat and light	Excellent	Excellent	Poor	Good	Fair
Resistance to corrosive attack	Very good	Very good	Very good	Good	Poor
Resistance to scratch and abrasion	Excellent	Very good	Poor	Poor	Poor
Resistance to brittleness and chipping	Good	Very good	Poor	Good	Fair
Hygienic	Very good	Fair	Fair	Good	Poor

The purpose of using a glass–ceramic coating, as a new and versatile engineering material, is to prevent abrasion, corrosion, thermal failure and oxidation during heat treatment. These are the primary objectives for choosing a glass–ceramic coating against all other types of available coating materials as mentioned in Table 2.1 and also its ranges of application is shown in Fig. 2.1. Glass science is an important and increasingly challenged technology in today's automotive business. Each year manufacturers use more glass surface area with more complex shapes [70]. Glass-ceramic enamel coatings around the outer periphery of automotive glass provide UV protection to the underlying adhesive holding the glass to the vehicle frame. The black enamel coatings also provide a decorative function by hiding adhesive layer unevenness and by enhancing the appearance of the glass. Enamels are screen printed on cut sheets of soda-lime-silica float glass, dried, and sintered during the forming and heat strengthening of the substrate.

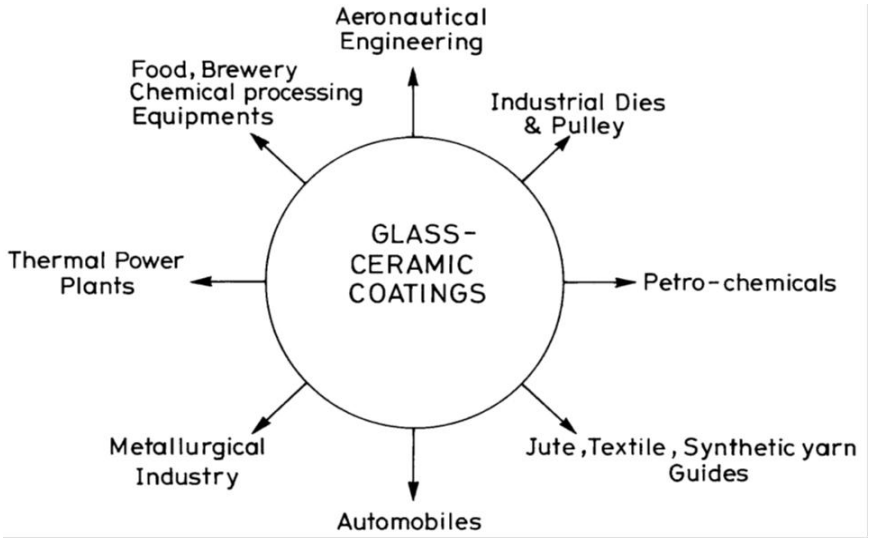

Fig. 2.1: Areas of application of glass–ceramic coatings [71].

Basalt-based glass coating was performed on AISI 1040 steel substrate which was pre-coated with Ni–5 wt% Al by using plasma spray gun and crystallized at 800, 900 and 1000 °C for 1–4 h in orders to transform glass to glass–ceramic structure [72]. It was found that, the lower the crystallization temperature with longer treatment time led to harder coating layer.

Metallic amorphous coating on a mild steel substrate revealed that the corrosion resistance of the coating deteriorated with the increase in the amount of crystalline phase. The detailed investigation by SEM/EDX indicated that pits always initiated at the boundaries around the carbide precipitates. To passivate the corrosion, a chromate treatment was performed on the crystallized coating, which leads to the recovery of the corrosion resistance of the coating [73]. The amorphous coating possess three types of corrosion protections (i) functions as a local corrosion barrier, (ii) serves as a sacrificial anode, and (iii) supplies soluble ions used as corrosion inhibitors by engineering metallurgical and electrochemical properties [74]. Das et al. [75] employed microwave processing to obtain hard glass-ceramic coating on nickel based superalloy substrate. The glass-ceramic coatings were developed from a glass based on MgO–Al_2O_3–TiO_2 system. Results confirmed that the microwave processed coating possessed much higher hardness and lower surface roughness as compared to that of the conventionally processed coating. Protective SiO_2–Al_2O_3–CaO–Na_2O glass–ceramic based coating produced on titanium metal by slurry technique was investigated. It was found that the coating contains crystalline phases; $CaSiO_3$, $NaAlSiO_4$, Na_2CaSiO_4 and amorphous phase consisting mainly O, Si and Al. It was established that glass–ceramic coating formed on TIMETAL 834 essentially improves the alloy selected properties, e.g. its hardness and high temperature oxidation resistance [76].

2.3.1. Effect of additives in the glass composition

Basically, the composition of raw materials used for glass making plays an important role in the formation of glass and its crystallization leading to formation of various crystalline phases during enamelling operation. Therefore, the role of initial constituents and their molar ratio is also key point of discussion. Several additives are used to optimize the properties of the glass coating. However, the choice of additives is restrictive as they do not influence just one property of the coating but they also affect the other properties of glasses. Al_2O_3, for instance, improves flux, thus making a better join. On the other hand, higher content of Al_2O_3 decreases the thermal expansion, as it promotes the formation of a detrimental crystalline phase, which exhibit low thermal expansion coefficient [77]. Similarly, Na_2O acts as the most effective flux, but it makes the glass soluble in water. Na_2O can be replaced by K_2O but K^+ cations enhance the volatility of chromium [78-79] leading to the formation of undesirable low TEC phases [80-83]. Bloom et al. [84] evaluated a commercial glass, Corning 0080, for possible use as coating. It is a soda-lime glass, with TEC of 9.35 x 10^{-6} /^{o}C. The effects of various additives on the properties of glass used to have better seal (coating) are listed in Table 2.2.

Table 2.2: Effect of additives on various properties of glasses [85-87, 77, 88-91].

Additive	Effect
Al_2O_3	Improves flux. Prevents rapid crystallization of glass during heat treatment and also increases surface tension of glass. Too much Al_2O_3 decreases thermal expansion as it promotes the formation of crystalline phase with low TEC.
Na_2O, K_2O	Act as effective flux but the alkali cations react vigorously and increases dissolution in water
La_2O_3, Nd_2O_3, Y_2O_3	Increase TEC, T_g, T_M
B_2O_3	Improves flux, reduces T_g, surface tension and stability of glass
ZnO, PbO	Improves flux, reducing agent
Cr_2O_3, V_2O_5	Reduces surface tension
NiO, CuO, CoO, MnO	Improves adhesion
TiO_2, ZrO_2, SrO, MgO, Cr_2O_3, Ni	Stimulates crystallization
Sb_2O_5	Oxidizing agent
P_2O_5	Decreases volatilization, reduce TECs and mechanical strength

The effect of small additions of TiO_2 and P_2O_5 has been studied. These agents enhance the nucleation of crystals in the glasses and induced phase separation in glasses. Tomozawa [92] explained the greater tendency of phase separation of P_2O_5 over TiO_2 as a result of higher ionic potential (Z/r) of phosphorous than titanium ions. TiO_2 is quite soluble in silicate glasses and

lowers their viscosity considerably. At least three different mechanisms have been proposed for the action of nucleating agents. Their role can be classified such as nucleation agent for crystallization, catalysts of phase separation, and reduction of interfacial tension. Barry et al. [93] have extended this idea in developing a detailed model for the enhancement of nucleation by titania in lithium aluminosilicate glasses. According to them, Ti^{4+} ions associate with the non-bridging oxygen ions, causing these ions and alkalis to concentrate at the edge of domains enclosing bridging oxygens.

2.3.2. Some examples of interaction between glass and steels

Pech et al. [94] investigated wetting and sticking of soda-lime glass on two types of stainless steel as well as on platinum. The glass/steel specimens exhibited two different behaviours during cooling. With the oxidized steel, sticking down to room temperature was observed. With non-oxidized steel, detachment was observed before reaching room temperature. Further analysis of the surface leads to the conclusion that there is no significant chemical reaction between glass and stainless steel in a neutral gas environment. The main effect of glass/steel interaction is an enhancement of grain boundary grooving on the stainless steel surface. The glass wets stainless steel with a final contact angle ( ) close to 70°. However, temperature has a negligible effect on

but strongly affects the spreading rate. Some of the results of glass coatings on surface of steels are summarized in Table 2.3.

Table 2.3: Interaction between various systems of glasses with steels.

Author	Materials used	Results
Smeacetto et al. [95, 96]	Sodium–Calcium–Aluminosilicate Glasses / Crofer22 APU and AISI 430	Strong adhesion between samples in which glasses have less silicon oxide.
Nielsen et al. [97]	Sodium Aluminosilicate Glass with MgO-filler / Fe78Cr22 steel	Reducing the average grain size and amount of MgO-filler further reduced the depletion of the sodium glass in the interface zone.
Batfalsky et al. [98]	Glass (BaO, CaO, Al_2O_3, SiO_2) with minor amount PbO/Ferritic steels	Increasing the Si content of the ferritic steel increases the corrosion rate.
Meinhardt et al. [99]	Barium Aluminosilicate Glasses modified with CaO and $B_2O_{3/}$ FeCrAlY and AISI 446	A reaction zone developed between the glass and the stainless steels contain oxide of both chromia and alumina.
Iost et al. [100]	Na_2O-CaO-P_2O_5 glass/ Aluminized steel	Alumina layer formed in a reaction zone and acts as a barrier for the iron diffusion.
US Patent [101]	Borosilicate glass with Co as additive/ Ballistic steel	Ni content of steel and Co additive promotes the adhesion.

References

1. G. W. Morey, Indust. Eng. Chem. 17 (1925) 389-392.
2. D.E. Clark, E. Y.-B. Lue, Surf. Sci. 100 (1980) 53-70.
3. M.T. Tognonvi, J. Soro, J.-L. Gelet, S. Rossignol, J. Non-Cryst. Solids 358 (2012) 492–501.
4. H. Franz, J. Non-Cryst. Solids 42 (1980) 529-534.
5. Schott, Zts. Instrumentenkunde 9 (1889) 86-90.
6. F. Foerster, Ber. Deutsch. Chem. Ges. 26 (1893) 2915-2922.
7. Barus, Am. J. Sci. 4, (1900) 161.
8. R. H. Doremus, Diffusion in Glasses and Melts,(1994) 1-9.
9. W.H. Zachariasen, J. Am. Chem. Soc. 54 (1932) 3841.
10. G.N. Greaves, in: Glass Science and Technology, Vol. 4B eds. N. Kreidl and D. Uhlmann, Academic Press, New York, 1990.
11. W. Beier, G.H. Frischat, J. Non-Cryst. Solids 73 (1985) 113-133.
12. G.S. Henderson, Can. Mineral. 43 (2005) 1921-1958.
13. A.C. Hannon, B. Vessal, J.M. Parker, J. Non-Cryst. Solids 150 (1992) 97-102.
14. S.J. Gurman, J. Non-Cryst. Solids 125 (1990) 151-160.
15. G.N. Greaves, W. Smith, E. Giulotto, E. Pantos, J. Non-Cryst. Solids 222 (1997) 13-24.
16. B. Tischendorf, C. Ma, E. Hammersten, P. Venhuizen, M. Peters, M. Affatigato, S. Feller, J. Non-Cryst. Solids 239 (1998) 197-202.
17. F. G. K. Baucke, Electrochim. Acta, 39 (1994) 1223-1228.
18. B.C. Bunker, J. Non-Cryst. Solids 179 (1994) 300-308.
19. C.T. Lee, D.E. Clark, Appl. Surf. Sci. 20 (1985) 397-412.
20. D.E. Day, G.E. Rindone, J. Amer. Ceram. Soc. 45 (1962) 496.
21. T.D. Taylor, G.E. Rindone, J. Non-Cryst. Solids, 14 (1974) 157-164.
22. Naresh Pandya, David W. Muenow, Shiv K. Sharma, Barbara L. Sherriff, J. Non-Cryst. Solids 176 (1994) 140-146.
23. M. Tomozawa, C.H. Kim, R.H. Doremus, J. Non-Cryst. Solids 19 (1975) 115-123.
24. M.R. Pranesh, Corrosion in marine industry, Technology appreciation programme on corrosion prevention in industry (1993) 34-44.
25. D. Peckner, I.M. Bernstein (Eds.), Handbook of stainless steels, McGraw-Hill, 1977.
26. M.T. Gudze, R.E. Mechers, Corros. Sci. 50 (2008) 3296-3307.
27. S.K. Coburn, Corrosion source book American Society for Metals, Library of Congress catalog, USA, 1984.
28. J.K. Robert, Wood, Wear 261 (2006) 1012–1023.
29. Emilie Malard, Dominique Kervadec, Otavio Gil, Yves Lefevre, Sophie Malard, Electrochim. Acta 54 (2008) 8–13.
30. C. Garcı´a de Andre´s, F.G. Caballero, C. Capdevila, L.F. A ´lvarez, Mater. Charact. 48 (2002) 101– 111.
31. Y. Ma, Y. Li, F. Wang, Mater. Chem. Phys. 112 (2008) 844–852.
32. H.P. Seifert, S. Ritter, H.J. Leber, Corros. Sci. 59 (2012) 20-34.
33. T. Nishmura, Corros. Sci. 52 (2010) 3069-3614.
34. J. Guo, S. Yang, C. Shang, Y. Wang, X. He, Corros. Sci. 51 (2008) 242–251.
35. F. F. Eliyan, E.-S. Mahdi, A. Alfantazi, Corros. Sci. 58 (2012) 181–191.
36. D. Hou-fu, C. Fang-ming, D. Xiao-dong, Mater. Sci. Eng. A 421 (2006) 161–167.
37. P.M. Natishan, F.J. Martin, E.J. Lemieux, T.M. Newbauer, R. Rayne, R.A. Bayles, Mater. Sci. Tech., NRL Review (2008) 171-172.
38. W. Ye, Y. Li, F. Wang, Electrochim. Acta 54 (2009) 1339–1349.
39. J. Charles, Duplex Stainless Steels 97-5th world conference, Stainless Steel World, 29-42.
40. J. Olsson, M. Snis, Desalination, 205 (2007) 104-113.

41. E. I. Kivineva, N. E. Hannerz, Proceedings of the Fourth International Conference on Duplex Stainless Steels, 2 (1994) 13-16 November.
42. I. Calliari, M. Zanesco, E. Ramous, P. Bassani, JMEPEG, 16 (2007) 109-112.
43. V. Muthupandi , P. Bala Srinivasan , S.K. Seshadri, S. Sundaresan, Mater. Sci. Eng A358 (2003) 9- 16.
44. L. F. Garfias, J. M. Sykes, C. D. S. Tuck, Corros. Sci. 38 (1996) 1319- 1330.
45. S. S. M. Tavares, J. M. Pardal, L. D. Lima, I. N. Bastos, A. M. Nascimento, J. A. de Souza, Mater. Charact. 58 (2007) 610-616.
46. I.-ul-Haq Toor, P. J. Hyun, H. S. Kwon, Corros. Sci. 50 (2008) 404-410.
47. J.W. Elmer, T.A. Palmer, E.D. Specht, Mater. Sci. Eng. A 459 (2007) 151–155.
48. K.W. Wong, C.H. Shek, W. Zhang, J.K.L. Lai, Mater. Letters 62 (2008) 3991–3994.
49. H.-S. Kwon and H. S. Kim, Mater. Sci. Eng. A172 (1993) 159-166.
50. J. Wang, P. J. Uggowitzer, R. Magdowski, M.O. Speidel; Scripta Materialia 40 (1999) 123–129.
51. Yoon-Seok Choi, Jae-Joo Shim, Jung-Gu Kim, Mater. Sci. Eng. A 385 (2004) 148–156.
52. Xinhua Chen, Junhua Dong, Enhou Han, Wei Ke, Mater. Letters 61 (2007) 4050–4053.
53. H. M. Ezuber, A. El-Houd, F. El-Shawesh, Desalination 207 (2007) 268–275.
54. H.M. Ezuber, Mater. Des., 10.1016/j.matdes.2009.03.028.
55. K. Al-Muhanna, K. Habib, Desalination 250 (2010) 404–407.
56. P. J. Uggowitzer, R. Magdowski, M. O. Speidel, ISIJ International 36 (1996) 901-908.
57. E.J. Czyryca, Key Eng. Mater. 84-85 (1993) 491-521.
58. A. Augusto Gorni, P. Roberto Mei, J. Mater. Process. Tech. 155–156 (2004) 1513–1518.
59. A. Ghosh, S. Das, S. Chatterjee, P. Ramachandra Rao, Mater. Charact. 56 (2006) 59–65.
60. S. Das, A. Ghosh, S. Chatterjee, P. Ramachandra Rao, Mater. Charact. 50 (2003) 305– 315.
61. S. Das, A. Ghosh, S. Chaterjee, P. R. Rao, Scand. J. Metal. 33 (2004) 203-210.
62. Y. Yu, J.L. Gu, L. Xu, F.L. Shou, B.Z. Bai, Y.B. Liu, Mater. Desig. 47 (2010) 262–271.
63. Gan Yang, Li Ying, Lin Haichao, Corros. Sci. 43 (2001) 397-411.
64. Yoon-Seok Choi, Jae-Joo Shim, Jung-Gu Kim, J. Alloy. Comp. 391 (2005) 162–169.
65. M. Itagaki, R. Nozue, K. Watanabe, H. Katayama, K. Noda, Corros. Sci. 46 (2004) 1301–1310.
66. Y.H. Tuan, C.S.Wang, C.Y. Tsai, C.G. Chao, T.F. Liu, Mater. Chem. Phys. 114 (2009) 595–598.
67. A.I. Andrews, Porcelain enamel (Illinois- The Garrard Press).
68. T. A. Dmitrienko, Corrosion Resistance of Glass Ceramic Enamel.
69. A. Majumdar, S. Jana, Bull. Mater. Sci. 24 (2001) 69–77.
70. J. Dolenga, Glass Magazine, May (1986) 69-76.
71. T. E, Schmid, Heeht, Ceram. Engg. Proc. 9 **(**1988) 1089.
72. S. Yılmaz, G. Bayrak, S. Sen, U. Sen, Mater. Desig. 27 (2006) 1092–1096.
73. Y. Yang, C. Zhang, Y. Peng, Y. Yu, L. Liu, Corros. Sci. 59 (2012) 10–19.
74. F. Presuel-Moreno, M. A. Jakab, N. Tailleart, M. Goldman, J. R. Scully, Mater. Today, 11 (2008) 10, 14-23.
75. S. Das, A.K. Mukhopadhyay, S. Datta, G.C. Das, D. Basu, J. Eur. Ceram. Soc. 28 (2008) 729–738.
76. T. Moskalewicz, F. Smeacetto, A. Czyrska-Filemonowicz, Surf. Coat. Tech 203 (2009) 2249–2253.
77. D. Bahadur, N. Lahl, K. Singh, L. Singheiser, K. Hilpert, D. Bahadur, J. Electrochem. Soc. 151 (2004) A558.
78. S. P.Jiang, L. Christiansen, B. Hughan, K. Foger, J. Mater. Sci. Lett. 20 (2001) 695.

79. N. Lahl, L. Singheiser, K. Hilpert, K. Singh, D. Bahadur, Solid Oxide Fuel Cells-VI, edited by S. Singhal, M. Dokiya (Electrochemical Society, Pennington, NJ, PV 99-19 (1999) 1057.
80. C. Lara, M. J. Pauscal, A. Duran, J. Non-Cryst. Solids 348 (2004) 149.
81. D. Stolen, E. Monreal, W. Miller, In Fuel Cell Seminar Abstracts, Tucsan, AZ, November 29th - December 2nd (1992) 53.
82. Y. Harufuji, Jpn Kokai Tokyo JP 04-47, 672 (Feb. 17, 1992).
83. Z. Yang, J. W Stevenson and K. D. Meinhardt, Solid State Ionics 160 (2003) 213.
84. I. D. Bloom, K. L. Ley, U.S. Pat. 5453331, Sept. 26, 1995.
85. K. Ley, M. Krumplet, R. Kumar, J. Meiser, I. Bloom, J. Mat. Res. 11 (1996) 1489.
86. I. Gutzow and J. Schmelzer, The Vitreous State, Springer, Berlin, 1995.
87. N. Lahl, K. Singh, L. Singheiser, K. Hilpert, D. Bahadur, J. Mater. Sci. 35 (2000) 3089.
88. P. H. Larsen, F. W. Poulsen, R. W. Berg, J. Non-Cryst. Solids 244 (1999) 16.
89. Robert A Meyers, Encyclopedia of Physical Science and Technology, (Academic Press Inc. 1987) Vol. 6.
90. K. Singh, N. Gupta, O. P. Pandey, J. Mater. Sci. 42 (2005) 6426.
91. T. Schwickert, R. Sievering, P. Geasee and R. Conradt, Mat.-wiss.u. Werkstofftech. 33 (2002) 363.
92. M. Tomozawa, Amer. Ceram. Soc. 27 (1971) 41.
93. T. J. Barry, D. Clinton, L. A. Ray, R. A. Mercer, and R. P. Miller, J. Mater. Sci. 4 (1969) 496.
94. J. Pech, M. Braccini, A. Mortensen, N. Eustathopoulos, Mater. Sci. Eng. A 384 (2004) 117-128.
95. F. Smeacetto, M. Salvo, M. Ferraris, V. Casalegno, P. Asinari, J. Eur. Ceram. Soc. 28 (2008) 611–616.
96. F. Smeacetto, M. Salvo, M. Ferraris, V. Casalegno, P. Asinari, A. Chrysanthou, J. Eur. Ceram. Soc. 28 (2008) 2521–2527.
97. K.A. Nielsen, M. Solvang, S.B.L. Nielsen, A.R. Dinesen, D. Beeaff, P.H. Larsen, J. European Ceramic Society 27 (2007)1817–1822.
98. P. Batfalsky, V.A.C. Haanappel, J. Malzbender, N.H. Menzler, V. Shemet, I.C. Vinke, R.W. Steinbrech, J. Power Sources 155 (2006) 128–137.
99. K.D. Meinhardt, D.S. Kim, Y.S. Chou, K.S. Weil, J. Power Sources 182 (2008) 188–196.
100. A. Iost, R. Bigot, F. Barbieux, P. Vast, J. Mater. Sci. 34 (1999) 3991-3996.
101. United States Patent, Glass coated high strength steel, 6087013, 2000.

Chapter 3

EXPERIMENTAL TECHNIQUES

Overview

In this chapter, experimental procedures followed to prepare glasses of different compositions, the specifications of different steels used and procedure adopted to prepare diffusion couple from these materials is described. Further the preparation of working electrode, cell and testing solution for corrosion testing is also discussed. The characterization procedures along with instrument's model number, working and operating conditions have been given.

3.1. Introduction

Processing parameters play very important role to tailor the properties of the prepared samples. The characterization and testing of materials using different techniques are described in this chapter.

3.2. Materials

3.2.1 Preparation of glasses

In the present study, raw materials used for preparing glass samples were SiO_2 (99%, CDH), Al_2O_3 (99.9%, CDH), CaO (99.9%, CDH), TiO_2 (99%, Sigma Aldrich), and Na_2CO_3 (99.995%, Sigma Aldrich). All these materials were used without any further purification. Glass compositions with their level are given in Table 3.1.

Table 3.1: Glass compositions (mol %) with their label.

Sample Label	SiO_2	CaO	Al_2O_3	Na_2O	TiO_2
N-25	45	15	10	25	5
N-20	50	15	10	20	5
N-15	55	15	10	15	5
N-10	60	15	10	10	5

For each composition, required amount of raw materials as per the stoichiometric ratio were taken. The mixture was ground in agate motor and pastel to break agglomerate particles. After grinding, the mixture was transformed to ball mill and ground further for two hours in dry medium. The ball milling was done using agate balls in agate jar (Retsch, Germany, Model PM100). The mass to ball ratio for each system was 1**:**2 which was kept constant for each milling. The mixed powder of the homogenous mass was transformed in recrystallized alumina crucible and heated in an automized Molybdenum Disilicide ($MoSi_2$) high resistance furnace in oxidizing atmosphere. The crucible containing powders was initially heated to 1000 ºC at a heating rate of 10 °C/min. The temperature was maintained at 1000 ^oC for 45 minutes to facilitate the calcination. During heating process moisture is released and the calcination occurs. After that the temperature was increased to 1200 ^oC at a rate of 5 ºC/min and kept at this temperature for 30 minutes to facilitate the fusion and melting process. Then, the temperature was raised to 1500 ºC by keeping constant heating rate (5 ºC/min) and kept at this temperature for 1 h 45 minutes in order to achieve the homogeneous molten glass. The schedule followed for sample melting is also shown in Fig. 3.1.

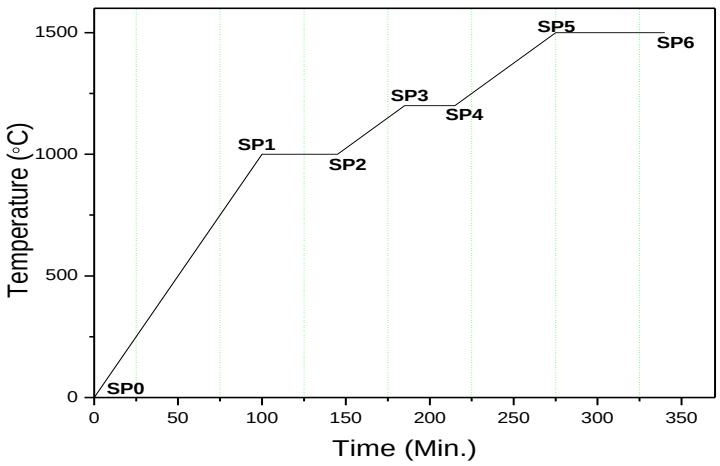

Fig. 3.1: Typical schedule followed for the melting of the glass samples.

The molten mass was poured in a preheated steel mould as shown in Fig. 3.2. The remaining melt was poured on the flat copper plate and quenched by other copper plate in air to obtain flakes. All the samples were prepared using the same route as described above. Before melting, the furnace was calibrated where fluctuation in temperature in hot zone was within ± 2 ^{o}C. The glass ingots were annealed at 400 ^{o}C (below T_g) for 10 hs in air. The annealing process is done to remove the internal stresses generated during quenching process.

Fig. 3.2: Process of pouring the glass in steel mould at 1500 ^{o}C.

Apart from above mentioned glasses, two commercial grade glasses used in automobile industries and manufactured by Saint Gobain Glass industries, Mumbai were also selected for this work and has been designated as S and X glass. The compositions of S and X glass are given below:

Table 3.2: S and X glass composition (wt. %) with their label.

Substance	S glass	X glass
SiO_2	72.46	72.46
Al_2O_3	1.23	1.23
CaO	9.23	9.23
MgO	2.23	2.23
Na_2CO_3	14.23	14.85
Synthetic Fe_2O_3	0.61	--

3.2.2. Preparation of steel specimen

Steel is the most commonly employed material utilized for the construction of major structural units used in aqueous environments. Three types of steels were selected for the study. The composition of these steels as provided by the supplier is given in Table 3.4. Samples of 1 cm × 1 cm and 2.0 cm × 2.0 cm were cut for further study from the supplied sheet. The surfaces of the test specimens were initially prepared by polishing them using a series of successively finer grades of silicon carbide abrasive papers.

Table 3.3: Chemical composition of steel (wt. %).

Element	Fe	Mn	P	S	Si	Ti	Ni	Cu	N	Mo	Cr	V	Al	Nb	Sb	As	Ta	C
Crofer	76.6	0.4	0.013	--	0.017	0.06	--	--	--	--	22.6	--	--	--	--	--	--	--
HSLA	94.03	1.0	0.09	0.001	0.34	0.003	1.77	1.23	--	0.51	0.61	0.004	0.025	0.037	0.003	0.005	--	0.05
Duplex	69.88	0.82	0.032	0.003	0.053	--	10.09	0.34	0.04	2.02	16.22	--	--	--	--	--	--	0.02
SS	73	0.1	0.01	0.008	0.01	--	3	3	0.01	2	12.3	--	0.75	0.3	--	--	0.45	0.04

3.2.3. Glass coating

The steel pieces were degreased by ultrasonic cleaner in acetone media. After that, these pieces were dipped in a solution of 5% HNO_3 for 5 min to dissolve any oxide layer existing on the surface and washed properly. The glass coating was applied onto the cleaned substrate surface of steel by slurry method. Basically, slurry method is enameling technique which is already in use in different industries, where glass is crushed to finer than granulated sugar but coarser than flour. This powder is applied on the metal surface by preparing slurry of glass in different liquid. After that, slurry article is dried and heated up to the melting point of glass for desired time period. The article after heat treatment is removed from furnace and cooled to room temperature. In the present study, slurry containing 50% glass powder was prepared by dispersing fine glass powder in ethanol. The slurry of thickness 1 mm was manually deposited on steel surface with the help of fine stick. The as deposited slurry on substrate was dried at room temperature. After draying, the entire assembly was heated at 900 °C for 1 h in air atmosphere at a heating rate of 10 °C/min.

3.2.4. Corrosion testing

3.2.4.1. Preparation of electrochemical cell

For corrosion experiments, Cu wire was soldered at the center of the bottom end of steel. The size of diffusion couple for corrosion testing was 20 × 20 mm. On the top portion of couple a cylindrical plastic tube (Fig. 3.3.) was fixed. The bottom side of tube was sealed and insulated from the remaining part of the specimen using 'Rapid Araldite' two-component epoxy resin to give the required area of 10 mm diameter which is exposed area for corrosion study as shown in Fig. 3.3.

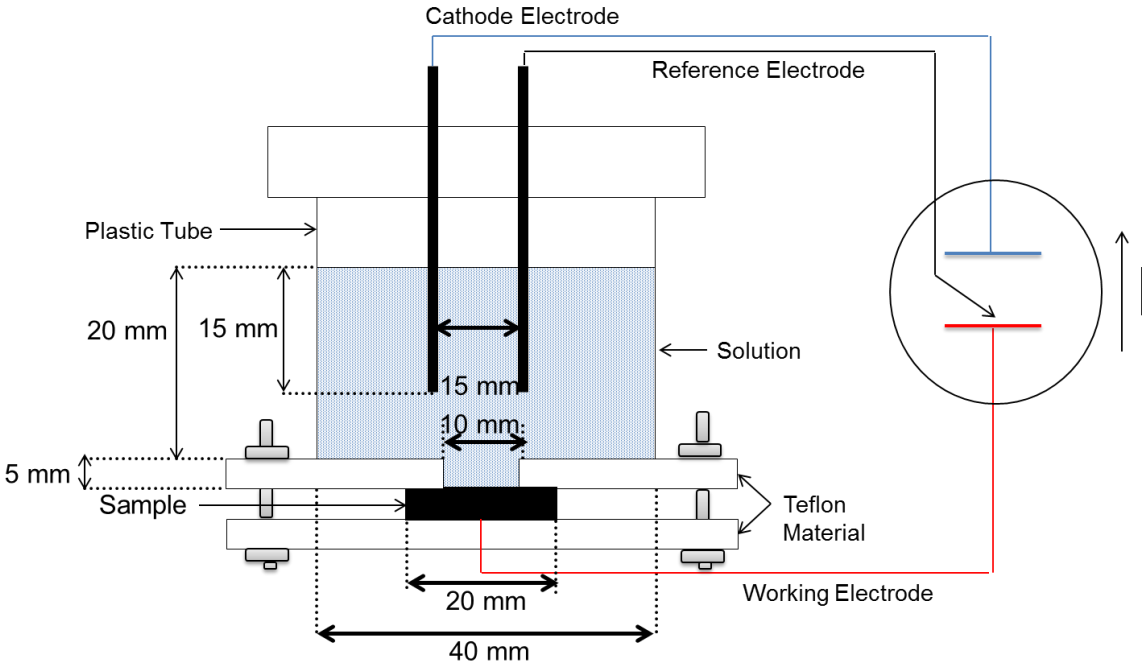

Fig. 3.3: Schematic diagram of the experimental setup.

3.2.4.2. Preparation of testing solution

The chemical composition chosen to prepare the artificial seawater electrolyte solution was based on the standard formulation given by Lyman and Fleming [1]. The chemical formulation of it is given in Table 3.5. The pH of the testing solution varied between 7.4 and 7.6, but was usually around 7.5.

Table 3.4: Chemical composition of artificial seawater [1].

Composition	NaCl	$MgCl_2$	Na_2SO_4	$CaCl_2$	KCl	$NaHCO_3$	KBr	H_3BO_3	$SrCl_2$	NaF
g (as per 1000g solution)	23.939	5.079	3.994	1.123	0.667	0.196	0.098	0.027	0.024	0.03

For each set of experiments, 1 liter of artificial seawater solution was prepared. The sequence of steps followed to prepare the solution is as follows:

(a) Initially, 23.939 grams of sodium chloride was added to 200 ml of deionized water in a beaker. The solution was stirred till the salt was completely dissolved. This initial saline solution was then poured into 1 liter high density polyethylene bottle. This solution was the primary stock salt solution. All further solutions prepared were then added in turn to this main stock solution.

(b) Similarly $MgCl_2$, Na_2SO_4 and $CaCl_2$ solution was prepared by taking required quantity of salts as given in Table 3.5 in 100 ml of deionized water separately as mentioned above. Each prepared additional solution was then added to the original stock sodium chloride solution prepared previously, and stirred until totally mixed.

(c) The remaining 6 compounds listed in Table 3.5 were prepared by adding each compound in turn the mass given in Table 3.5, to 100 ml of deionized water in a separate beaker, whilst continuously mixing using a magnetic stirrer. This final solution was then added to the original main stock solution prepared previously. Finally, additional amount of deionized water was added to get a final solution of exactly 1liter. The stability of solution was checked by keeping it for one day ensuring no precipitation phenomenon.

3.3. Characterization of materials

Glasses and glass ceramics along with diffusion couple (before and after corrosion test) prepared from different steels were characterized using different techniques. These are described below:

3.3.1. X-ray diffraction

The amorphous and crystalline nature of samples was characterized by X-ray diffraction technique (XRD) using X'Pert Pro, PANalytical model of Philips, Netherlands. During the experiment, the scan speed was 0.02º/ min with Cu Kα (λ=1.54 Å) radiation. The crystalline phases obtained after heat treatment was identified by International Centre for Diffraction Data (ICDD) files. The process of X-ray diffraction actually measures the d-spacings of the crystal, and from this information it is possible to determine the crystal structure and lattice parameters. A typical X-ray diffraction pattern is in the form of a graph, with a series of peaks with the horizontal axis being 2θ, or twice the Bragg angle and the vertical axis is the intensity or the X-ray count measured by the detector, which is a function of the crystal structure and the orientation of the crystallites. Although the diffraction pattern is given as a 2-dimentional graph, the radiation diffracted by any sample is in the form of cones, known as Debye Cones.

3.3.2. Differential thermal analysis

Differential thermal analysis (DTA) is a thermoanalytic technique, similar to differential scanning calorimetry. In DTA, the material under study and an inert reference are heated (or cooled) under identical conditions, while recording any temperature difference between sample

and reference. This differential temperature is then plotted against time, or against temperature (DTA curve). Changes in the sample, either exothermic or endothermic, can be detected relative to the inert reference. Thus, a DTA curve provides data on the transformations that have occurred, such as glass transitions, crystallization and melting.

In the present work differential thermal analysis of the powdered samples was done by Perkin Elmer (Diamond TG/DTA) in nitrogen atmosphere using platinum crucibles at different heating rates from room temperature to 1200 °C. The reference sample taken was α-alumina.

3.3.3. Dilatometric measurement

Thermal dilatometric analysis (TDA), often called "dilatometry", measures the dimensional change of a material (ceramics, glasses, metals, composites and others) as a function of temperature or time. This test determines both reversible and irreversible changes in length (expansion and shrinkage) during heating and cooling, and pinpoints where reactions that occur cause expansion or contraction. The dilatometer is used to determine Coefficient of Thermal Expansion (CTE), softening point, glass transition temperature, Curie point, crystalline transformation, phase transition, shrinkage, warping, bloating, sintering rate, isothermal creep and stress relaxation. In the present work dilatometery of the well-polished glass frits was done by dilatometer, Netzsch (DIL 402 PC) in air using alumina kit including alumina push rod at a heating rate of 5^{o}C/min from room temperature to a specific temperature depending upon the sample requirement. Thermographs has been taken between temperature and percentage change in length of the sample. Thermal expansion coefficient of all the glass samples was measured at various temperature ranges.

3.3.4. Fourier transform infra-red spectroscopy

Fourier transform infra-red spectroscopy (FTIR) spectra of original glass and dipped glass were taken to compare the change after dipping in solution. It can identify their functional groups and their attachment with other groups. FTIR spectra were recorded in the range 400-2000 cm^{-1} using Perkin –Elmer's spectrum RX-1. Samples were prepared by taking glass (2 mg) and KBr (200 mg) powders. The powder was mixed and compacted into 13 mm diameter pellets.

3.3.5. UV/Visible spectroscopy

For UV/visible spectroscopy, fine powders of glass were made as a homogenous by dissolving it in a transparent solvent. Liquids contained in a vessel known as a cell or cuvette made of transparent material (plastic). Then sample's intensity was measured using UV-Visible detector (ELICO 120 double beam spectrophotometer). The absorption spectrums were recorded at room temperature in the range 200-700 nm.

3.3.6. Dielectric measurements

The dielectric response of glass samples was measured over a frequency range of 20 Hz to 1 MHz using an Agilent 4284A analyzer in the temperature range of 30 °C to 450 °C. All the measurements were performed in air at the heating rate of 5 °C/min with temperature stability ± 1 °C. Silver paste was applied on both sides of the glass samples to connect it with electrode for dielectric measurements.

3.3.7. P-E loop measurements

Ferroelectric hysteresis loop measurements of glass samples were performed using TF Analyzer 2000 (aixACCT Systems). The values of remnant polarization (P_r) and coercive field (E_c) were determined from hysteresis loop.

3.3.8. Scanning electron microscopy

The Scanning Electron Microscopy (SEM) investigations in this study were undertaken using a SEM (JSM-6510lv, JEOL) which has a resolution of around 3 nm. Gold sputtering on the surface of specimen was done to avoid charging effect [2]. The associated analytical facility of OXFORD EDS was used to identify and quantify the elemental composition of the deposited surface films on the sample surfaces, formed as a result of immersion in different electrolytes. Energy Dispersive X-Ray Analysis (EDS) was also used to determine the distribution of elements over the surface of the sample. The analyses performed using the Imaging Mode of the EDS facility were carried out using the system operating in either Electron Mapping Mode or Line Scan Mode. The Electron Mapping Mode indicates the occurrence and distribution of selected elements over the sample surface; either singly, or in combination, and/or overlaid over the corresponding secondary electron image. The Line Scan Mode shows the quantitative variation in the relative percentages of several selected elements over a pre-determined line on the sample surface.

3.3.9. Inductively coupled plasma spectrometry

The sector field inductively coupled plasma spectrometry (ICPS) instrument used was tile ELEMENT (Finnigan MAT, Bremen, Germany) equipped with an ASX 500 sample changer (CETAC Technologies Inc., Omaha, USA). In this study, the device was operated in low resolution mode (LRM, *m/Dm* about 300) to analyse dissolved quantity of glass elements in 3.5% NaCl solution.

3.3.10. Potentiostatic studies

Potentiostat made by BioLogic Science Instruments (SP-300) was used to provide a constant voltage and the value of the applied voltage could be adjusted using an in-built variable

resistance and calibration board. Thus a calibration routine allows running after 24 h to ensure reliable and accurate measurements. An electrochemical Impedance Spectroscopy (EIS) measurement was added as an option to the **SP-300**. The built-in FRA has a frequency range of 10 μHz up to 7 MHz. The high frequency measurement was made with an accuracy of 1%/1° up to 3 MHz and 3%/3° to 7 MHz. The **EC-Lab®** software used for interpretation of corrosion data as well as equivalent circuit modeling for impedance data. A saturated calomel electrode (SCE) was used as reference and a platinum wire as counter. The surface area of the test coupons (Fig. 3.3) exposed to the electrolyte solution was $1cm^2$. The temperature of the solution was determined by the laboratory temperature which during the period of the experiments reported here varied between 18 to 22 °C. Polarization curves of samples were recorded after 2h immersion time in the solution within the range of -1 V to at least +1 V vs. open circuit potential (OCP) at a scan rate of $0.167mVs^{-1}$. All potential values were referred to SCE. The impedance data were obtained at the open circuit potential. When the corrosion potential remained stable, a sinusoidal AC signal of 10 mV (rms) amplitude at the open circuit potential (OCP) was applied to the electrode over the frequency which ranged from 10^{-2} Hz to 10^5 Hz with 10 points per decade.

References

1. F. J. Millero, Chemical Oceanography, Taylor and Francis, CRC, Miami, 2006.
2. J. Goldstein, D. E. Newbury, D. C. Joy, C. E. Lyman, P. Echlin, E. Lifshin, L. C. Sawyer, and J. R. Michael. Scanning Electron Microscopy and X-Ray Microanalysis, Springer. 2002.

Chapter 4

RESULTS AND DISCUSSION

Overview

This chapter consists of three sub sections namely: structural, thermal and dielectric properties of prepared glasses. In the second section, the interaction study between glasses and different steels has been investigated. Finally, the corrosion study has been carried out on the glasses, steel and their diffusion couples. The structural, thermal, optical and dielectric properties of glasses have been investigated to check their applicability as coating materials. The results obtained by Differential Thermal Analysis (DTA), Thermal Dilatometric Analysis (TDA), X-Ray Diffraction (XRD), Scanning Electron Microscopy (SEM) with EDS, Fourier Transform Infrared Spectroscopy (FTIR), UV-Visible and dielectric measurement of the glass samples are analyzed and discussed. The properties which are required for making the glass suitable for coating are glass transition temperature (T_g), crystallization temperature (T_c) and thermal expansion coefficient (TEC). For second part of study, glass powder was coated by slurry method on steel and heated at 900 °C (prepared glasses) and 700 °C (S and X glasses) for 1 h in air. The reaction products at the surface as well as the interface were analyzed under SEM. In the third section, corrosion studies of N-series glasses followed by their characterization using XRD, FTIR and ICPS methods have been discussed. The electrochemical testing of N-series glasses is described as it is a critical study to check the dissolution characteristic of glasses in varieties of aqueous solution. Corrosion study of steels used in this work is presented. This study is essential to see the type of corrosion including pitting that takes place in present experimental set-up. Though data on steels are available but not for the acquired laboratory set-up where all materials are tested under similar environment. The electrochemical study of the diffusion couples which have shown better adherence in the present investigation have been done. The electrochemical study was done for short time as well as long time to understand their stability in these conditions. After the electrochemical study, the surface of the diffusion couple was characterized by SEM with EDS attachment to have a better understanding of the surface morphology from industrial point of view.

4.1. Structural, thermal and dielectric properties of glasses:

4.1.1. Thermal properties of glasses

The plots of N-25, N-20, N-15 and N-10 glass samples at different heating rates are shown in Fig. 4.1, 4.2, 4.3 and 4.4, respectively. Since no transition upto 600 ^{o}C was observed so results are presented for 600 -1200 ^{o}C temperatures for all the glass samples.

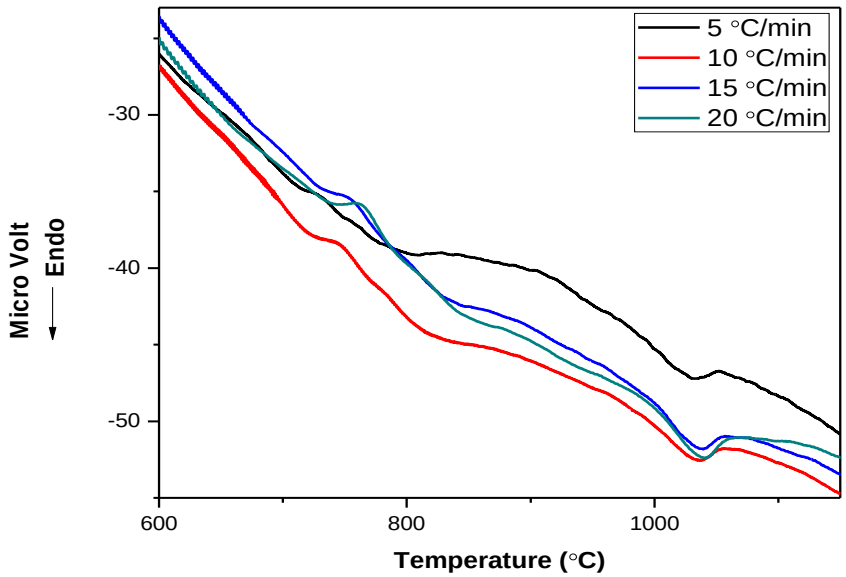

Fig. 4.1: DTA plot of N-25 glass sample at 5, 10, 15, 20 °C/min from 600-1200 °C.

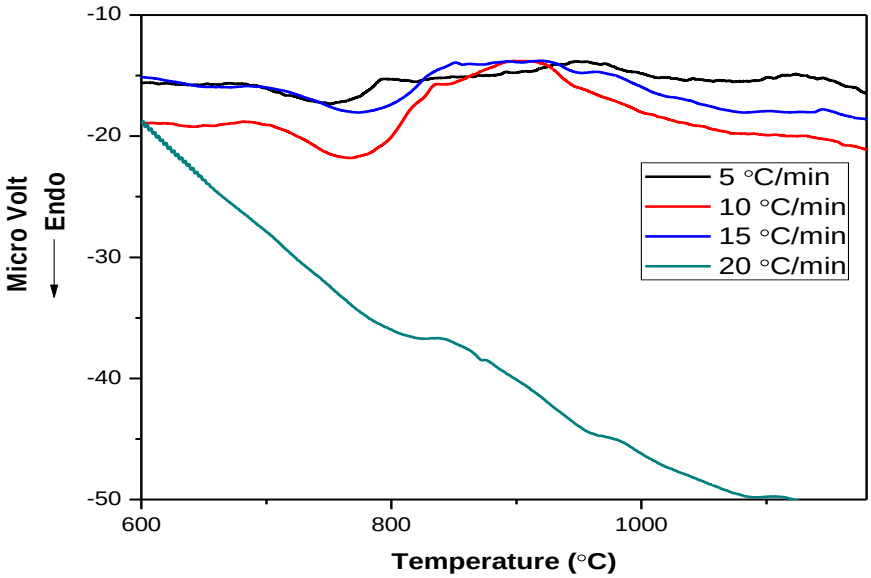

Fig. 4.2: DTA plot of N-20 glass sample at 5, 10, 15, 20 °C/min from 600-1200 °C.

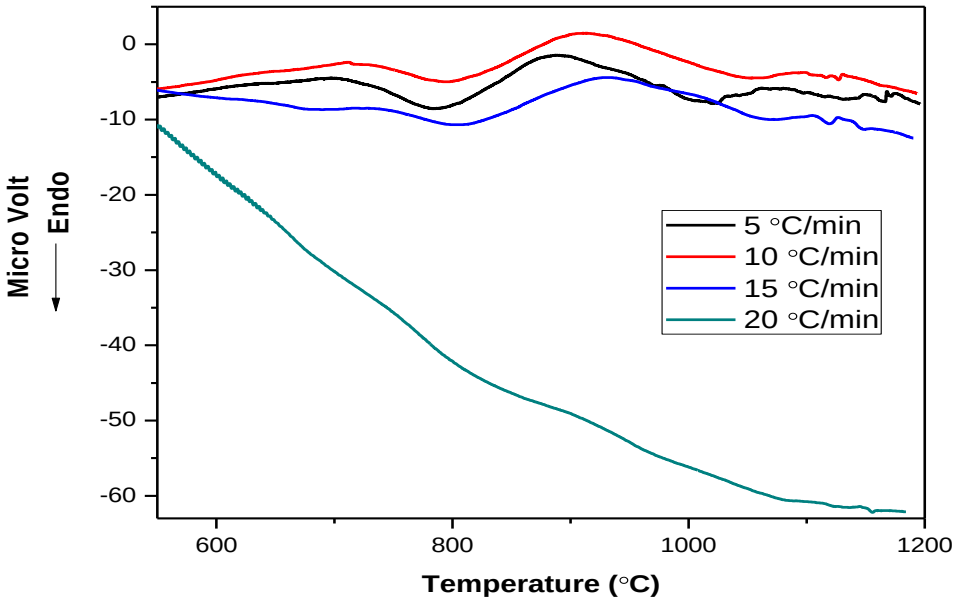

Fig. 4.3: DTA plot of N-15 glass sample at 5, 10, 15, 20 °C/min from 600-1200 °C.

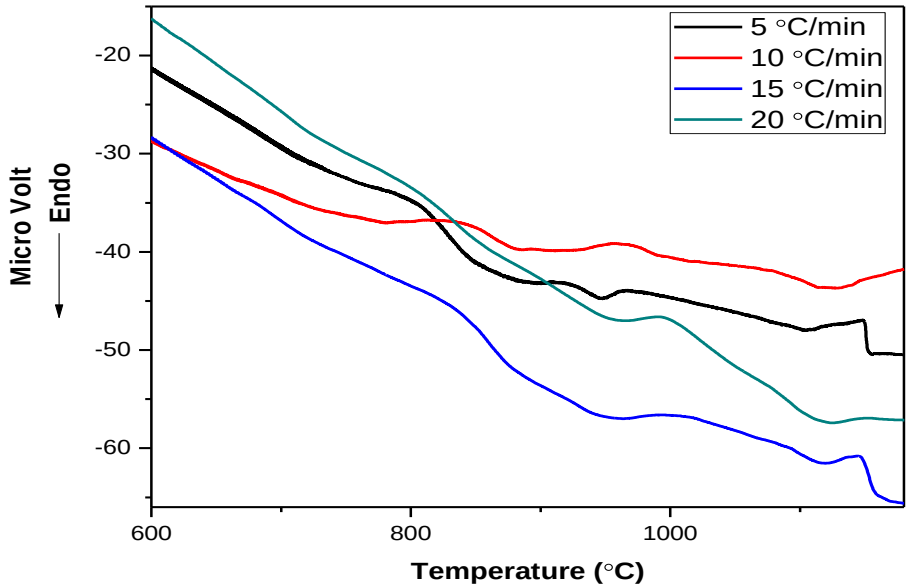

Fig. 4.4: DTA plot of N-10 glass sample at 5, 10, 15, 20 °C/min from 600-1200 °C.

The values of T_g (glass transition temperature), T_c (crystallization temperature) and T_p (peak crystallization temperature) as obtained from the DTA study at various heating rates are summarized in Table 4.1. The crystallization peak maximum in DTA scan corresponds to the temperature at which the rate of transformation of the viscous liquid into crystals becomes

maximum. When the crystallization phase has the same composition as that of the liquid, the transformation rate will depend on the density of crystallization sites. However, when the composition of crystalline phase is different from that of the liquid, the rate of transformation will be controlled by the rate of diffusion through the viscous liquid and the number of crystallization sites to which diffusion can occur. If the number of nucleation sites is increased, e.g. by using slower heating rates, the peak maximum will occur at a temperature at which the melt viscosity is higher, i.e. at a lower temperature.

Table 4.1: T_g, T_c, T_p and T_m values of N series glasses.

Sample Identity	T_g (^oC)	T_c (^oC)	T_p (^oC)	T_m (^oC)
N-25-5	687	714, 812	729, 840	1032
N-25-10	692	721, 826	741, 864	1037
N-25-15	707	730, 842	753, 887	1040
N-25-20	723	740, 867	759, 910	1043
N-20-5	600	651, 806	680, 947	1070
N-20-10	616	655, 837	705, 915	1097
N-20-15	625	658, 850	707, 921	1147
N-20-20	731	815, 960	860, 982	1157
N-15-5	605	670, 784	705, 825	1164
N-15-10	607	684, 795	711, 910	1127
N-15-15	614	690, 800	738, 930	1117
N-15-20	650	711, 825	750, 930	1114
N-10-5	700	766, 883	800, 916	1102
N-10-10	720	795, 910	815, 950	1130
N-10-15	742	800, 959	835, 1012	1166
N-10-20	800	853, 966	895, 1005	1180

Fig. 4.5 shows the DTA curves of all the N-glasses at a heating rate of 10 °C/min. DTA curves exhibit two exothermic peaks, which indicate phase separation in the glasses. Basically, phase separation occurs due to the formation of a second glass matrix within the glass matrix. Higher modifier contained glasses, in general, exhibit phase separation tendency [1]. The T_g of glasses is observed in the range of 600-800 °C followed by two exothermic peaks, which belongs to crystallization of the glasses. Endothermic peaks at around 1050-1200 °C are denoted for melting of the glasses. The modifier (Na_2O) decreases the T_g and T_c whereas T_m is increasing in the present glasses. These observations are similar to that of reported in sodium silicate glasses [2].

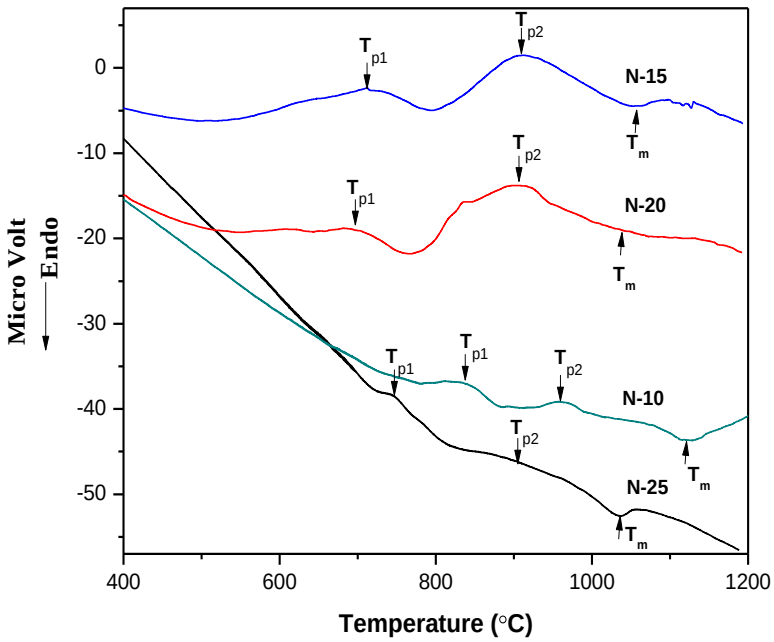

Fig. 4.5: DTA curves of N-series glasses at the heating rate of 10 °C/min.

Out of four synthesized glass samples designated as N-25, N-20, N-15 and N-10, sample N-10 shows better thermal stability (Fig. 4.6) as it exhibits minimum weight change as compared to other glass samples (Table 4.2).

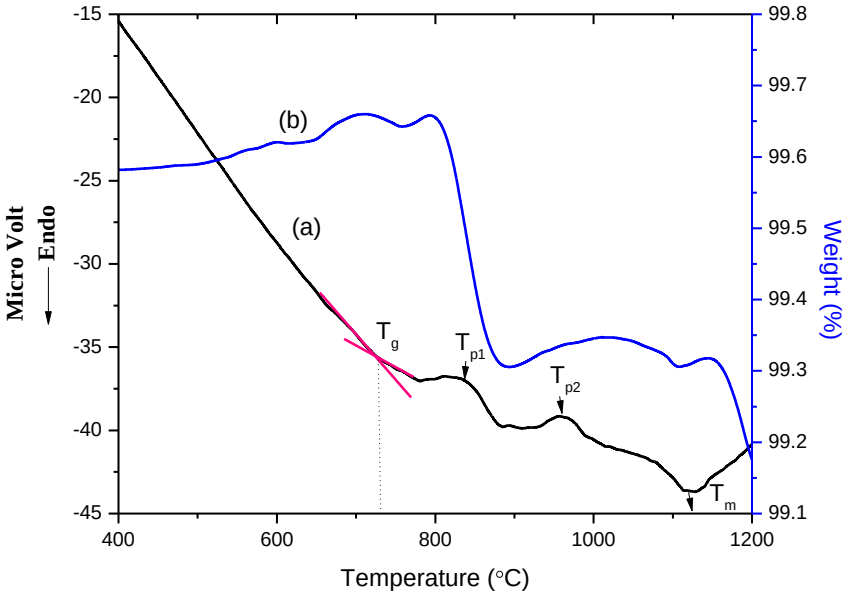

Fig. 4.6: Curves of (a) DTA and (b) TGA of the N-10 glass showing transition temperature and weight loss, respectively.

Table 4.2: Change in weight % in N glass samples.

Sample ID	Change in weight (%)
N-25	-7
N-20	-2.5
N-15	-1.5
N-10	-0.8

In Fig. 4.6 (a), the glass transition temperature (T_g) is observed at 720 °C followed by two exothermic peaks, which is a typical characteristic of phase separation within the glass matrix. The peak crystallization temperatures T_{p1} and T_{p2} are observed at 815 °C and 950 °C, respectively. In Fig. 4.6 (b), an opposite phenomenon is observed when compared with DTA curve. The weight loss in TGA curve is ascribed due to first crystallization of the glass. The second crystallization occurs due to the formation of a second matrix within the glass matrix [3-4]. Consequently, TGA curve showed the fluctuating weight gain behavior corresponding to the second crystallization phenomena in the glass. The first crystallization peak, as observed from XRD and SEM analysis, (discussed in subsequent section) corresponds to the nucleation of SiO_2 phase (815 °C). During its growth, the surrounding area becomes rich in Al and Na. The matrix nearer to SiO_2 phase becomes rich in Al, Na and SiO_2 constituents. For the growth of AlNa (SiO_4) phase (950 °C), it takes oxygen from the atmosphere and thus TGA curve shows weight gain. An endothermic peak at 1130 °C is denoted for the melting of the glass as shown in Fig. 4.6 (a). DTA /TGA analysis of S and X glasses are shown in Fig. 4.7 and 4.8, respectively.

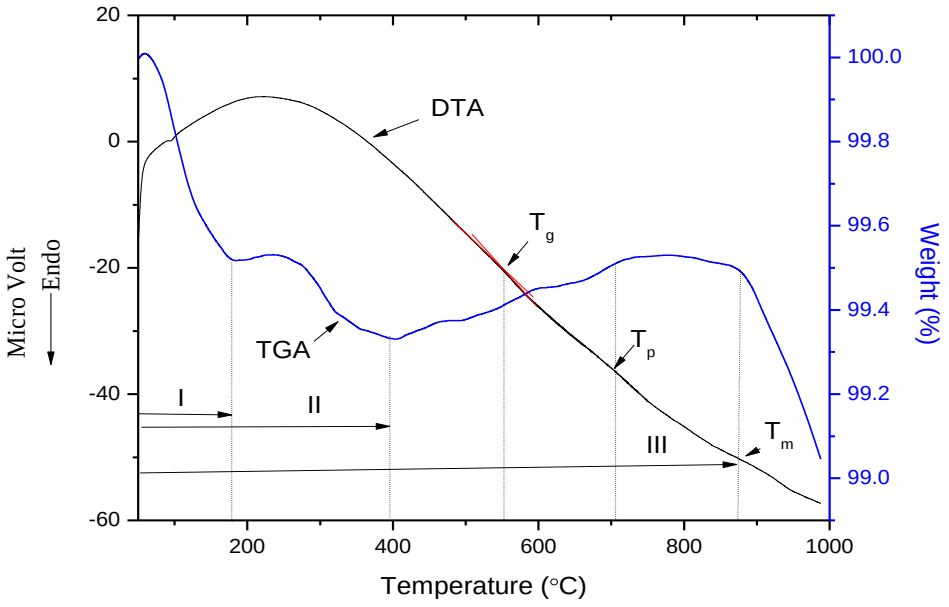

Fig. 4.7: DTA and TGA analysis of S glass.

The TGA graph of S glass indicates weight loss upto 200 °C. This weight loss is because of absorbed moisture in the I region. The weight loss between 200 °C and 400 °C is due to bonded elements in the closed pores marked as II [5]. The weight gain is because of oxidation of Fe constituent in the III region. However, this gain is only 0.1% which is very less and can be ignored for all practical purposes. The glass transformation temperature was identified at 555 °C from change in the slope of DTA curve. The exothermic peak at 710 °C in DTA indicates crystallization temperature of the glass. The endothermic peak at 880 °C in DTA indicates melting temperature of the glass and correspondingly weight changes occur in TGA curve.

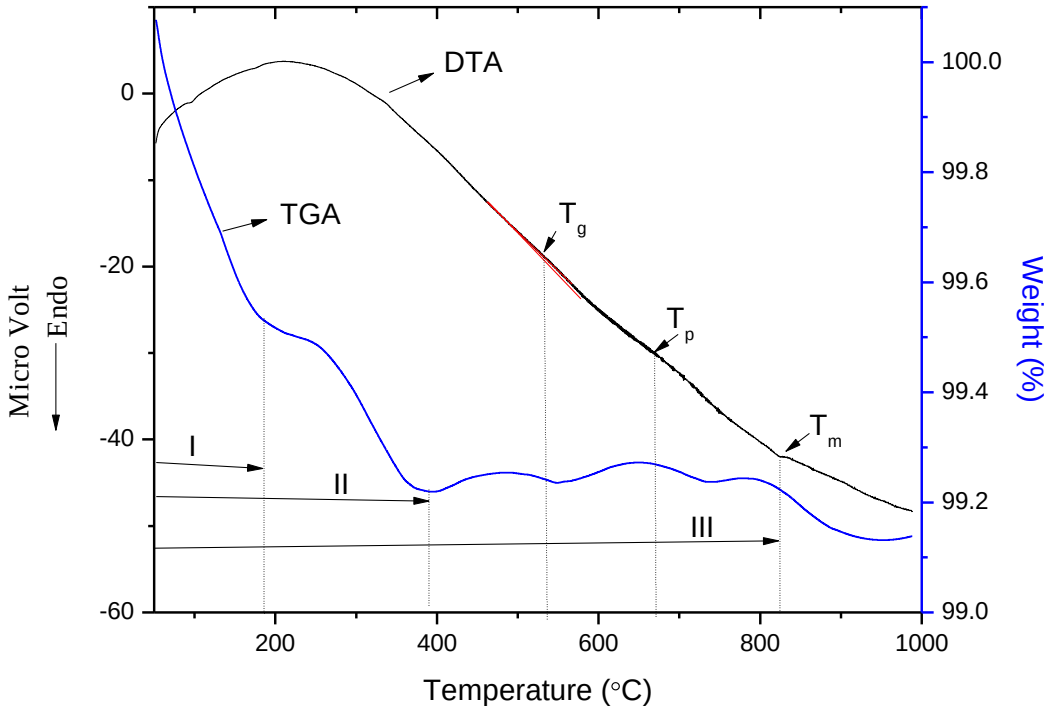

Fig. 4.8: DTA and TGA analysis of X glass.

The TGA graph of X glass indicates weight loss upto 200 °C. This weight loss is because of absorbed moisture in the I region as shown in Fig. 4.8. The weight loss between 200 °C and 400 °C is due to bonded elements in the closed pores marked as II [5]. TGA analysis of X glass sample indicates the weight loss nearly 0.8% in the region III. The glass transformation temperature was identified at 545 °C from change in the slope of DTA curve. The exothermic peak at 680 °C in DTA indicates crystallization temperature of the glass and correspondingly weight changes occur in TGA curve. The endothermic peak at 820 °C in DTA indicates melting temperature of the glass and correspondingly weight changes occur in TGA curve.

4.1.1.1. Calculation of activation energy

Based on the DTA results, the theoretical calculations were done using different models. The activation energy of the glass transition (E_g) and crystallization (E_c) can be obtained by the following relationship [6]:

$$\ln \alpha = - \frac{\quad}{\quad} + \text{constant} \qquad (4.1)$$

where E is the activation energy and R is the gas constant.

The second approach to evaluate of the activation energy for the glass transition (E_g) and crystallization (E_c) is Kissinger equation as given below [7]:

$$\ln \left(\frac{\quad}{\quad} \right) = - \frac{\quad}{\quad} + \text{constant} \qquad (4.2)$$

The slope of the plot ln (versus (K^{-1}) gives the value of activation energy.

Additionally, activation energy was also calculated using the method proposed by Augis and Bennett [8]:

$$\ln \left(\frac{\quad}{\quad} \right) = - \frac{\quad}{\quad} + \ln K_o \qquad (4.3)$$

The activation energy for the glass transition and the crystallization processes are calculated and compared with the values as obtained from the Kissinger and Mahadevan models as summarized in Table 4.3.

Table 4.3: Activation energy (kJ/mol) for the glass transition and crystallizations using various models.

Sample Identity	Mahadevan Method			Kissinger Method			Augis and Bennett Method		
	E_g	E_{p1}	E_{p2}	E_g	E_{p1}	E_{p2}	E_g	E_{p1}	E_{p2}
N-25	271.11	386.11	215.55	254.86	369.21	196.47	262.98	265.03	258.59
N-20	58.80	51.29	68.45	43.17	33.92	48.14	242.57	236.49	263.59
N-15	149.38	216.61	124.04	134.40	199.99	104.96	260.47	260.76	255.27
N-10	100.77	142.73	167.32	83.78	124.07	146.77	249.55	254.84	256.42

Kissinger and Mahadevan methods give nearly same value of activation energy but Augis and Bennet's method gives relatively large value as compared to others. The average value of activation energy of glasses except N-20 is large as compared to another borosilicate glasses [9]. From Table 4.3, it can be observed that N-20 glass shows very less value of activation energy. It is well reported in literature that with the increase in the modifier content the network weakens, which decreases the value of activation energy [1]. However, the value of activation energy follows the opposite trend in this system. This anomaly arises due to the presence of minor amount of SiO_2 (Zeolite) phase in the microcrystalline glass matrix containing higher Na_2O. The increase in Na_2O content with a decrease of SiO_2 content increases the phase separation tendency

in glasses as observed in Fig. 4.5. It can be explained on the basis of the diffuse and broad exothermic/ endothermic peaks in DTA curve. However, the trend observed for activation energy of all the glasses is same. Fig. 4.9 depicts such variation for N-25 glass.

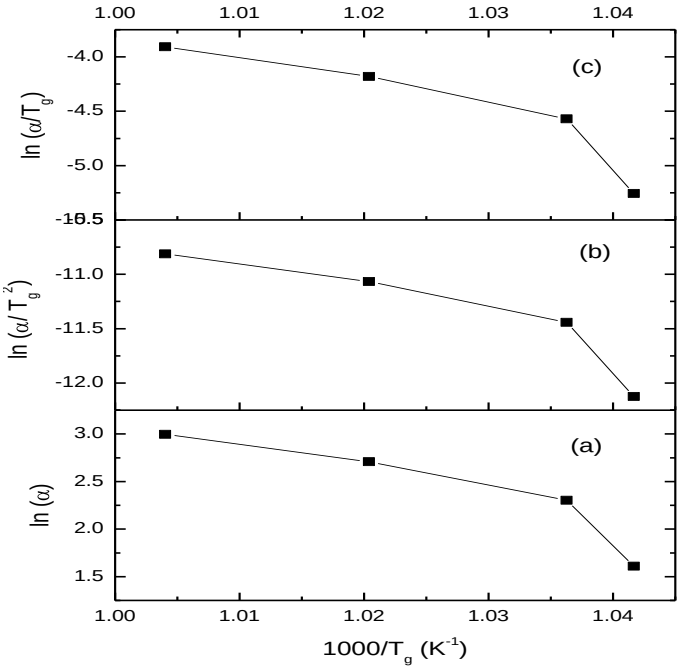

Fig. 4.9: Activation energy plot with (a) Mahadevan (b) Kissinger and (c) Augis and Bennett methods for N-25 glass.

4.1.1.2. Thermal Stability Parameter (S)

From the point of view of technological application, the glass should be thermally stable. A parameter usually employed to estimate the glass stability is the thermal stability (ΔT) [4], which is defined by the following equation:

$$\Delta T = T_c - T_g \tag{4.4}$$

The larger difference between T_c and T_g, the higher is the kinetic resistance to crystallization. In other words, the glass is thermally stable.

The difference between T_g and T_c also indicate the thermal stability of the glasses. According to this approach, N-10 glass is more stable as compared to the other glasses as is evident from Fig. 4.5. Another thermal stability parameter, S, proposed to check the stability of the glasses by Saad and Poulain [10], is given in equation 4.5.

$$S = (T_p - T_c)(T_c - T_g)/T_g \tag{4.5}$$

The thermal stability parameter, S, reflects the resistance to devitrification after the formation of the glass. (T_p-T_c) is related to the rate of devitrification transformation of the glassy phases, while a high value of (T_c-T_g) delays the nucleation process.

According to this approach, N-10 glass exhibit higher S value which indicates the higher stability of this particular glass. The S parameter with respect to the Na_2O is shown in Fig. 4.10.

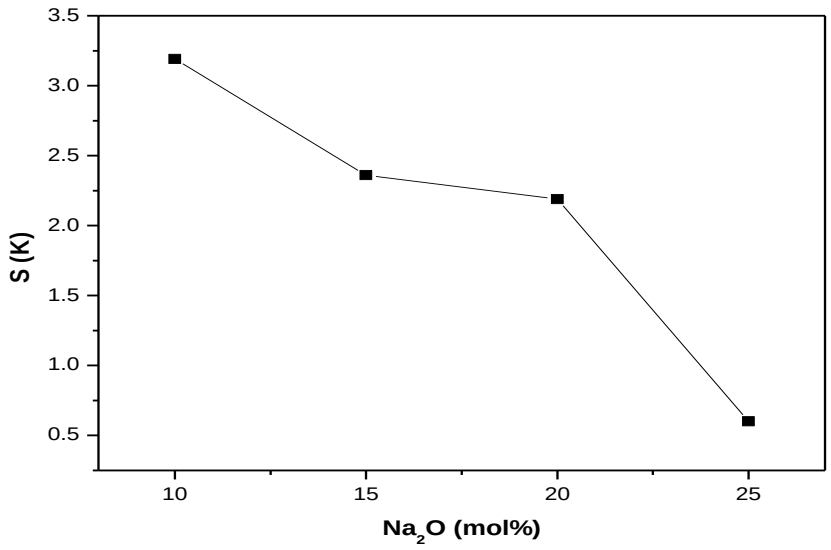

Fig. 4.10: The graphical representation of S parameter with respect to Na_2O (mol %) at heating rate 10 °C/min.

4.1.1.3. Hruby Parameter Calculations

Hurby [11] has given a factor which combines both nucleation and growth aspects of glass transformation and is given by eqn. 4.6.

$$H_r = \frac{\quad}{\quad} \qquad (4.6)$$

where T_m is the melting temperature of glass.

Fig. 4.11 shows the variation in H_r parameter for the second crystallization peak of different compositions at different heating rates. The H_r parameter of N-10 glass is higher than other glasses as shown in Fig. 4.11. In general, the modifier weakens the glass network and decreases the glass transition temperature so the less content of Na_2O in glass composition shows better thermal stability [12].

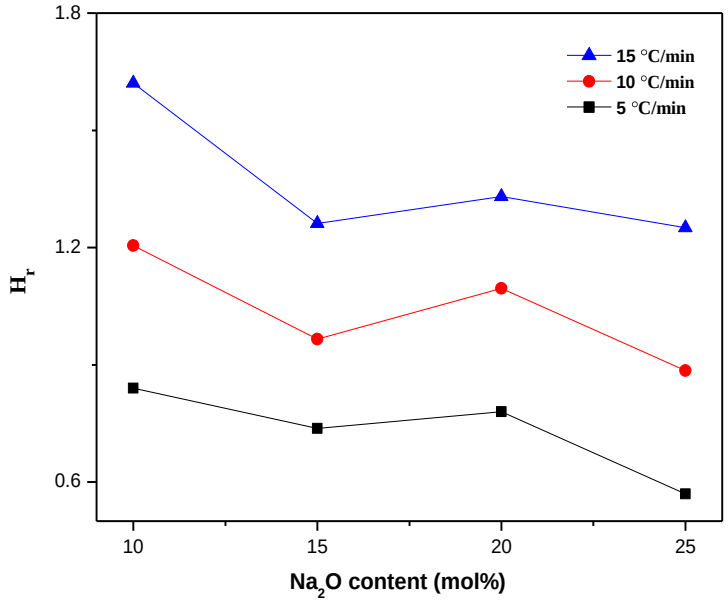

Fig. 4.11: The graphical representation of Hruby parameter with respect to Na_2O (mol %).

4.1.2. Thermal dilatometric analysis (TDA)

The dilatometer study was performed to know the variation in a thermal expansion coefficient and values of softening temperature of all the pristine glasses. The dilation plots obtained are shown in Fig. 4.12 for N-25, N-20, N-15 and N-10 samples.

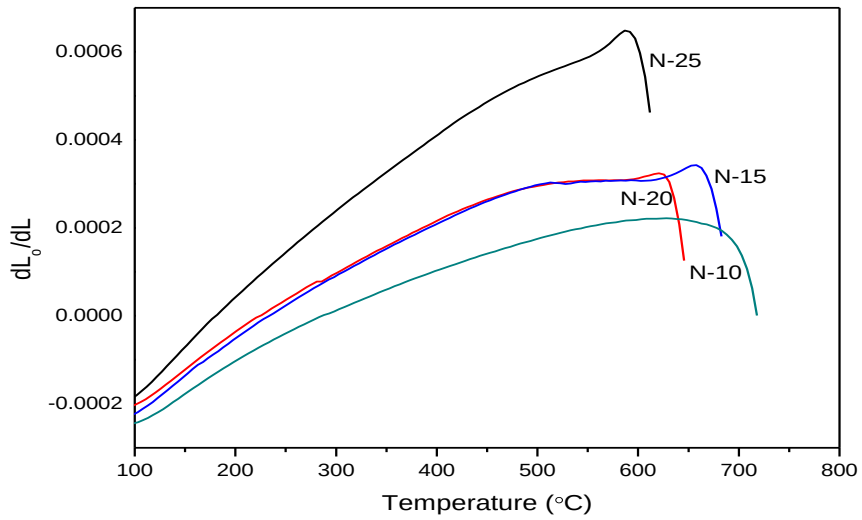

Fig. 4.12: Plot of Dilatometer of N-series polished glass frits.

It is clear from the above plot that with the increase in SiO_2 contents from N-25 to N-10 the softening temperature of glass frits are increasing. N-25 glass shows a higher thermal expansion

coefficient (TEC) as compared to the other glasses. TEC originated due to asymmetric potential well of the solids [13]. In the present glasses, the observed TEC decreases as the modifier content decreases except N-20. But the increasing trend of T_s value is observed (Table 4.4).

Table 4.4: T_g, T_s and TEC values obtained from dilatometer for N series.

Sample Identity	T_g (°C)	T_s (°C)	TEC (10^{-6}/K) (200-550 °C)
N-25	562	589	8.88
N-20	572	629	8.31
N-15	628	657	8.34
N-10	654	709	8.19

Glass that best fulfills the coating requirement such as thermal expansion coefficient should lie in the range 8.5-12 X $10^{-6}/^{\circ}$C [14]. The values of TEC obtained in our glass samples are close to this specified range so, they may act as suitable coating materials for steels. For high temperature applications of glasses, the viscosity of glasses at different transformation temperature plays important role. So the viscosity of glasses are also calculated and summarized in Table 4.5.

According to the simple liquid theory [15], there is a relationship between pseudo-critical temperature (T_k) and the absolute melting point (T_m):

$$\frac{}{} = \frac{}{} \tag{4.7}$$

For glass-ceramics, the above equation becomes:

$$\frac{}{} = \frac{}{} \tag{4.8}$$

Hence T_m can be calculated as given in Table 4.5. The viscosity value (η) at T_g, T_s, T_m is fixed and independent of materials and reported to be 10^{12}, $10^{6.6}$, 10^4 Pa.s, respectively, at these temperatures [16]. Systematic studies of the viscosity–temperature relation in glasses was initiated by Vogel [17], Fulcher [18] and Tammann et al. [19] and resulted in the widely accepted Vogel–Fulcher–Tammann (VFT) Equation:

$$\log \eta = A + \frac{}{}\ , \tag{4.9}$$

where A, B and T_o are all constants. It is possible to determine all these constants by substituting the values for T_g, T_s, T_m in VFT equation. The modified VFT equation for N-25, N-20, N-15, N-10 glasses can be written as follows:

$$\log \eta = 2.475 + \frac{}{}, \tag{4.10}$$

$$\log \eta = 2.1645 + \frac{}{}, \tag{4.11}$$

$$\log \eta = 3.36 + \frac{\qquad}{\qquad}, \tag{4.12}$$

$$\log \eta = 2.594 + \frac{\qquad}{\qquad} \tag{4.13}$$

At 900 °C, the viscosity value of prepared glasses is given in Table 4.5.

Table 4.5: Properties of the glasses.

Sample	N-25	N-20	N-15	N-10
T_m (ºC)	779	806	923	950
Density (g cm^{-3})	2.25	2.69	2.85	3.08
Viscosity (at 900ºC)	$10^{3.57}$	$10^{3.59}$	$10^{4.05}$	$10^{4.22}$

Shelby [20] reported that a soda-lime-silica melt has viscosity 10^3 Pa.s at 900 °C. Phase separation has almost no effect on the thermal expansion coefficient of glasses, while the glass transformation, dilatometric softening temperature and viscosity are strongly affected by phase separation. In general, if the difference between T_g and T_s is more than 50 ºC, the sample is probably phase separated, with a continuous higher viscosity phase. It is well known that addition of TiO_2 as a nucleating agent leads to order phase separation in the glasses [21].

The variation in length as compared to original length (dL/dL_o) is shown in Fig. 4.13 for both S and X glasses. As such it depicts linear behavior. The variation in length with increasing temperature is uniform.

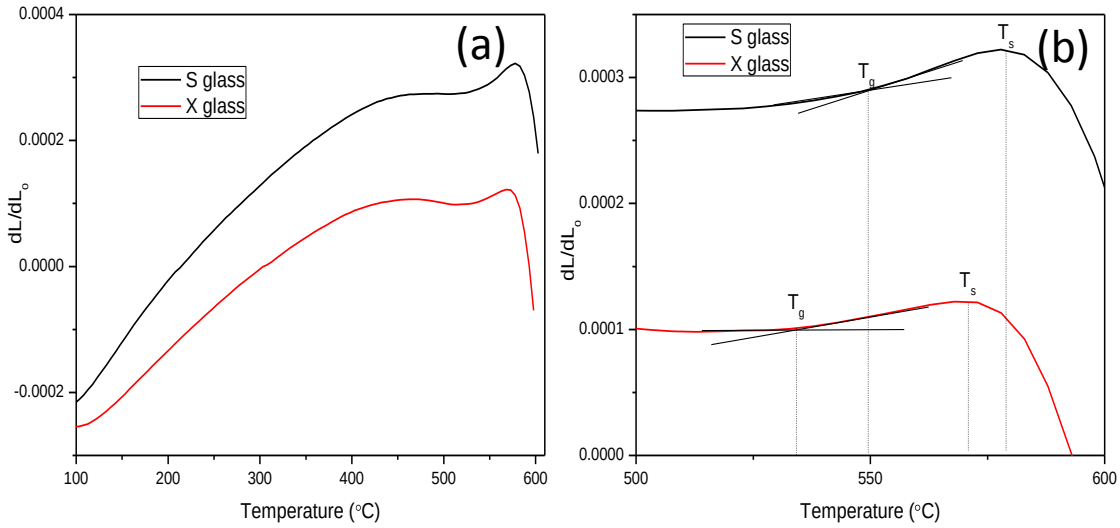

Fig. 4.13: Variation in TEC values of the S and X glasses.

However, when analyzed carefully some minute kinks are observed in between 200-400 °C. These kinks are for minute quantity elements/ materials which undergo phase transition or get

detached from base matrix of glass causing void inside the matrix of glass. Though, this analysis is a symptom but not confirmatory test. Glass in general exhibit linear characteristic having coefficient of thermal expansion of the order of 10^{-6} K^{-1} which is in order as shown in Fig. 4.13 (a) [22]. The observed values of measured thermal properties of these glasses from Fig. 4.13 (b) are shown in Table 4.6.

Table 4.6: Measured thermal properties of both glasses.

Glass Identity	T_g (°C)		T_s (°C)	TEC (10^{-6} K^{-1})
	From dilatometer	From DTA		
S Glass	550	555	580	8.0677 X 10^{-6}
X Glass	535	545	570	7.7278 X 10^{-6}

4.1.3. X-ray diffraction analysis of glasses

All the synthesized glass samples were characterized by XRD. This amorphous nature of glasses was confirmed by a broad halo as obtained in XRD pattern (Fig. 4.14).

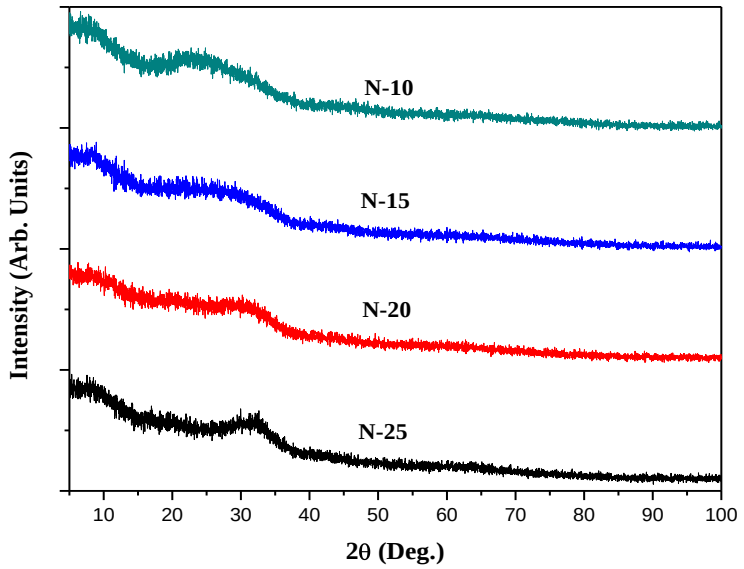

Fig. 4.14: XRD patterns of as prepared N-series glasses.

The XRD patterns showed two broad humps around 10° and 30° for N-25, N-15 and N-10 glasses. The pattern of N-20 glass showed formation of three humps around 10°, 20° and 30°. These humps clearly indicate the phase separation in glass system. Phase separation leads less activation energy for crystallization, which is essential for good adhesion with other metallic materials [23]. Also, the pattern of higher modifier containing glasses exhibits a sharp hump around 30° which is due to zeolite phase [24].

For enameling, heat treatment was done to convert glass into the glass ceramics that facilitates the maximum crystallization of glass for diffusion into steel. To understand the formation phases, pristine glasses were subjected to heat treatment. The peak crystallization temperatures T_{p1} and T_{p2} of N-10 glass are observed at 780 °C and 925 °C, respectively. Based on the analysis of crystallization kinetics of the N-10 glass, the heat treatment temperatures selected for all glass samples were 900 and 950 °C for 1 h. The X-ray diffraction pattern of glass sample N-25 heat-treated at 900 ^{o}C and 950 ^{o}C for 1 h is as shown in Fig. 4.15. The heat treated glass exhibits two different crystalline phases, i.e. sodium aluminium silicate (ICDD #01-079–0993) and sodium calcium silicate (ICDD #01-077–2189) as shown in Fig. 4.15. The presence of these crystalline phases in the glass matrix changes the TEC.

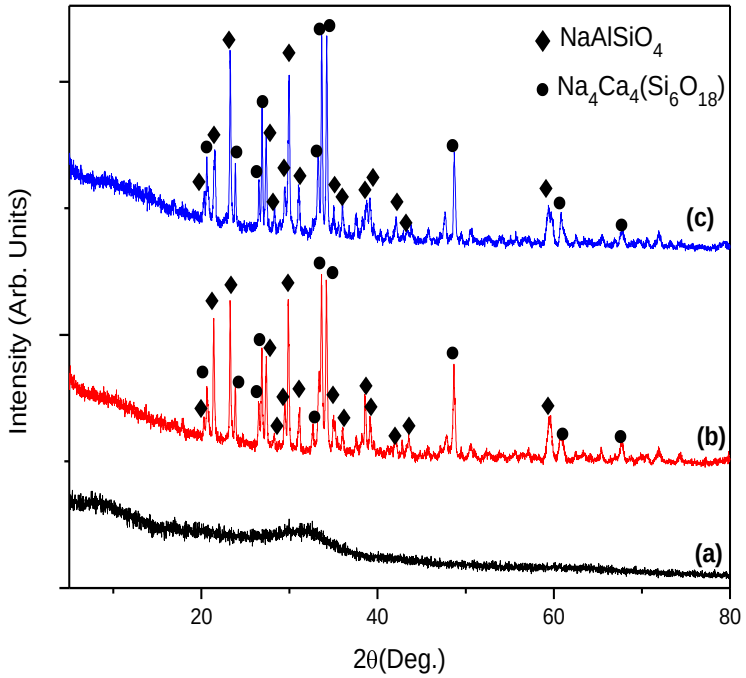

Fig. 4.15: XRD patterns of (a) N-25 glass, (b) N-25 heat treated glass at 900 °C and (c) N-25 heat treated glass at 950 °C for 1 h.

The X-ray diffraction pattern of glass sample N-20 heat-treated at 900 ^{o}C and 950 ^{o}C for 1 h is as shown in Fig. 4.16. The heat treated glass exhibits three different crystalline phases, i.e. sodium aluminium silicate (ICDD #01-079–0993), sodium calcium silicate (ICDD #01-079–1089) and calcium titanium oxide (ICDD #01-076–2400) as shown in Fig. 4.16.

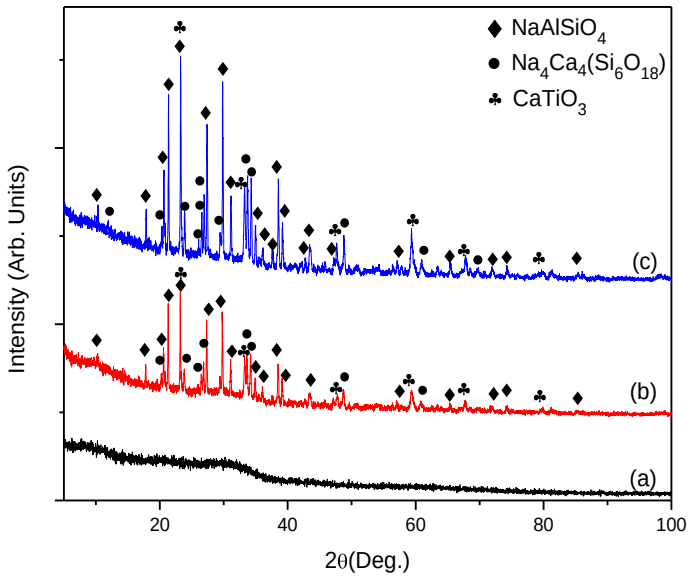

Fig. 4.16: XRD patterns of (a) N-20 glass, (b) N-20 heat treated glass at 900 °C and (c) N-20 heat treated glass at 950 °C for 1 h.

The X-ray diffraction pattern of glass sample N-15 heat-treated at 900 ^{o}C and 950 ^{o}C for 1 h is as shown in Fig. 4.17. The heat treated glass exhibits amorphous character. However, very small kinks of crystalline phase such as silicon dioxide (ICDD #01-082–1570) are observed as shown in Fig. 4.17. This indicates the nucleation of crystalline phase in the matrix.

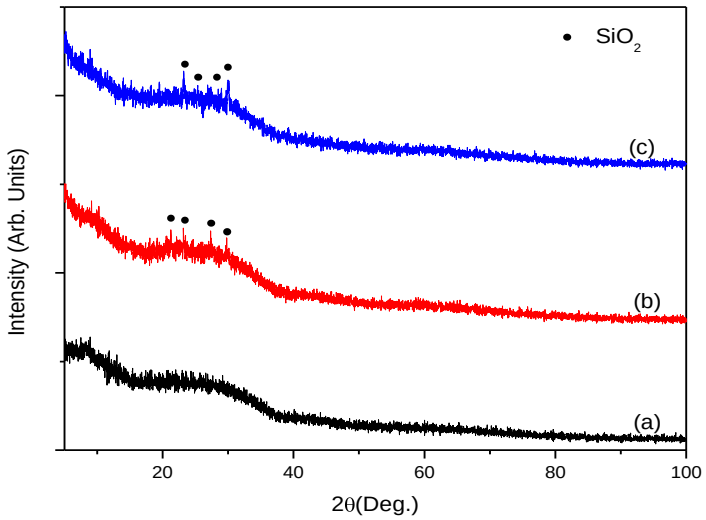

Fig. 4.17: XRD patterns of (a) N-15 glass, (b) N-15 heat treated glass at 900 °C and (c) N-15 heat treated glass at 950 °C for 1 h.

The X-ray diffraction pattern of glass sample N-10 heat-treated at 900 ^{o}C and 950 ^{o}C for 1 h is as shown in Fig. 4.18.

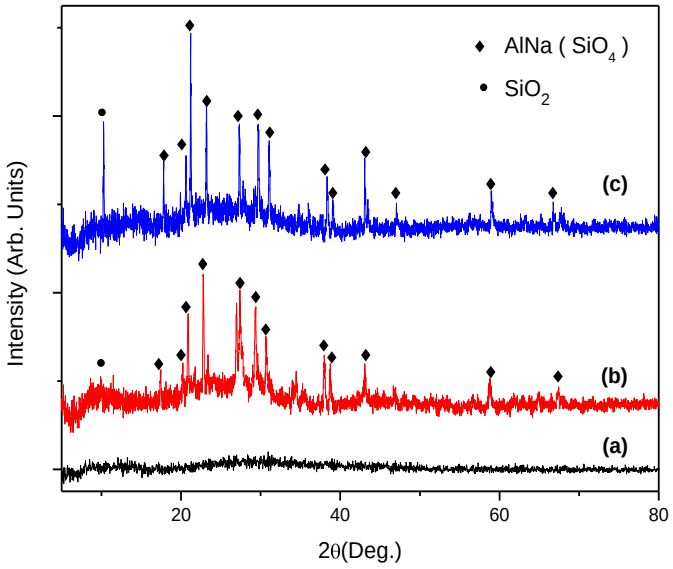

Fig. 4.18: XRD patterns of (a) N-10 glass, (b) N-10 heat treated glass at 900 °C and (c) N-10 heat treated glass at 950 °C for 1 h.

The heat treated glass exhibits two different crystalline phases, i.e. aluminium sodium silicate (ICDD #00-002–0625) and zeolite (ICDD #01-085–0459) as shown in Fig. 4.18.

From the XRD results of heat treated N-series glasses, it can be concluded that N-15 glass shows low crystallization even at higher temperature. This study indicates that N-15 glass is most suitable glass for coating with steels among the N-series of glasses. However, other glasses where the nucleation of crystalline phase(s) leads to achieve the matching coefficient of thermal expansion will also be suitable for glass coating. The volume fraction of the different phases after heat treatment is shown in Table 4.7. It is easily concluded that initially $NaAlSiO_4$ phase is formed in all the glasses. At later stage of the heat treatment at higher temperature, the volume fraction of this phase reduced and more stable phase is formed. Additionally, the Na_2O contained is responsible for higher precipitation of this phase.

Table 4.7: Volume fraction of phases obtained from XRD for glasses.

Sample Name	Phases	Volume fractions (%)	
		At 900 °C	At 950 °C
N-25	$NaAlSiO_4$	60	54
	$Na_4Ca_4(Si_6O_{18})$	40	46
N-20	$NaAlSiO_4$	63	67
	$Na_4Ca_4(Si_6O_{18})$	26	21
	$CaTiO_3$	11	12
N-10	$NaAlSiO_4$	71	84
	SiO_2	29	16

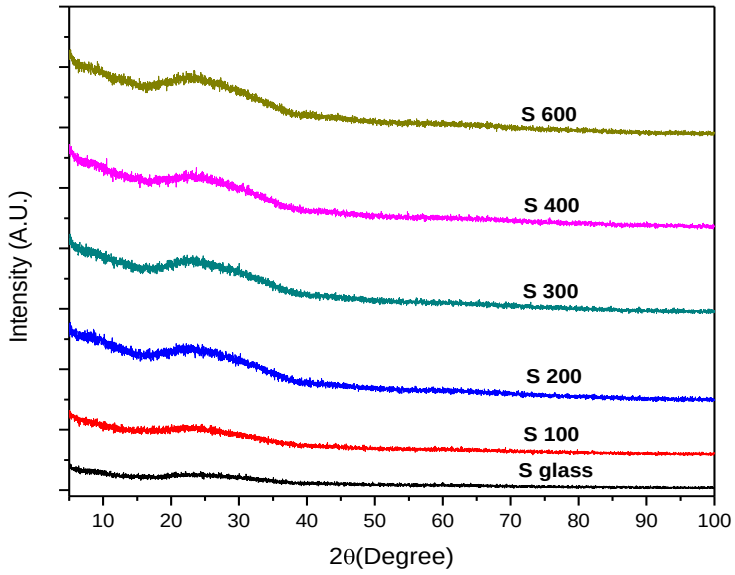

Fig. 4.19: X-ray diffractogram of S glass in as received condition and after heat treatment.

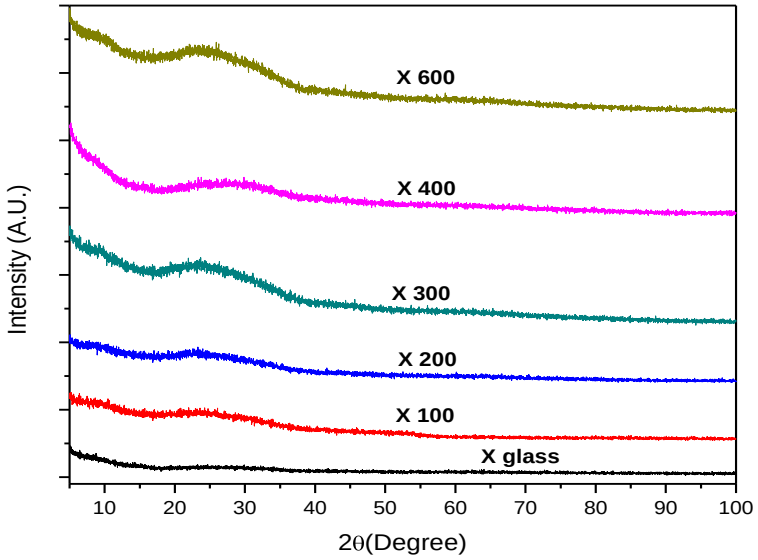

Fig. 4.20: X-ray diffractogram of X glass in as received condition and after heat treatment.

The amorphous state of glasses was confirmed by X-ray analysis of both S and X glass samples. In order to check their stability with temperature, glasses were heat treated at 100, 200, 300, 400 and 600 °C for one hour. This is shown as S 100, S 200, S 300, S 400 and S 600 in the diffractogram for S glass. Similarly for X it is shown as X 100, X 200, X 300, X 400 and X 600 respectively. The corresponding XRD is shown in Fig. 4.19 and 4.20, respectively. It is observed that both the glasses did not show any crystalline peak even when heat treated up to 600 °C. The hump characteristic which is for amorphous nature is existing till 600 °C. This

analysis clearly indicates that there is no crystalline phase present in both the glasses. Therefore, these glasses exhibit amorphous nature even after heat treatment like conventional enamel coatings [25].

4.1.4. SEM and EDS analysis

To estimate the composition of pristine N-series glasses, Energy Dispersive X-ray spectroscopy (EDS) of the samples were done. EDS spectra of N-series glasses are shown below:

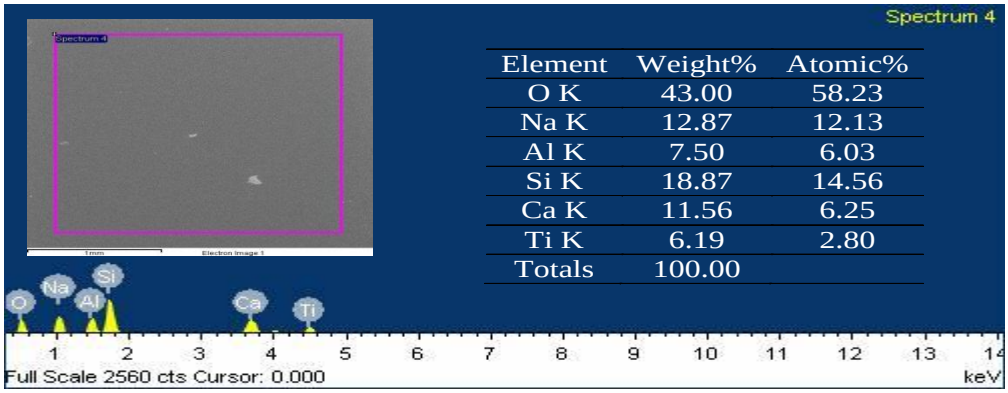

Fig. 4.21: EDS spectrum with elemental analysis of the N-25 glass.

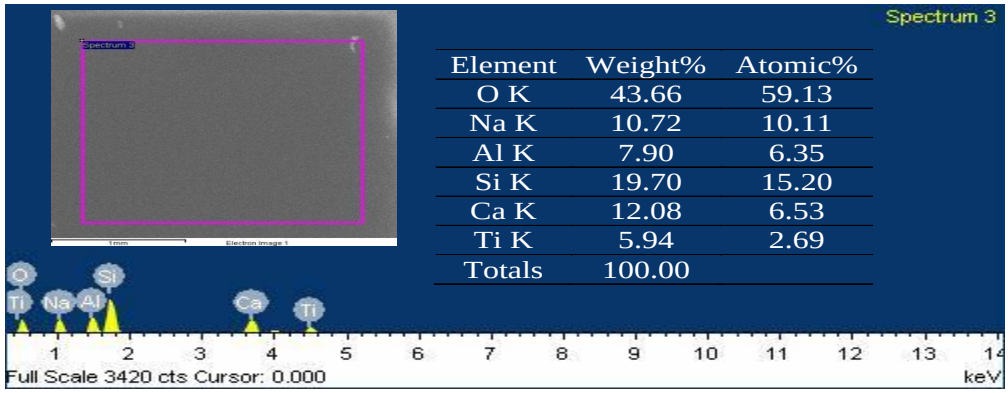

Fig. 4.22: EDS spectrum with elemental analysis of the N-20 glass.

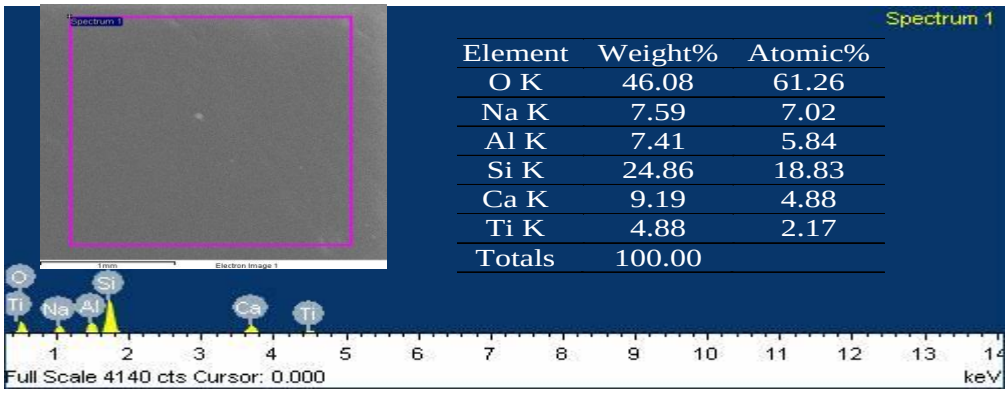

Fig. 4.23: EDS spectrum with elemental analysis of the N-15 glass.

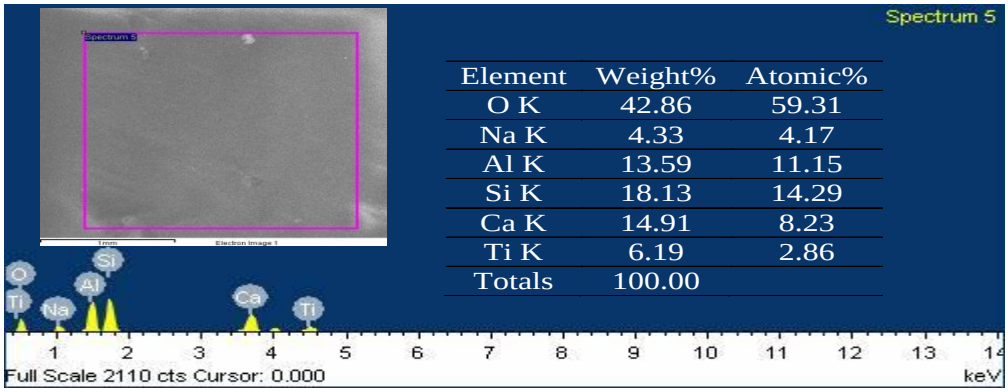

Fig. 4.24: EDS spectrum with elemental analysis of the N-10 glass.

The sodium content decreases from N-25 to N-10. EDS results also confirmed the decrease in sodium content. Titanium content was almost same in all the compositions. Aluminium, calcium, silicon contents showed similar ratios as in the prepared composition in all glasses except N-10 glass. Since EDS analysis gives approximate composition, so the variation in composition observed is within the limit. In order to understand the mode of nucleation of crystalline phases, a detailed microstructural analysis of the heat treated N-10 glass was also done as shown in Fig. 4.25.

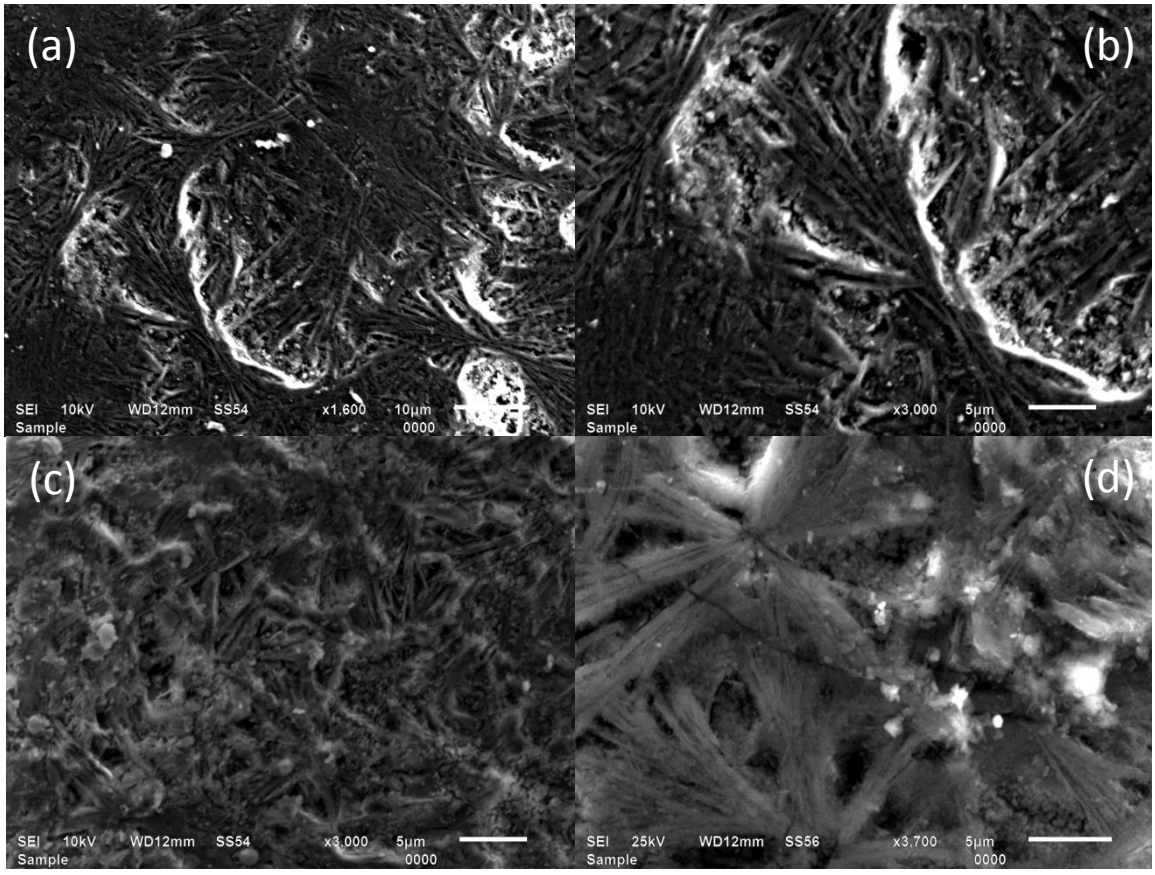

Fig. 4.25: Scanning electron micrograph of the N-10 heat treated glass at 900 °C for 1 h.

From above microstructures, it is observed that two types of phase formation occur. One is flowery type and other is spherical granules in between these flowery patterns. In order to confirm the composition of these phases, EDS analysis of these phases was also done and is shown in Fig. 4.26. The weight percentage of Al, Si, Ca and Ti content in flowery pattern is more as compared to the other phase. The flowery pattern represents the aluminium sodium silicate phase which is hexagonal in nature as observed in XRD pattern. The other pattern presented SiO_2 phase. There is no major change in the weight percentage of sodium content before and after thermal treatment i.e. sodium is present in the glass network. Since the EDS analysis was done over a wide area so variation in other constituents is observed.

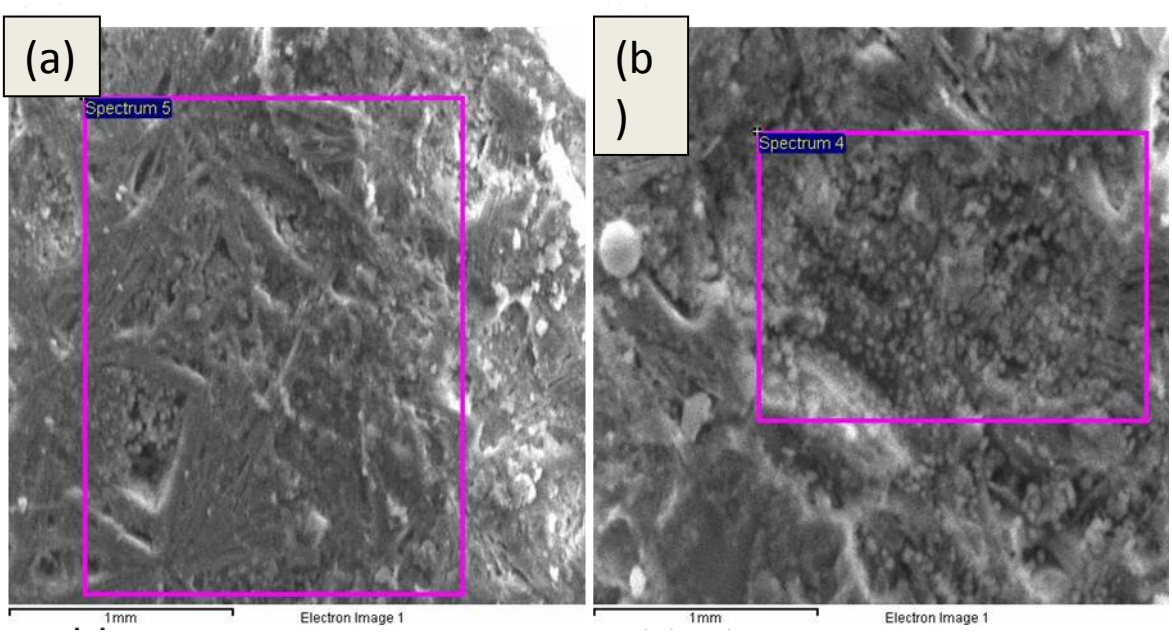

Fig. 4.26: SEM of the heat treated N-10 glass at 900 °C for 1 h.

Table 4.8: EDS analyses of the glass-ceramic marked in the micrographs of Fig. 4.26.

Table: a

Element	Weight%	Atomic%
C K	8.97	14.43
O K	47.14	56.92
Na K	4.50	3.78
Al K	7.23	5.18
Si K	21.60	14.86
Ca K	7.38	3.56
Ti K	3.18	1.28
Totals	100.00	

Table: b

Element	Weight%	Atomic%
C K	12.08	18.54
O K	49.52	57.07
Na K	4.64	3.72
Al K	6.86	4.69
Si K	19.16	12.58
Ca K	5.68	2.61
Ti K	2.07	0.79
Totals	100.00	

4.1.4.1. Structural analysis of S Glass

Microstructural analysis of the surface of as received S glass piece was done as shown in Fig. 4.27. From Fig. 4.27 (a), the glass surface appeared to be smooth and defect free. However, the

presence of inclusions was seen at certain areas which are marked with circle. Moreover, clusters of such inclusion were also seen at different area as shown in Fig. 4.27 (b). The light color inclusions seem to be of carbon. In order to confirm it, we have done EDS analysis by selecting the specific area.

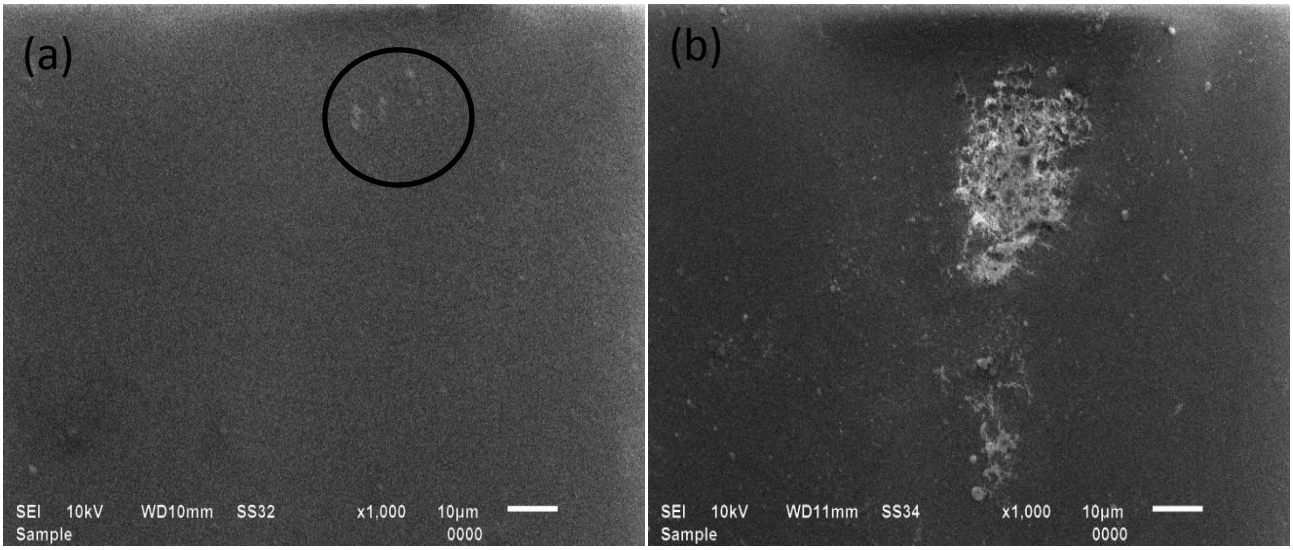

Fig. 4.27: Scanning electron micrograph of the surface of S glass as received.

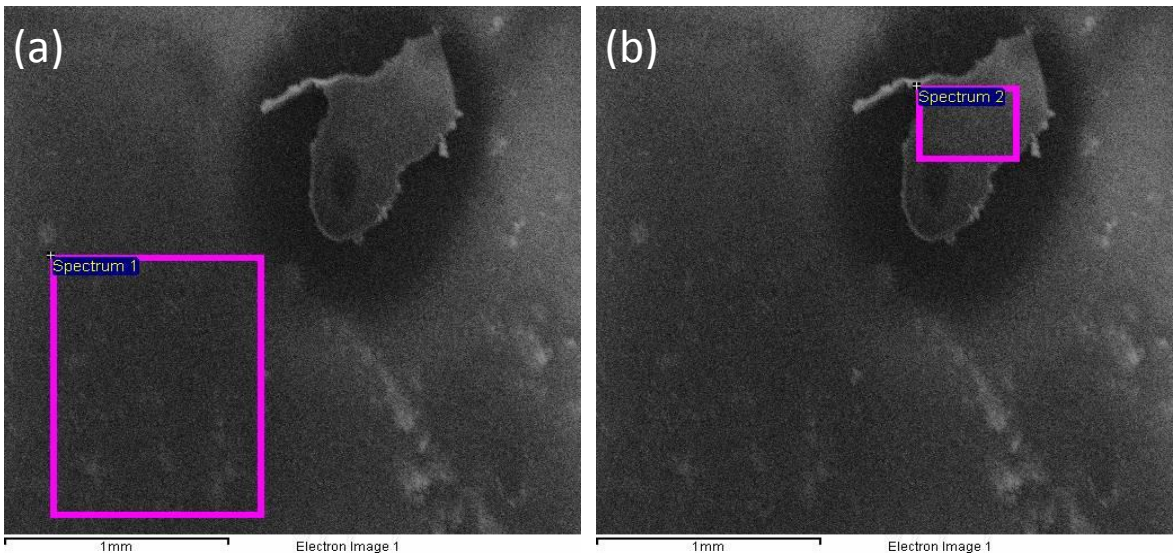

Table: a

Spectrum 1

Element	Weight%	Atomic%
O K	48.02	62.51
Na K	6.99	6.34
Si K	35.06	25.99
Ca K	9.93	5.16
Totals	100.00	

Full Scale 1760 cts Cursor: 0.000 keV

Table: b

Spectrum 2

Element	Weight%	Atomic%
C K	39.22	51.79
O K	34.15	31.67
Na K	4.43	3.05
Si K	18.84	10.64
Ca K	3.36	1.33
Totals	100.00	

Full Scale 1440 cts Cursor: 0.000 keV

Fig. 4.28: Back scattered electron micrograph with EDS analysis from the cleaned surface of S glass.

Fig. 4.28 corresponds for area which has been selected. The small area as shown in box was analyzed first in Fig. 4.28 (a). The corresponding EDS spectra below along with elemental analysis is shown below (Table: a). From Table (a), one can see that the analyzed area is free from carbon content. We have analyzed another zone which appears distinct as shown in Fig. 4.28 (b). This indicated the presence of carbon content as inclusions and is also confirmed from EDS analysis (Table: b).

The dark cavity observed around this area indicates that carbon particles have occupied the area where the solute rejection is maximum (solid-liquid interface). This further confirmed that carbon has not come from outside, rather it is integral part of the glass system. Presence of other constituent elements also confirms that it is completely bonded carbon.

4.1.4.2. Structural analysis of X Glass

The secondary electron image of the surface of X glass is shown in Fig. 4.29. Here also at certain places surface gives appearance of flow lines and presence of inclusions. These inclusions are distributed throughout the section of the structure. It gives appearance of heterogeneous type of microstructure where unwanted heterogeneities get segregated throughout the section. We have done EDS analysis at these heterogeneities which is shown in Fig. 4.30. Since the area analysis was enhanced where inclusion is well within the glass, the carbon obtained is less (18.0%). In the same area EDS done in separate zone shows carbon 15.44% (Fig. 4.30 (b)). These inclusions are of carbon element. It looks that pieces of glass sent to us was from the end potion of the last castings where chances of such heterogeneity is more.

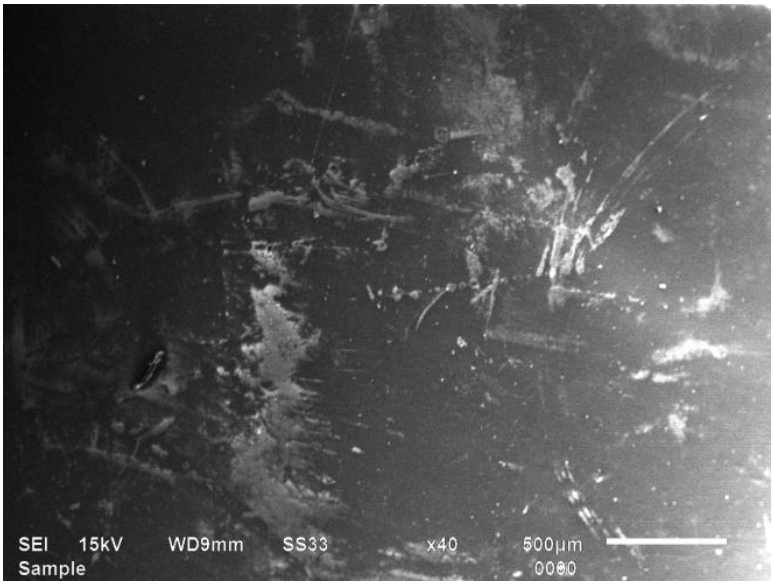

Fig. 4.29: Scanning electron micrograph of the surface of X glass as received.

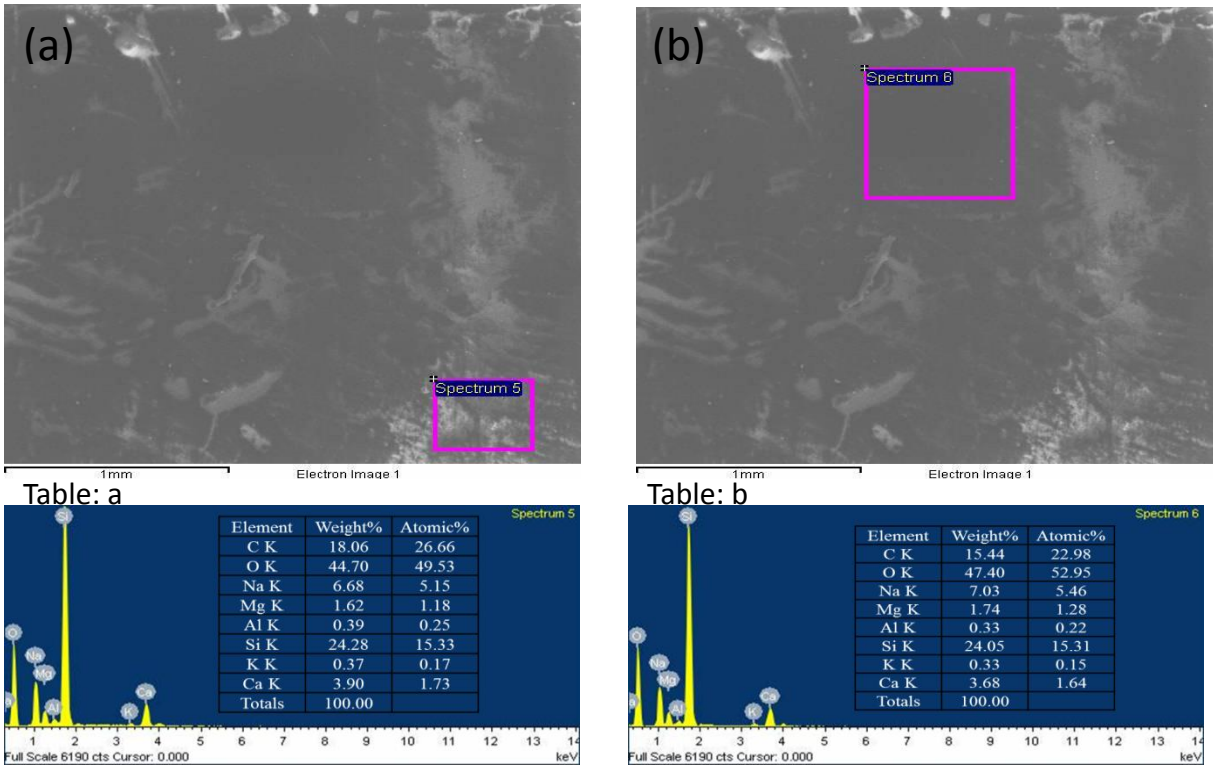

Fig. 4.30: Back scattered electron micrograph with EDS analysis from the surface of X glass.

4.1.5. FTIR studies of N-series glasses

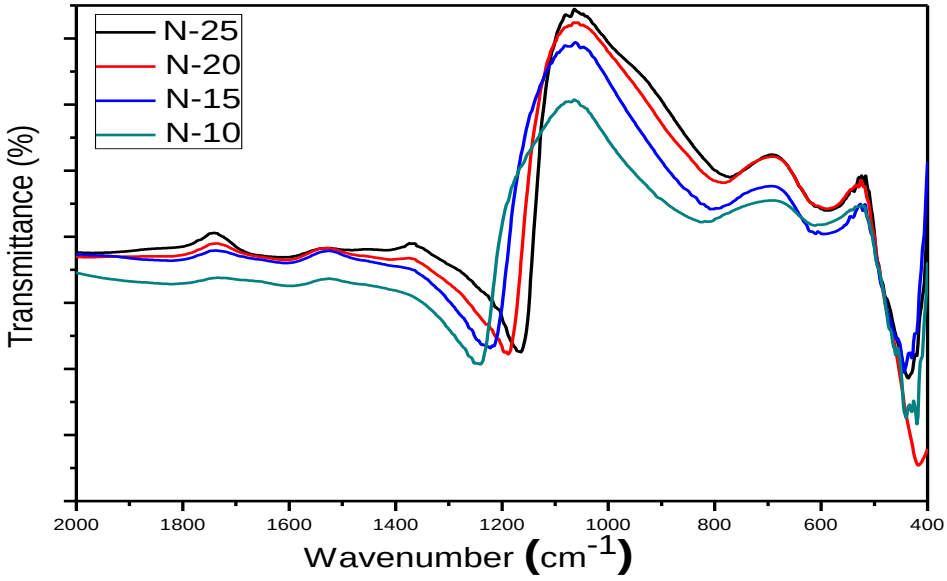

Fig. 4.31: FTIR spectra of N-25, N-20, N-15, N-10 glasses.

The FTIR transmittance spectrums of N-series samples are presented in Fig. 4.31. Obtained spectra for each glass shows three broad bands in the middle infrared region (400–1600 cm^{-1}).

Additionally, the FTIR spectra shows the shifting of band at lower wavenumber which broadens with addition of Na_2O (modifier). This might be attributed due to creation of higher number of NBOs with increasing modifier in glasses. Similar results have also been reported by Ma et al. [12] for CaO-MgO-Al_2O_3- SiO_2-Na_2O glass system. The most intense bands are observed in the 1200–800 cm^{-1} and 800–650 cm^{-1} region. It is known that the band 1300–850 cm^{-1} is assigned to antisymmetric vibration of Si–O–Si within [SiO_4] [26]. Its width is the result of the occurrence of Q^n units in the glass structure [27]. The band 800–650 cm^{-1} is due to Si–O–Si symmetric stretching vibration between the tetrahedrons. Also, the transmission bands in the 650–800 cm^{-1} region are related to the stretching vibrations of the Al–O bonds with Al^{3+} ions in fourfold coordination. Since the atomic weights of Al and Si are almost equal in aluminosilicate glasses, the vibrational mode of [SiO_4] and [AlO_4] tetrahedral are coupled with each other. The Al–O force constant is smaller than the Si–O force constant due to the lower valence of Al^{3+}. The vibrational frequency of AlO_4 tetrahedral is less than that of SiO_4 tetrahedral [28]. The band 650–400 cm^{-1} is due to bending vibration of Si–O–Si and Si–O–Al linkage. The maximum intensity of this band does not change its position with the change of alkaline earth ions [29]. Khalil et al. [30] have reported that the addition of transition metal ions in low percentage do not cause structural changes and hence could not be detected by the IR spectra.

4.1.6. UV-visible analysis

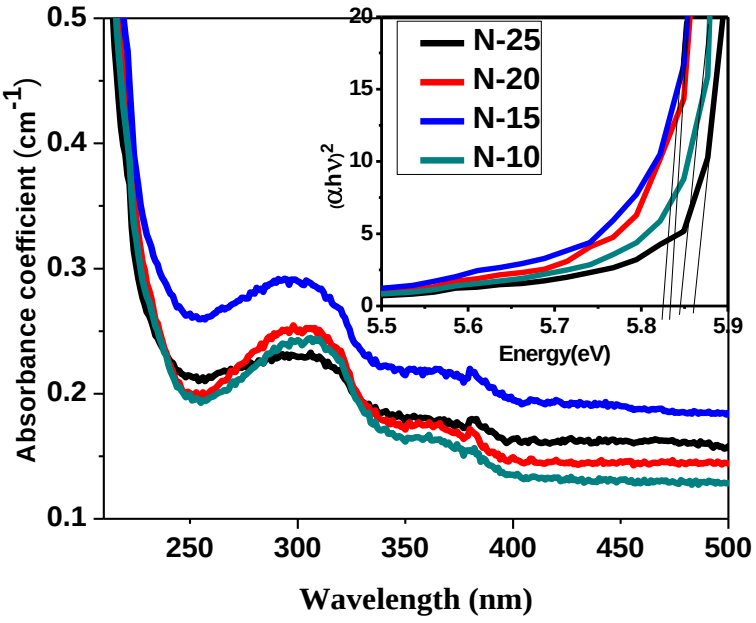

Fig. 4.32: UV-Visible spectra of N-25, N-20, N-15, N-10 glasses.

Fig. 4.32 shows the optical absorption spectra of the samples. The band gap energy values for samples were estimated by the following equation:

$$\alpha (h\nu)\ \alpha\ (h\nu - E_g)^m \qquad (4.14)$$

where α is the optical absorption coefficient. As shown in inset of Fig. 4.32, $h\nu$ is the photon energy and E_g is the band gap energy. Fig. 4.32 shows the plot for m=1/2 (direct allowed transition). The band gap values are obtained by extrapolating the fittings of Fig. 4.32, with $(\alpha h\nu)^{1/m} = 0$. Previous studies showed that with increasing content of SiO_2, the number of bridging oxygen per aluminum/ or silicon tetrahedral increases [31, 32]. In this way, the decrease in the number of NBOs for higher SiO_2 content should result in an increase in the band gap energy [33]. In the present glass systems, the optical band gap could not show any particular pattern with decreasing modifier contents. Duffy et al. [34] have reported that the higher content of NBO in glass increases the ionicity of oxygen which raises the top of the valence band and leads to the reduction of the band gap energy. The optical absorption coefficient near the fundamental absorption band has an exponential dependency, which is given by the Urbach's rule as follows [35]:

$$\alpha = \qquad \exp (h\nu/E_r) \qquad (4.15)$$

Here α_o is a constant and E_r is the Urbach's energy. E_r corresponds to the optical transitions between localized tail states adjacent to the valence band and extended states in the conduction band above the mobility edge. The absorption coefficient value (in log scale) was plotted against the photon energy and summarized in Table 4.9.

Table 4.9: Optical properties of the glasses.

Sample	**N-25**	**N-20**	**N-15**	**N-10**
Band Gap, E_g (eV)	5.68	5.38	5.26	5.49
Urbach's Energy, E_r (meV)	28	34	39	38

The value of E_r is quite low which clearly indicates that present glasses exhibit lower value of NBO as compared to other reported glasses [33, 36]. According to Mott and Davis [37] model, this energy depends on the degree of both disorder and defects in the amorphous structure. If the glass has more polymerized network, Urbach's energy is lower.

4.1.7. Dielectric properties of N-series glasses

Number of NBOs leads a change in physical properties of glasses such as glass formation temperature, electrical conductivity, density and refractive index. These properties get modified when glasses are exposed in reducing or wet environment [38]. In order to identify the factors which affect the bulk diffusion and release of cations from glasses under wet condition, the

arrangement of local structural environment of glasses by optical and dielectric relaxation studies has been done [39]. The mobile ions like alkali cations in glasses generate polarization by reorienting themselves locally in glass matrix. The generation of polarization is also responsible for the conduction in lower frequency range by separating itself from the immediate neighborhood [40-41].

4.1.7.1. Dielectric characterization

Room temperature dielectric constant (ε□) as a function of frequency for N-25, N-20, N-15 and N-10 samples are shown in Fig. 4.33. It was observed that ε□ shows frequency independent behavior above 20 kHz particularly, for the N-25 sample. But frequency independent behavior for other samples was observed above 1 kHz. Fig. 4.33 illustrate that the values of dielectric constant decrease up to N-15. As the sodium content decreases, the number of NBO also decreases causing strong networking of Si-O-Si bond [42].

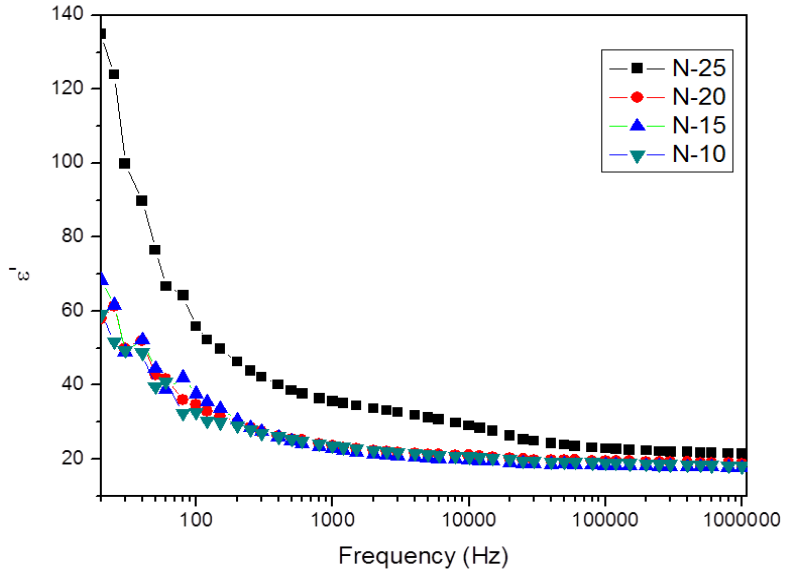

Fig. 4.33: ε□ of N-25, N-20, N-15 and N-10 glasses with variation in frequency at room temperature.

This in turn reduces the polarization and therefore the dielectric constant (ε□) also reduces. For N-10, Al/Na ratio becomes 1. So in this particular glass, bridging oxygens (BOs) may be higher than other glasses. Additionally, sodium ion act as charge compensator for aluminate groups and coordinate to BOs and two silicons that build up space charge in the glasses [43-44]. The development of the space charge polarization increases the dielectric constant values as compared to orientation or ionic polarization. The frequency dependence of dielectrics constant (ε□) at 380 °C is shown in Fig. 4.34 for N-25, N-20, N-15 and N-10 glass samples.

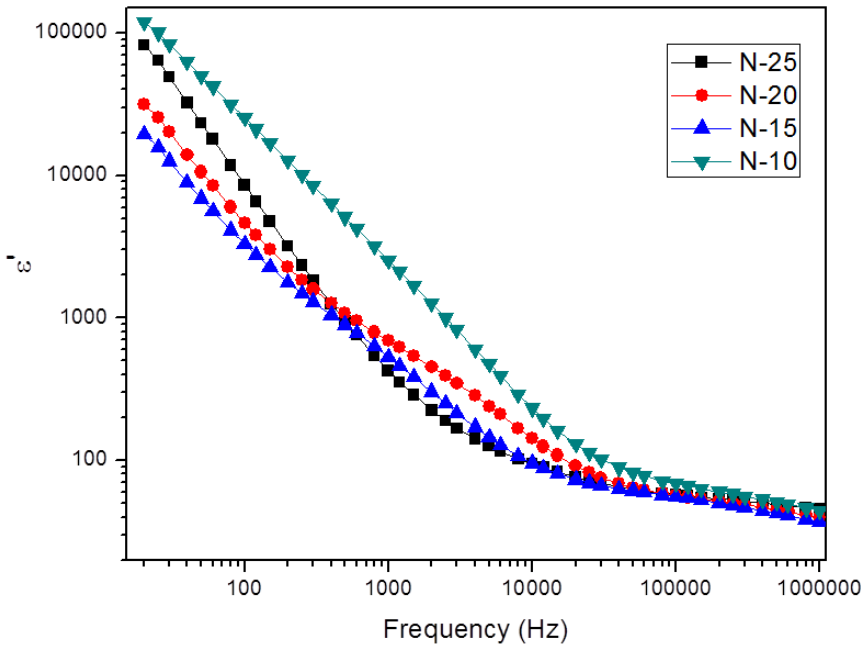

Fig. 4.34: ε′ of N-25, N-20, N-15 and N-10 glasses with variation in frequency at 380 °C.

From Fig. 4.34, it is clear that the frequency independent behavior of ε′ shifts towards a higher frequency range above ~ 20 kHz in all the samples. The ε′ values in the low frequency range were anomalously large and showed step-like behavior for all the samples. The value of dielectric constant increases with increasing temperature, which could be explained by taking into account that at higher temperature the intermolecular forces are weakening and hence increases the orientational vibration. Thus, at higher temperature, the jump frequency of the charge carrier becomes large and comparable with the frequency of the applied field.

Fig. 4.35 shows the dielectric constant ε′ versus frequency plots of glasses at various temperatures. It is evident that at a particular temperature the value of ε′ decreases with increasing frequency and attains a constant limiting value ε'_{∞} which is not related to the hopping dynamics of mobile ions and may be due to much more rapid polarization process occurring in the material. The increment in dielectric constant with respect to frequency at a higher temperature is due to dominating interfacial polarization as compared to the orientation polarization. The high value ε′ in low-frequency region is a bulk phenomenon arising due to the presence of metallic or blocking electrodes which do not permit the mobile ions to transfer into the external circuit. As a result mobile ions pile up near the electrodes and give rise to large bulk polarization in the materials. With increasing temperature, a high degree of dispersion of the permittivity curve is observed at lower frequency (1 kHz), which is related to storage of NBOs. The storage of NBOs is related to a conduction process or defects [45]. The large value of the dielectric constant observed at low frequencies is attributed due to interfacial polarization

process. At higher frequencies, dielectric constant decreases slowly and the maximum peak shifts to higher frequency with increase in temperature. Therefore, in a higher-frequency region dielectric constant follows Debye behavior ω^n. In the low frequency region, the ions jump in the applied field direction and pile up at the higher energy barrier sites. It could be arrived due to increase in capacitance in the applied field direction. At higher frequencies, the periodic reversal of the field takes place so rapidly that there is no excess ion jumps in the field direction. The capacitive effect disappears at higher frequencies, which reduces the contribution of the charge carriers to the dielectric constant.

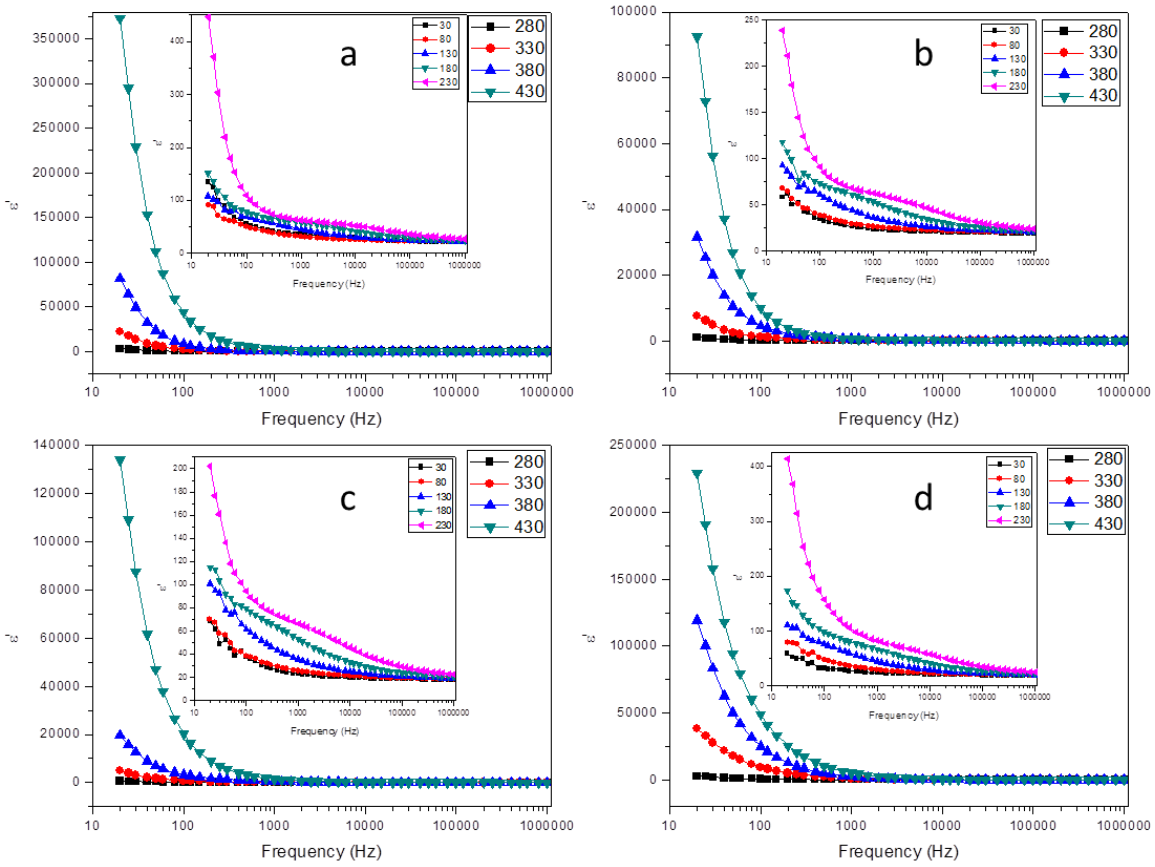

Fig. 4.35: Frequency dependent ε□ of (a) N-25 glass, (b) N-20 glass, (c) N-15 glass and (d) N-10 glass at various temperatures.

The imaginary parts of dielectric constant (ε□□) as a function of frequency for all the glass samples at temperature 380 °C are presented on a logarithmic scale in Fig. 4.36. The straight linear lines represent the theoretical fit based on the Johnscher-law [46] as follows:

(4.16)

The magnitude of the exponent (n) can be considered to be very small, reflecting the level of non-ideality for the capacitance. So, the deviation of capacitance from the ideal behavior with increase in Na_2O content is clear evidence of the existence of disorder structure [47].

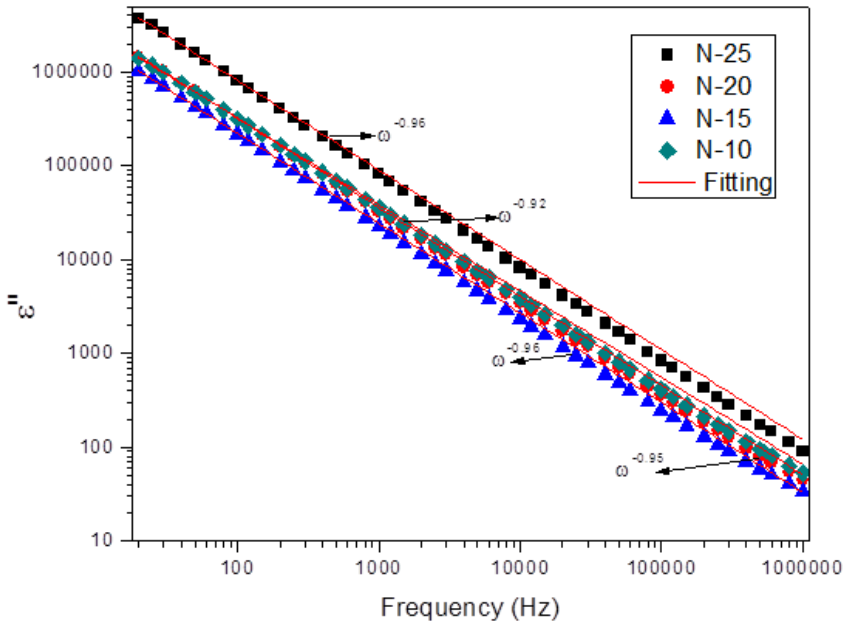

Fig. 4.36: Plots of universal dynamic response for N-25, N-20, N-15 and N-10 glasses at 380 °C.

The frequency dependent of dielectric loss (tan δ) at different temperatures for all the glass samples is shown in Fig. 4.37. The tan δ versus frequency curve exhibits a distinct peak in the low- frequency region. It is evident from Fig. 4.37 that the position of the dielectric loss peak shifts to higher frequencies with increase in temperature. This phenomenon is called thermaly activated Debye-like relaxation. The relaxation process is determined by Debye-like relaxation time given by $\omega_{max}\,\tau = 1$, where ω_{max} is the maximum angular frequency. The entire phenomenon is related to actuation of a hopping type mechanism [48].

The effect of Na_2O content on the dielectric behavior of the present samples can be clearly seen in terms of maxima shifting toward higher-frequency region, peak broadening and asymmetry in the peak. The shifting of maxima toward the higher-frequency region with decreasing concentration of Na_2O indicates a decrease in the relaxation time. As the concentration of Na_2O increases, there is an increase in the broadening and asymmetry of peaks which suggests an increase in the distribution of relaxation time. According to the dielectric theory, the activation energy for dielectric relaxation can be calculated from the dielectric loss factor ε□. However, in the present oxide system, the loss factor (ε□) cannot give any idea of the dielectric relaxation process as also reported for other oxide systems because it is attributed entirely to dc-conductivity which is usually dominant at higher temperatures and low frequencies [49]. Therefore, the activation energy for the relaxation will be estimated by considering that the loss factor ε□ which is proportional to tan δ [50].

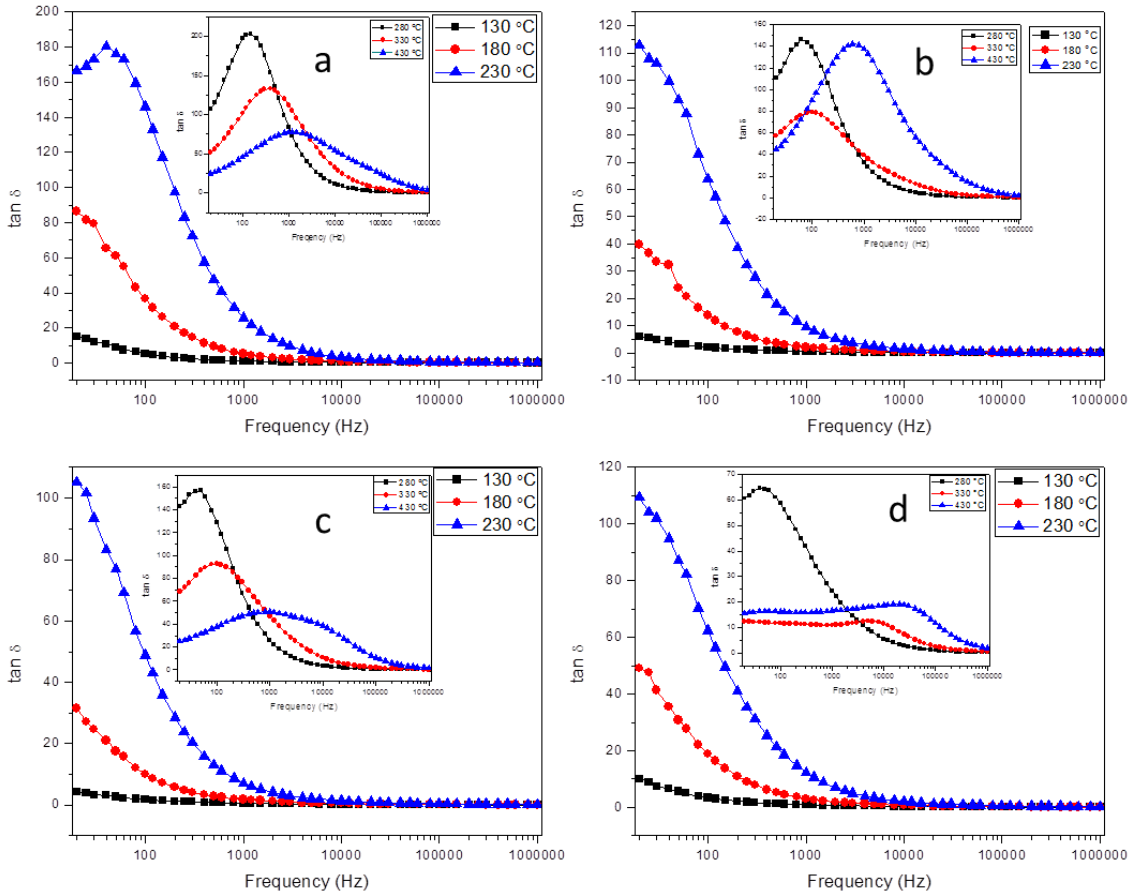

Fig. 4.37: Frequency dependent tan δ of (a) N-25 glass, (b) N-20 glass, (c) N-15 glass and (d) N-10 glass at various temperatures.

The activation energy for relaxation can be calculated by the following Arrhenius equation:

— (4.17)

where τ_o is a pre-exponential factor, k is Boltzmann constant, T is the temperature at which the relaxation peak has a maximum and E_a is the activation energy required for the dielectric relaxation process.

4.1.7.2. Temperature and frequency dependence of dielectric constant

The variation of dielectric constant as a function of temperature at 1 kHz for all the glass samples is illustrated in Fig. 4.38. The dielectric constant decreases with decrease in Na_2O content of the glass. The value of ε□ increases slowly up to temperature T_a, and beyond this temperature there is a sudden rise in ε□. This may be attributed to the space charge polarization owing to the enhanced degree of disorderness in the glass network [51]. In other words, as the Na_2O content is decreased in the glass network, the concentration of non-bridging oxygen decreases that leads to the formation of order structure. Additionally, T_a temperature increases with increasing frequency for the same composition. This type of behavior may arise due to high frequency as

the dipoles are able to follow the applied field due to the slow process of space polarization as compared to ionic and electronic polarizations [52].

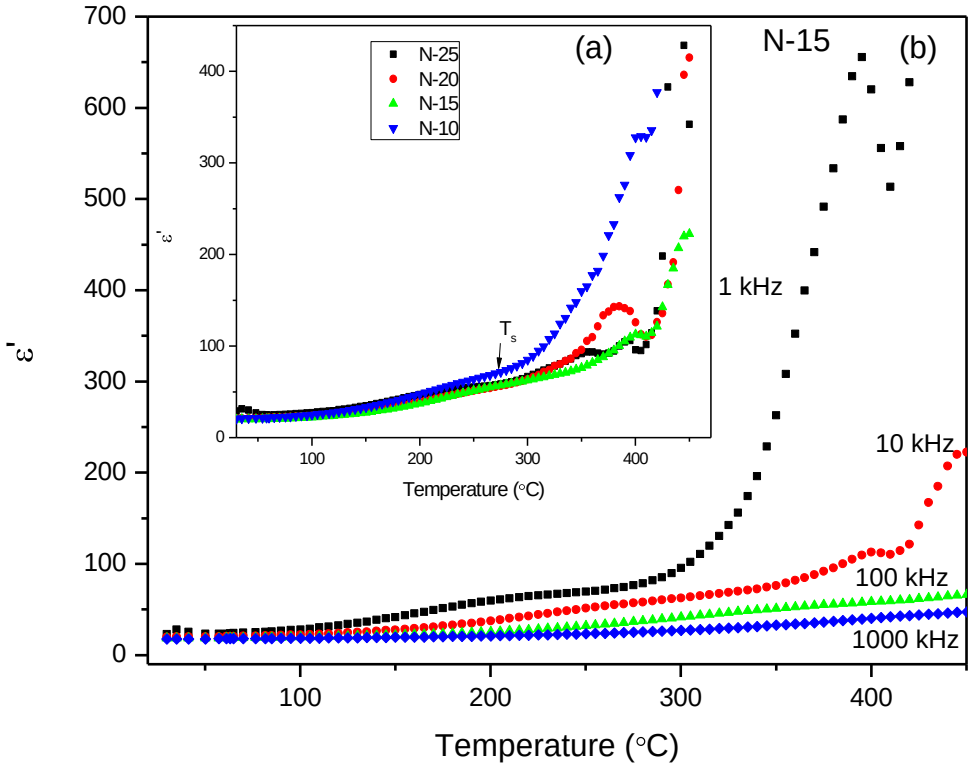

Fig. 4.38: (a) ε′ versus temperature measured at 1 kHz for all glasses and **(b)** ε″ measured at various frequencies for N-15 glass.

4.1.7.3. Electrical conductivity analysis

A.C. conductivity, σ_{ac}, has been calculated at different temperatures, using the following relation [53]

$$\sigma_{ac} = \omega \varepsilon_o \varepsilon'' \tan \delta \qquad (4.18)$$

Fig. 4.39 shows the angular frequency ω (=2πν) dependence of log of a.c. conductivity, at various temperatures. It is evident from the Fig. 4.39 (a-d) that at low-frequencies and higher temperatures, conductivity shows frequency independent nature for all glasses i.e. N-10, N-15, N-20 and N-25, which gives rise to dc-conductivity arising from the random diffusion of the ionic charge carriers via activated hopping process. However, at higher frequencies, there is a crossover into a dispersive regime where the conductivity increases with frequency [54].

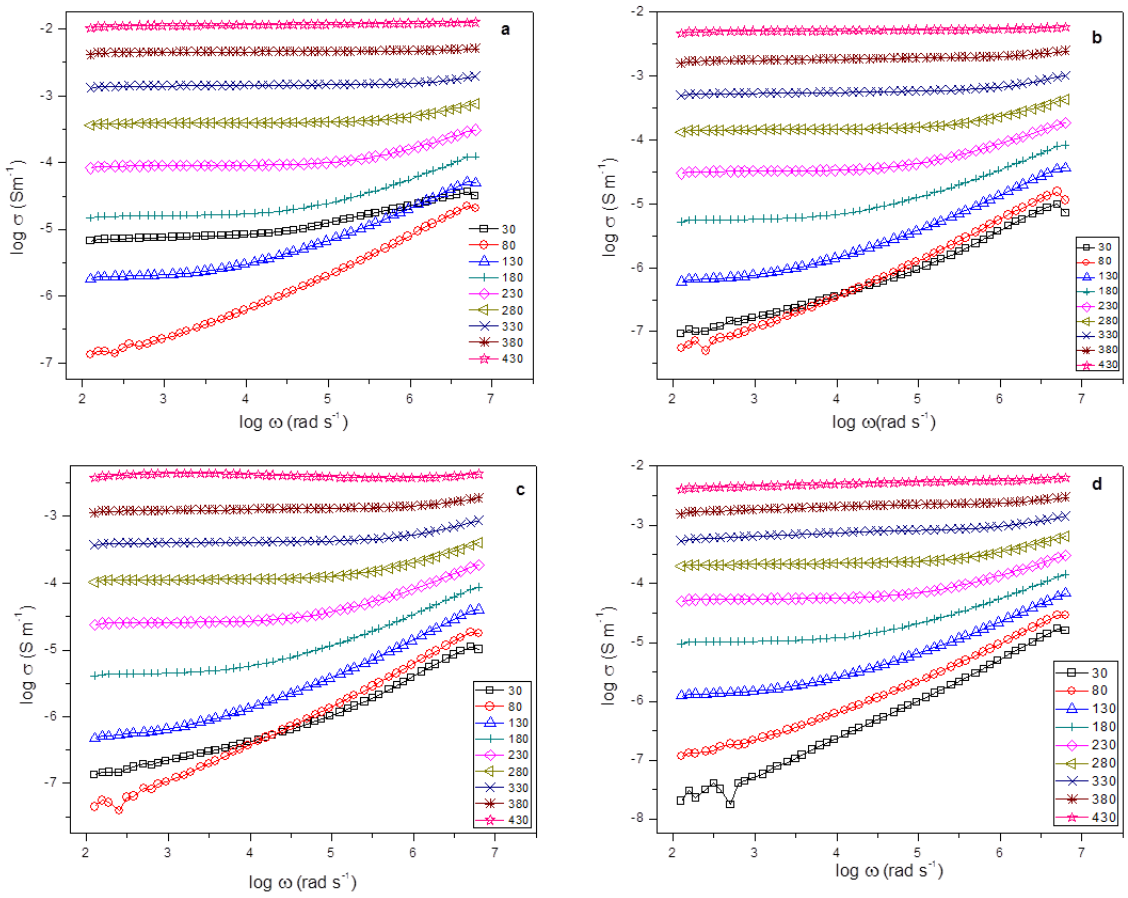

Fig. 4.39: Frequency (angular) dependence of the conductivity (σ) at various temperatures for (a) N-25, (b) N-20, (c) N-15 and (d) N-10 glasses.

Table 4.10: Values of various parameters of glasses.

Name of Sample	Relaxation Time (280 °C)		E_a (eV) from		Refractive index (n)
	Tan delta	M"	ln τ	Log σ_{ac}	
N-25	5.23E-06	3.98E-07	0.65	0.77	1.70
N-20	1.81E-05	7.96E-07	0.51	0.74	1.69
N-15	2.03E-05	1.06E-06	0.45	0.73	1.67
N-10	6.17E-05	5.31E-07	0.65	0.75	1.69

The activation energy for conduction in the high temperature region is evaluated and presented in Table 4.10. The activation energy is also found to decrease gradually with decrease in the Na_2O concentration except N-10. Na^+ enters the network of the glass as a modifier which means that Na_2O breaks up Si–O–Si bonds and introduce coordinated defects known as dangling bonds which increases disordering in structural network and increases the concentration of non-bridging oxygen (NBO). In this case, the structure of the glass could be considered as bonding defects (dangling bonds) with non-bridging oxygen [42, 44]. The concentration of such bonding

defects in the glass network depends upon the concentration of Na_2O which leads to decrease in the activation energy of conduction as in case of N-15 and N-20 samples.

4.1.7.4. Refractive index of glasses

The measured values of refractive index of glasses are given in Table 4.10. N-15 glass has least refractive index among the series that corresponds to optically dense glass. The dielectric constant of a glass sample results from electronic, ionic and orientation contribution to the polarizability. The electronic contributions are always present and are the main contributor in the optical range of frequencies. By comparing the Lorentz equation and the Mosotti equation, the relation between dielectric constant (ε') and the refractive index (n) is

$$\varepsilon' = n^2 \tag{4.19}$$

The higher values of dielectric constant and refractive index for N-25 glass follow the above relation.

The introduction of Al_2O_3 into alkali silicate glass is known to form AlO_4 tetrahedral units when the amount of Al_2O_3 is less than alkali oxide, R_2O ($[Al_2O_3] < [R_2O]$). AlO_4 unit has a negative unit charge, and an equal amount of non-bridging oxygen is reduced. Therefore, R/Al ratio gives a measure of the negative charge distribution on the glass network. In other words, it is for site distribution of alkali ions in alkali aluminosilicate glass system. Glass N-25 to N-15 has an R/Al>1, which means that almost half of R^+ ions interact with non-bridging oxygens (NBO), and the other half are located near AlO_4 tetrahedral units. Here after, R^+ ion site to which an NBO contributes is called NBO-site while the other R^+ site to which AlO_4 contributes is called charge compensation-site (CC-site). In Glass N-10, R/Al=1. This means that all R^+ ions are in CC-sites and this glass lead to different behavior than other glasses [55].

4.2. Interaction study between glasses and steels

Glass coating on metallic substance may be useful in manufacturing industries as it may lead to development of heat and corrosion resistant material. A strong joining of two materials depends on chemical and physical factors of the interfaces. The better mechanical properties with excellent corrosion resistant to different environments make glass indispensable. Its high chemical resistance can provide good corrosion resistant on the surface of steel. Though the glass coating might be difficult as compared to the other coating materials but it can provide good corrosion resistance. The density of the glass is less as compared to the metallic coating which has additional advantage. Considering these aspect it is fruitful to study the coating parameters to achieve adherent coating of glass on steel surfaces. Interaction study of N-series glasses with crofer, and stainless steel (SS) steels was done and studied extensively which are presented in subsequent sections. However, interaction study of N-10 glass was done on duplex steel as this glass exhibited better results with other steels.

4.2.1. N-series glasses and crofer steel

At 800 °C, N-15 glass showed adhesion with crofer steel and formed stable layer on it as shown in Fig. 4.40. However, all glasses interacted with crofer steel at 900 °C as shown in Fig. 4.41.

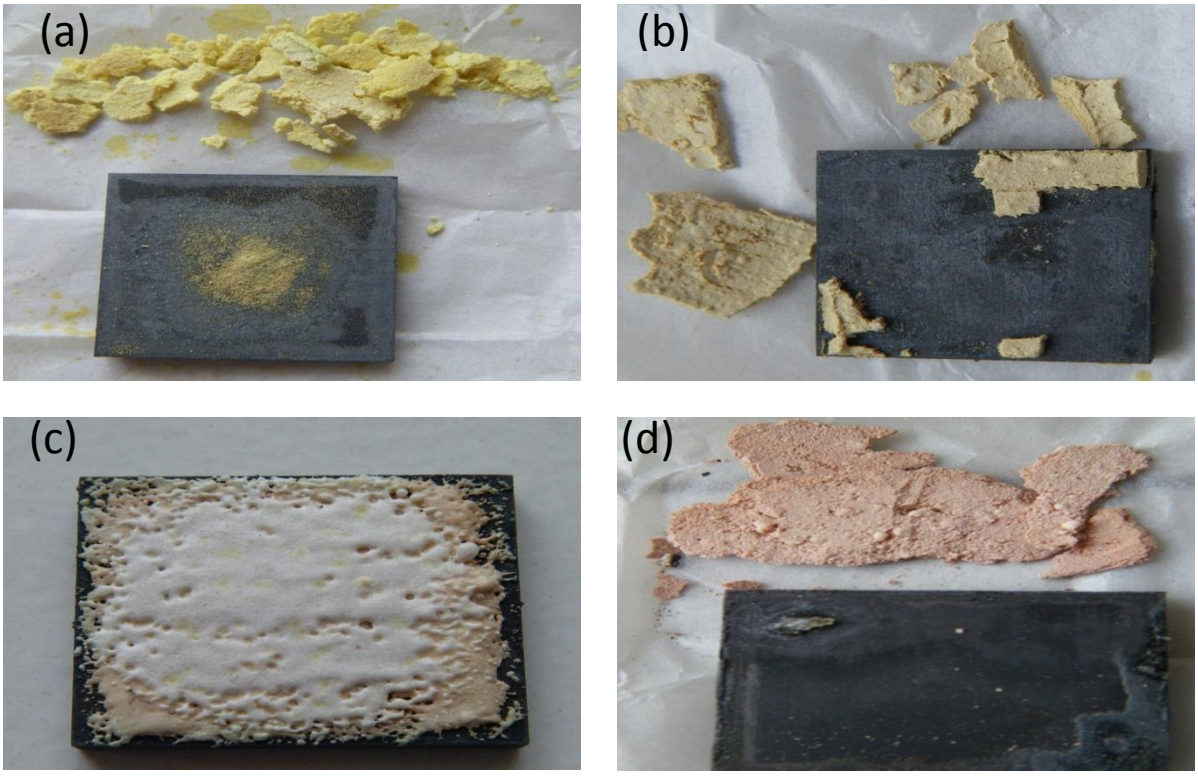

Fig. 4.40: Photographs of diffusion couple of crofer steel with (a) N-25, (b) N-20, (c) N-15 and (d) N-10 glasses at 800 °C.

N-15 glass coating was smooth and defect free among these diffusion couples. In order to understand the nature and behavior of glass coating on steel surfaces, we have done the detailed microstructural study of obtained surface of coated glass-ceramic and the interface because this will enable us an insight into the surface adhesion characteristic of glass.

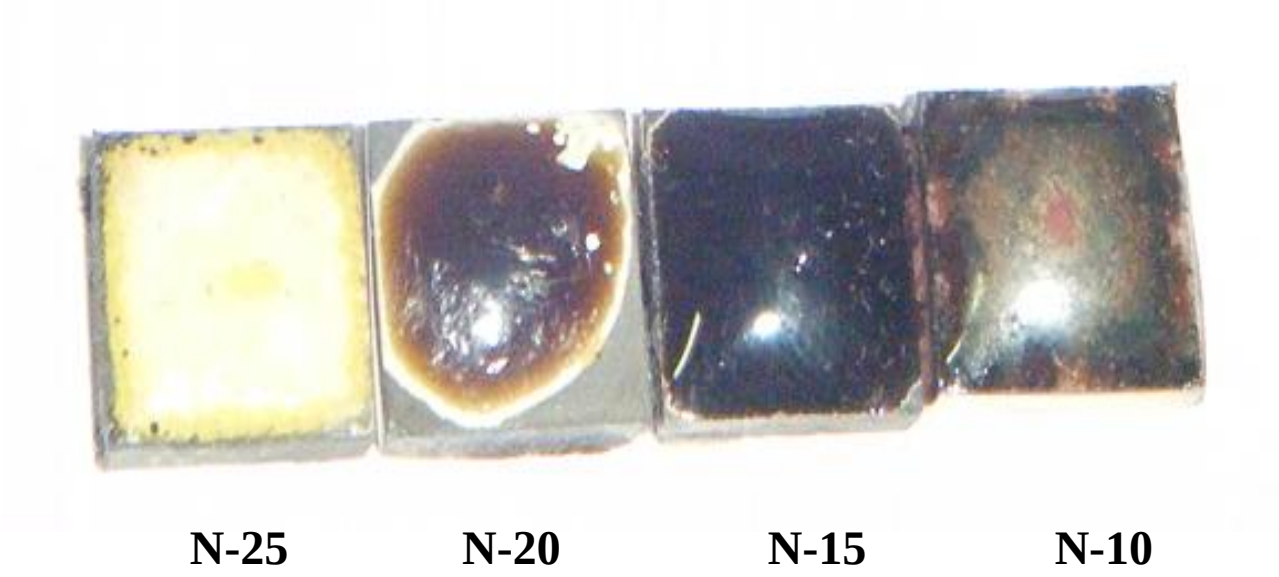

Fig. 4.41: Photographs of diffusion couple of crofer steel with N-25, N-20, N-15 and N-10 glasses at 900 °C.

4.2.1.1. N-25 glass and crofer steel

4.2.1.1.1. Surface analysis

Fig. 4.42 (a-d) shows the micrographs of the N-25 glass coating done at 900 °C on crofer steel by heating the couple for 1 h. The diffusion couple appears to be adherent with non-smooth surface as shown in Fig. 4.42, a, b. The higher magnification micrograph (Fig. 4.42, c, d) present the growth of crystalline phases in glass matrix. In the structure, one can visualize two types of morphological features of the crystalline phases. One is a staircase like structure trying to form a hexagonal shape i.e. $NaAlSiO_4$ phase which is sodium rich phase. Second is a granules type structure that grow between lines which is $Na_4Ca_4(Si_6O_{18})$ phase. In some places of micrographs, the growth of the staircase like structure is more pronounced. Both phases have sodium content which proves the presence of sodium after heat treatment [56]. Also N-25 glass has maximum sodium content as compared to others. In order to further quantify the nature of interface, the EDS spectrum of the top layer of glass along with the elemental analysis to know the depth of diffusion (Fig. 4.43) was also taken.

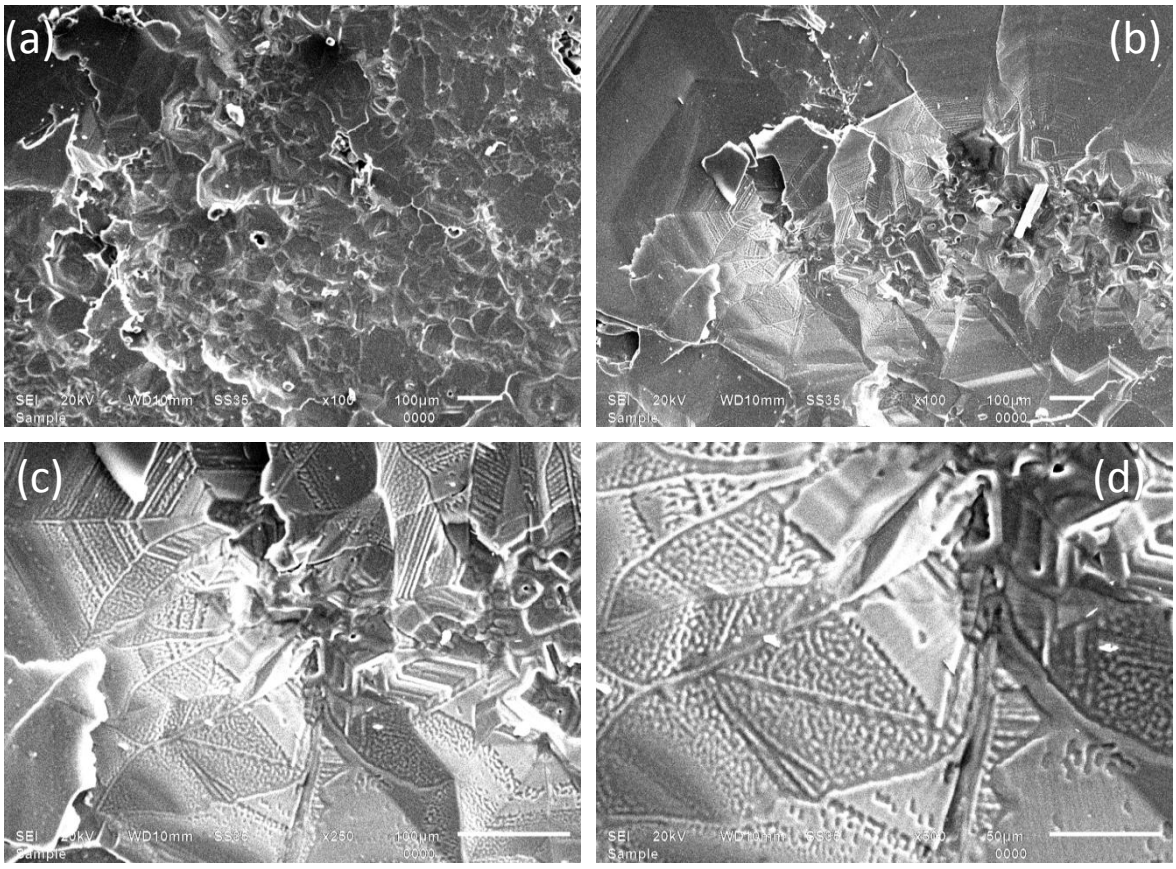

Fig. 4.42: Scanning electron micrographs of the N-25 glass-ceramic coating on crofer steel showing the nucleation and growth of crystalline phases.

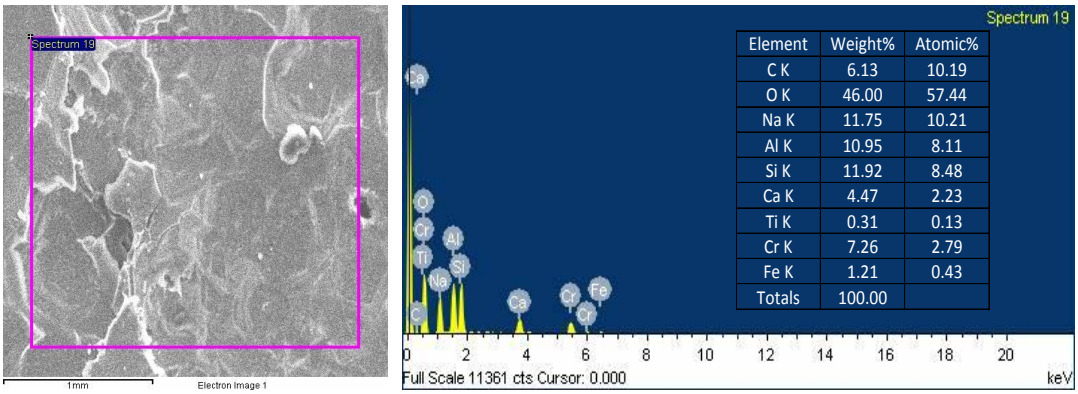

Fig. 4.43: EDS spectrum with elemental analysis of the area marked.

The overall analysis indicates that chromium and iron from the steel is diffusing into glass. The X-ray dot mapping of Si, Ca, Al, Ti, Na, Cr, Fe and O taken from area shown in Fig. 4.44 (a) are given in Fig. 4.44 (b-i), respectively. These results further confirmed the diffusion of Cr and Fe which is also required for good bonding between crofer and glass. The diffusion of Cr is more prominent than other elements. Similar results have been reported in interaction study between glasses and crofer [57].

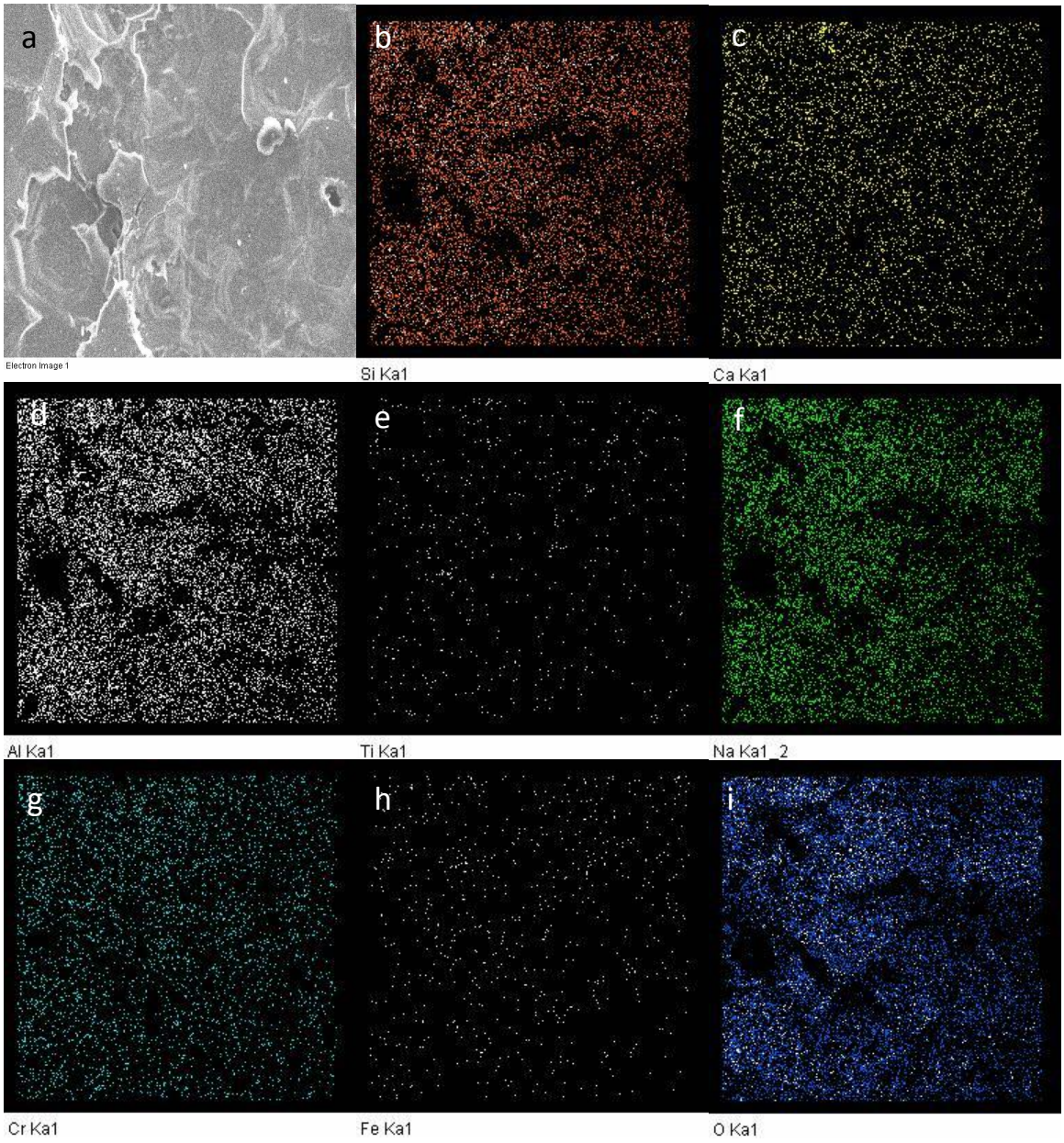

Fig. 4.44: X-ray dot mapping of Si, Ca, Al, Ti, Na, Cr, Fe and O of the N-25 glass-ceramic coating on crofer steel.

4.2.1.1.2. Analysis of interface

Cross-sectional microstructure of the interface between N-25 glass and crofer is shown in Fig. 4.45. The interface between glass and steel shows adhesion. The interfacial layer seemed to be weak at some places. However, some voids and porosity are observed at the interface. The EDS analysis at the marked area as shown in Fig. 4.46 was done to understand the diffusion and inter-diffusion of the elements. This is shown in Fig. 4.47 (a-c) for the areas marked as 1, 2 and 3, respectively.

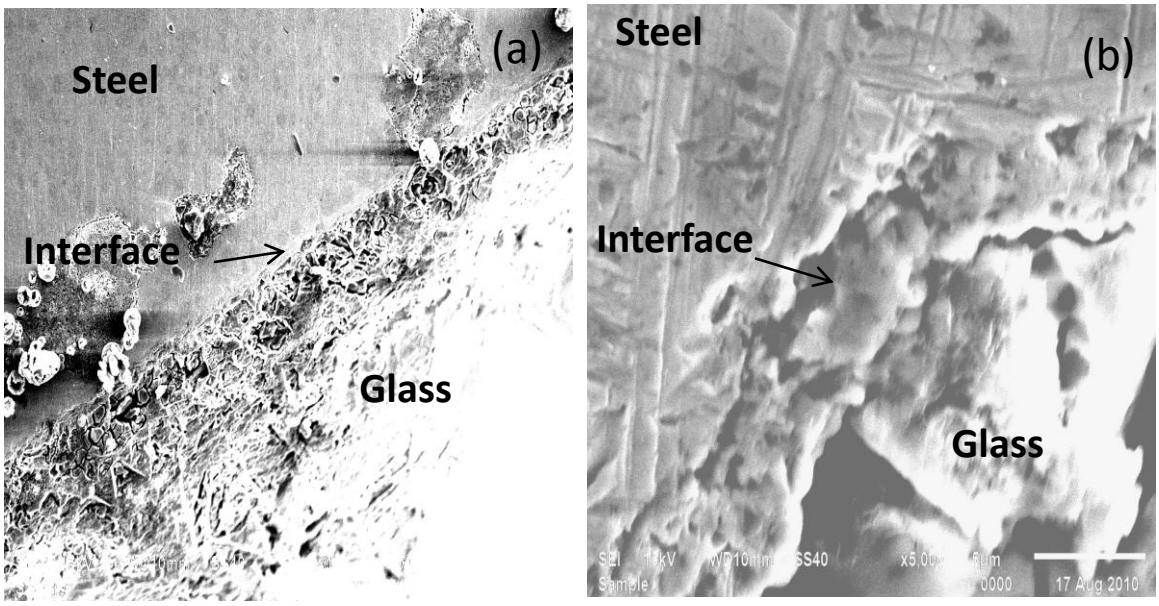

Fig. 4.45: SEM micrograph of interface between N-25 glass and crofer steel showing the overall view of interface.

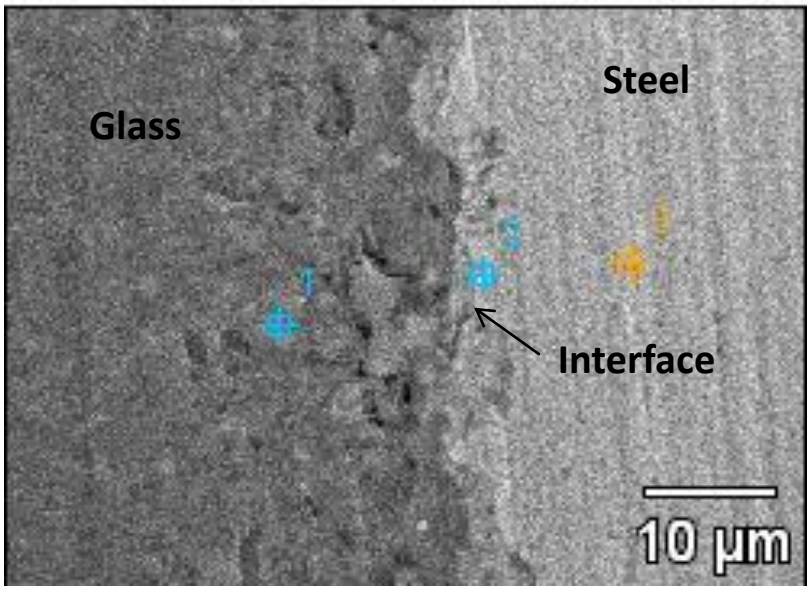

Fig. 4.46: Back scattered electron micrograph of interface between N-25 glass and crofer steel.

As observed from the EDS of surface analysis, it also confirms the diffusion of Fe and Cr from the steel side into glass. However, the interface is very weak. Cr and O elements are main constituents at the interface. Apart from this, diffusion of carbon and titanium also occurs. These elements being smaller in size gets easy path for their diffusion. It is well reported in the literature that the Cr diffuses more vigorously than other species [57]. Presence of Au is because of Au coating on surface of glass.

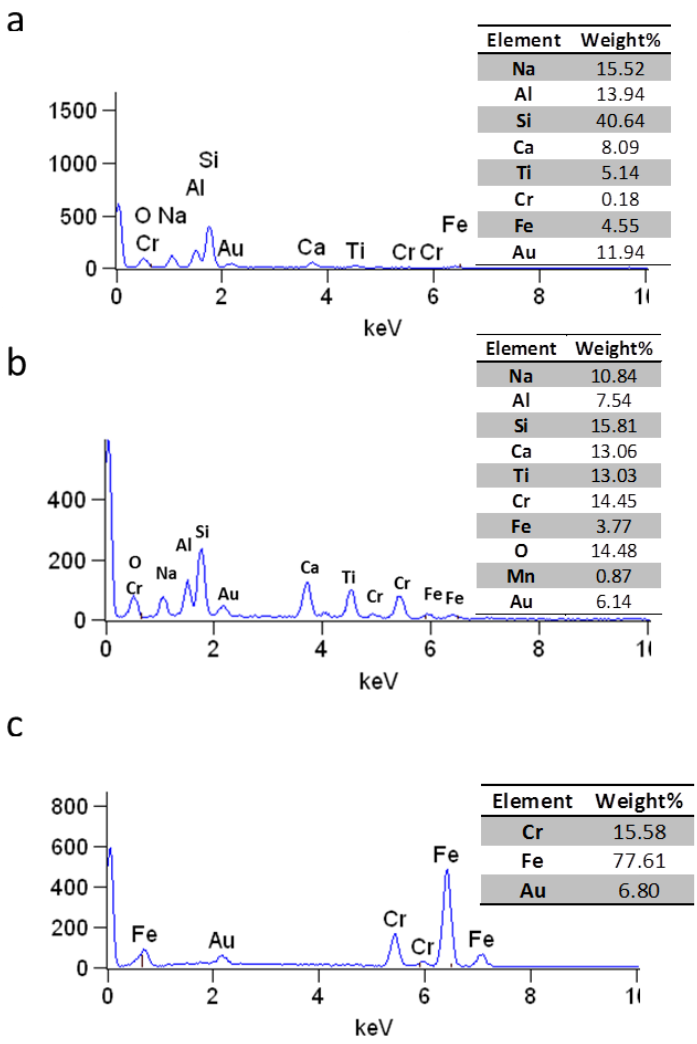

Fig. 4.47: EDS spectrum of the glass of the diffusion couple (a) marked 1 in Fig. 4.46, (b) marked 2 in Fig. 4.46 and (c) marked 3 in Fig. 4.46.

4.2.1.2. N-20 glass and crofer steel

4.2.1.2.1. Surface analysis

As discussed in section 4.1.3, this glass exhibit three crystalline phases after heat treatment at 900 °C for 1 h. Fig. 4.48 (a) shows the micrograph of the N-20 glass coated on crofer steel at 900 °C for 1 h. In the structure, one can visualize the growth of needle shaped dendritic crystals that grow towards the top surface [58]. The sizes of the as grown crystals vary widely which is evident from the corresponding microstructure as viewed under high magnifications (Fig. 4.48, b-d). In order to further quantify the nature of surface, the EDS spectrum of the top layer of glass was taken along with the elemental analysis to know the depth of diffusion (Fig. 4.49).

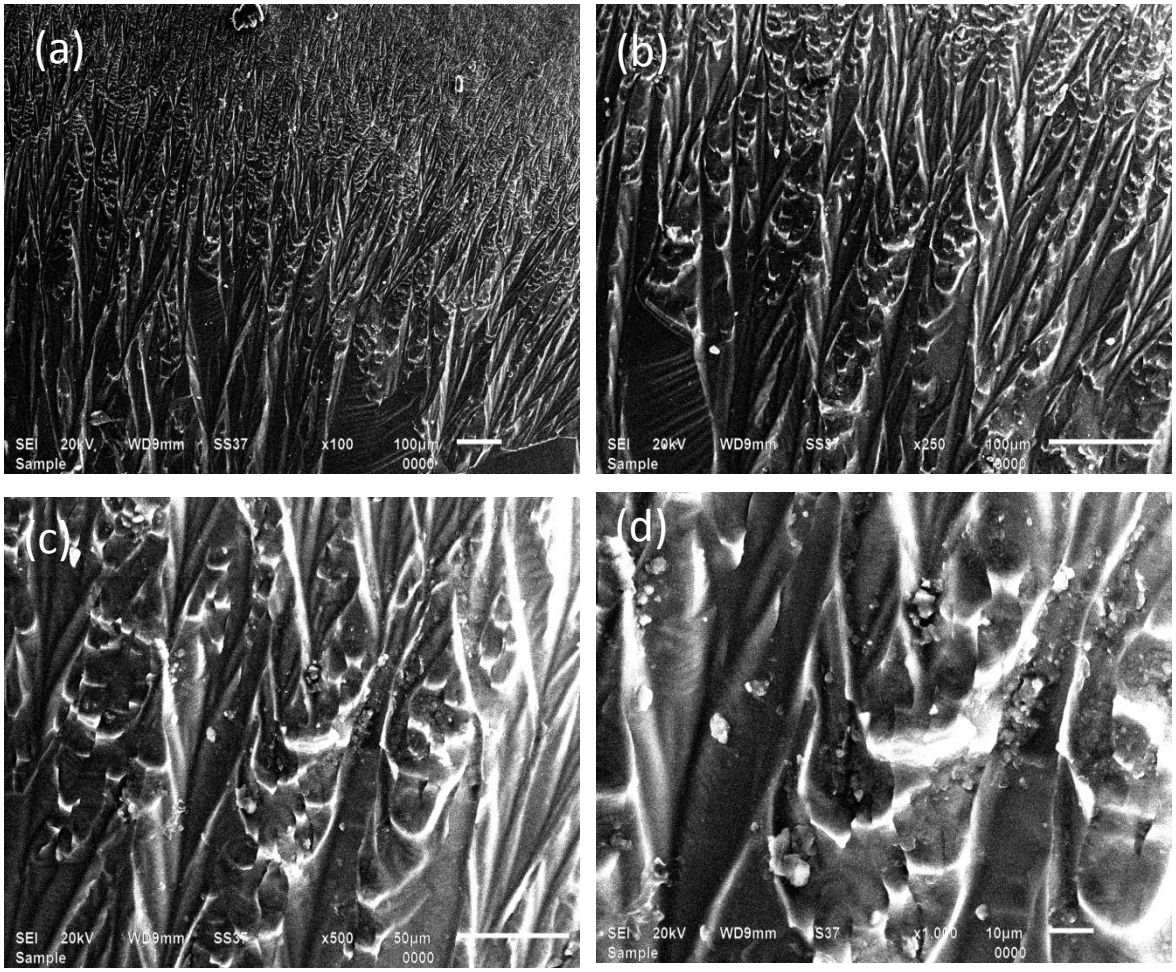

Fig. 4.48: Scanning electron micrographs of the N-20 glass-ceramic coating on crofer steel showing the nucleation and growth of crystalline phases.

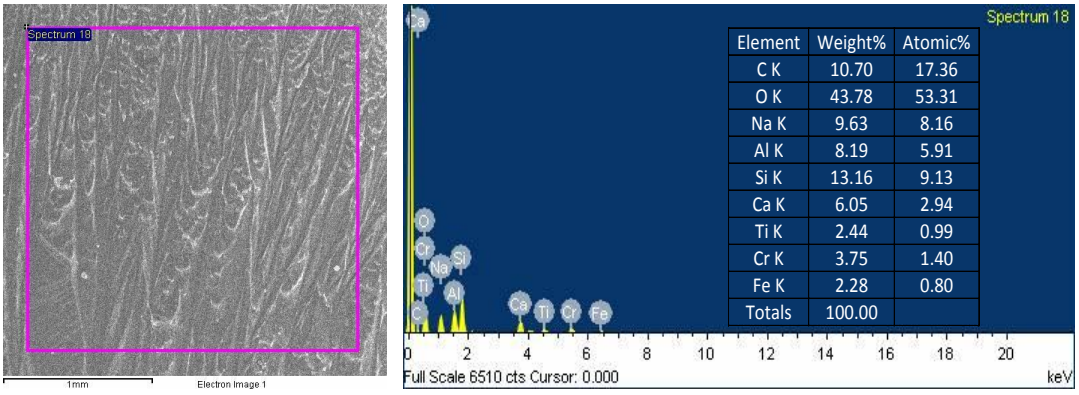

Fig. 4.49: EDS spectrum with elemental analysis of the area marked.

The overall analysis indicates that chromium and iron from the steel is diffusing into glass but the percentage is very less as compared to N-25 glass-crofer diffusion couple. The X-ray dot mapping of Si, Al, Ca, Ti, Na, O and C are shown in Fig. 4.50 (b-h) respectively. Cr and Fe in X-ray dot mapping could not be detected.

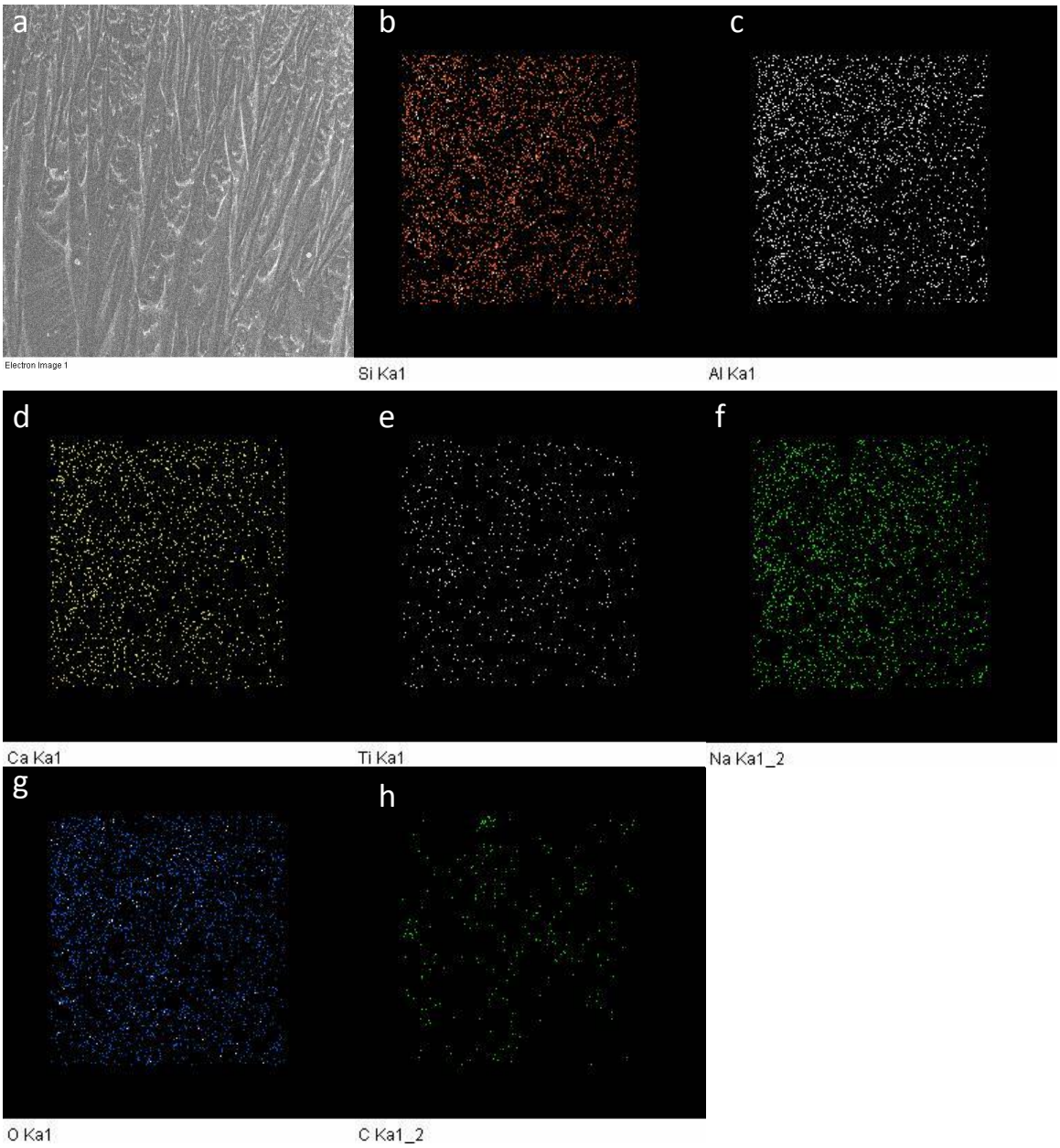

Fig. 4.50: X-ray dot mapping of Si, Al, Ca, Ti, Na, O and C of the N-20 glass-ceramic coating on crofer steel.

4.2.1.2.2. Analysis of interface

Cross-sectional microstructure of the interface between N-20 glass and crofer is shown in Fig. 4.51. The interface between glass and steel shows good adhesion. However, the interfacial layer seemed to be weak. There are some voids and porosity which are observed along the areas of the interface as can be seen Fig. 4.51 (a). However, these pores are not continuous but have appeared locally due to inter diffusion of elements as can be seen in Fig. 4.51 (b) which is further confirmed in BSE micrograph shown in Fig. 4.52. Pores are observed in glass side but not at the interface indicating good interfacial bonding [59]. The EDS analysis on the marked area as 1, 2

and 3(shown in Fig. 4.52) was done to understand the diffusion of the elements and are presented in Fig. 4.53 (a-c).

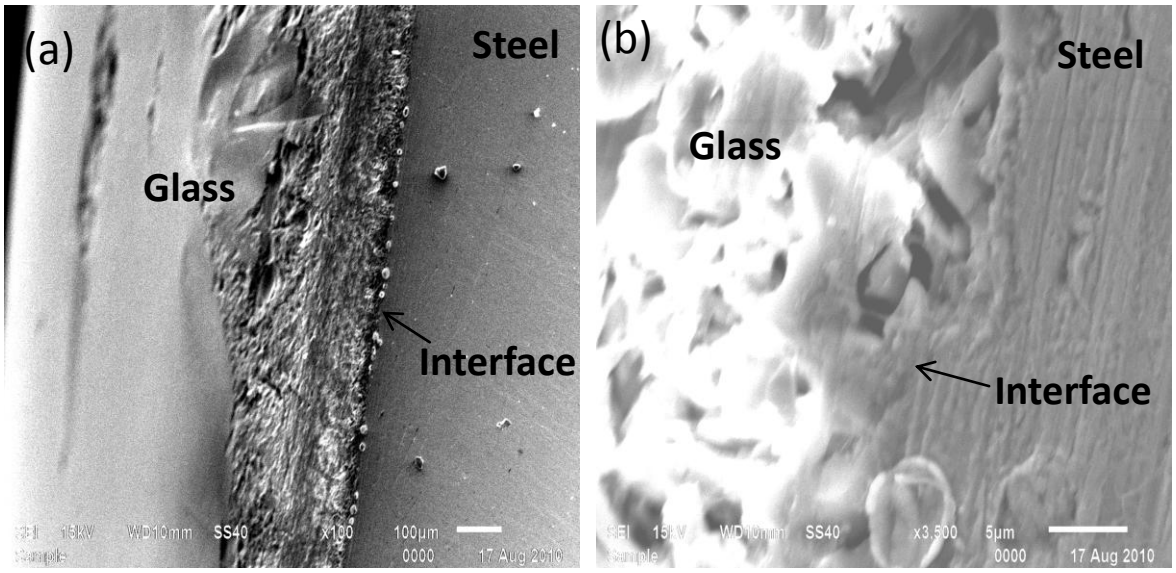

Fig. 4.51: SEM micrograph of interface between N-20 glass and crofer steel showing the overall view of interface.

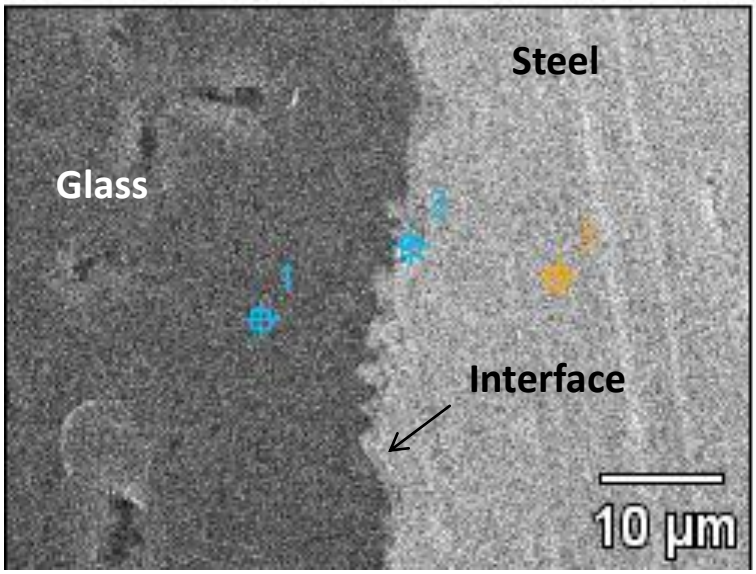

Fig. 4.52: Back scattered electron micrograph of interface between N-20 glass and crofer steel.

The X-ray dot mapping and EDS analysis of the coated glass surface also indicates the presence of only glass constituents. At the interface between N-20 glass and crofer steel, Cr and O elements are main constituents. Apart from Cr and O, diffusion of Ti, Al and Na has also occurred.

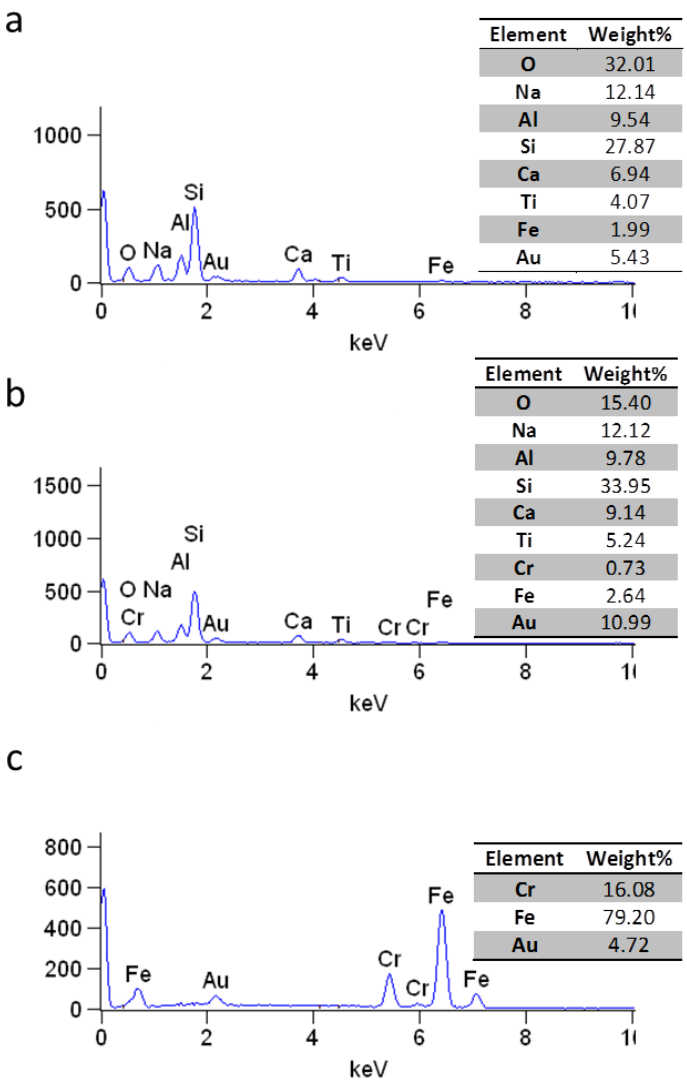

Fig. 4.53: EDS spectrum of the glass of the diffusion couple (a) marked 1 in Fig. 4.52, (b) marked 2 in Fig. 4.52 and (c) marked 3 in Fig. 4.52.

The X-ray dot mapping of the structure shown in Fig. 4.54 (a) for Fe, Cr, Mn, Ti, Al, Si, Na and O are shown in Fig. 4.54 (b-i) respectively. These results further confirmed the diffusion of Al and Na from glass into steel and diffusion of Cr and Fe from steel into glass.

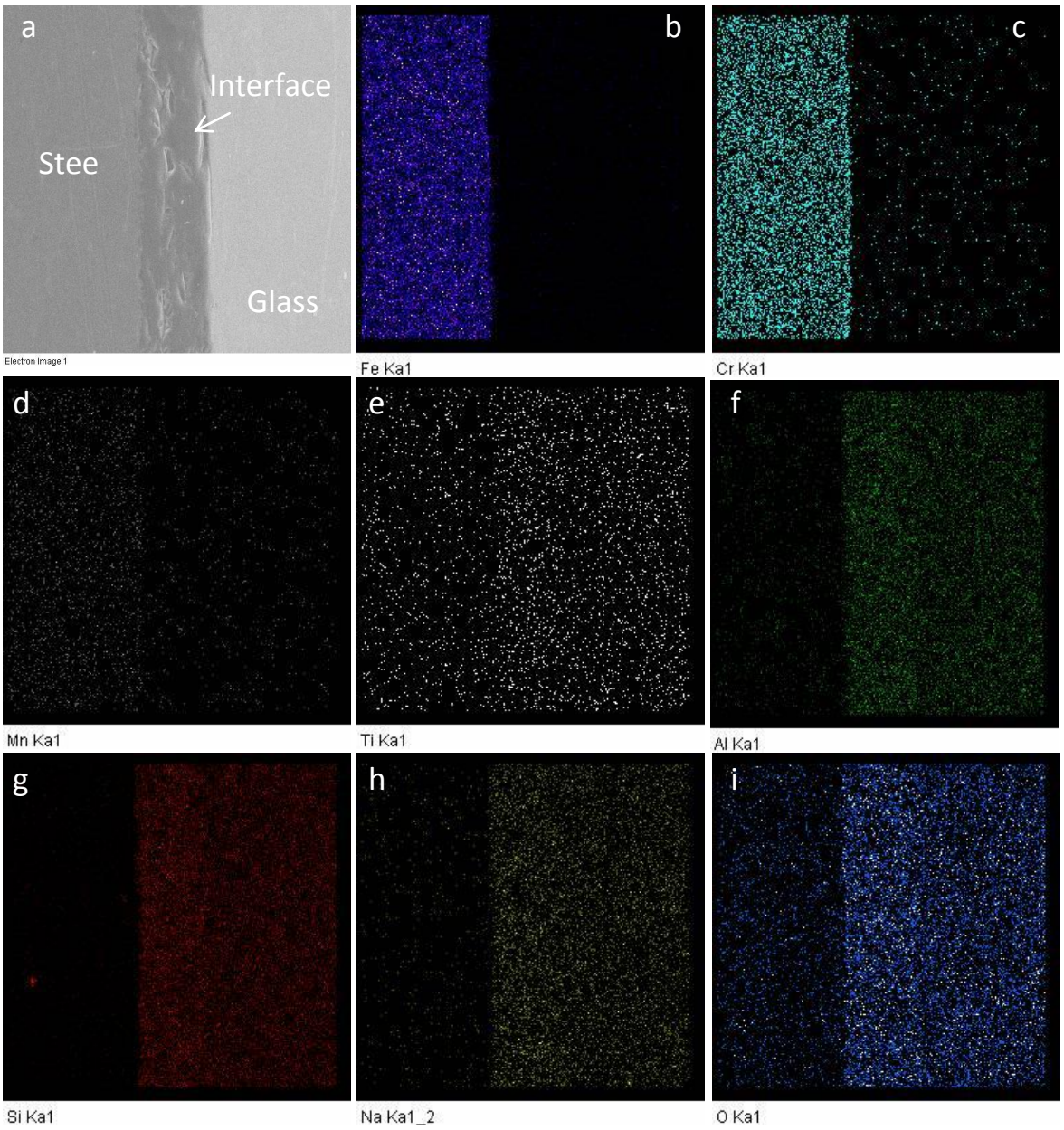

Fig. 4.54: X-ray dot mapping of Fe, Cr, Mn, Ti, Al, Si, Na and O of the interface of the diffusion couple.

4.2.1.3. N-15 glass and crofer steel

4.2.1.3.1. Surface analysis

From X-ray study of heat treated N-15 glass-ceramic, no indication of any crystalline phase was observed. Uniform and smooth coating of N-15 glass on crofer was observed as can be seen in the SEM micrograph of coated glass (Fig. 4.55(a)). However, at certain places aggregation of material like flowery pattern is found in the coated glass as shown in Fig. 4.55(b). These patterns grow as concentric circle where variation in structure from central part to periphery is observed [60]. The growth of such structure occurs because of the presence of defects in steel like

inclusions (eg. sulphide inclusion). These react with glass and diffuse in due course of time with heat treatment. This does not show any porosity or crack on the surface.

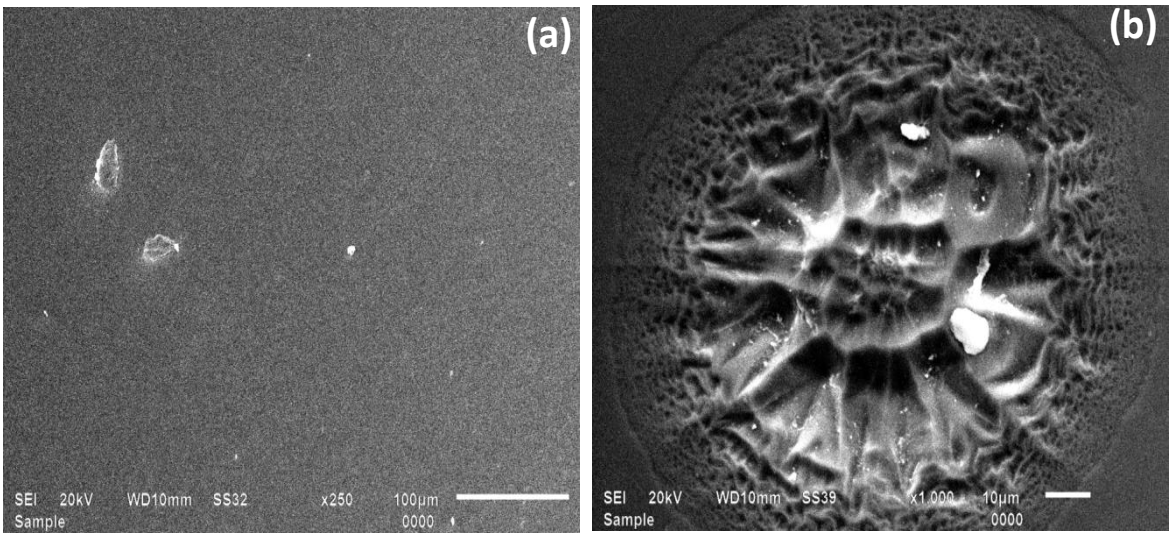

Fig. 4.55: Scanning electron micrographs of the N-15 glass-ceramic coating on crofer steel showing the nucleation and growth of crystalline phases.

In order to further quantify the nature of surface, the EDS spectrum of the top layer of glass was taken along with the elemental analysis to know the depth of diffusion (Fig. 4.56).

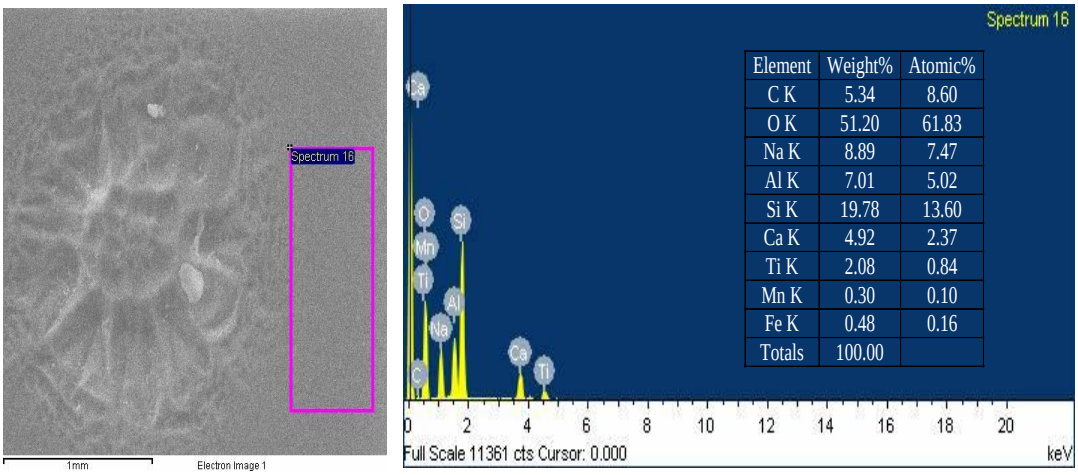

Fig. 4.56: EDS spectrum with elemental analysis of the area marked.

The EDS analysis indicates that Fe and Mn elements have diffused from steel side into smooth coated glass area. There is no indication of the presence of Cr from steel in smooth coated area. In order to confirm it, further X-ray dot mapping from the marked area was done as shown in Fig. 4.57. Detected Si, Ca, Al, Ti, O, Na, Mn and Fe elements are uniformly distributed in the selected area. EDS spectrum of the flowery pattern glass was also taken with the elemental analysis to know the depth of diffusion (Fig. 4.58).

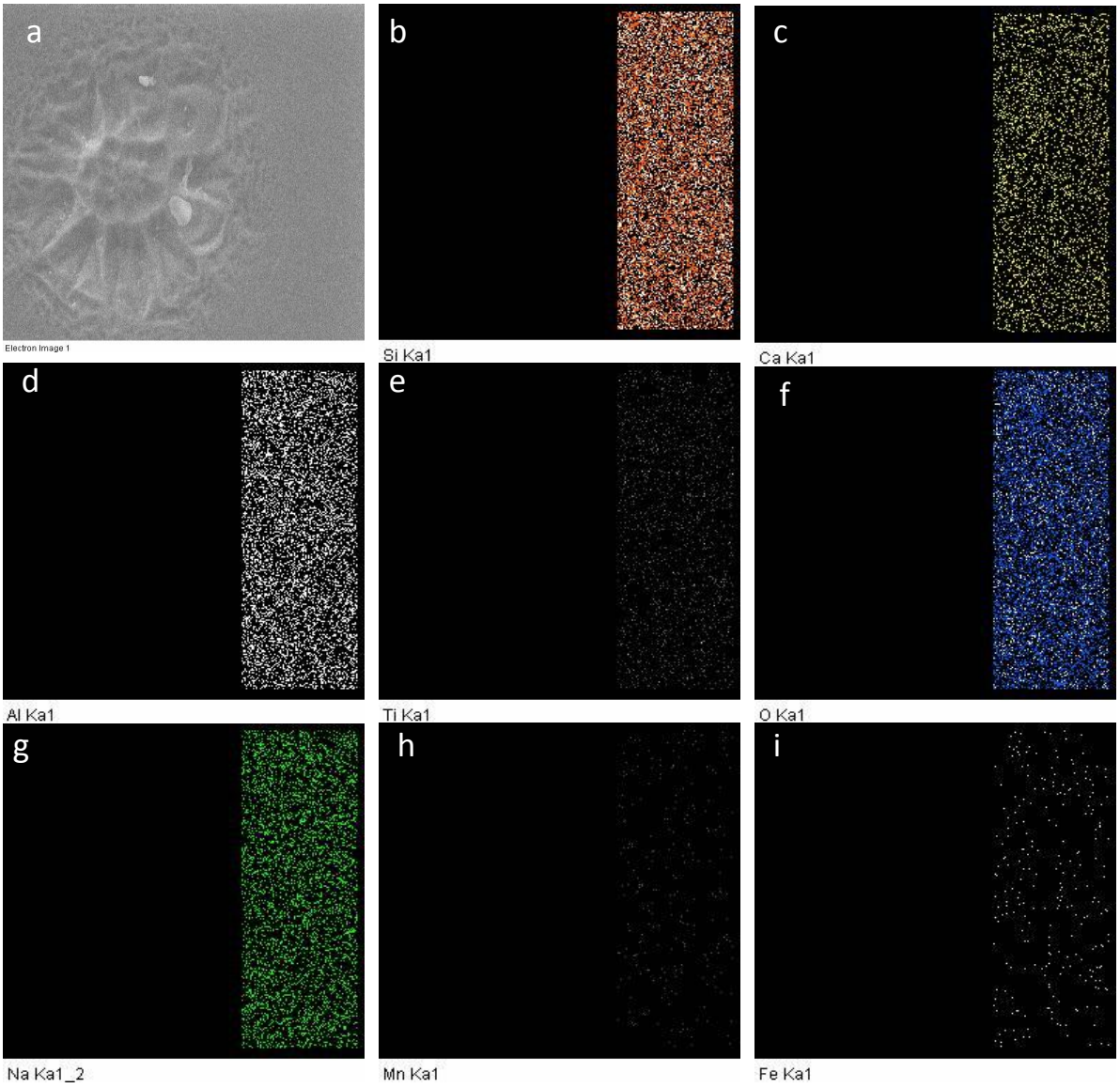

Fig. 4.57: X-ray dot mapping of Si, Ca, Al, Ti, O, Na, Mn and Fe of the N-15 glass-ceramic coating on crofer steel.

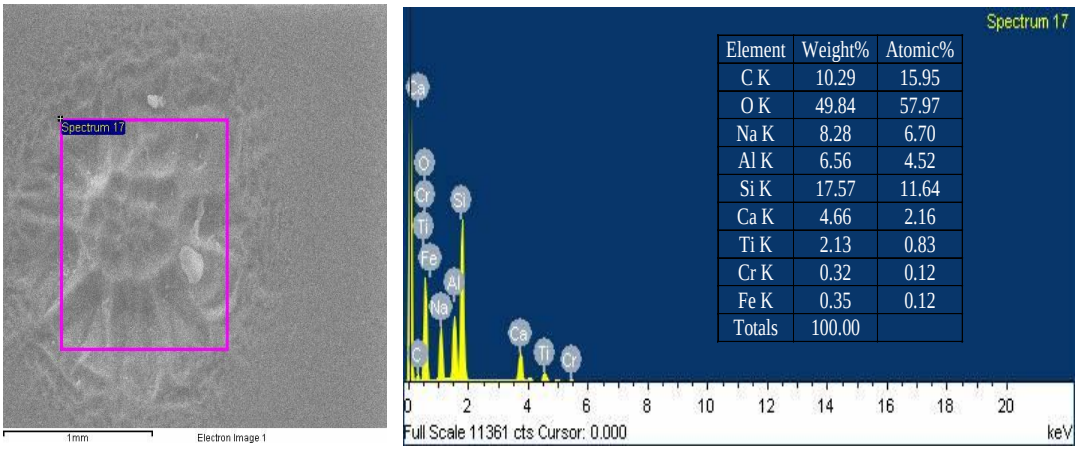

Fig. 4.58: EDS spectrum with elemental analysis of the area marked.

EDS analysis revealed that the diffusion of Cr from steel side into glass leads to the formation of flowery pattern which might have occurred due to presence of defect structure as this pattern is not observed in other areas. To further confirm these results X-ray dot mapping is done as shown in Fig. 4.59. Detected Si, Ca, Al, Ti, Na, O, Cr and Fe elements are uniformly distributed in the selected area.

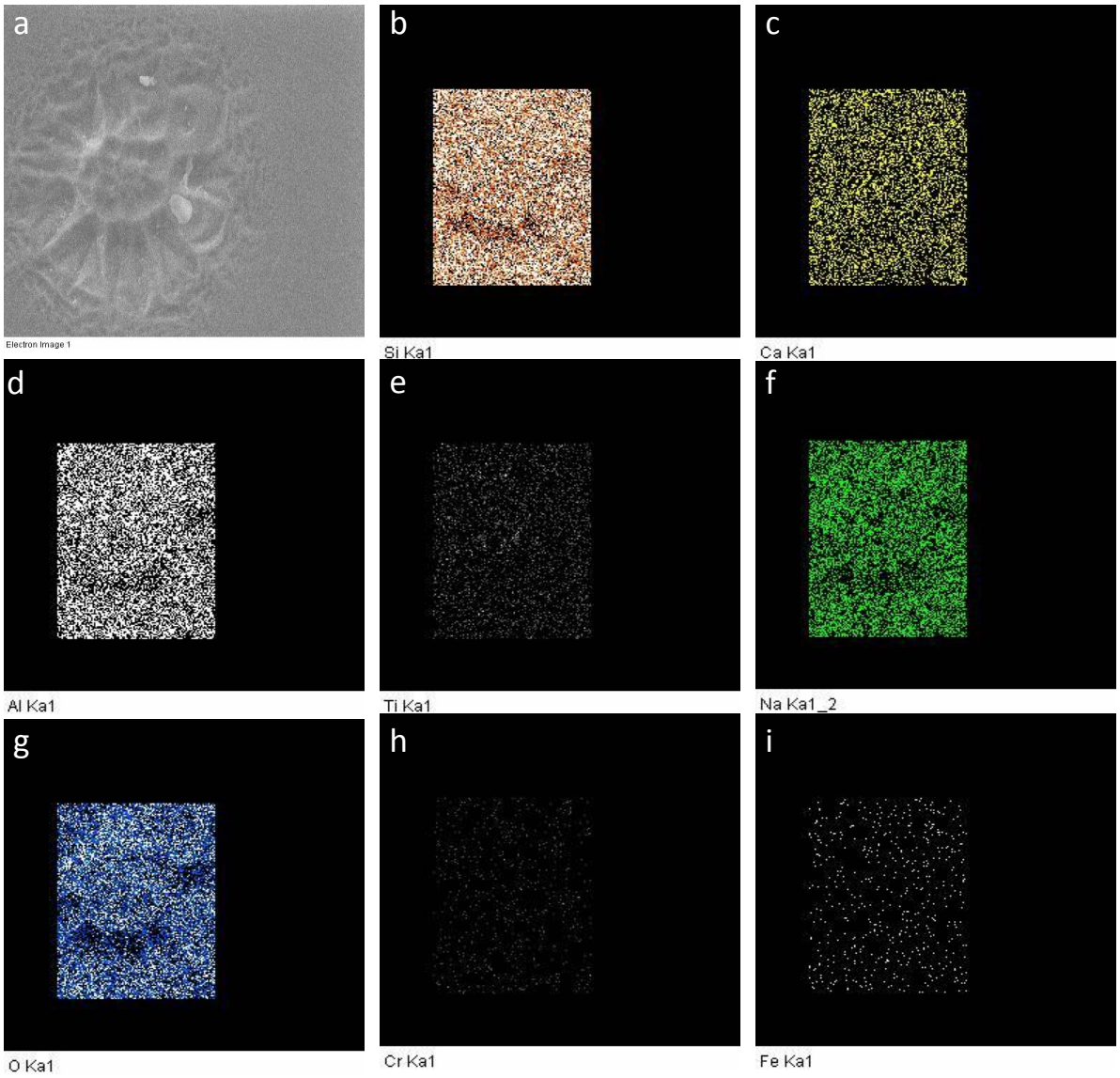

Fig. 4.59: X-ray dot mapping of Si, Ca, Al, Ti, Na, O, Cr and Fe of the N-15 glass-ceramic coating on crofer steel.

4.2.1.3.2. Analysis of interface

Cross-sectional microstructure of the interface between N-15 glass and crofer is shown in Fig. 4.60. As seen, the glass coating was highly bonded with base steel. However, lots of unexpected pores were visible through the interface [61]. The poor densification of the glass was mostly due the glass crystallization at the coating temperature. A glass powder compact composed of the

densely packed spheres would initially densify because of the viscous flow according to the frankel equation [62]. However, the increasing temperature caused the coalescence and expansion of small pores and led to the formation of pores. As the temperature increased, the pores would be vented out from the glasses and the final glass coatings were densified. The EDS analysis at the marked area as shown in Fig. 4.61 was done to understand the diffusion of the elements. This is shown in Fig. 4.62 (a-c) for the areas marked as 1, 2 and 3, respectively.

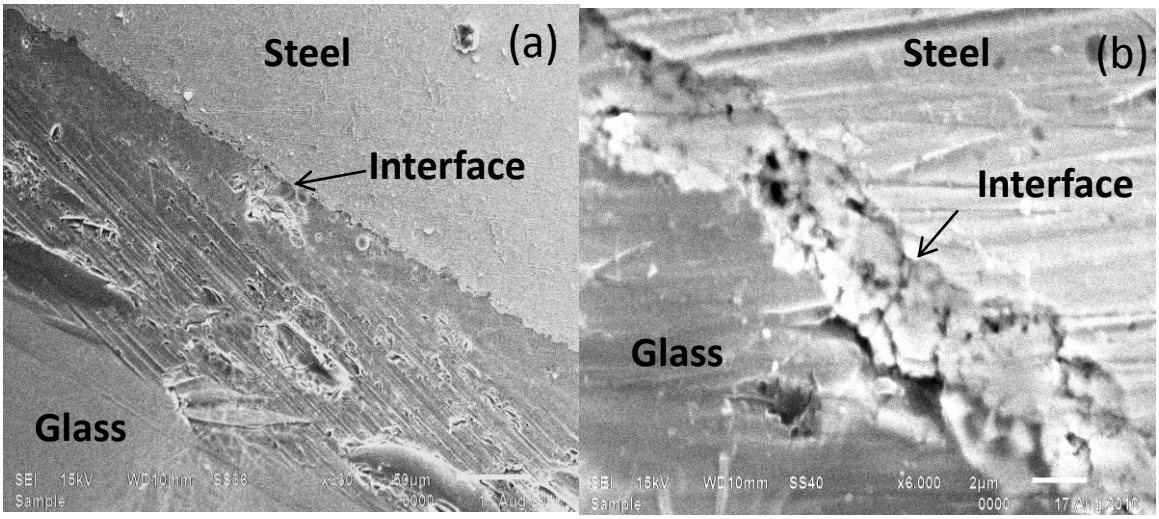

Fig. 4.60: SEM micrograph of interface between N-15 glass and crofer steel showing the overall view of the interface.

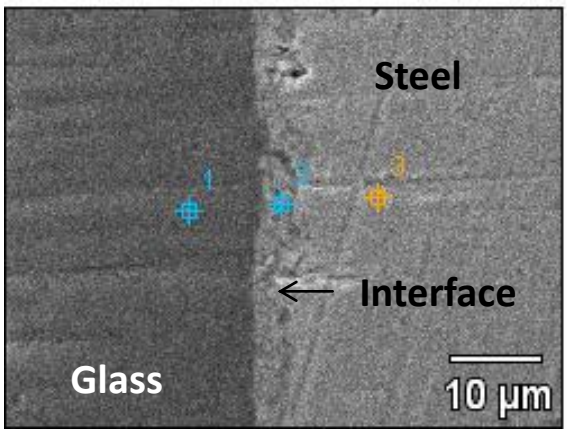

Fig. 4.61: Back scattered electron micrograph of interface between N-15 glass and crofer steel.

Point analysis of the coated glass indicates the presence of glass constituents with Cr. At the interface between N-15 glass and crofer steel, Cr and O elements are main constituents. For further confirmation of the diffusion from steel to glass and vice-versa, line profile (yellow line in Fig. 4.63) of the interface was done. The resultant spectrums are shown in Fig. 4.64. These results further confirmed the diffusion of Fe, Mn and Cr into glass which is more prominent than

other elements. However, the interface is very strong. Mainly Cr and O elements are present at the interface. Apart from this, diffusion of Ti, Al and Na from glass side into steel also occurs.

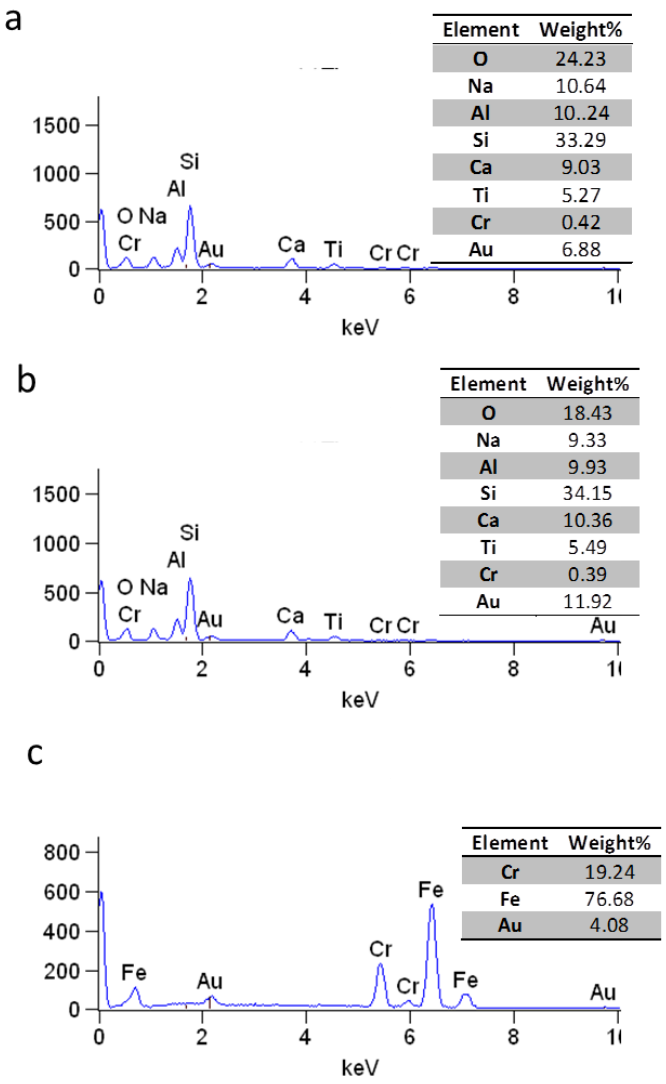

Fig. 4.62: EDS spectrum of the glass of the diffusion couple (a) marked 1 in Fig. 4.61, (b) marked 2 in Fig. 4.61 and (c) marked 3 in Fig. 4.61.

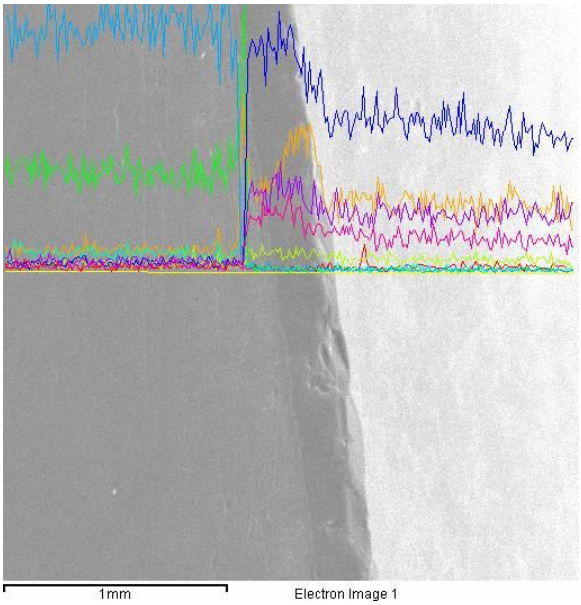

Fig. 4.63: Back scattered image of the cross-sectional area where yellow line is representative of line profile.

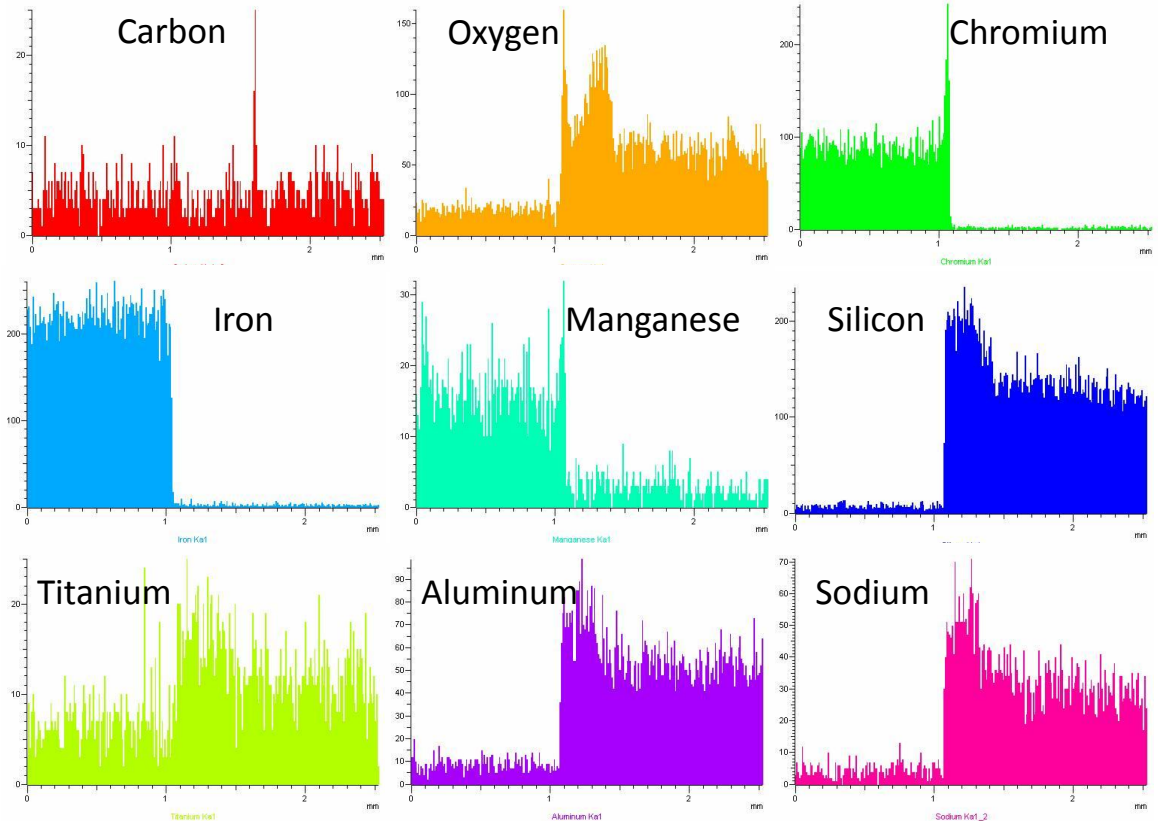

Fig. 4.64: Line profile across the cross-sectional area.

The X-ray dot mapping of the interfacial area shown in Fig. 4.65 (a) for Fe, Cr, Mn, Ti, Al, Si, O and Na are shown in Fig. 4.65 (b-i) respectively. All the elements are uniformly distributed in the

selected area. These results further confirmed the diffusion of Al and Na from glass into steel and diffusion of Cr and Fe from steel into glass. However, the interface is free from porosity.

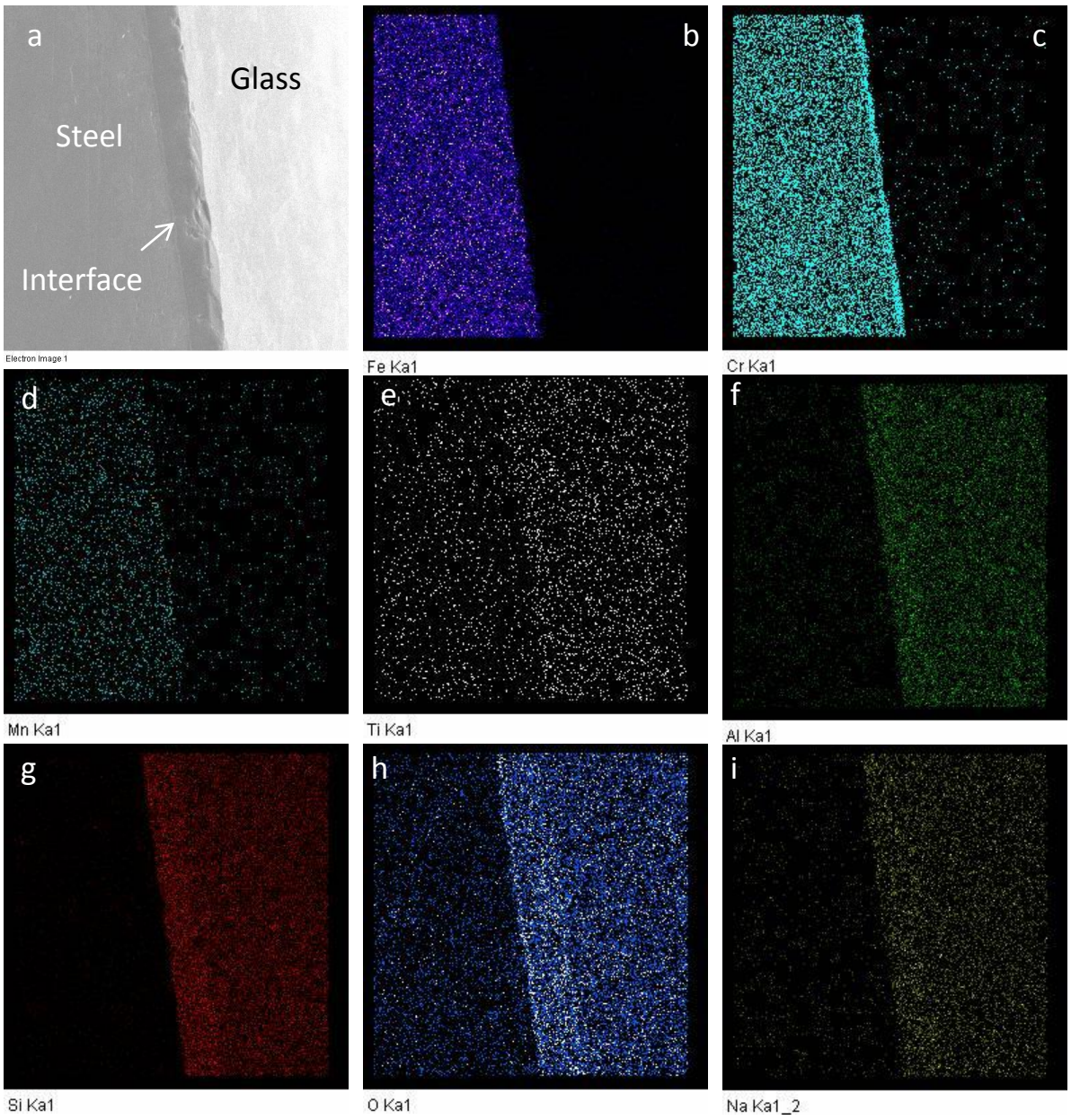

Fig. 4.65: X-ray dot mapping of Fe, Cr, Mn, Ti, Al, Si, O and Na of the interface of the diffusion couple.

4.2.1.4. N-10 glass and crofer steel

4.2.1.4.1. Surface analysis

Uniform and smooth coated structure of glass on steel surface is obtained as observed under SEM of coated glass and shown in Fig. 4.66 The low magnification micrograph (Fig. 4.66 (a)) indicates uniform structure. Here, two types of crystals with different morphologies were observed. One was aggregation of material like star shape flowery pattern (Fig. 4.66 (b)) and

other was flow pattern (like N-20 coated glass) near the edges of flowery pattern as shown in Fig. 4.66 (c-d) where needle like dendritic growth is observed [63].

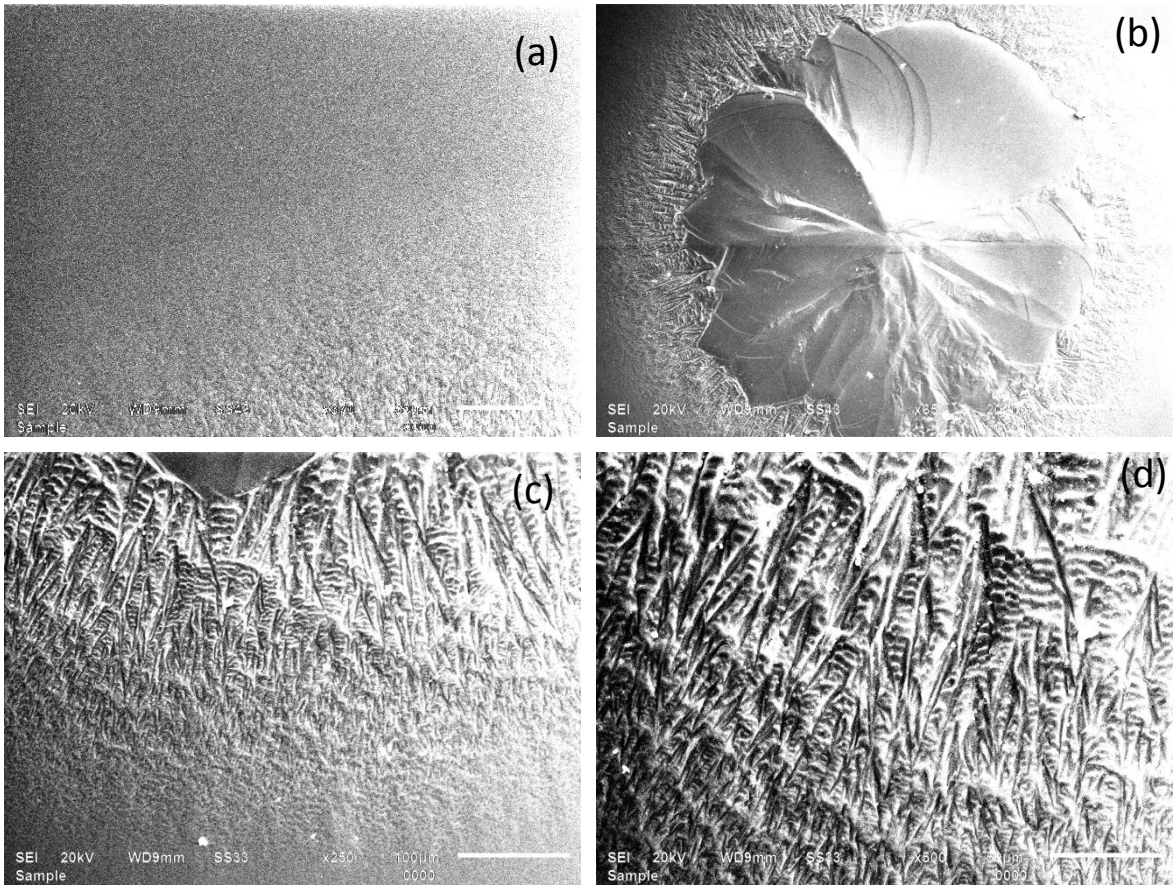

Fig. 4.66: Scanning electron micrographs of the N-10 glass-ceramic coating on crofer steel showing the nucleation and growth of crystalline phases.

In order to further quantify the nature of surface, the EDS spectrum of the top layer of glass was taken along with the elemental analysis to know the depth of diffusion (Fig. 4.67).

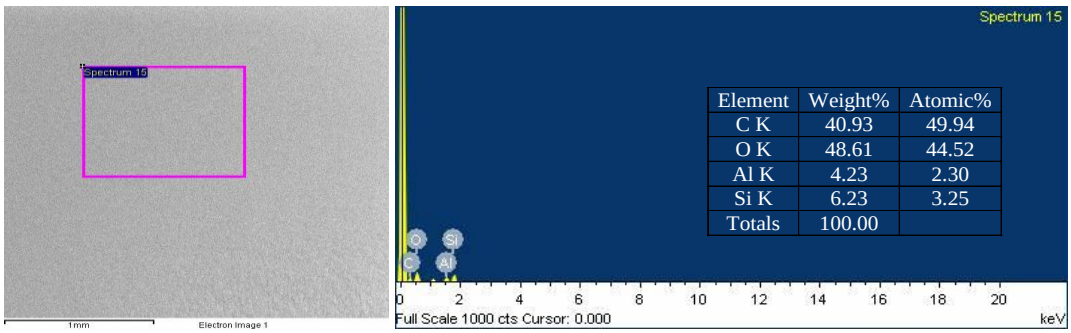

Fig. 4.67: EDS spectrum with elemental analysis of the area marked.

The EDS analysis indicates the presence of Al, Si and O elements. No element has diffused from steel side up to top surface of the smooth coated glass area. The EDS spectrum of the flow pattern of glass was taken with the elemental analysis to know the depth of diffusion (Fig. 4.68).

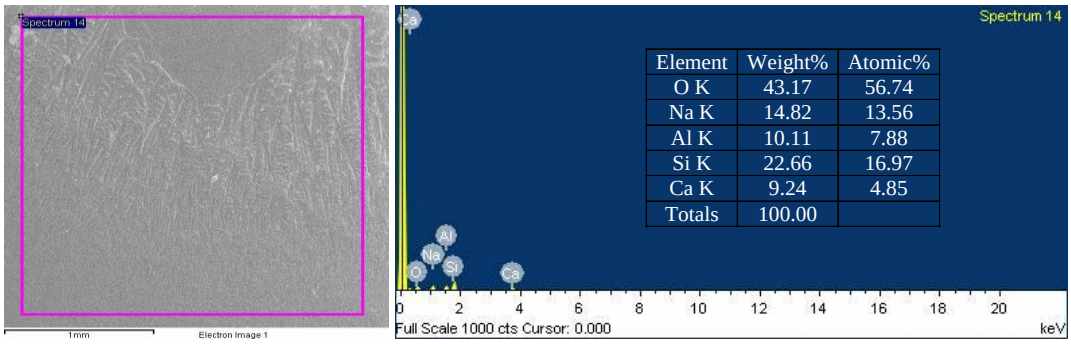

Fig. 4.68: EDS spectrum with elemental analysis of the area marked.

EDS analysis revealed that Na element is present in the flow pattern as compared to the segregated flowery pattern. Thus $NaAlSiO_4$ phase which is in 71% volume fraction has formed on the surface of the smooth area. Whereas SiO_2 phase formed flowery pattern within the coated glass. To further confirm these results X-ray dot mapping of uniform area is done as shown in Fig. 4.69. Detected Si, Al, Ca, Na, C, O, Cr and Fe elements are shown in the selected area.

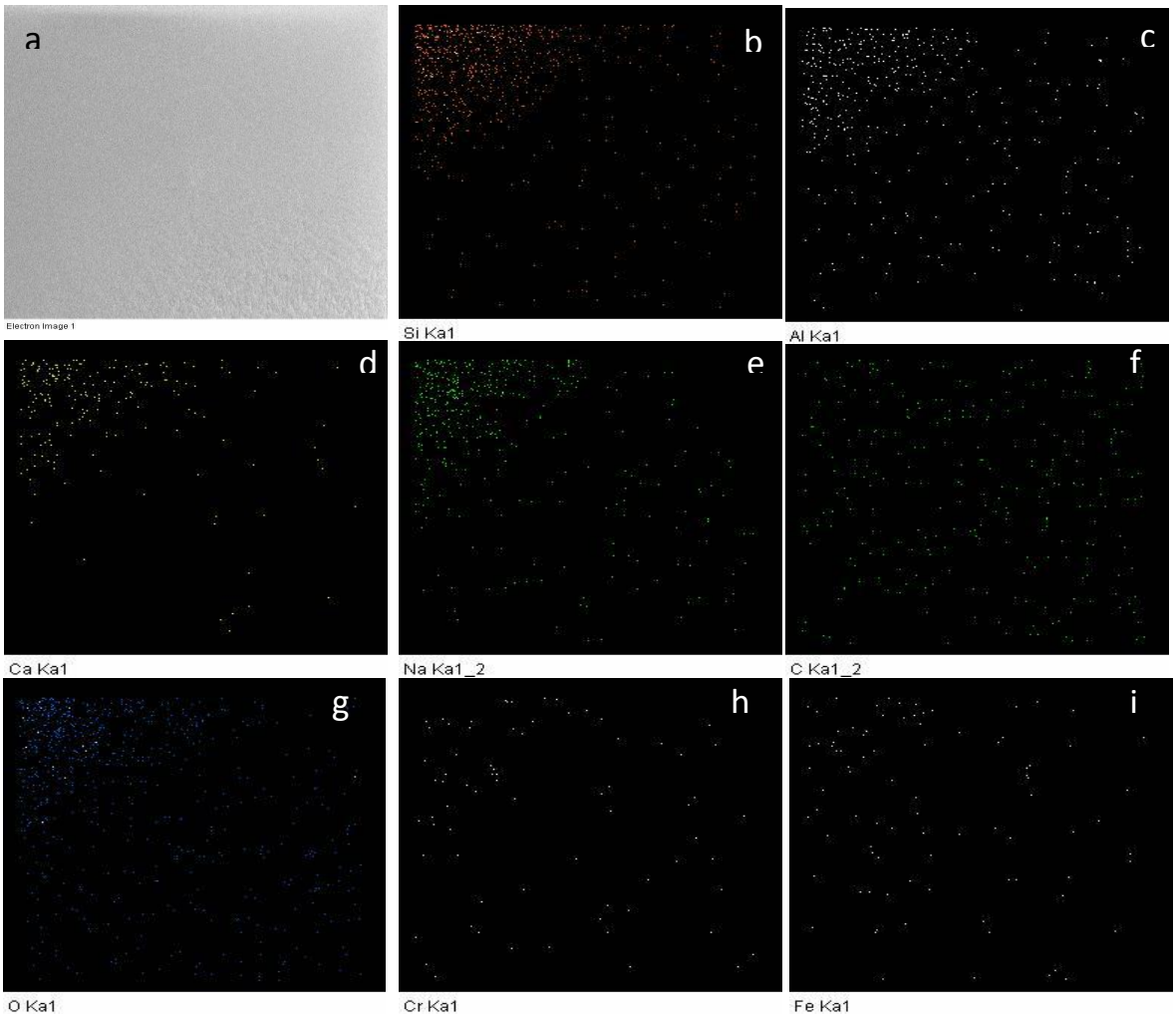

Fig. 4.69: X-ray dot mapping of Si, Al, Ca, Na, C, O, Cr and Fe of the N-10 glass-ceramic coating on crofer steel.

4.2.1.4.2. Analysis of interface

Cross-sectional microstructure of the interface between N-10 glass and crofer is shown in Fig. 4.70. The interface between glass and steel shows good adhesion. Fig. 4.70 (b) shows a higher magnification of the oxide layer formed between steel and coated glass which was due to internal oxidation occurred [64]. However, some voids and porosity are observed at the areas away from the interface. The EDS analysis at the marked area as shown in Fig. 4.71 was done to understand the diffusion and inter-diffusion of the elements. This is shown in Fig. 4.72 for the areas marked as 1, 2 and 3, respectively.

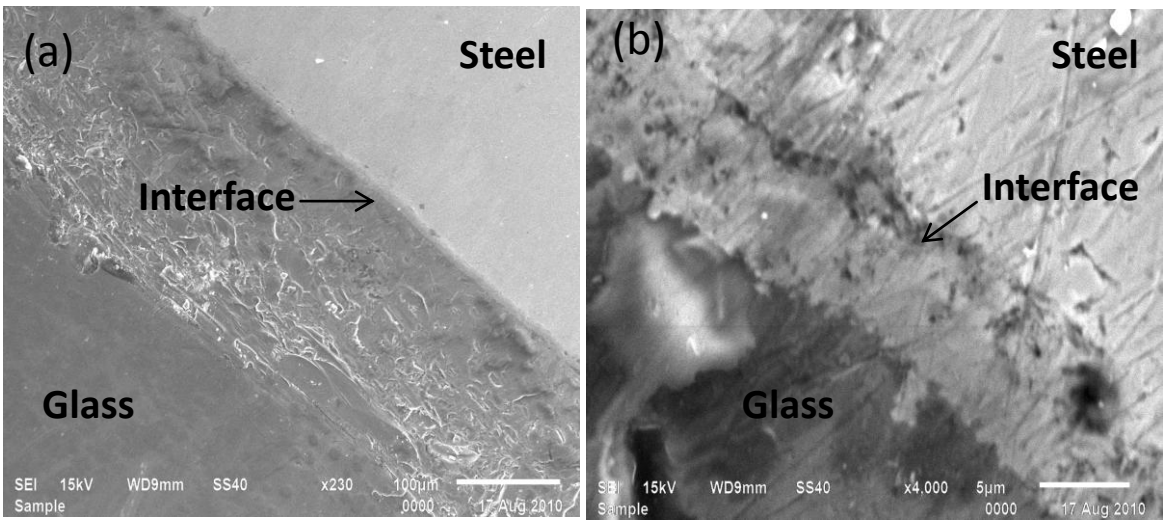

Fig. 4.70: SEM micrograph of interface between N-10 glass and crofer steel showing the overall view of interface.

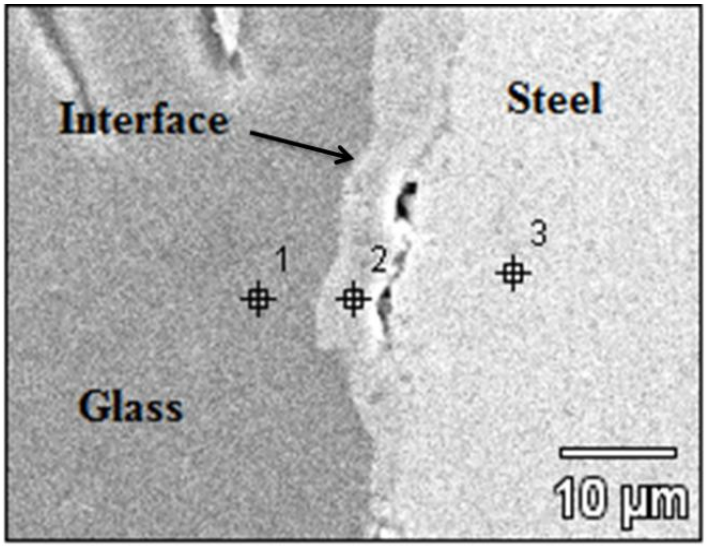

Fig. 4.71: Back scattered electron micrograph of interface between N-10 glass and crofer steel.

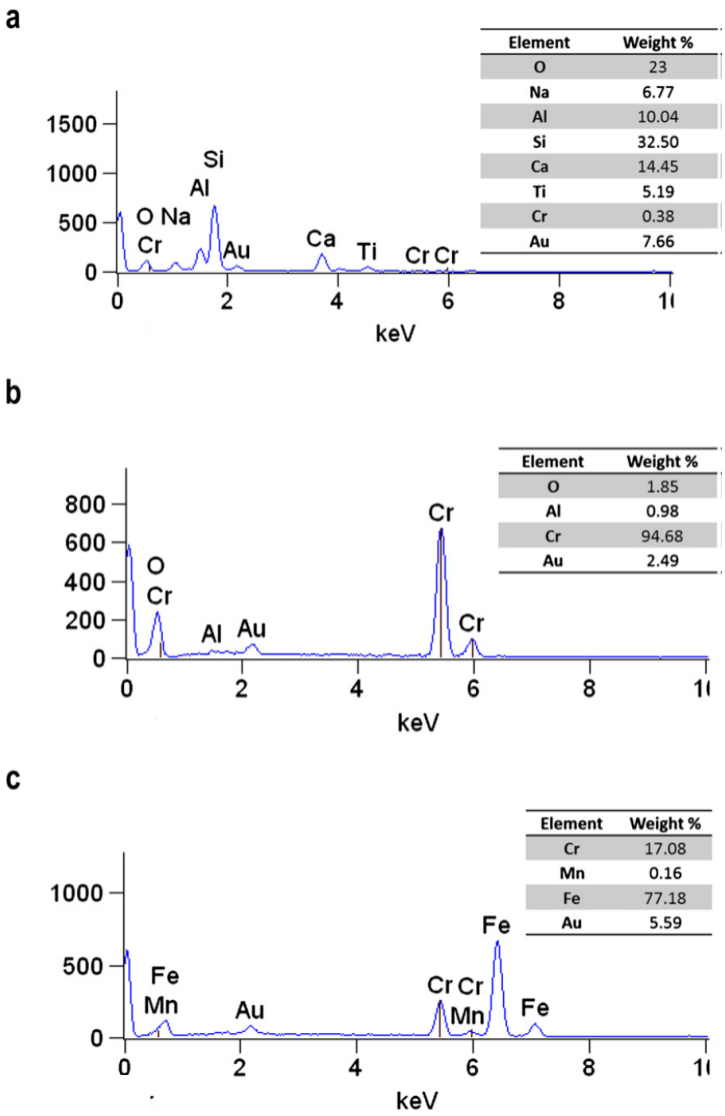

Fig. 4.72: EDS spectrum of the glass of the diffusion couple (a) marked 1 in Fig. 4.71, (b) marked 2 in Fig. 4.71, and (c) marked 3 in Fig. 4.71.

As observed from the EDS analysis, the maximum diffusion of Cr has taken place from the steel side. On the other hand, only Al^{3+} has diffused from the glass side to the interface which is very less in amount. Basically, the interface contained Cr^{3+} rich layer. Though its diffusion is within the permissible limit, but it has got a higher tendency as compared to other elements. The overall analysis indicates that layers of chromium oxide and a reaction layer of Cr diffusion into the glass identified by EDS were found at the interface between the glass and the steel. However, the interface is very strong. Cr and O elements are mainly present at the interface. Apart from this, diffusion of Ti, Al and Na also occurs. The X-ray dot mapping of the area shown in Fig. 4.73 (a) for Na, Al, Si, Cr and Fe are shown in Fig. 4.73 (b-f), respectively. These results further confirmed the diffusion of Cr^{3+} which is more prominent than other elements. However, the interface is smooth and free from porosity, which is required for good coating.

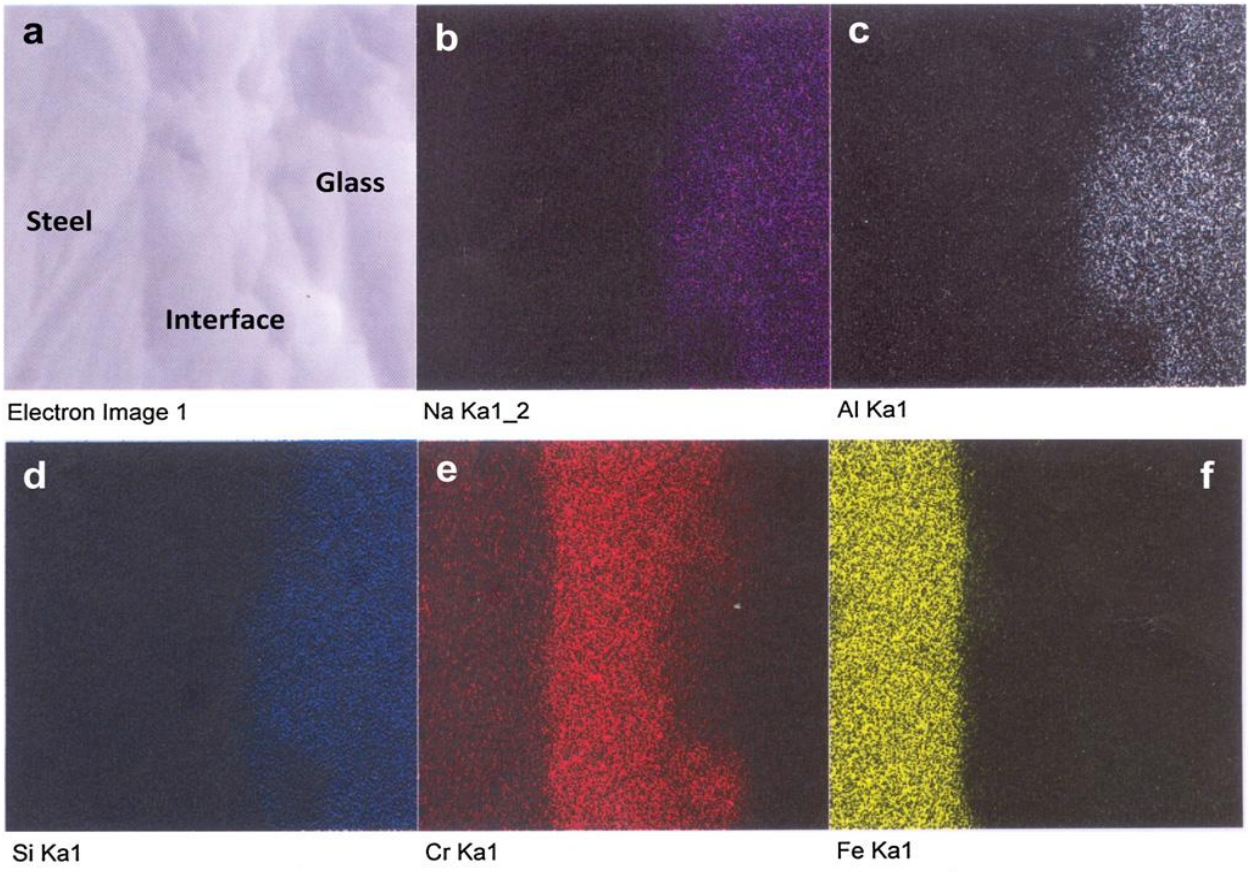

Fig. 4.73: X-ray dot mapping of Na, Al, Si, Cr and Fe of the interface of the diffusion couple.

4.2.2. S glass and crofer steel

In addition to as prepared glasses in our lab., some commercially available glasses were also investigated for their coating and interaction properties. Slurry method was used to make diffusion couple at 700 °C. Because of this temperature the chemical bonding of coating with substrate resulting in a high adherence and chemical stability relatively at lower temperature is better [65]. The temperature selected was near T_p.

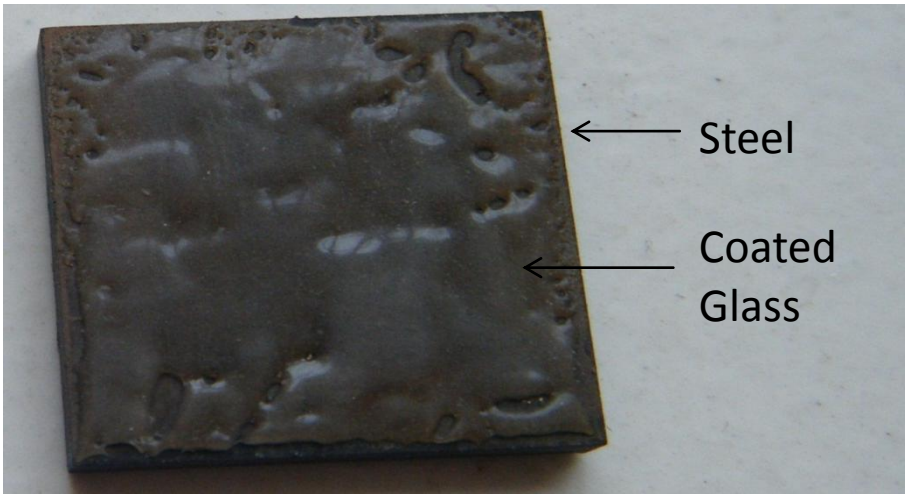

Fig. 4.74: Photograph of diffusion couple of S glass with crofer steel.

The photograph of S glass with crofer steel is shown in Fig. 4.74. The coated glass on the steel piece has transparent appearance. Open and closed pores were observed in the coating. The evolution of circular to elongated pores is because of entrapment of gas during the heat treatment [66]. In order to understand the nature and behavior of glass coating on steel surfaces, we have done the detailed microstructural study of coating.

4.2.2.1. Surface analysis

Fig. 4.75 shows the micrographs of the top layer of coated S glass on crofer at 700 °C for 1 h. In the micrographs, some pores are observed at the edges of the coating.

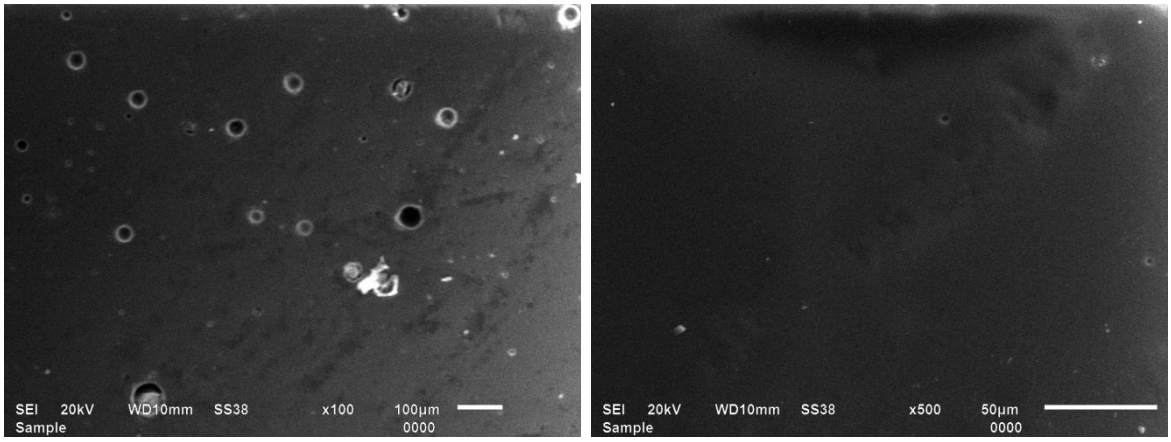

Fig. 4.75: Scanning electron micrographs of the S glass coating on crofer steel.

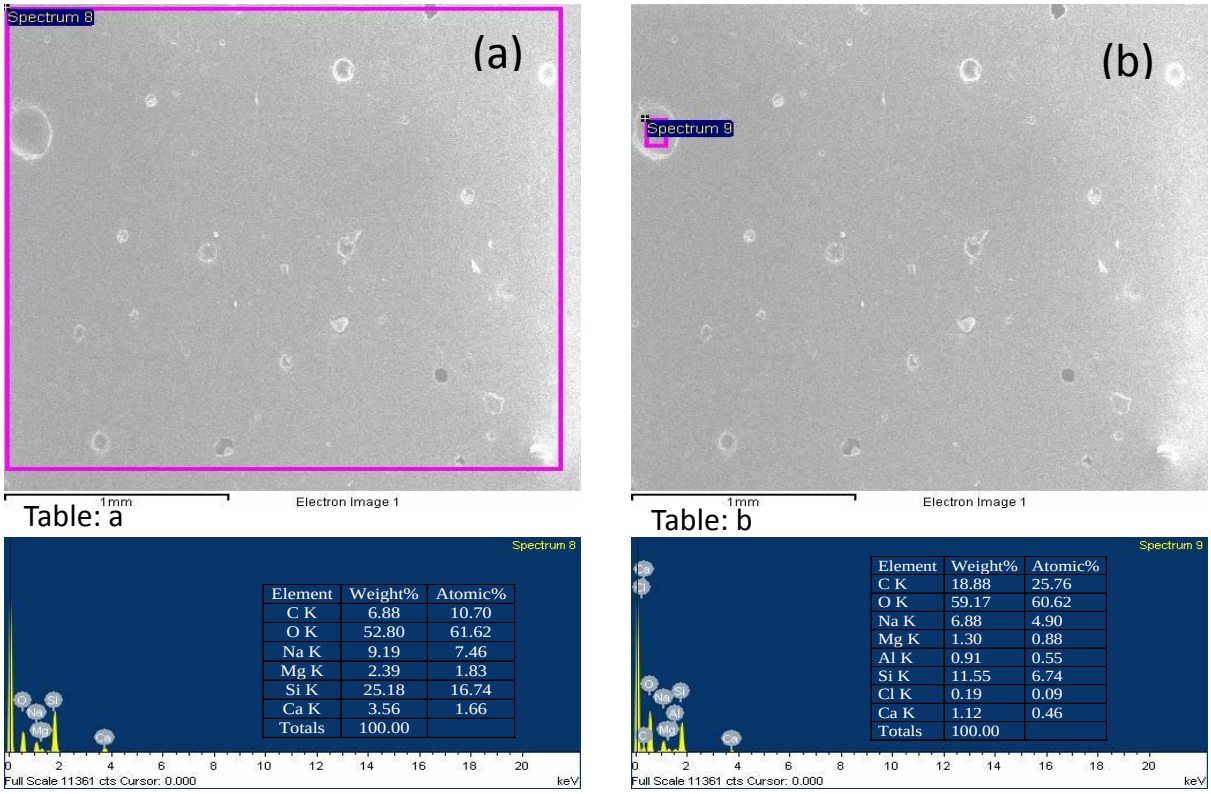

Fig. 4.76: Back scattered electron micrograph with EDS analysis of the area marked of the S glass coating on crofer steel.

In order to further quantify the nature of surface, the structure was observed in BSE mode. Fig. 4.76 shows the surface morphology in BSE mode indicating the closed nature of pores. The EDS spectrum of the top layer of glass was taken. The elemental analysis was done to know the depth of diffusion. As shown in Fig. 4.76 (a), the EDS analysis indicates that all glass elements are present of on top of the layer of coated glass except Al. The analysis of Fig. 4.76 (b) specifies that Al element is present in the inclusion area. Also, the percentage of C is high in this area. The X-ray dot mapping of C, Mg, Na, O, Al, Si and Ca shown in Fig. 4.77 (b-h), respectively. The analysis indicates that all the elements present in the glass were uniformly distributed on top surface. These results further confirmed that Cr and Fe have not diffused from steel to top layer of glass coating.

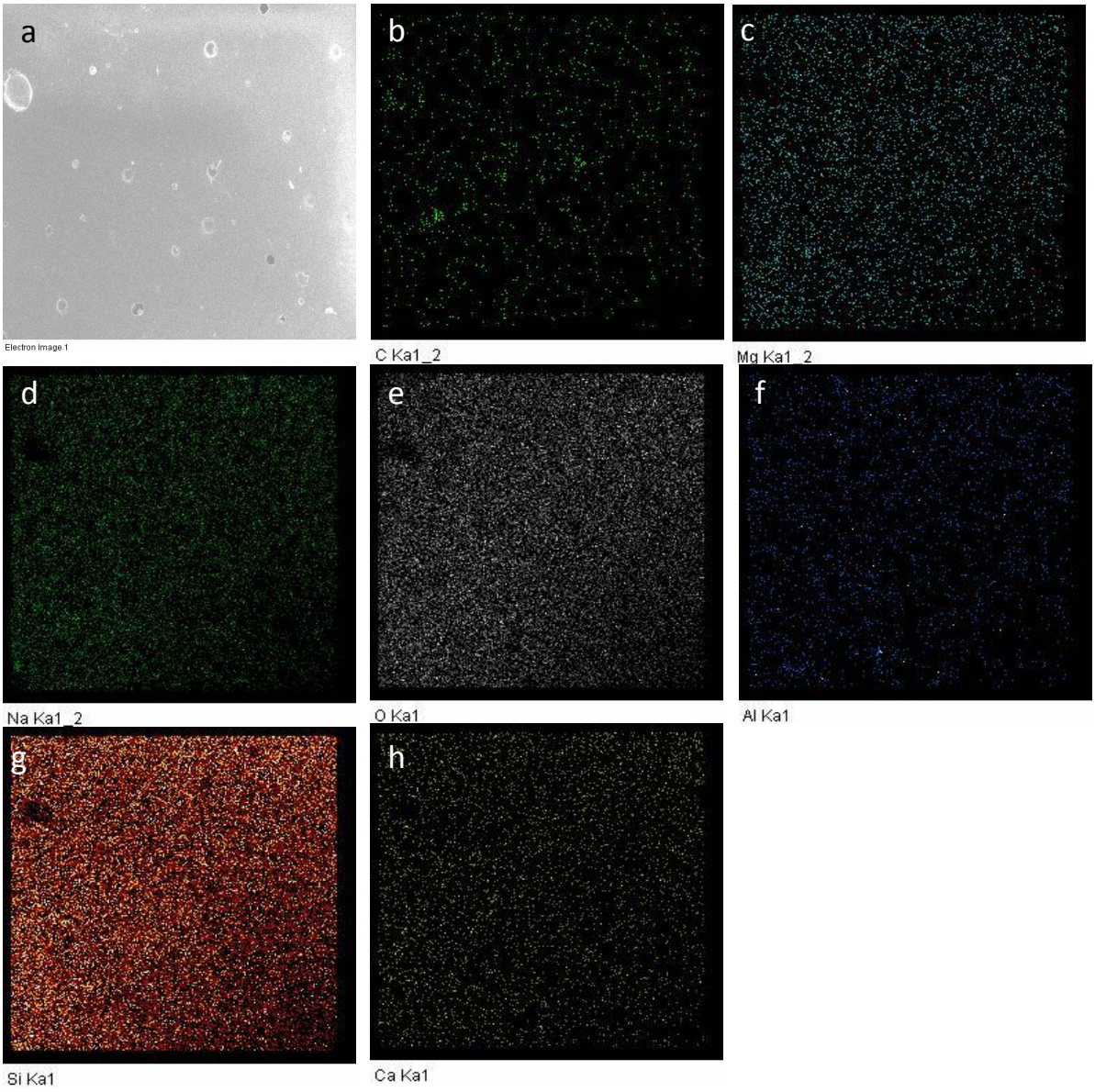

Fig. 4.77: X-ray dot mapping of C, Mg, Na, O, Al, Si and Ca of the surface of coated S glass on crofer steel.

4.2.2.2. Analysis of interface

Cross-sectional microstructure of the interface between S glass and crofer is shown in Fig. 4.78. The interface between glass and steel shows good adhesion. However, some voids and porosity are observed at the interface. During melting the glass is unable to meet the edges of the steel due to surface tension. Moreover, amount of glass at the interface is less but has gone under complete bonding which is evident in BSE micrograph shown in Fig. 4.79.

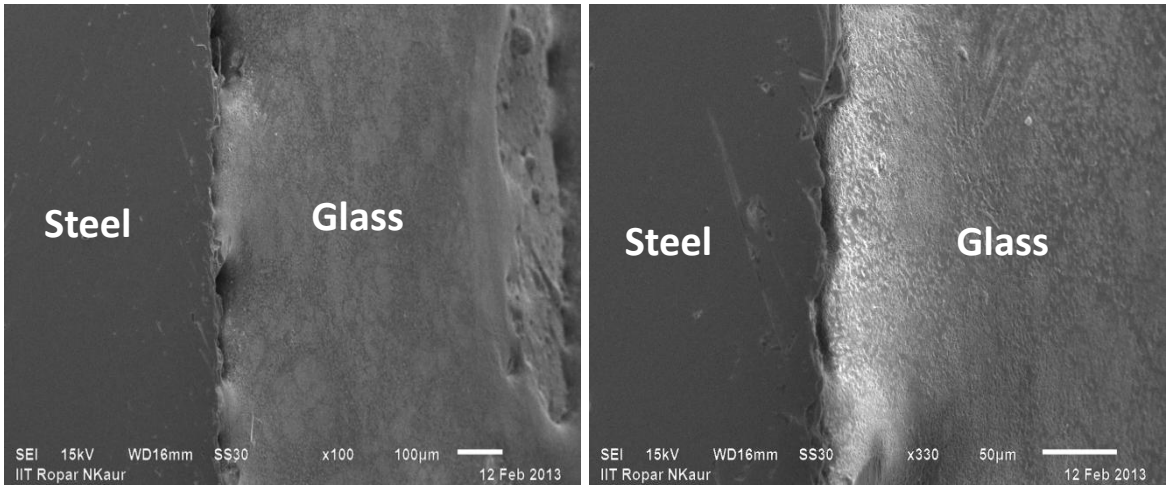

Fig. 4.78: SEM micrograph of interface between S glass and crofer steel.

The EDS analysis marked as square was done to understand the diffusion of elements as shown in Fig. 4.79.

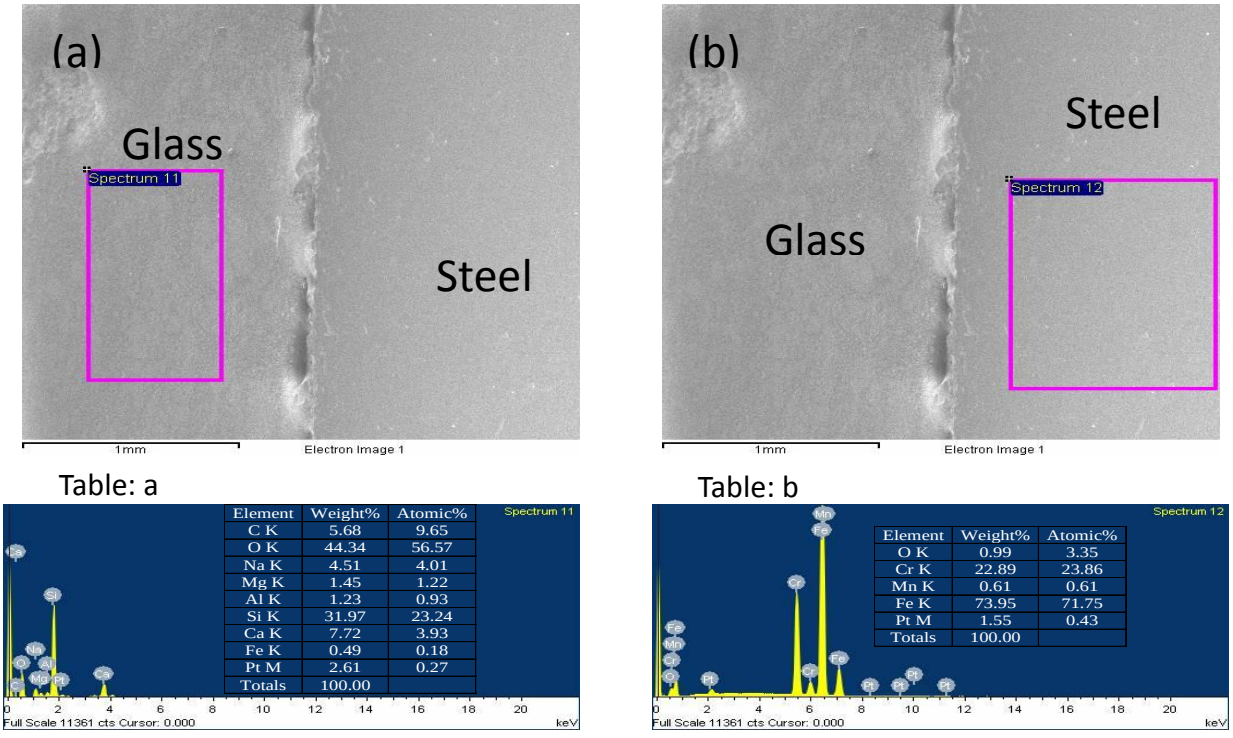

Fig. 4.79: Back scattered electron micrograph of interface with EDS analysis of the area marked for S glass coating on crofer steel.

As observed from the EDS analysis of surface, Cr has not diffused and Fe diffuses in very low quantity from steel side into glass. Fig. 4.79 (a) shows the presence of all glass elements. For further confirmation of the diffusion of elements from steel to glass and vice-versa, line profile (yellow line in Fig. 4.80) along the interface was taken. The resultant spectrums are shown in Fig. 4.81.

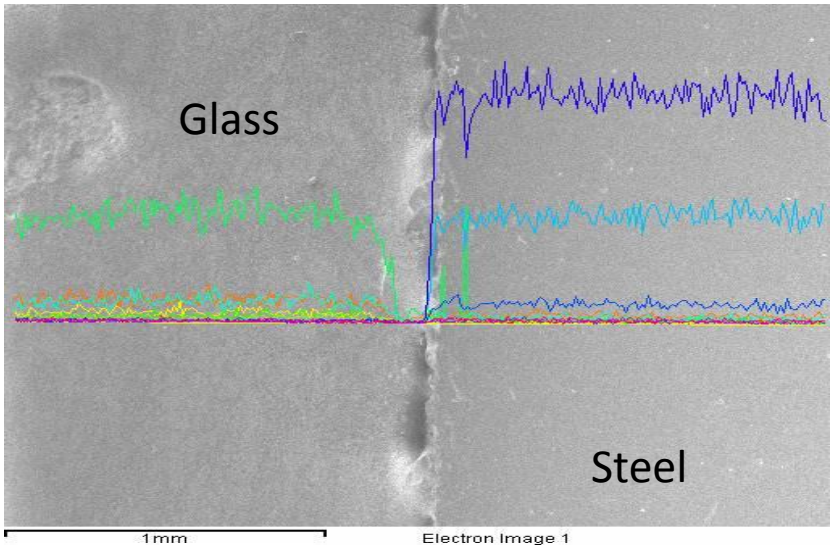

Fig. 4.80: Line profile along the cross-sectional area where yellow line is representative of line profile.

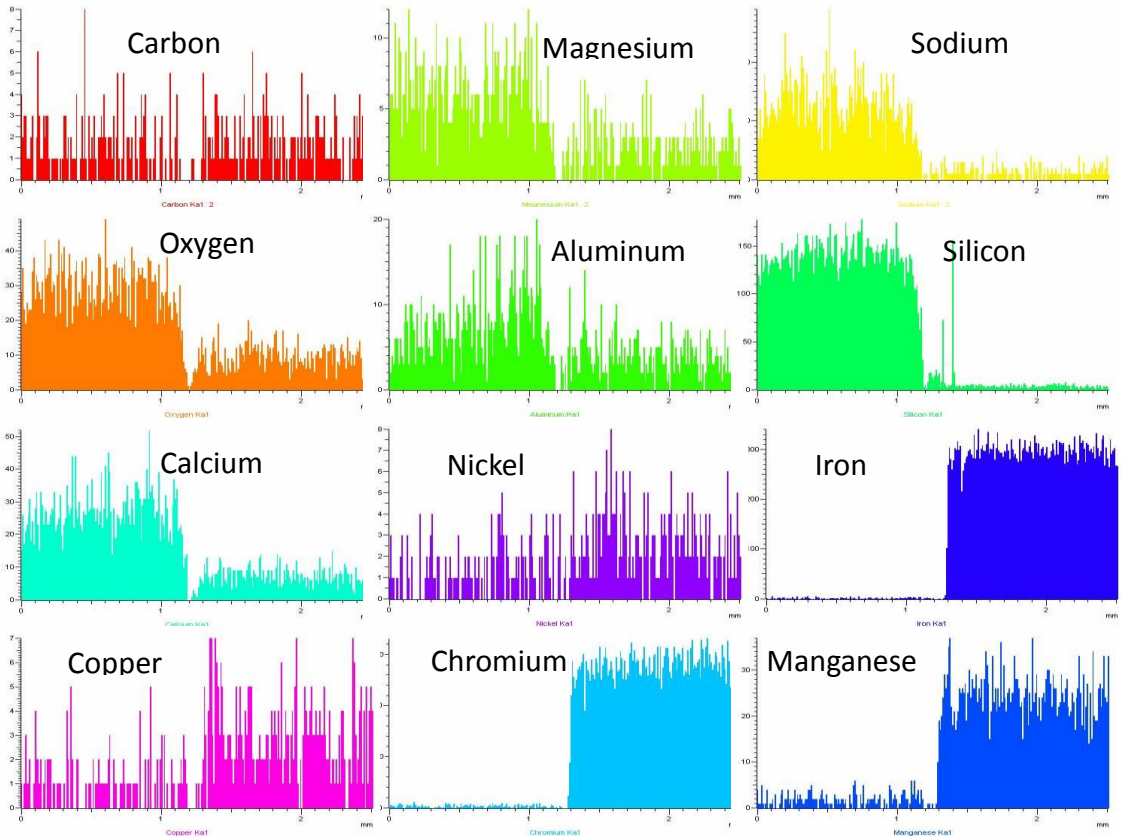

Fig. 4.81: Line profile spectrum across the cross-sectional area.

The results of line profile confirmed the formation of interfacial bond between steel and glass by diffusion of the elements. Diffusion of Ni, Fe, Cr, Cu and Mn occur from steel side into glass elements. However, the diffused amount of elements is low which does not affect the properties of glass.

4.2.3. X glass and crofer steel

The photograph of X glass coated on crofer steel is shown in Fig. 4.82. The coated glass on the steel piece has transparent appearance but not smooth in the upper part. Many bubbles have in the glass coating which have arised from the reaction between steel and glass.

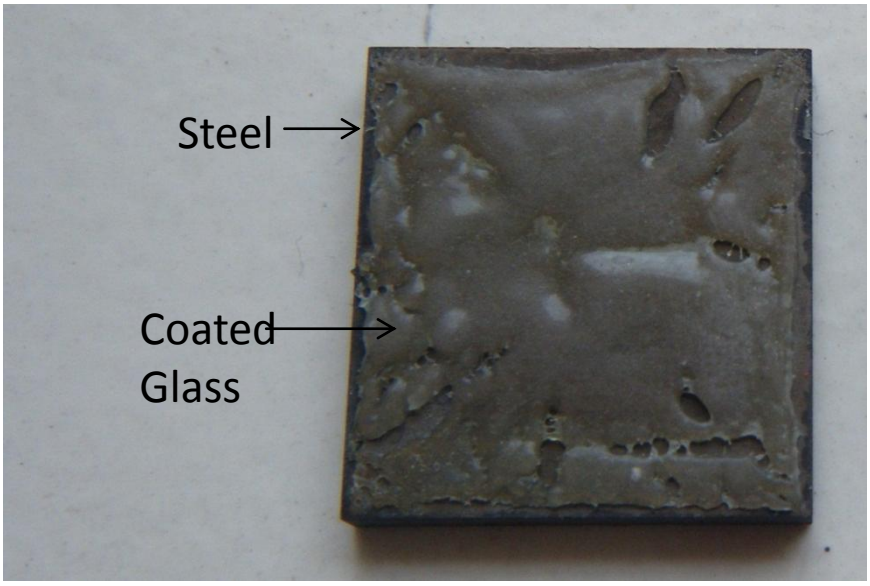

Fig. 4.82: Photograph of diffusion couple of X glass with crofer steel.

The detailed microstructural study of coating was done under scanning electron microscope along with EDS from coated surface and from the interface.

4.2.3.1. Surface analysis

Fig. 4.83 shows the micrographs of the top layer of coated X glass on crofer at 700 °C for 1 h. Number of globular pores on the surface are seen which is more than S glass coated crofer steel sample surface. This was probably due to low viscosity of the glass that was not sufficient enough at the treatment temperature and the overlapping of the sintering and the crystallization phenomena [67]. From microstructural point of view, it seems that S glass is corrosion resistance as compared to X glass.

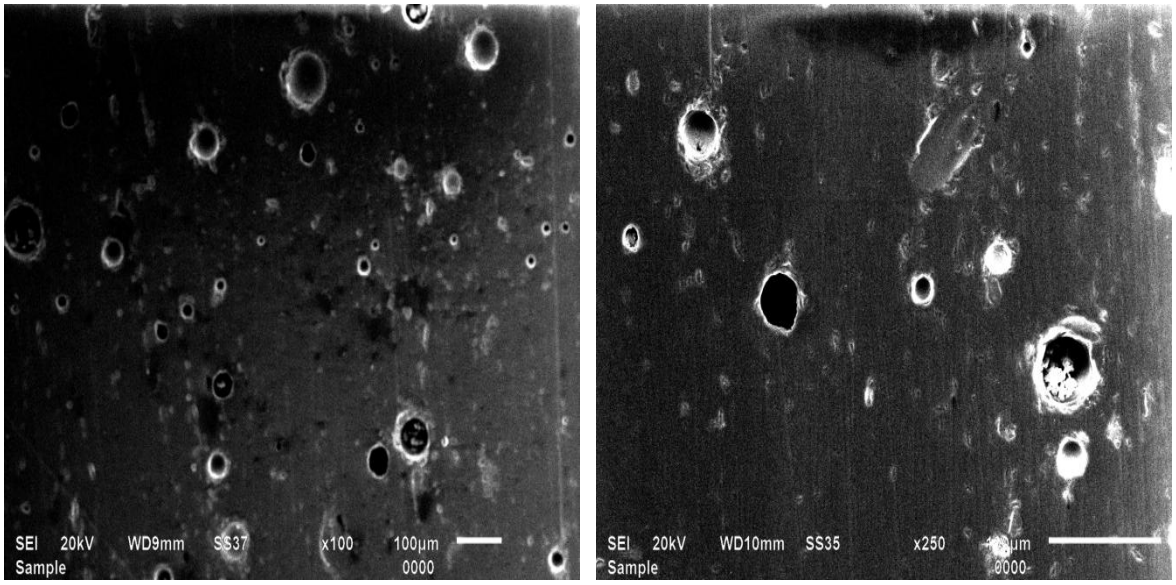

Fig. 4.83: Scanning electron micrographs of the X glass coating on crofer steel.

In order to further quantify the nature of surface, the structure was observed in BSE mode of SEM. Fig. 4.84 shows the surface morphology in BSE mode along with EDS analysis of the top layer of glass.

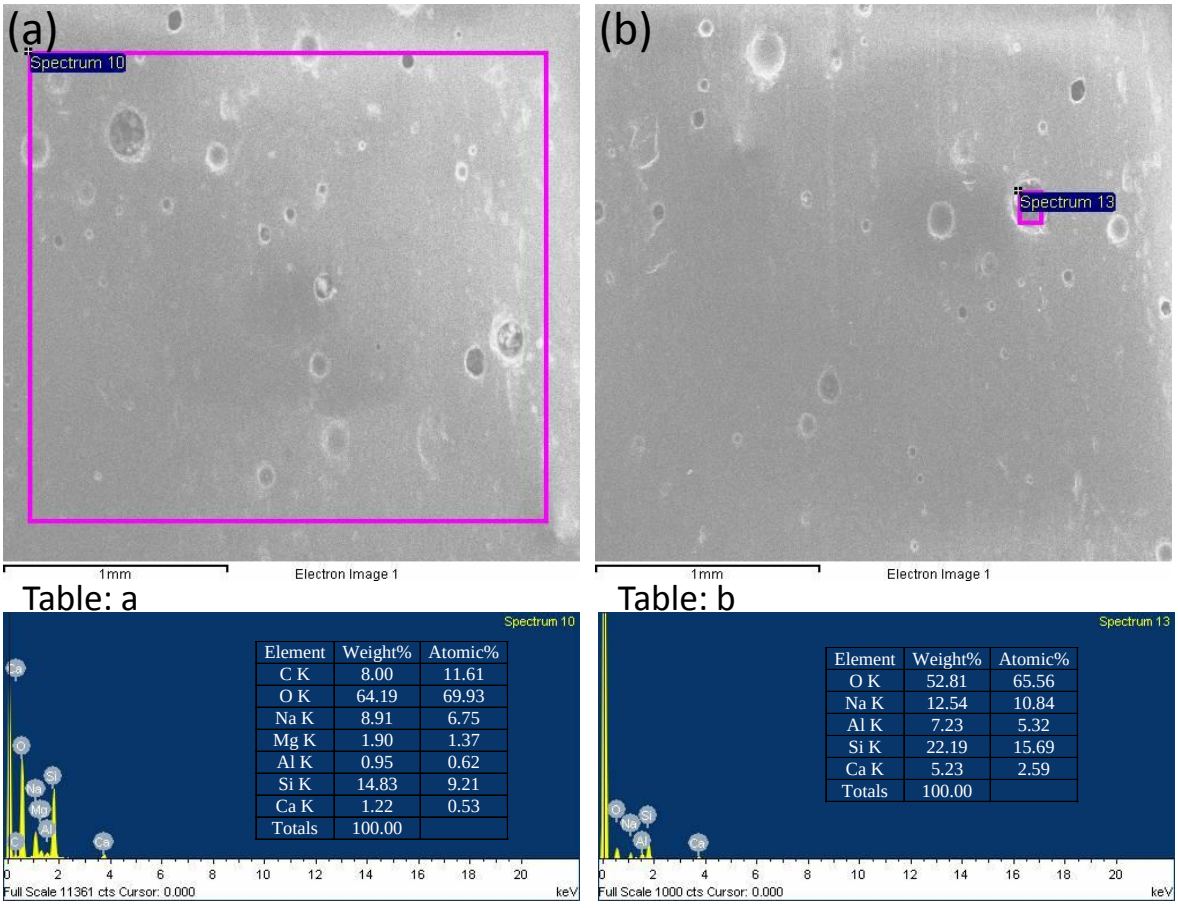

Element	Weight%	Atomic%
C K	8.00	11.61
O K	64.19	69.93
Na K	8.91	6.75
Mg K	1.90	1.37
Al K	0.95	0.62
Si K	14.83	9.21
Ca K	1.22	0.53
Totals	100.00	

Element	Weight%	Atomic%
O K	52.81	65.56
Na K	12.54	10.84
Al K	7.23	5.32
Si K	22.19	15.69
Ca K	5.23	2.59
Totals	100.00	

Fig. 4.84: Back scattered electron micrograph along with EDS analysis of the X glass coating on crofer steel.

In Fig. 4.84 (a), EDS analysis shows that all glass elements are present of on the top layer of coated glass. No element of steel could be detected. The analysis of Fig. 4.84 (b) specifies that C and Mg elements are not present in the inclusion area. The X-ray dot mapping of the area shown in Fig. 4.85 (a) for the elements C, Na, Ca, O, Mg and Si are shown in Fig. 4.85 (b-g), respectively. From X-ray dot mapping, we can see that C content is very less and not at all in the inclusion area. These results further confirmed that Cr and Fe have not diffused from steel to top layer of glass coating.

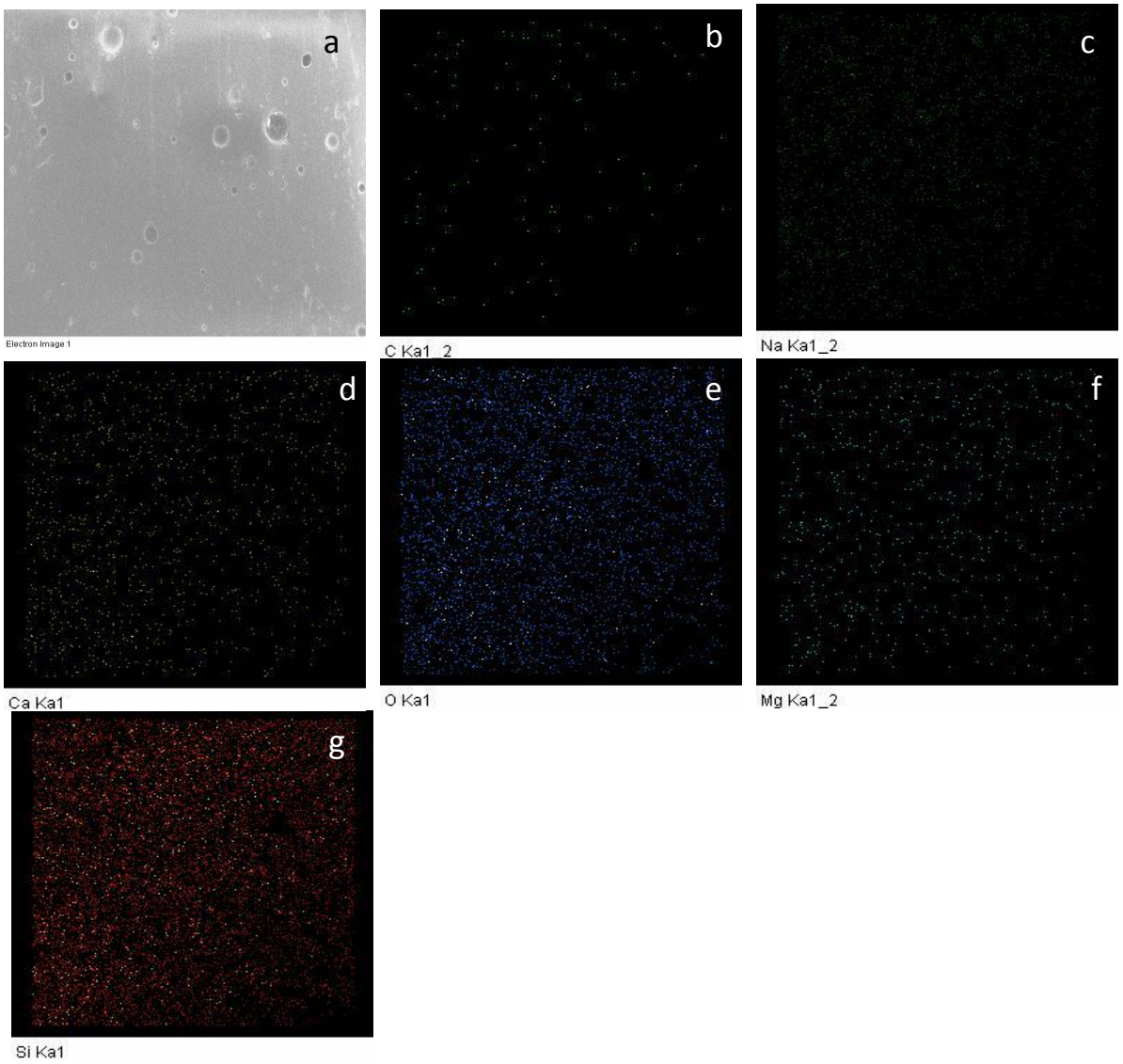

Fig. 4.85: X-ray dot mapping of C, Na, Ca, O, Mg and Si and of the surface of coated X glass on crofer steel.

4.2.3.2. Analysis of interface

Cross-sectional microstructure of the interface between X glass and crofer is shown in Fig. 4.86. The interface between glass and steel shows good adhesion. However, crystallinity at the edge of the glass coating was examined during the microstructural study [68].

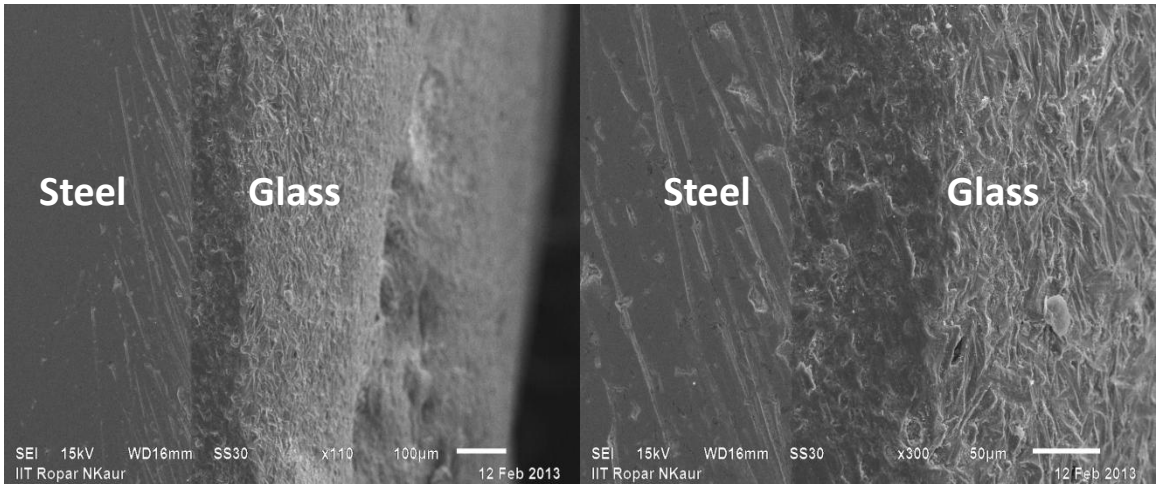

Fig. 4.86: SEM micrograph of interface between X glass and crofer steel showing the overall view of interface.

The EDS analysis marked as rectangular section was done to understand the diffusion of different elements as shown in Fig. 4.87. As observed from the EDS analysis of surface, Cr has not diffused and the diffusion of Fe from steel side into glass is very low. Fig. 4.87 (a) indicates the presence of all elements which are present in glass matrix.

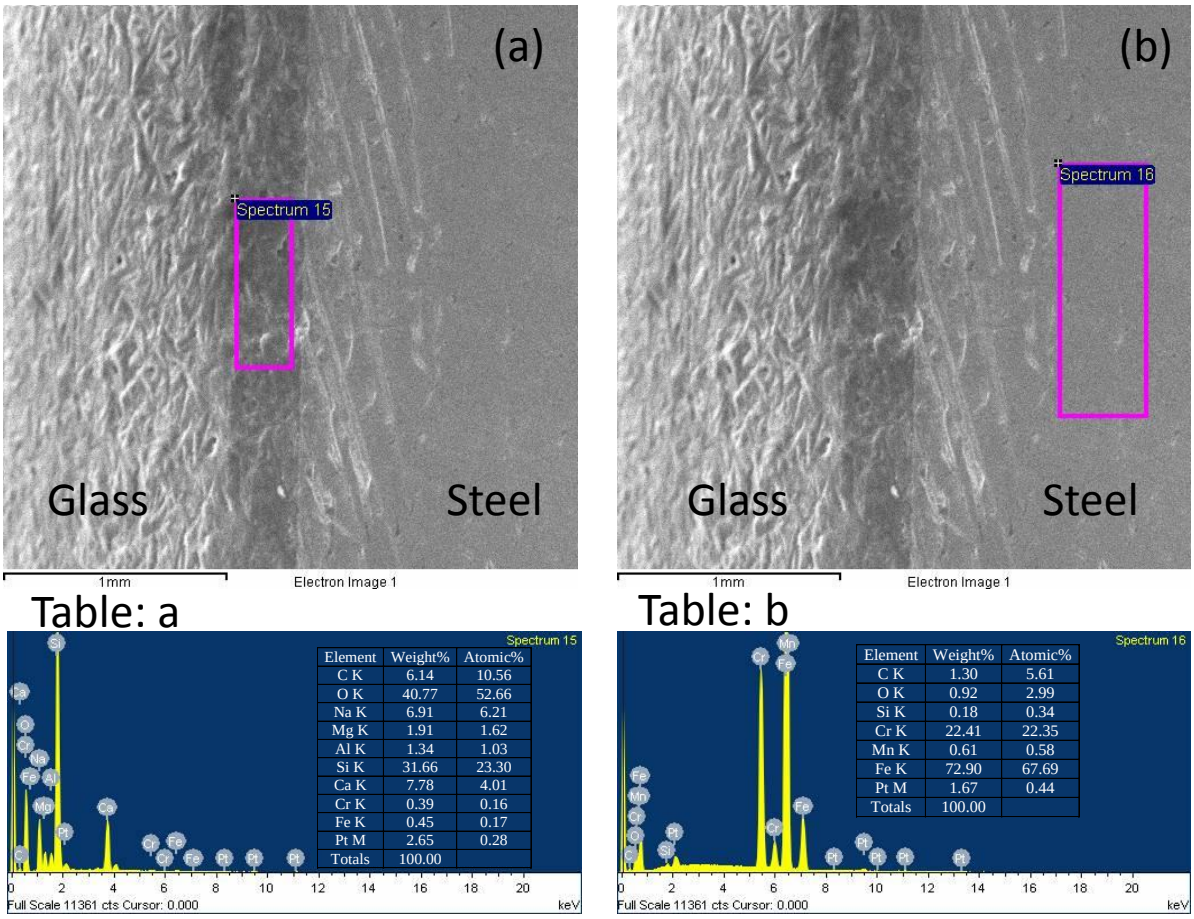

Table: a

Element	Weight%	Atomic%
C K	6.14	10.56
O K	40.77	52.66
Na K	6.91	6.21
Mg K	1.91	1.62
Al K	1.34	1.03
Si K	31.66	23.30
Ca K	7.78	4.01
Cr K	0.39	0.16
Fe K	0.45	0.17
Pt M	2.65	0.28
Totals	100.00	

Table: b

Element	Weight%	Atomic%
C K	1.30	5.61
O K	0.92	2.99
Si K	0.18	0.34
Cr K	22.41	22.35
Mn K	0.61	0.58
Fe K	72.90	67.69
Pt M	1.67	0.44
Totals	100.00	

Fig. 4.87: Back scattered electron micrograph with EDS analysis of the X glass coating on crofer steel from the interface.

For further confirmation of the diffusion from steel to glass and vice-versa, line profile (yellow line in Fig. 4.88) along the interface was taken. The resultant spectrums are shown in Fig. 4.89.

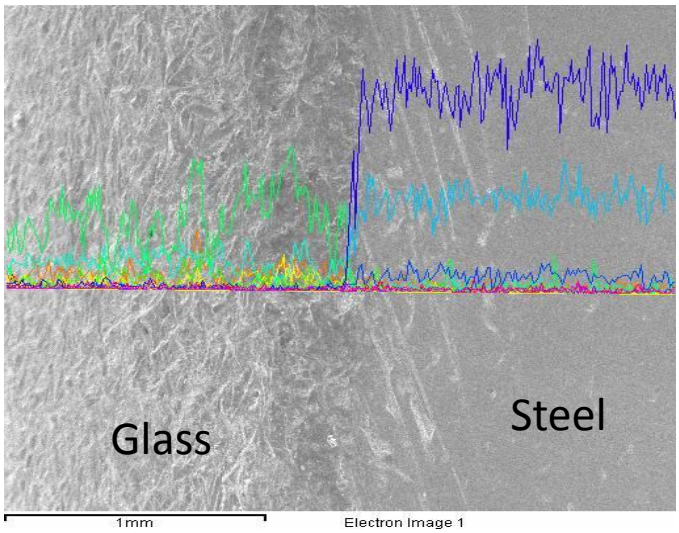

Fig. 4.88: Back scattered image of the cross-sectional area where yellow line is representative of line profile.

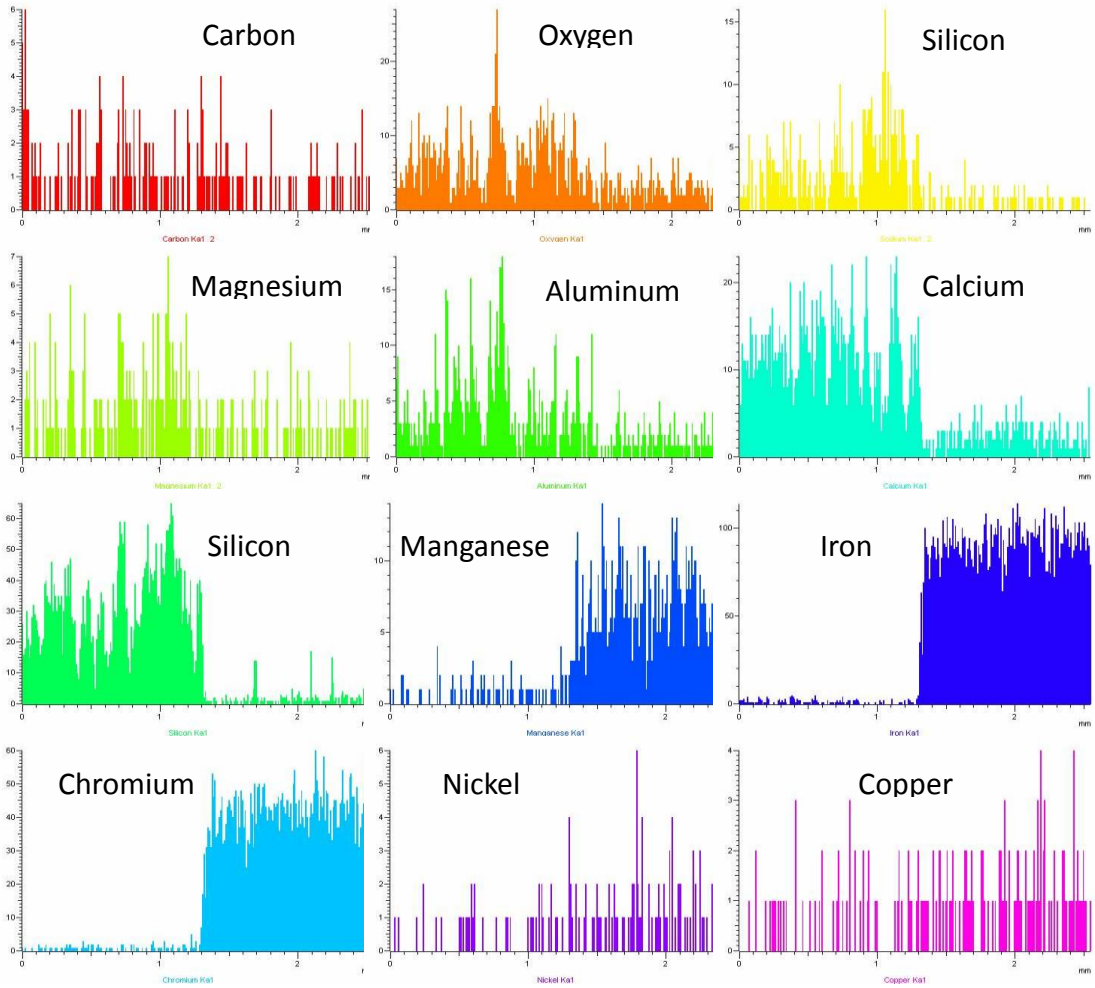

Fig. 4.89: Line profile spectrum across the cross-sectional area.

The results of line profile confirmed the formation of interfacial bond between steel and glass by diffusion of the elements. Diffusion of Fe, Cr, Cu and Mn from steel side into glass elements is weak and has the same value along the glass layer. The Ni content of the steel also promotes the bonding strength to the glass coating [69]. However, the diffused amount of elements is low which does not affect the properties of the glass.

4.2.4. N-series glasses and SS

Apart from crofer interaction with N-series glasses, the stainless steel (SS) was also used for interaction study. The glass coatings were not smooth and adhere very well with steel. However, N-10 glass shows some better results. The SEM analysis with EDS of the top surface of the steel sample after interaction shows the presence of glass constituents along with elements of the steel.

4.2.4.1. N-15 glass and SS

Fig. 4.90 shows the back scattered electron micrograph of the diffuse N-15 glass into stainless steel at 900 °C for 1 h.

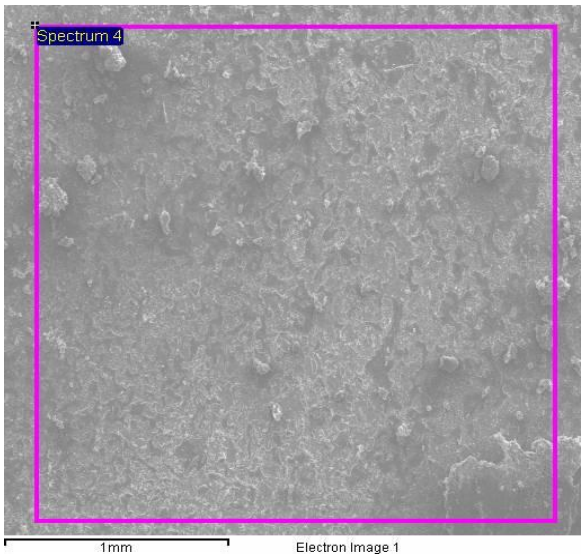

Fig. 4.90: Back scattered electron micrograph of the N-15 glass coating on stainless steel.

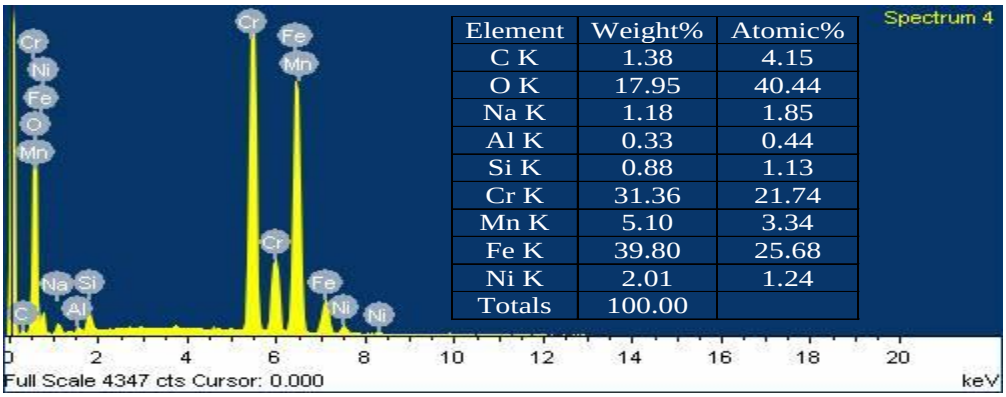

Element	Weight%	Atomic%
C K	1.38	4.15
O K	17.95	40.44
Na K	1.18	1.85
Al K	0.33	0.44
Si K	0.88	1.13
Cr K	31.36	21.74
Mn K	5.10	3.34
Fe K	39.80	25.68
Ni K	2.01	1.24
Totals	100.00	

Fig. 4.91: EDS spectrum with elemental analysis of the area marked in Fig. 4.90.

The EDS spectrum of the top layer of steel was taken with the elemental analysis to know the depth of diffusion (Fig. 4.91). EDS analysis shown that all glass elements are present of on the top layer of steel along with elements of steel.

4.2.4.2. N-10 glass and SS

Fig. 4.92 shows the back scattered electron micrograph of the diffuse N-10 glass into stainless steel at 900 °C for 1 h. The EDS spectrum of the top layer of steel was taken with the elemental analysis to know the depth of diffusion (Fig. 4.93). EDS analysis shown that all glass elements are present of on the top layer of steel along with elements of steel.

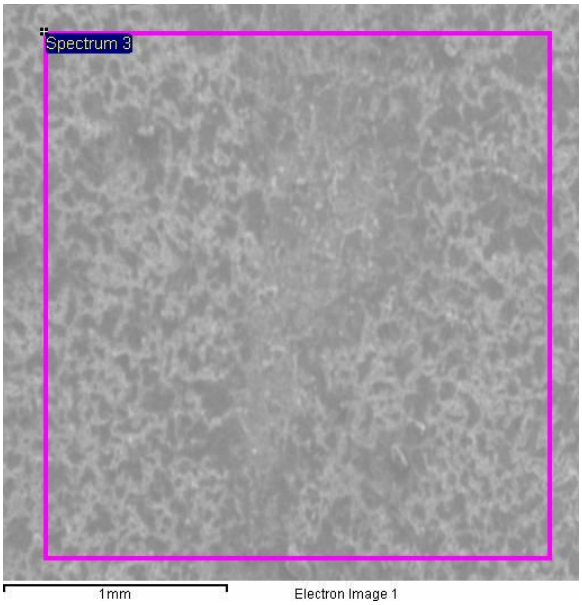

Fig. 4.92: Back scattered electron micrograph of the N-10 glass coating on stainless steel.

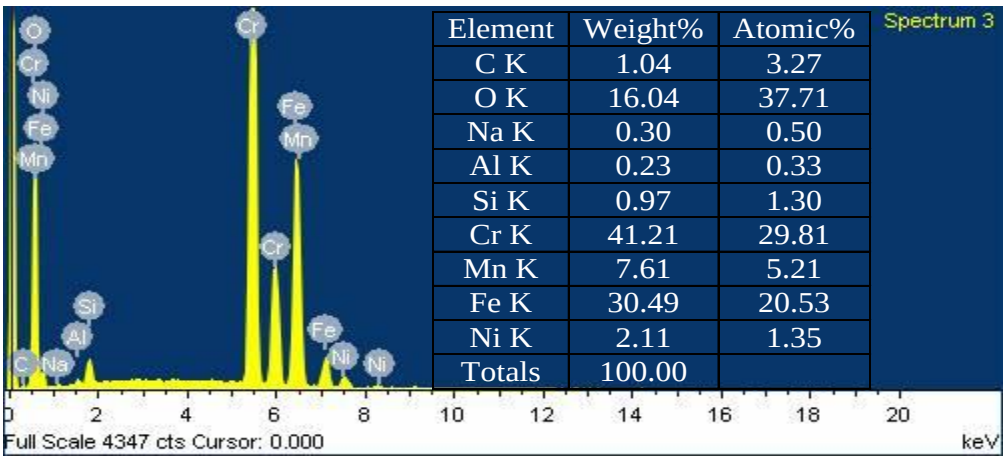

Element	Weight%	Atomic%
C K	1.04	3.27
O K	16.04	37.71
Na K	0.30	0.50
Al K	0.23	0.33
Si K	0.97	1.30
Cr K	41.21	29.81
Mn K	7.61	5.21
Fe K	30.49	20.53
Ni K	2.11	1.35
Totals	100.00	

Spectrum 3

Fig. 4.93: EDS spectrum with elemental analysis of the area marked in Fig. 4.92.

4.2.5. S and X glasses with SS

In order to check the interaction of S and X glasses with SS, couples were made by slurry coating method. Then these couples are heat treated to temperature 700 °C at 10 °C/min heating

rate. But glass coating agglomerate and chip out from the surface of steel during cooling. The photographs of S and X with SS are given in Fig. 4.94 and 4.95, respectively.

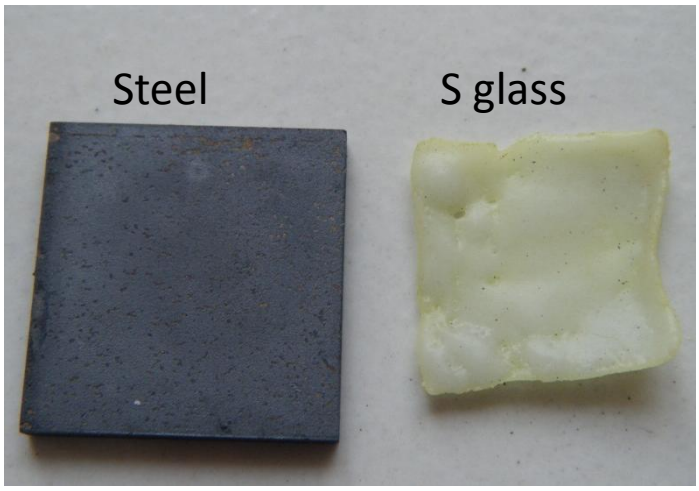

Fig. 4.94: S glass layer chip out from SS steel piece.

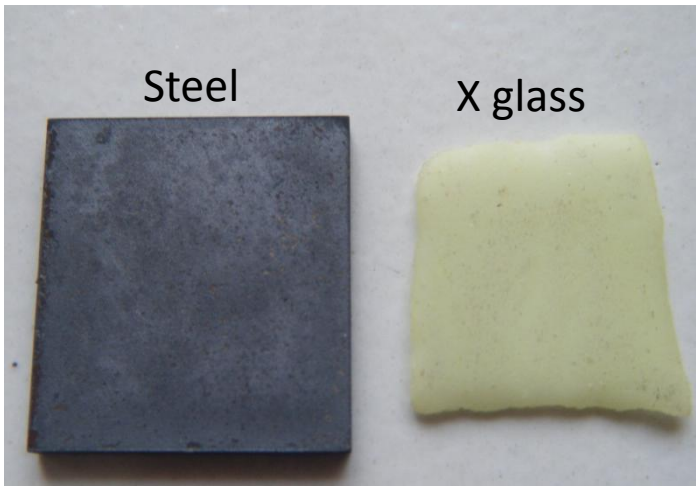

Fig. 4.95: X glass layer chip out from SS steel piece.

There is no sticking of oxide layer of steel on glass which indicates that SS steel shows resistance towards diffusion. From the chip out layers of glasses, it is confirmed that wetting angle of these glass on this steel is more than 90°. Clearly, the driving force for glass detachment is the elastic energy that builds up during cooling due to thermal contraction mismatch between the steel substrate and the glass drop [70].

4.2.6. N-10 glass and duplex steel

From the above study, it is apparent that better and smooth coating on Cr steel is with N-10 glass as compared to other glass systems. So, this glass was selected for detailed study for coating on duplex steel. Based on the analysis of crystallization kinetics of the prepared glass, heat treatment temperature selected for present study was 900 °C, which is above the first

crystallization and just below the second crystallization temperature. Moreover, chance of thermal fluctuation in a furnace was also one reason for selecting this temperature just below T_{p2}. From dilatometer measurements (Fig. 4.96 (a)), the TEC values between temperature 50–600 °C of glass, heat treated glass (900 °C) and duplex steel are 7.79×10−6 K^{-1}, 7.95×10−6 K^{-1} and 7.96×10−6 K^{-1} respectively. A comparative thermal study of base material with glass (as prepared) and heat treated glass (900 °C) in the different range of temperatures is shown in Fig. 4.96 (b). It is observed that there is a complete compatibility of steel with heat treated glass within the studied range. Since glass transforms to a glass-ceramic after T_g, a variation is observed in between 500 and 700 °C. However, once this transformation has occurred, the utility factor of glass-ceramic as coating substance increases as can be seen from the straight line matching of TEC values up to 700 °C. The variation in TEC values of glass and glass-ceramic with steel is within the limit (2%). This indicates that the glass may be useful for coating the steel surface [71].

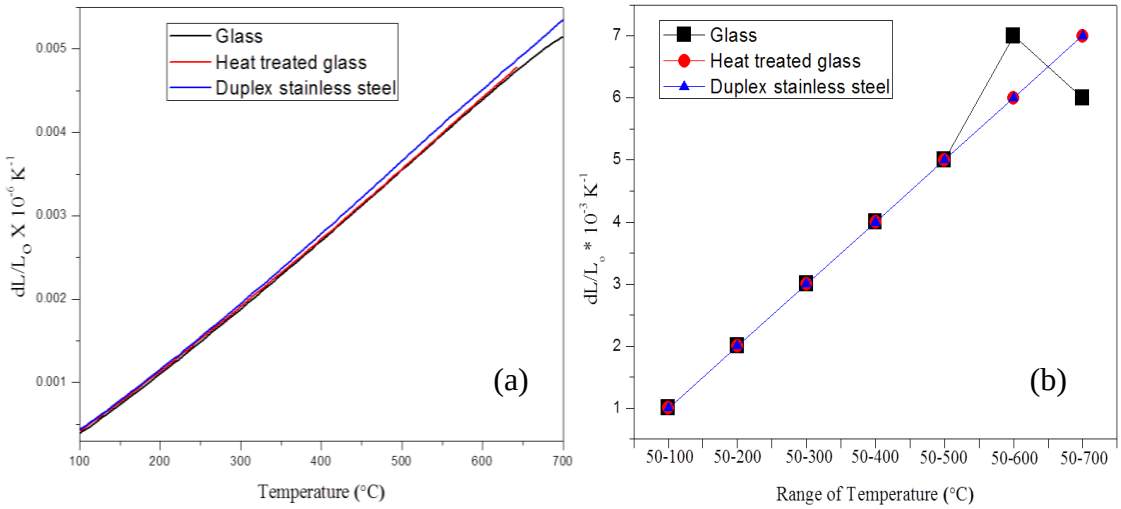

Fig. 4.96 (a): Thermal expansion curves of as prepared glass, heat treated glass and duplex steel and **(b):** Measured value of TEC in different temperature ranges for prepared glass, heat treated glass and duplex steel.

4.2.6.1. Microstructural study

X-ray study of heat treated glass-ceramic indicated the presence of AlNa (SiO_4) and SiO_2 phases. The crystal structure and volume fraction of AlNa (SiO_4) and SiO_2 phases are hexagonal (80%) and rhombohedral (20%) respectively. Glass when heated in between T_g and T_m, nucleation of crystalline phase in the glass matrix occurs. Normally, nucleation of these phases is derived from nucleating agents, which are deliberately added as a constituent in glass.

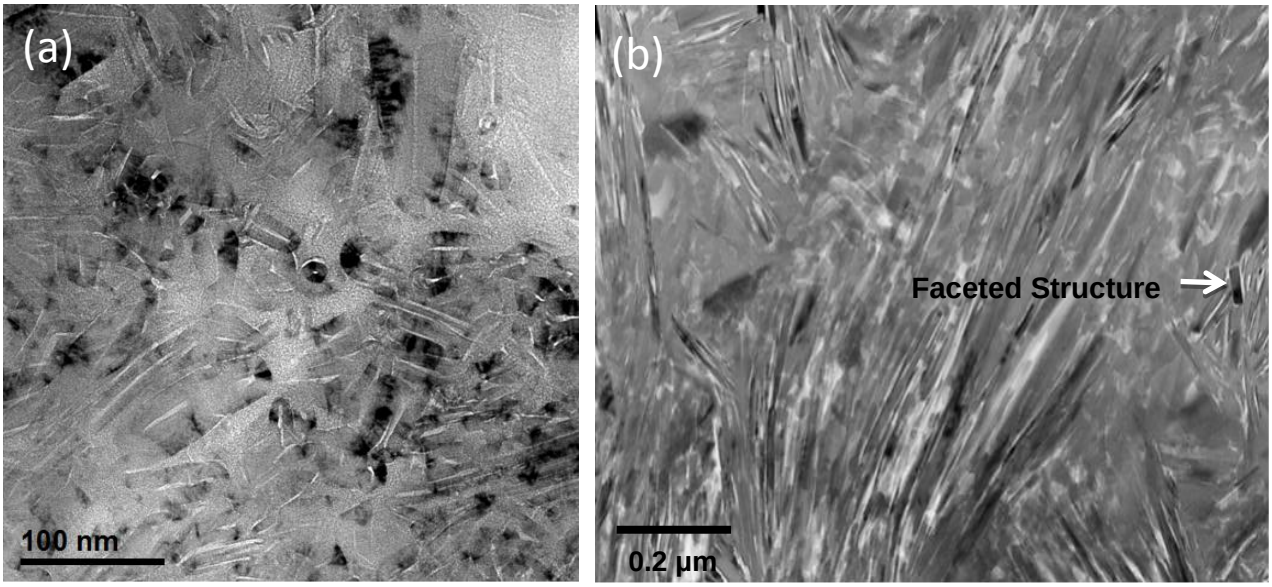

Fig. 4.97 (a): The low magnification micrograph of the glass-ceramic coating (900 °C for 1 h) showing the nucleation and growth of crystalline phases. **(b):** The high magnification surface micrograph of the glass-ceramic coating showing the growth of SiO_2 needle and faceted (AlNa (SiO_4)) structures.

Fig. 4.97 (a) shows the micrograph of the coated glass after the thermal treatment. In the structure, one can visualize two types of crystalline phases. One is a white needle like structure and other is a faceted dark structure. In some places, the growth of the needle is pronounced. On analyzing the entire feature, it appears that the first solid solution phase has nucleated in the matrix of glass as spherulite structure and from this the needle like phase of SiO_2 has spun out. This information is extracted because the needle like phase of SiO_2 is existing at the periphery of the black solid solution phase. Once SiO_2 grows, it takes Si from the glass matrix making surrounding areas less in Si content. At this stage, the most favorable condition for the growth of another crystalline phase exists. Since glass is a highly viscous liquid, the diffusion is the sluggish process. The SiO_2 phase once nucleated, finds favorable conditions for its growth making the surrounding area of the glass matrix in relaxed mode (Fig. 4.97 (b)). However, the solid solution phase from where the nucleation of SiO_2 has occurred becomes rich in Al and Na content. During isothermal heat treatment, highly viscous glass may enhance localized segregation of solute at the crystal/liquid interface. Here, the interface controlled growth may become the diffusion controlled. The faceted cellular structure corresponds to AlNa (SiO_4) phase, which is hexagonal. The faceted morphology depends upon whether the interface is smooth or rough. Jackson [72] has developed a model for nucleation and growth process. In this

model he has demonstrated that faceted or non-faceted growth is controlled by the fraction of the site occupied by the atoms in a growing system which depends upon α parameter, where

$$\alpha = \frac{}{} \xi \qquad (4.21)$$

Here L is the latent heat associated with transformation, k is the Boltzmann's constant, T_E is the transformation temperature, and ξ is the crystallography of interface. If α factor is less than 2, then the surface free energy at the interface is low and product phase is non-faceted. However, if α becomes more than 2, faceted features are observed. In this structure also similar behavior is observed.

4.2.6.2. Glass-steel interface

To study the interfacial phenomenon, glass-steel interface was analyzed under SEM. Fig. 4.98(a) presents the low magnification view of the interface. The interface is a corrugated type and has the wavy pattern. The high magnification micrograph presents a clear view of the interface (Fig. 4.98 (b)). From the structural analysis, one can see the wavy pattern on the glass surface of the coating. Because of thermal forces the glass is diffusing inside the matrix of steel. It appears that steel is offering resistance for diffusion. Because of this, the planar interface is broken and it becomes cellular type (non-planar). However, no crack is visualized at the interface. This indicates that the bonding of steel with glass is adherent in nature. The overall interfacial analysis present a view that the steel (Fe) is offering more resistance towards diffusion as compared to the glassy matrix, but the width of the interface shows that inter-diffusion of elements has occurred. The X-ray dot mapping of the interface (circular area marked in Fig. 4.98 (b)) indicate that iron has migrated, but it has no continuous structure.

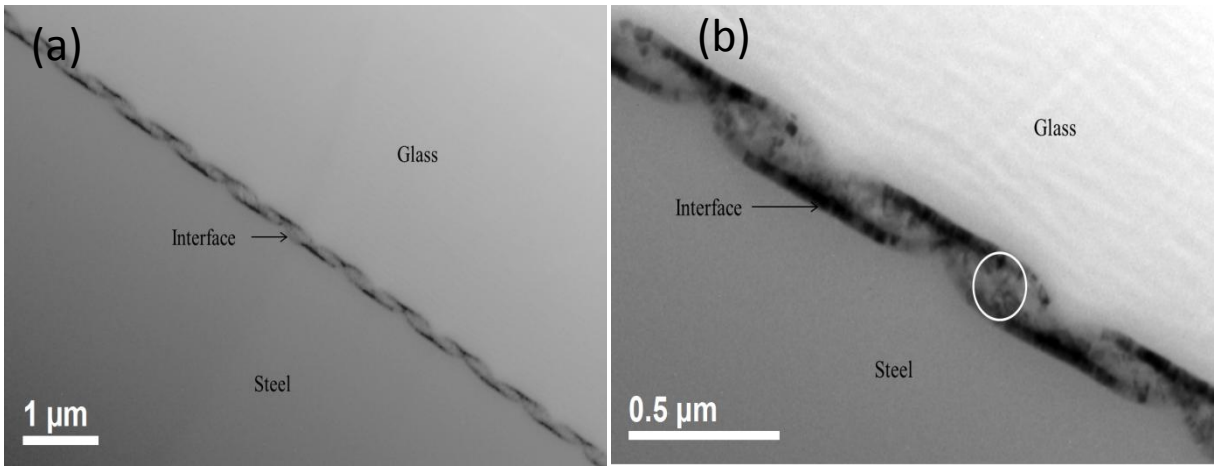

Fig. 4.98 (a): SEM micrograph of interface showing the overall view of interface. **(b):** SEM micrograph of interface showing the bonding characteristic.

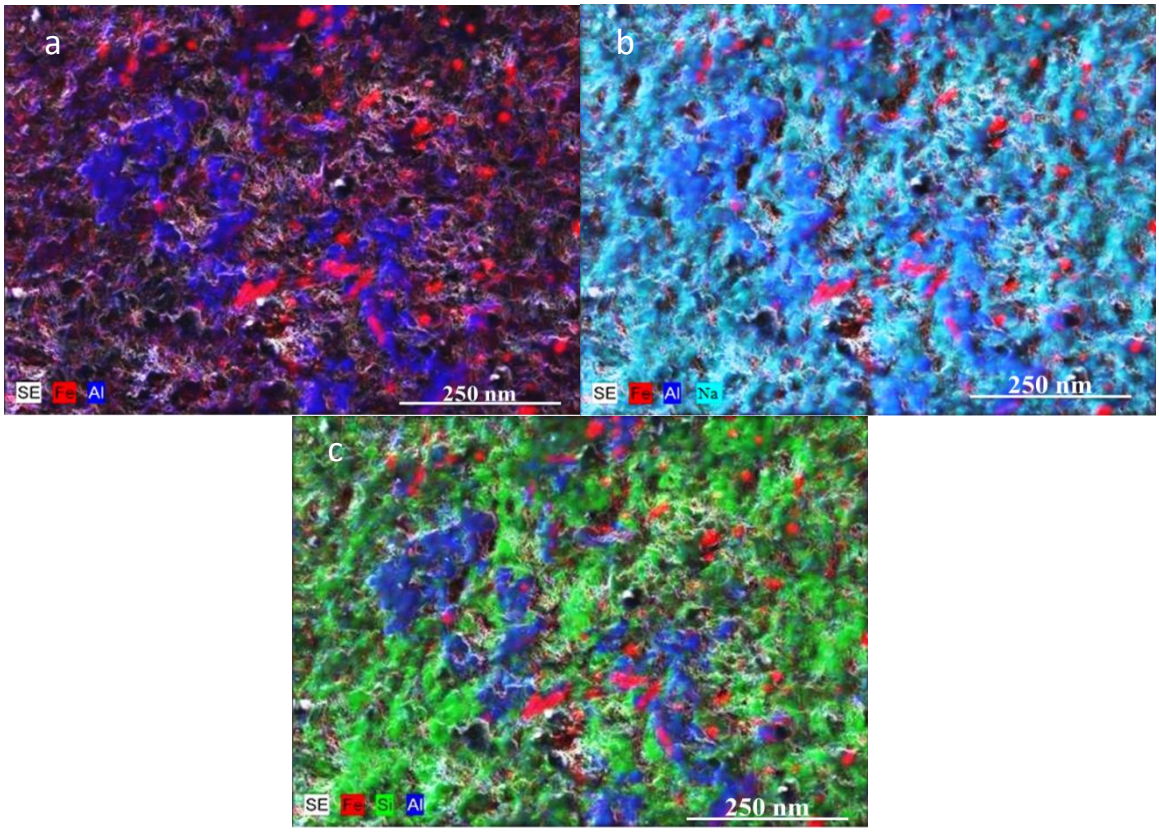

Fig. 4.99 (a): X-ray dot mapping of Fe and Al at interface. **(b):** X-ray dot mapping of Fe and Al along with Na at interface. **(c):** X-ray dot mapping of Fe and Al along with Si at interface.

Fig. 4.99 (a–c) gives the dot mapping of the interface where Na and Si have migrated as the continuous network. Aluminum is known for preventing the crystallization in glasses [73, 74]. Obviously, Aluminum may diffuse in less quantity as compared to Na and Si. Since Na is a smaller ion so it has a tendency to migrate at the faster rate.

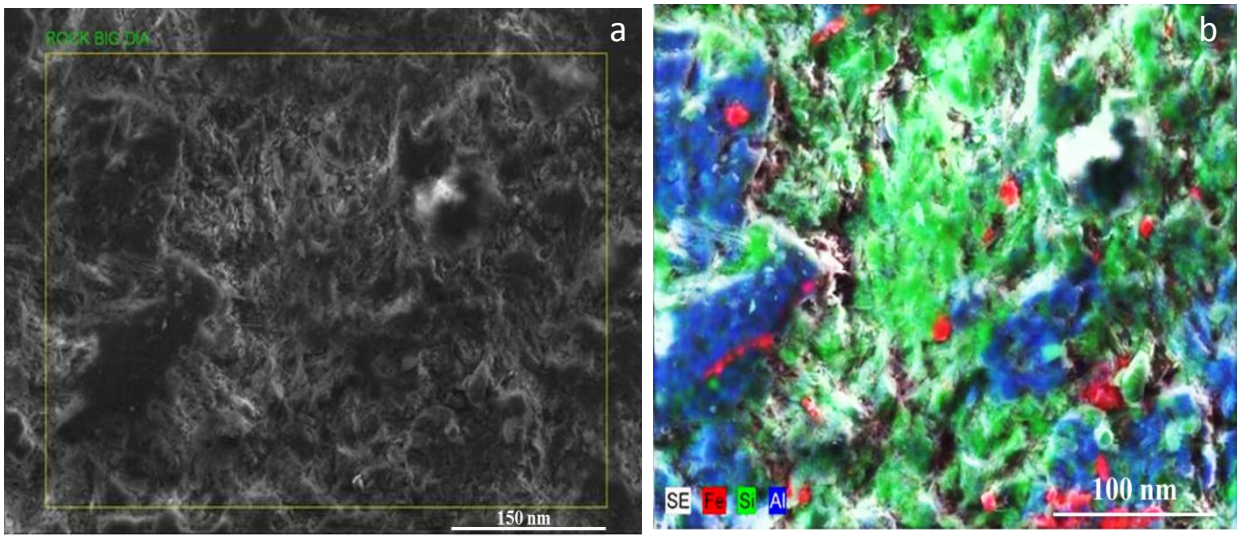

Fig. 4.100 (a): Back scattered electron micrograph of interface. **(b):** X-ray dot mapping of Fe, Si and Al at interface.

The back scattered micrograph (Fig. 4.100 (a)) followed by dot mapping (Fig. 4.100 (b)) also indicate that migration of iron is lesser as compared to other constituents of glass. At the beginning of the heat treatment cycle, the viscosity of glass is high, which leads to controlled growth of the nucleated phase. High viscosity may lead localized segregation of solute or impurity at the interface which grows with time. For its growth, solute from neighboring areas migrates and thus the interface morphology changes from planar to cellular one. During the growth of cellular part, the remaining constituents migrate in opposite direction which creates the atmosphere for the growth of other crystalline phases. Since this process occurs simultaneously so the interface becomes a corrugated type. As it can be visualized from SEM micrographs followed by EDS analysis, the migration of ions is taking place through the interface which leads to building up colonies consisting of Al-rich and Si-rich phases. However, the migration of Fe is not much and it is not in bulk. The entire structural feature shows that Fe exhibits better stability and do not dissolve in the glass matrix in large amount. Slight migration of iron is required to have better bonding with glass, which is visible in our present work.

4.2.7. S glass and duplex steel

The photograph of S glass coated on duplex steel is shown in Fig. 4.101. The coated glass on the steel piece has milky white appearance and is smooth on the upper part. Less number of defects appears in the coating.

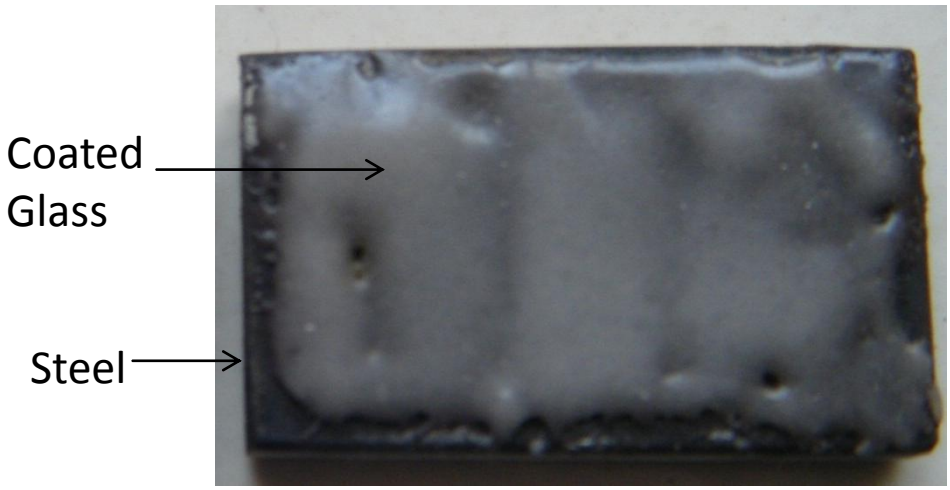

Fig. 4.101: Photograph of diffusion couple of S glass with duplex steel.

The detailed microstructural study of coating was done under SEM along with EDS on the top layer of coated glass and also on the interface between glass and steel.

4.2.7.1. Surface analysis

Fig. 4.102 shows the micrographs of the S glass coating on duplex steel at 700 °C for 1 h. In the structure, we can clearly see the flow of melted glass. In order to further quantify the nature of

surface, the structure was observed in BSE mode. Fig. 4.103 shows the surface morphology in BSE mode. The EDS spectrum of the top layer of glass was taken along with the elemental analysis to know the depth of diffusion as shown in Fig. 4.103.

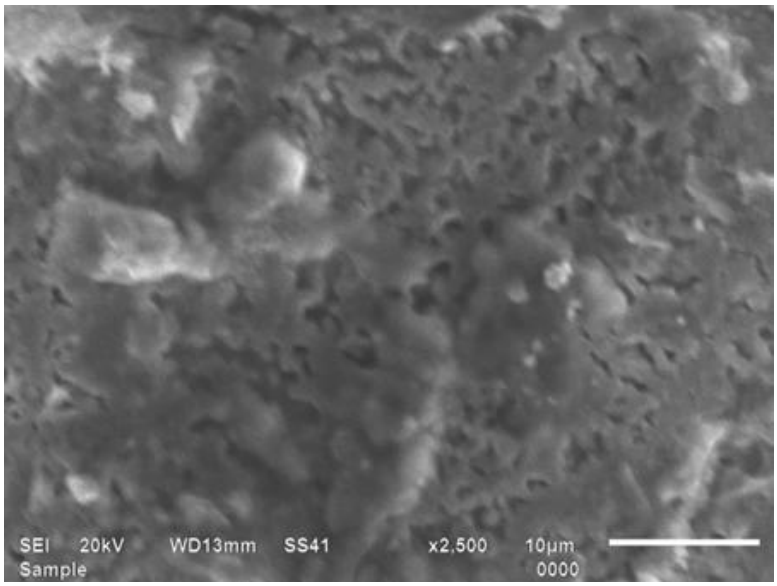

Fig. 4.102: Scanning electron micrograph of the S glass coating on duplex steel.

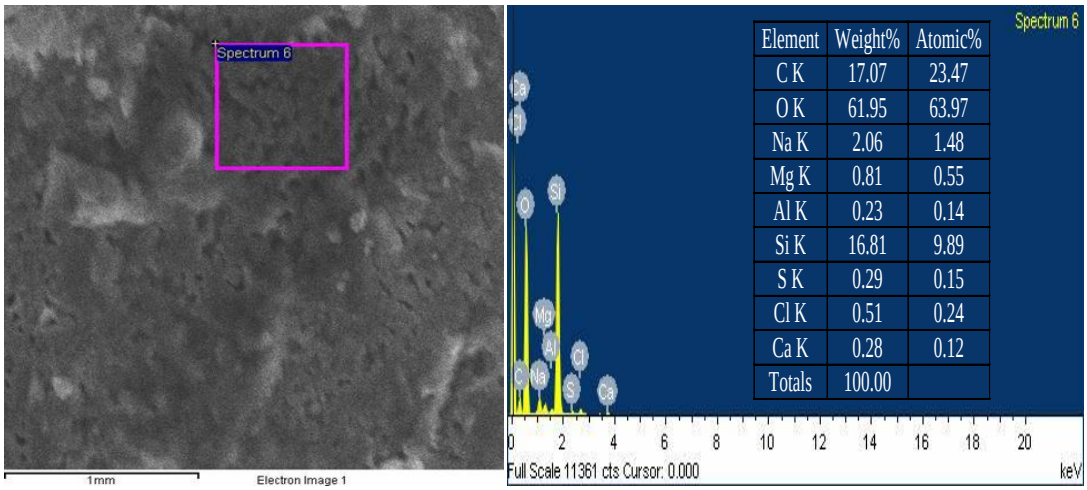

Fig. 4.103: Back scattered electron micrograph with EDS elemental analysis of the area marked.

EDS analysis shows that all glass elements are present of on the top layer of coated glass. There is no element present on the top layer of coated S glass which has diffused from the steel.

4.2.7.2. Analysis of interface

Cross-sectional microstructure of the interface between S glass and duplex steel is shown in Fig. 4.104. The interface between glass and steel shows good adhesion. No porosity is observed at the areas of the interface. The micrograph shows devitrified structure of glass after thermal treatment. Spherulites phase is grown inside the glass matrix [75].

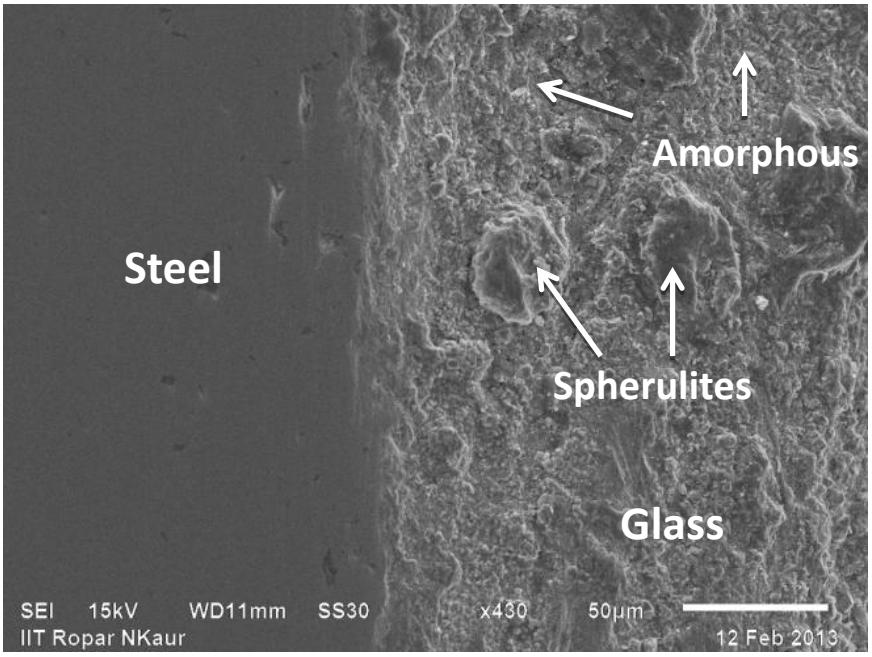

Fig. 4.104: SEM micrograph of interface between S glass and duplex steel showing the overall view of interface.

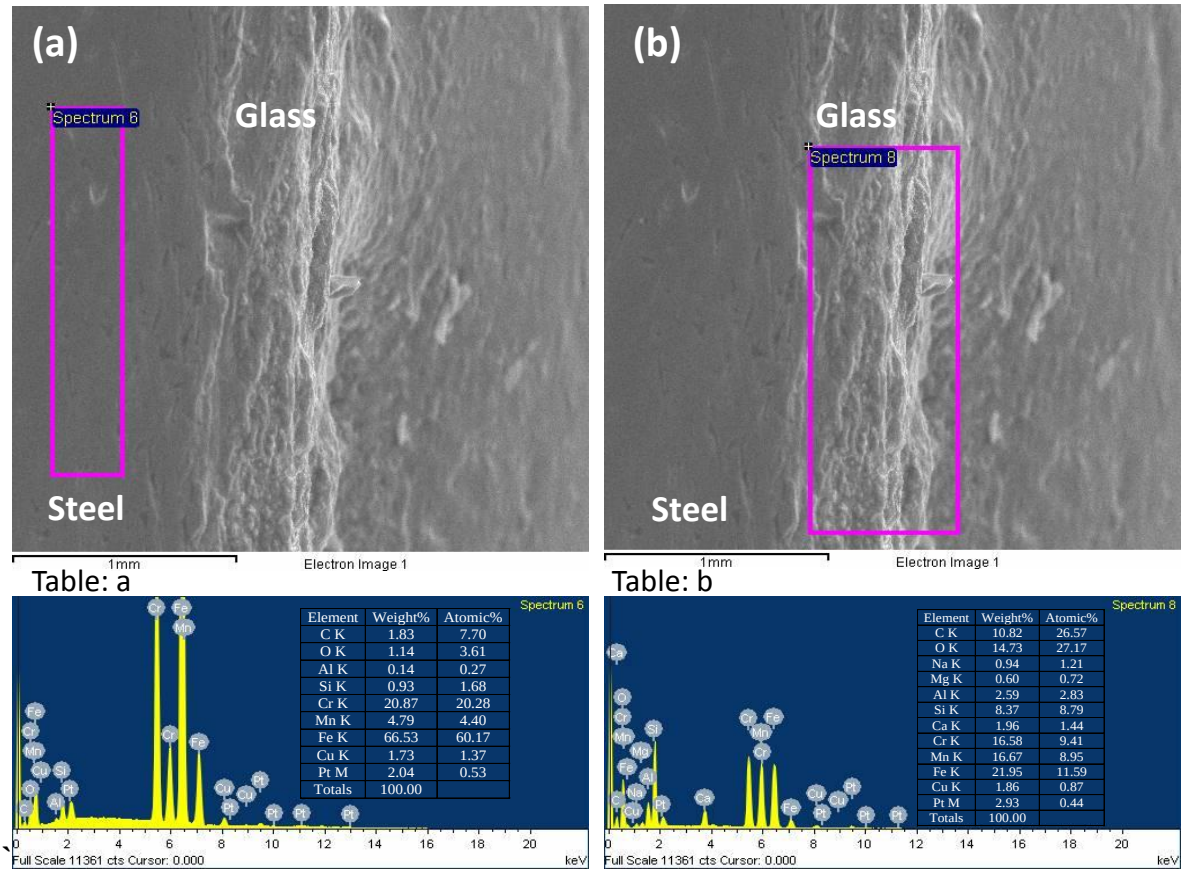

Fig. 4.105: Back scattered electron micrograph with EDS analysis of the area marked of the S glass coating on duplex steel.

The EDS spectrum of the interface between glass and steel was taken along with the elemental analysis to know the depth of elemental diffusion as shown in Fig. 4.105. Table (a) shows the analysis done on marked area in Fig. 4.105 (a) that clearly indicates the diffusion of Si and Al elements from glass side into steel. Also table (b) shows the analysis done from the marked area of Fig. 4.105 (b). Cr, Fe, Cu and Mn along with glass elements are responsible to form strong adhesion between S glass and duplex steel. Even in non-reactive glass/metal systems, adhesion may be due to chemical interactions that are entirely localized at the common interface. In the case of steel substrates, such interactions could take place between the oxygen of the glass and the chromium of the steel, a metallic element that has a strong affinity with oxygen [76].

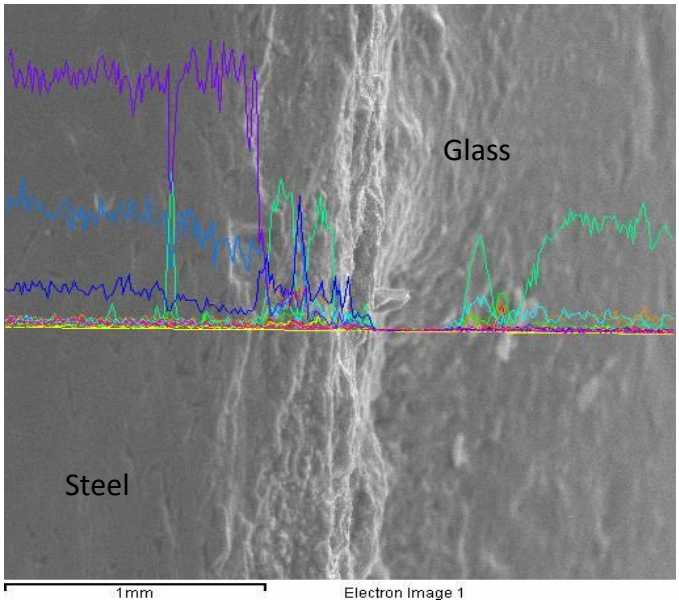

Fig. 4.106: Back scattered image of the cross-sectional area where yellow line is representative of line profile.

In order to confirm the inter diffusion of elements from glass to steel and vice-versa, the line profiles were taken as shown in Fig. 4.106. The obtained spectrum of C, O, Na, Ca, Si, Al, Fe, Cr, Cu, Mn and Mg are presented in Fig. 4.107. These spectrums again confirmed the inter-diffusion of elements from both sides [77].

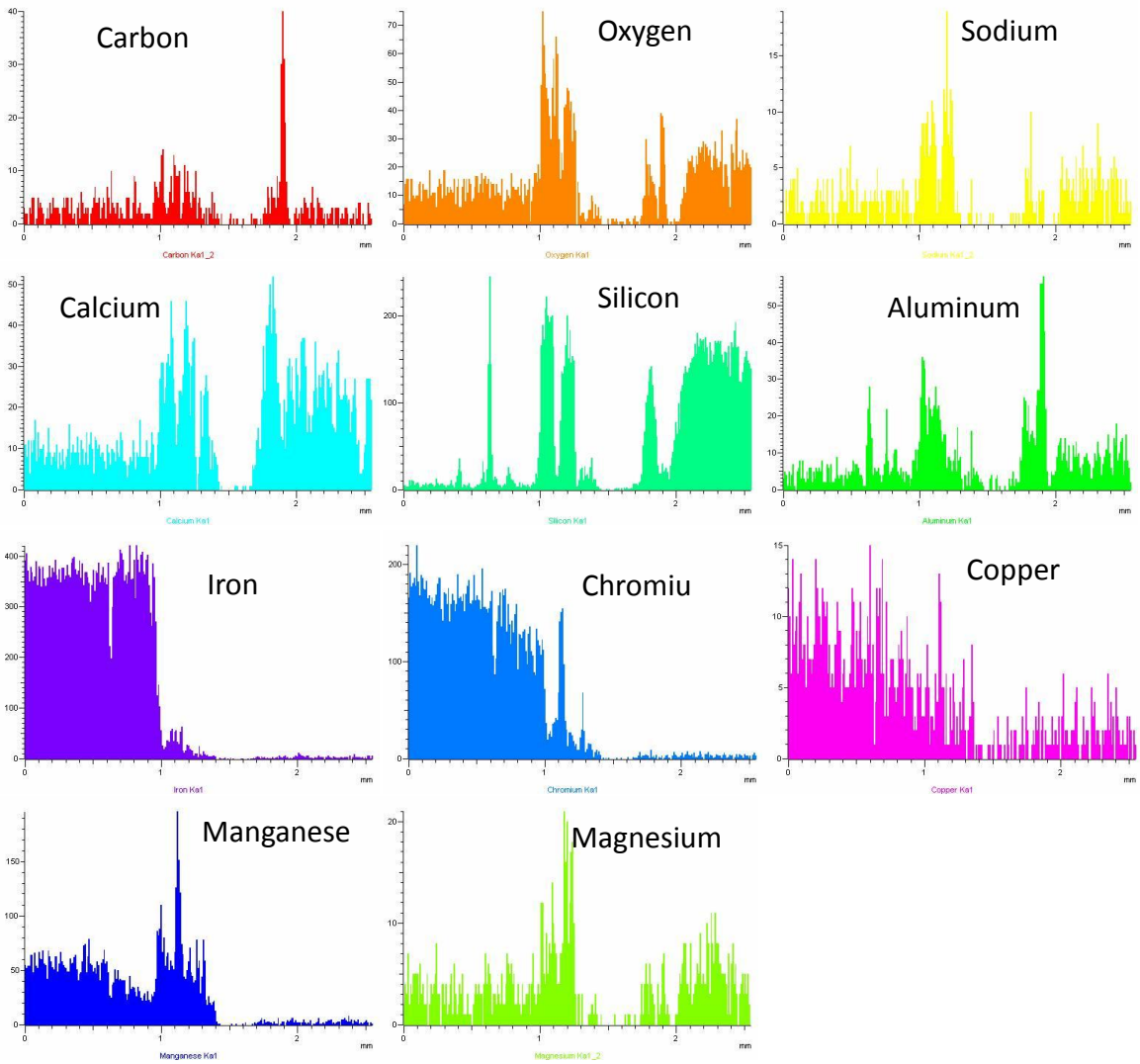

Fig. 4.107: Line profile spectrum across the cross-sectional area.

4.2.8. X glass and duplex steel

The photograph of coated X glass on duplex steel is presented in Fig. 4.108. The coated layer is smoother as compared to S glass on duplex steel. X glass again shows transparent nature on duplex steel wherever S glass coating on duplex steel has milky white appearance. Good wettability of the glass on the steel substrate is achieved.

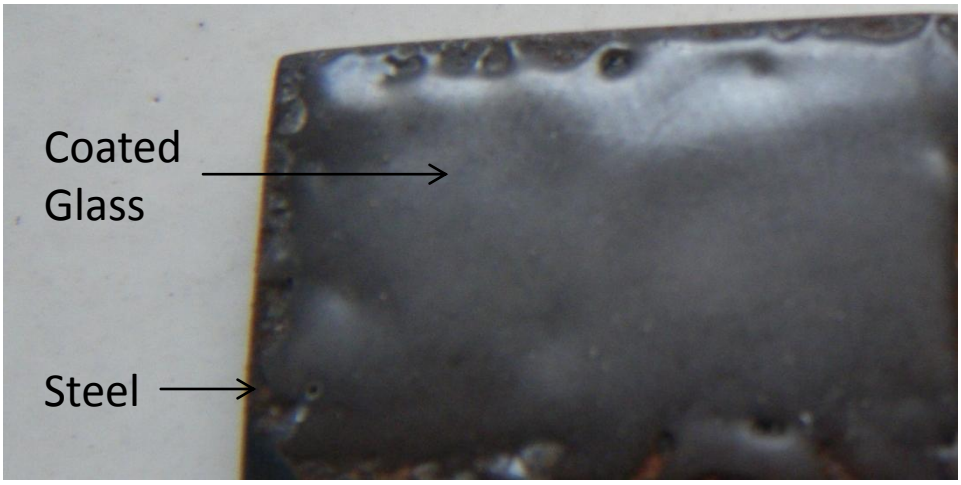

Fig. 4.108: Photograph of diffusion couple of X glass with duplex steel.

The diffusion of elements along the interface and structure of coated glass was analyzed with the help of scanning electron microscope along with EDS.

4.2.8.1. Surface analysis

Fig. 4.109 shows the micrographs of the X glass coating on duplex steel at 700 °C for 1 hr. In the structure, we can clearly see the coated glass with net like inclusion. In order to further quantify the nature of surface, the structure was observed in BSE mode. Fig. 4.110 shows the surface morphology in BSE mode. The EDS spectrum of the top layer of glass was taken with the elemental analysis to know the depth of diffusion.

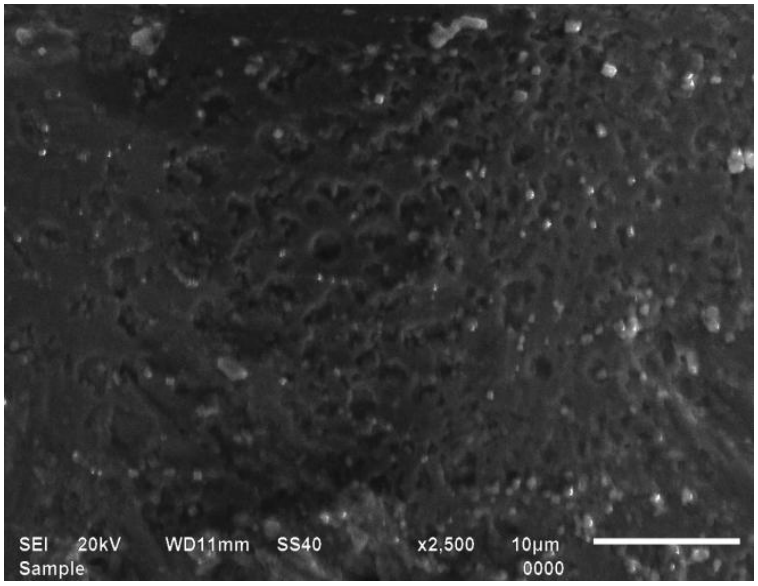

Fig. 4.109: Scanning electron micrograph of the X glass coating on duplex steel.

EDS analysis shows that all glass elements are present of on the top layer of coated glass. No elemental diffusion from steel on the top surface is deserved.

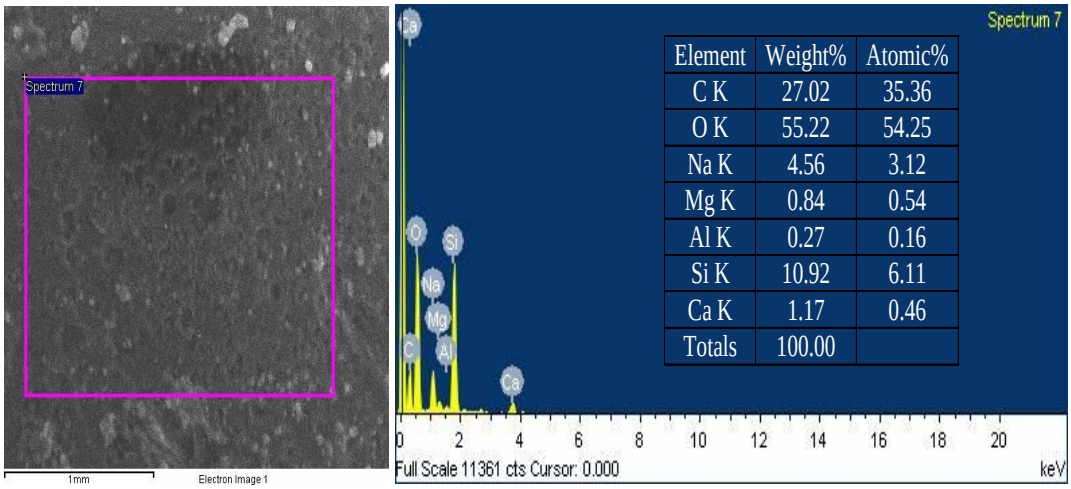

Fig. 4.110: Back scattered electron micrograph with EDS analysis of the area marked.

4.2.8.2 Analysis of interface

Cross-sectional microstructure of the interface between X glass and duplex steel is shown in Fig. 4.111. The interface between glass and steel shows some porosity at the interface with good adhesion.

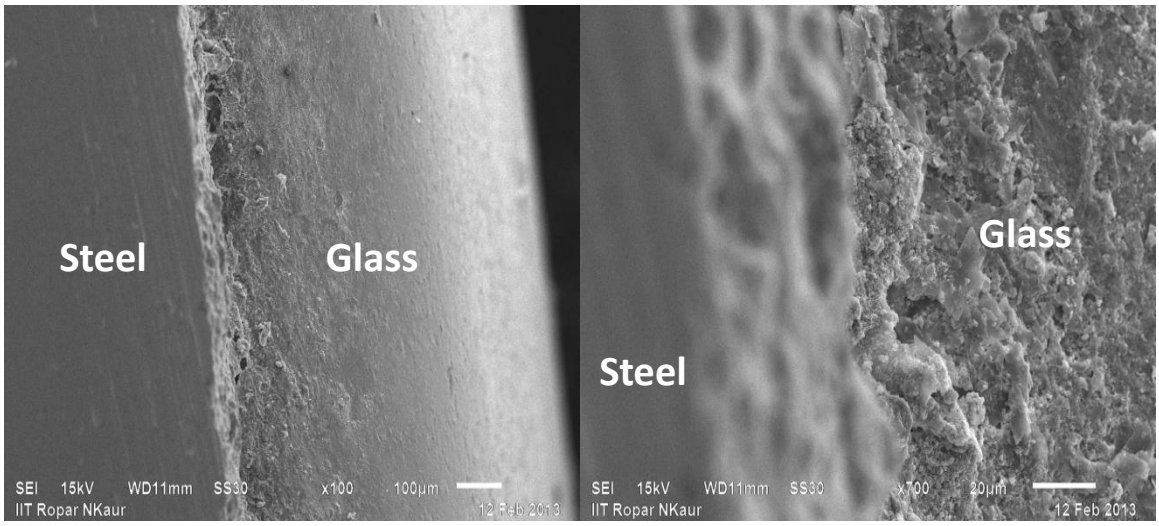

Fig. 4.111: SEM micrograph of interface between X glass and duplex steel showing the overall view of interface.

In order to know the elemental diffusion, EDS of glass and steel of diffusion couple was done as shown in Fig. 4.112. Table (a) taken from Fig. 4.112 (a) showed that only Si diffused from glass into steel side. Whereas in the glass network, Fe diffused from steel into glass as shown in table (b) of Fig. 4.112 (b).

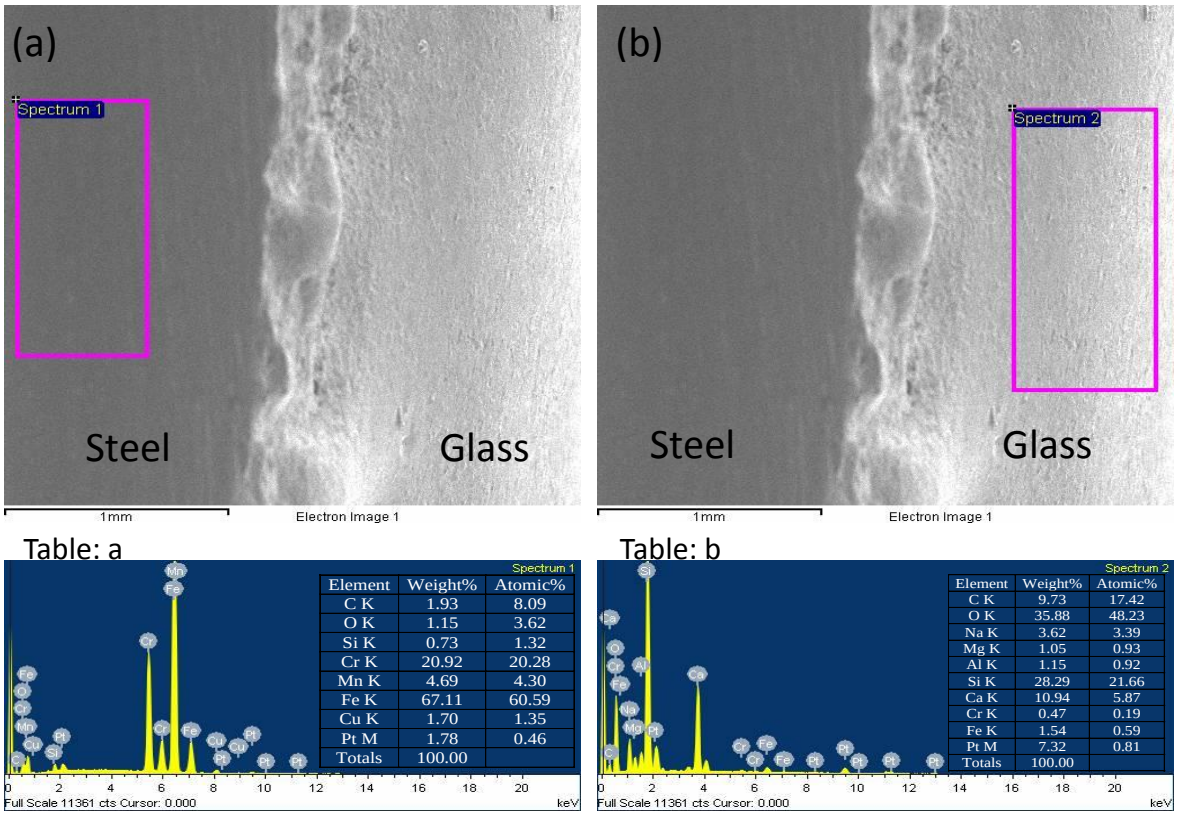

Fig. 4.112: Back scattered electron micrograph along with EDS analysis of the area marked of the X glass coating on duplex steel.

For further confirmation of the diffusion from steel to glass and vice-versa, line profile (yellow line in Fig. 4.113) along the interface was taken.

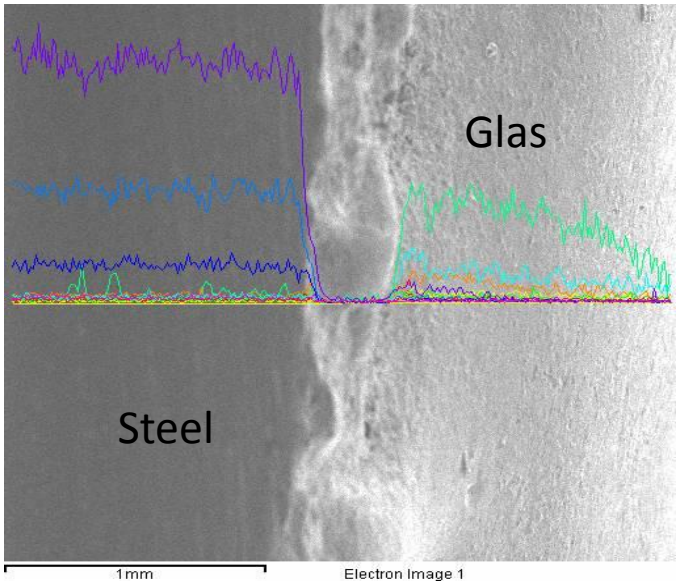

Fig. 4.113: Back scattered image of the cross-sectional area where yellow line is representative of line profile.

The obtained spectrums of C, O, Na, Mg, Al, Si, Ca, Fe, Cr, Mn and Cu along the interface are shown in Fig. 4.114. These spectrums clearly indicate the diffusion of elements into another network.

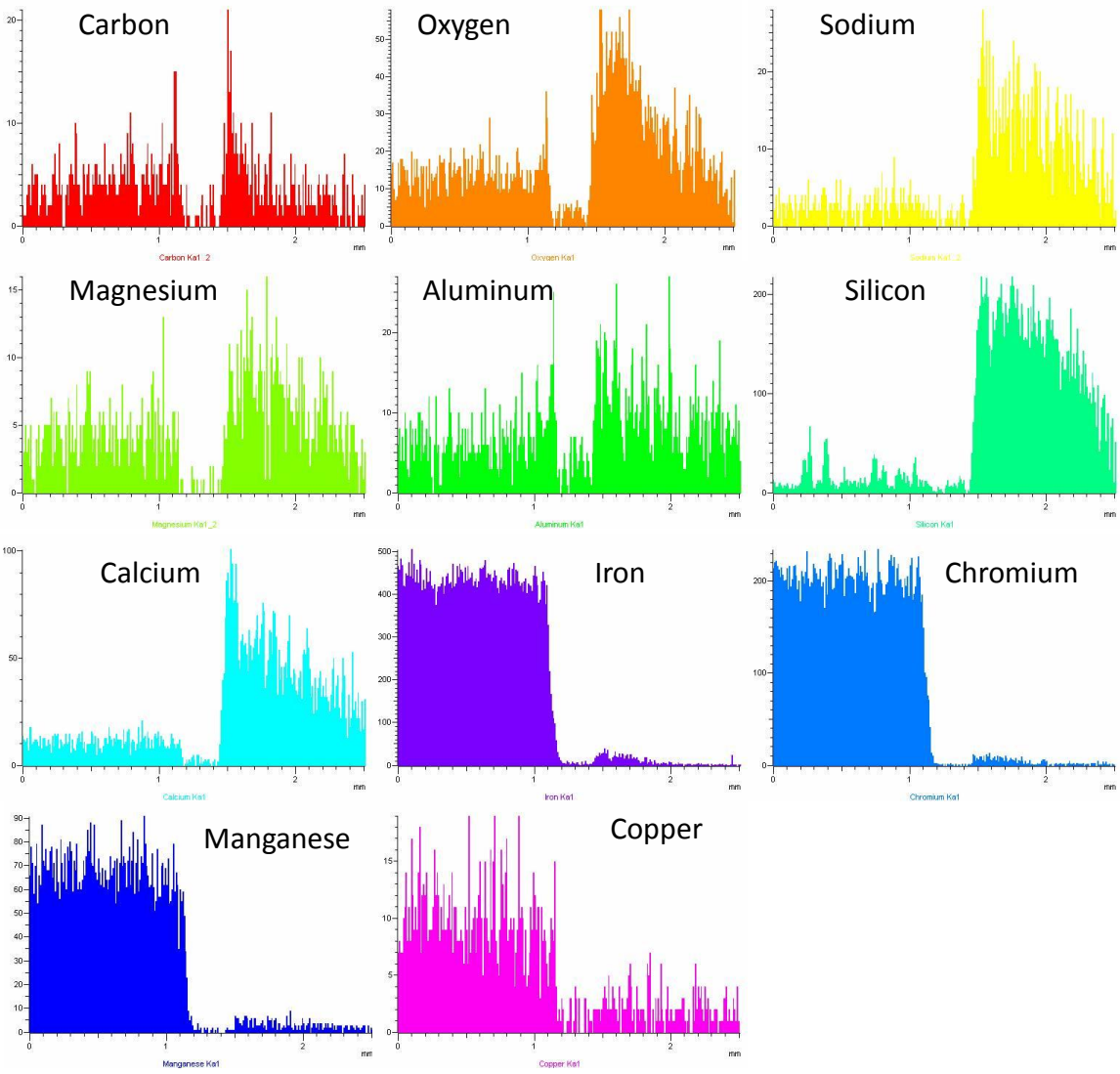

Fig. 4.114: Line profile spectrum across the cross-sectional area.

4.2.9. N-series glass and HSLA steel

Interaction of N-series glasses with HSLA steel at 900 °C was shown in Fig. 4.115. N-15 and N-10 glasses were formed a layer on the steel piece. But HSLA steel was heavily oxidized at 900 °C. As a result coating layer was detached from steel piece as shown in Fig. 4.116.

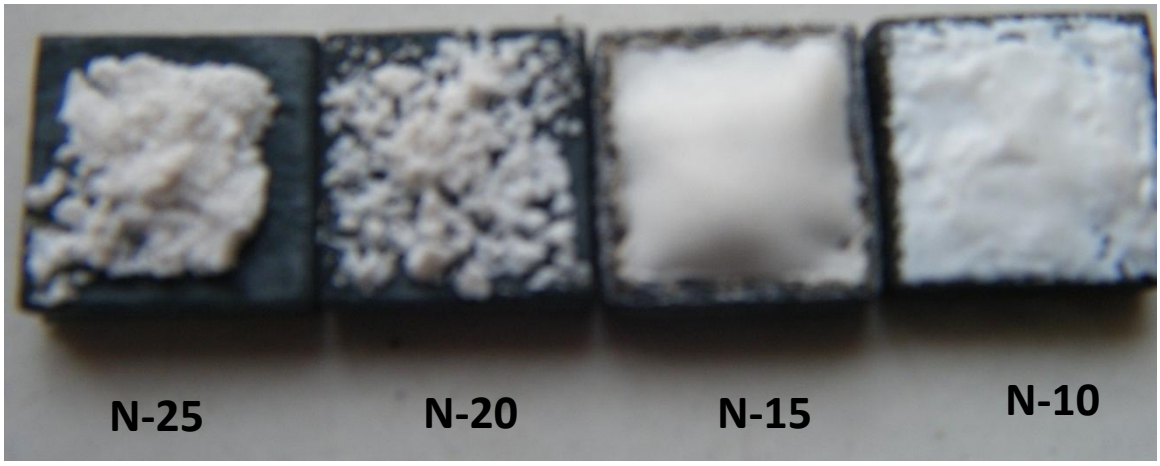

Fig. 4.115: Photographs of diffusion couple of HSLA steel with N-25, N-20, N-15 and N-10 glasses at 900 °C.

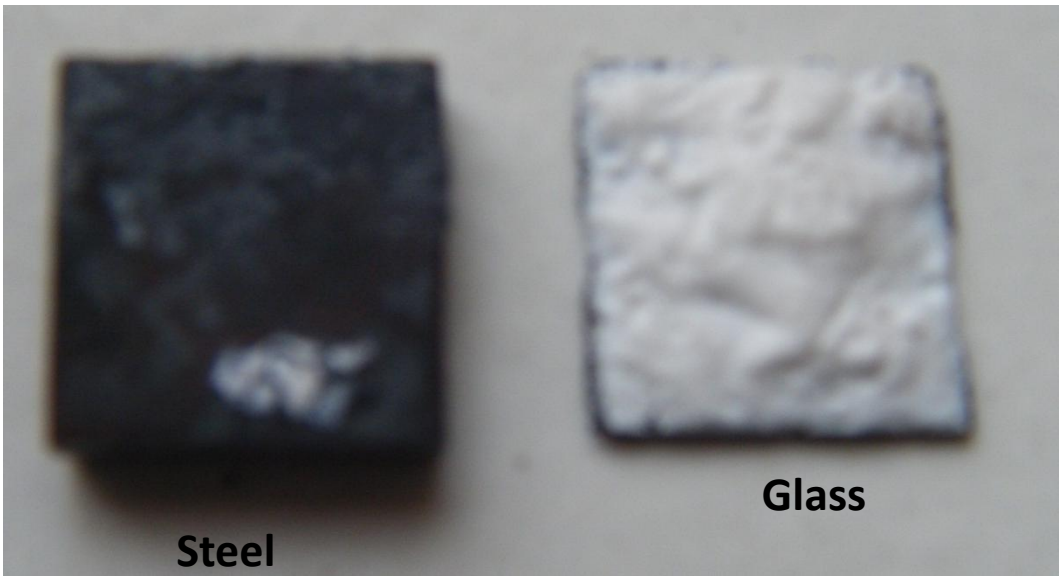

Fig. 4.116: Photograph of detached diffusion couple of HSLA steel with N-10 glass.

4.2.10. S glass and HSLA steel

The photograph of S glass with HSLA steel is shown in Fig. 4.117. As compared to previous coating of this glass has more white appearance. Some bubbles like structure appears in the coating.

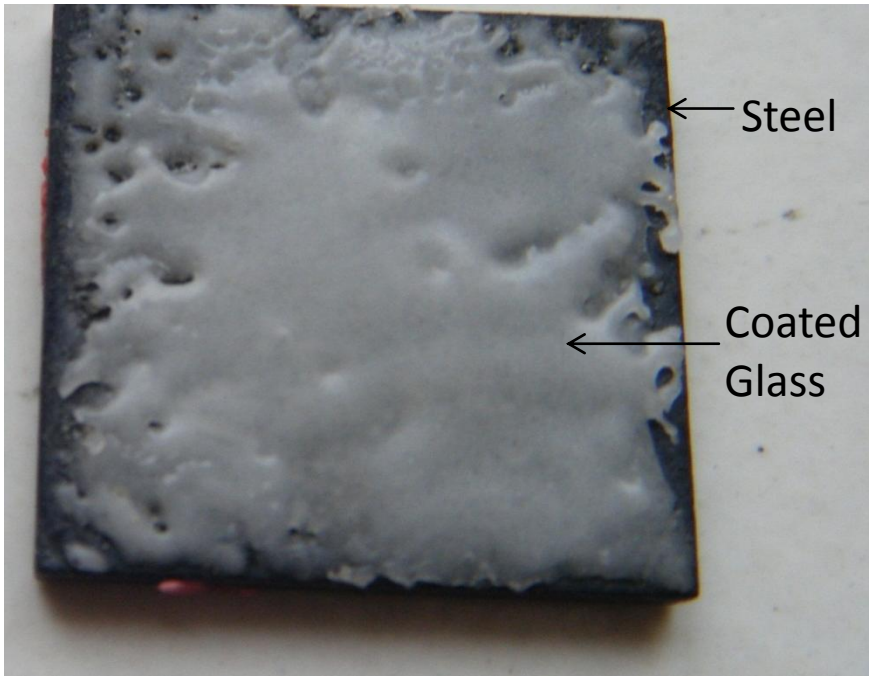

Fig. 4.117: Photograph of diffusion couple of S glass with HSLA steel.

The structural analysis of coating along with elemental analysis of this diffusion couple was done from the top layer of coating and from the interface.

4.2.10.1. Surface analysis

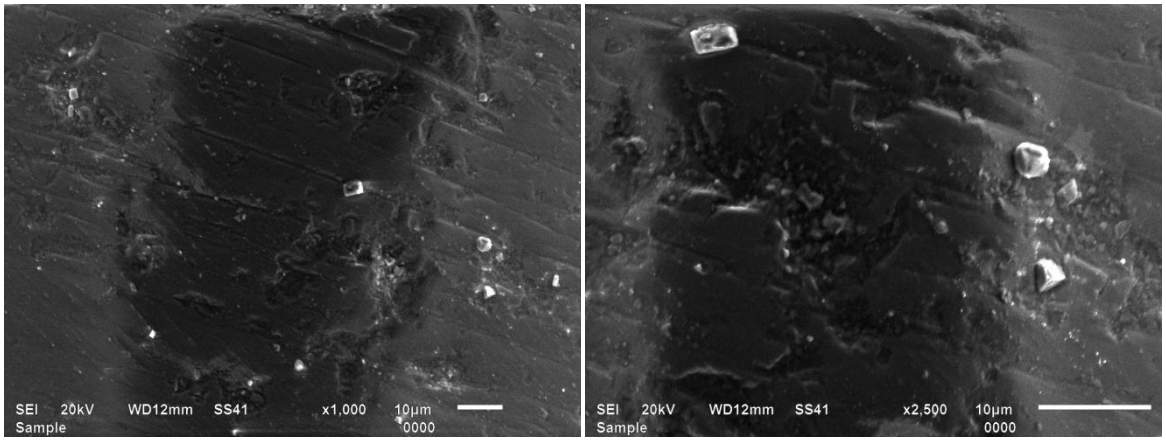

Fig. 4.118: Scanning electron micrographs of the S glass coating on HSLA steel.

Fig. 4.118 shows the micrographs of the S glass coating on HSLA steel at 700 °C for 1 h. In order to further quantify the nature of surface. Fig. 4.119 shows the surface morphology in BSE mode. The EDS spectrum of the top layer of glass was also taken with the elemental analysis to know the depth of diffusion.

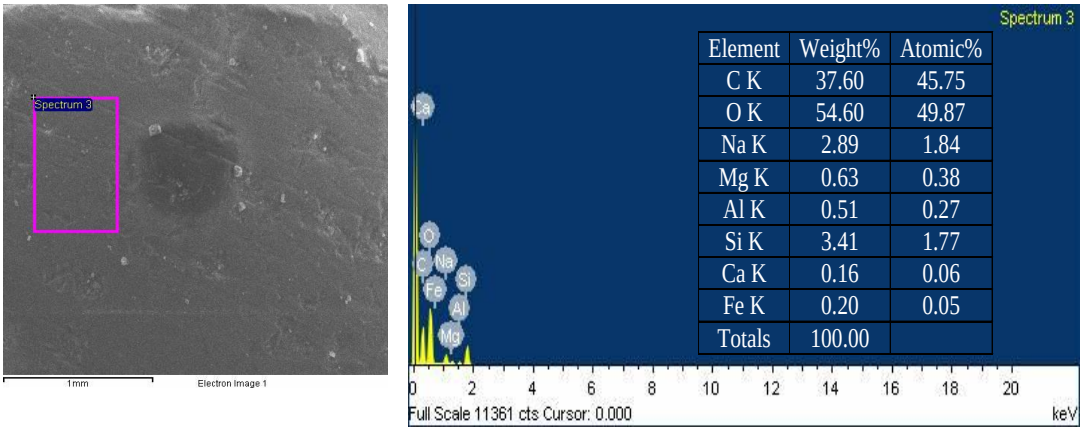

Fig. 4.119: Back scattered electron micrograph of the S glass coating on HSLA steel.

EDS analysis shows that all glass elements are present of on the top layer of coated glass. The presence of Fe element on the top layer of coated S glass clearly indicates the diffusion of it from the steel.

4.2.10.2. Analysis of interface

Cross-sectional microstructure of the interface between S glass and HSLA steel is shown in Fig. 4.120. The interface between glass and steel shows good adhesion. However, voids are observed along the steel side areas of the interface.

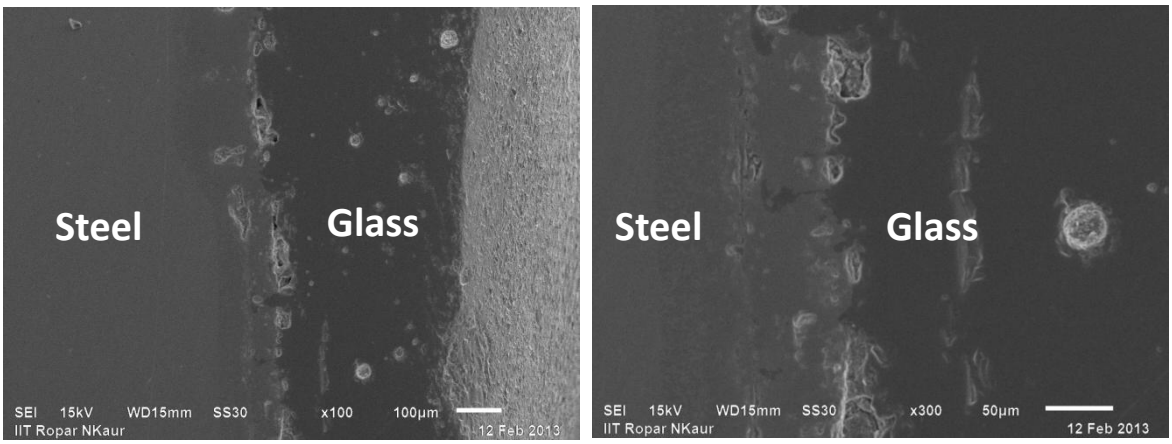

Fig. 4.120: SEM micrograph of interface between S glass with HSLA steel showing the overall view of interface.

The EDS analysis from the marked area was done to understand the diffusion of elements as shown in Fig. 4.121. As observed from the EDS analysis of glass coating (Fig. 4.121 (a)), only glass elements are present away from the interface. Analysis of Fig. 4.121 (b) has shown the presence of Si element in the steel side.

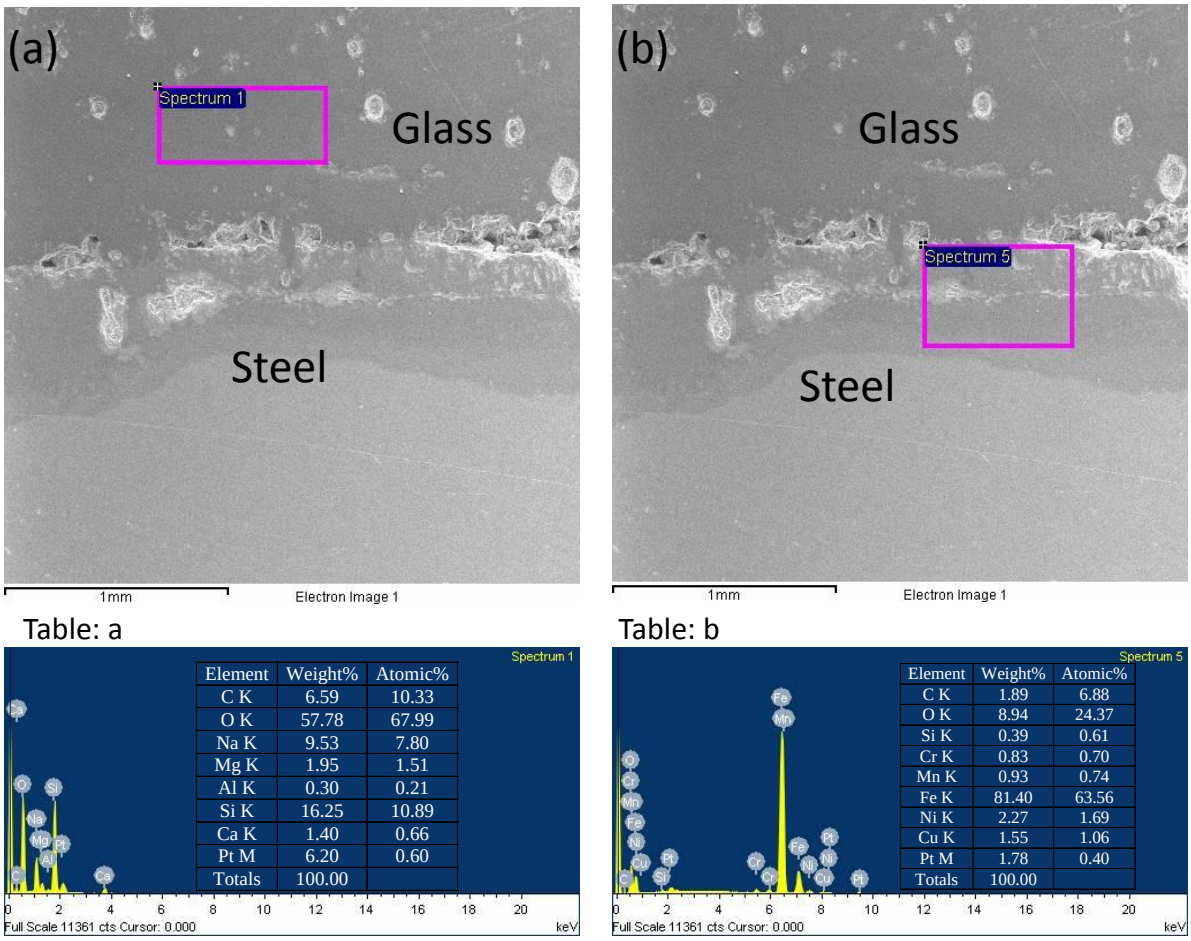

Fig. 4.121: Back scattered electron micrograph with EDS analysis of the area marked of the S glass coating on HSLA steel.

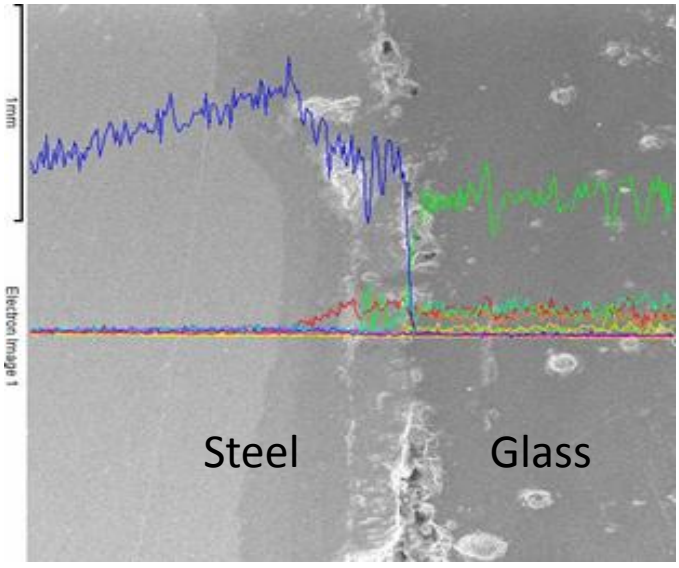

Fig. 4.122: Back scattered image of the cross-sectional area where yellow line is representative of line profile.

For further confirmation of the diffusion from steel to glass and vice-versa, line profile (yellow line in Fig. 4.122) along the interface was taken. The resultant spectrums of different elements

are shown in Fig. 4.123. These results showed that Fe, Cr and O are main elements which are present on the interface. A thick layer of Cr diffusion into the glass was also observed at this interface. Therefore, bonding at this interface could have taken place by diffusion of the chromium from steel joining with the glass. No other crystalline phase was observed. The results confirmed that appropriate wettability and flowability of glass were achieved by increasing the interfacial bonding [78-79]. Ni diffusion has also occurred along the interface between glass and steel which enhances the adhesion [76].

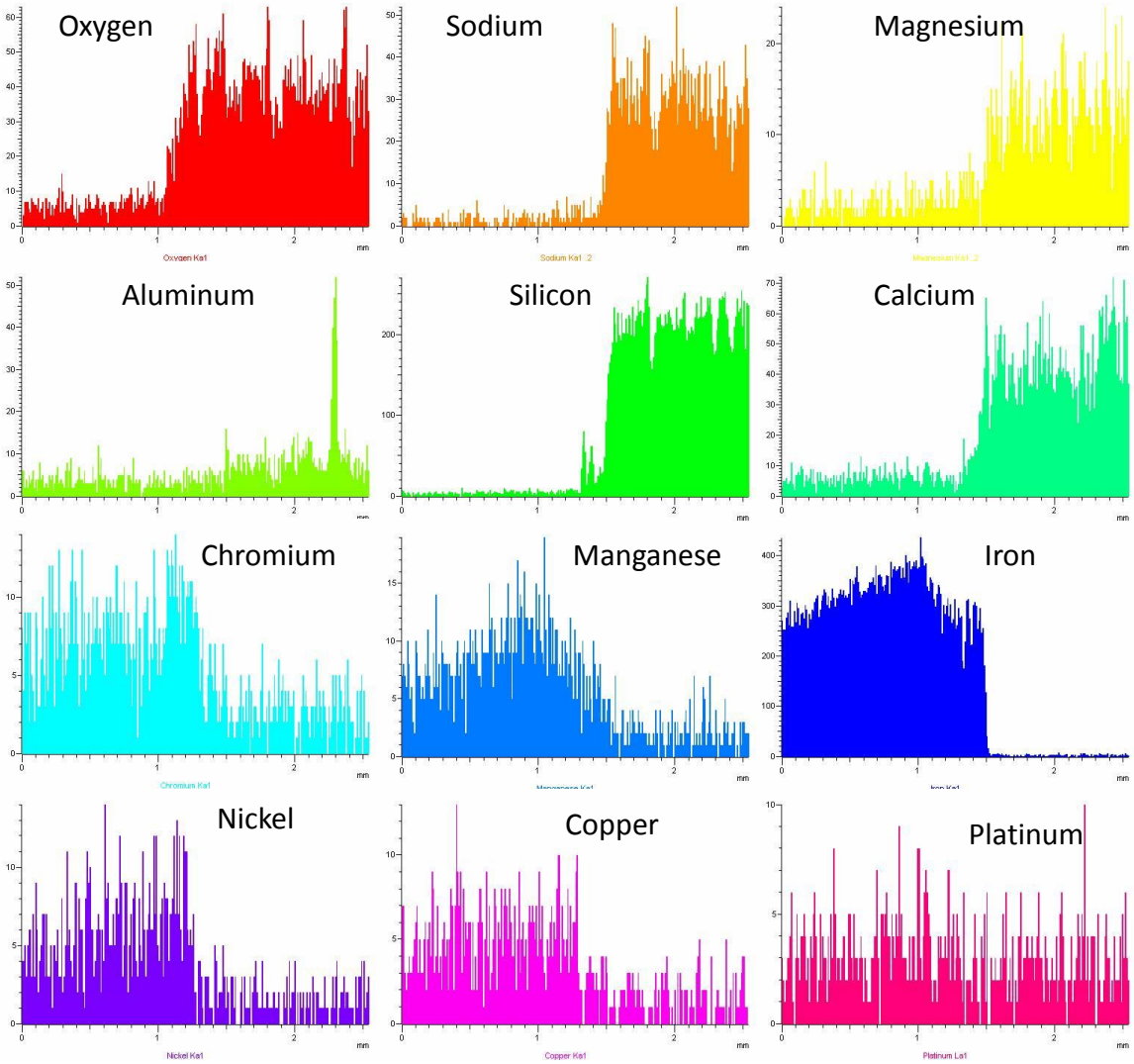

Fig. 4.123: Line profile across the cross-sectional area.

4.2.11. X glass and HSLA steel

The photograph of coated X glass on HSLA steel is presented in Fig. 4.124. Like earlier coating of this glass, it again shows amorphous state. The coating form drain like structures during glass melting at coating temperature.

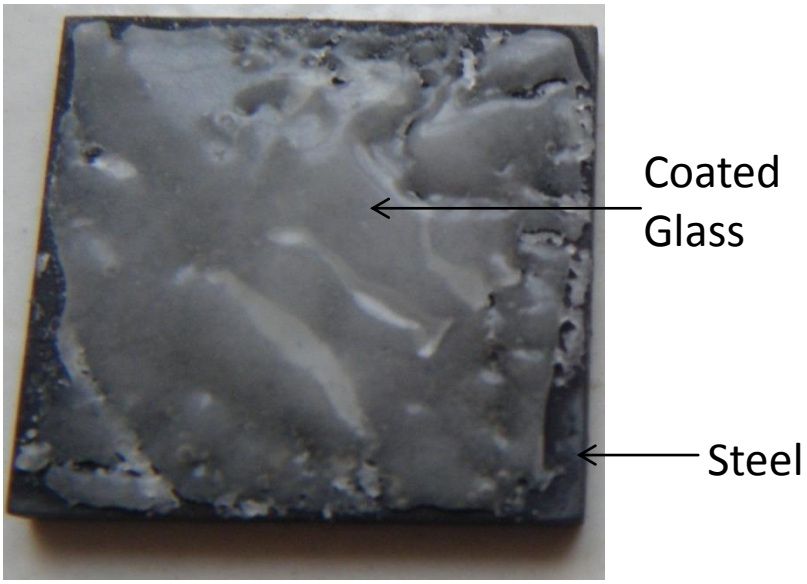

Fig. 4.124: Photograph of diffusion couple of X glass with HSLA steel.

The detailed microstructural study of coating was done scanning electron microscope with EDS from coated surface and from the interface.

4.2.11.1. Surface analysis

Fig. 4.125 shows the micrographs of the X glass coating on HSLA steel at 700 °C for 1 hr. Uniform glass structure was obtained after coating. In order to further quantify the nature of surface, the structure was observed in back scattered mode (BSE). Fig. 4.126 shows the surface morphology in BSE mode. The EDS spectrum of the top layer of glass was taken along with the elemental analysis to know the depth of diffusion.

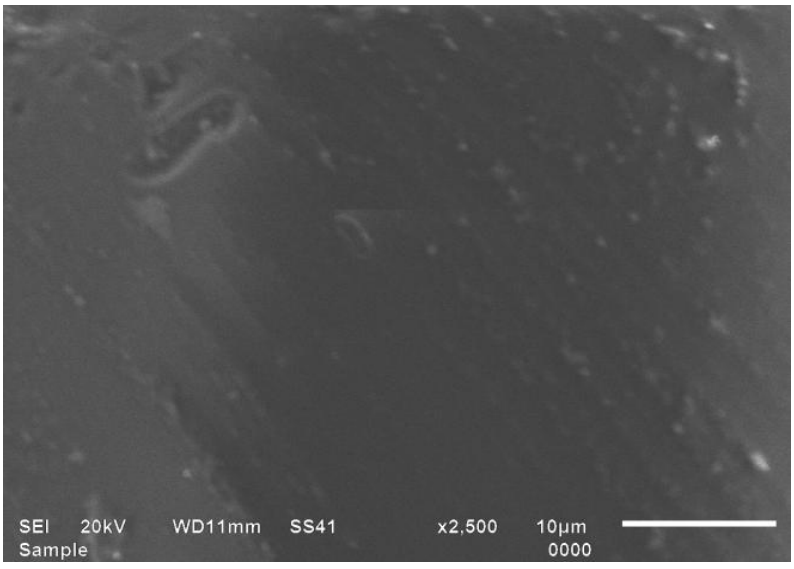

Fig. 4.125: Scanning electron micrograph of the X glass coating on HSLA steel.

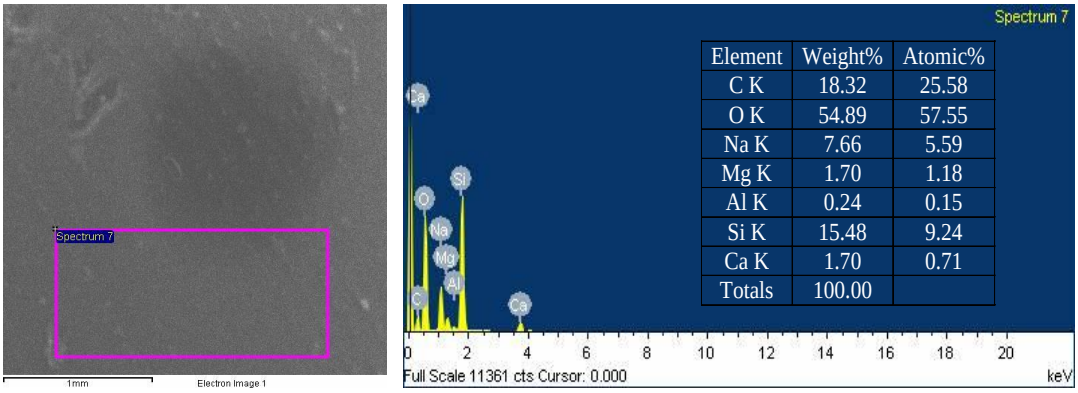

Fig. 4.126: Back scattered electron micrograph EDS analysis of the X glass coating on HSLA steel.

EDS analysis shows that all glass elements are present of on the top layer of coated glass. There is no element present on the top layer of coated X glass which has diffused from the steel.

4.2.1.1.2. Analysis of interface

Cross-sectional microstructure of the interface between X glass and HSLA steel is shown in Fig. 4.127. The interface between glass and steel shows good adhesion without any porosity at the areas of the interface. Glass has flowed to fill the pores and formed layers [80]. The layer of glass near the interface is more compact and dense as shown in Fig. 4.127. Moreover, a clear interface is seen which containing porosity.

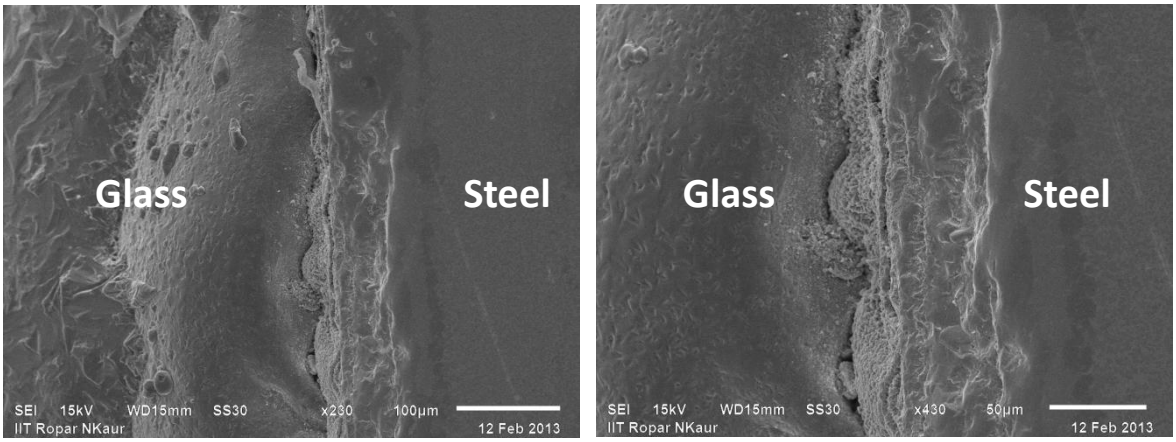

Fig. 4.127: SEM micrograph of interface between X glass and HSLA steel showing the overall view of interface.

The EDS analysis marked as square was done to understand the diffusion of elements as shown in Fig. 4.128. As observed from the EDS analysis of surface, Cr has not diffused and Fe diffusion from steel side into glass is very low. Fig. 4.128 (a) shows the presence of all glass elements. Table (b) taken from Fig. 4.128 (b) shows that Si element diffuses from glass into steel matrix.

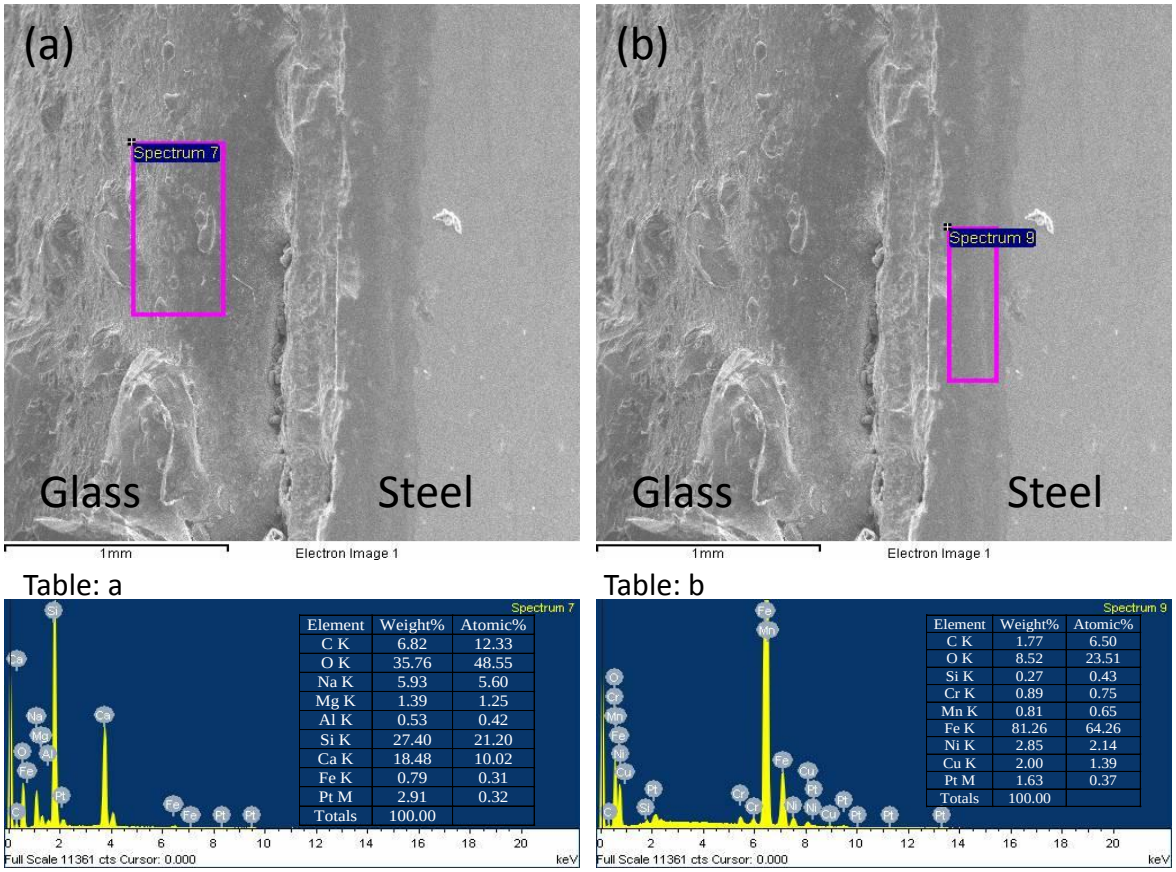

Fig. 4.128: Back scattered electron micrograph with EDS analysis of the area marked of the X glass coating on HSLA steel.

For further confirmation of the diffusion from steel to glass and vice-versa, line profile (yellow line in Fig. 4.129) along the interface was taken.

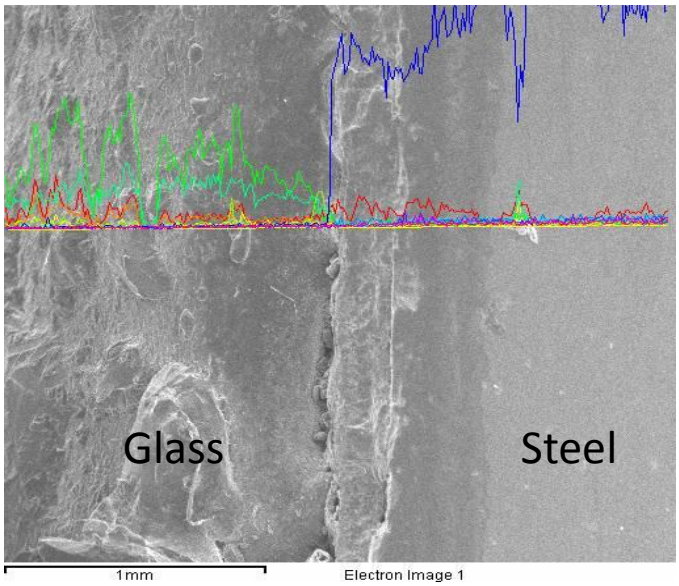

Fig. 4.129: Back scattered image of the cross-sectional area where yellow line is representative of line profile.

The results of line spectrum profile (Fig. 4.130) confirmed the formation of interfacial bond between steel and glass by diffusion of the elements. Diffusion of Ni, Fe, Cr, Cu and Mn has occured from steel side into glass elements. Ribbon shaped phase layer in steel was generated due to diffusion of Na from glass into steel matrix [81].

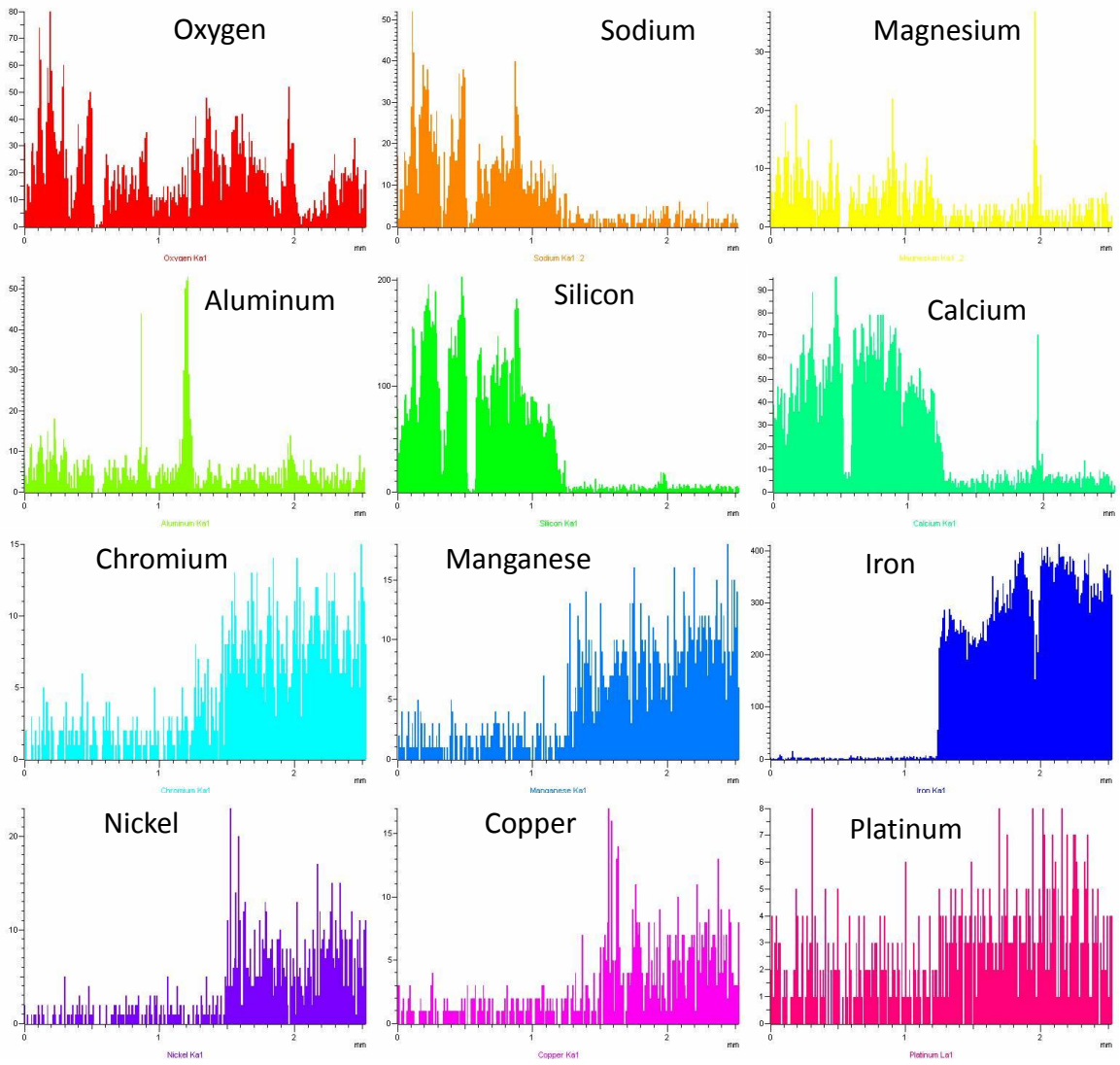

Fig. 4.130: Line profile spectrum across the cross-sectional area.

4.3. Corrosion tests

4.3.1. Corrosion analysis of glasses

Study of reactions on glass surfaces in different aqueous solutions to select a better engineering design parameter is important from industrial point of view. To accomplish this goal, one gram of small kinks of glasses of 2 to 3 mm size were dipped in 50 ml solutions for 745 h in distilled water and artificial seawater. Various techniques were used to analyze the chemical changes that occur on the glass surfaces during exposure. After the exposure, these glasses were characterized by different techniques. The detail results and discussion below.

4.3.1.1. XRD analysis

Powders of dipped glasses were examined by XRD. The X-ray diffraction patterns of the pristine glasses and solution dipped glasses are shown in Fig. 4.131.

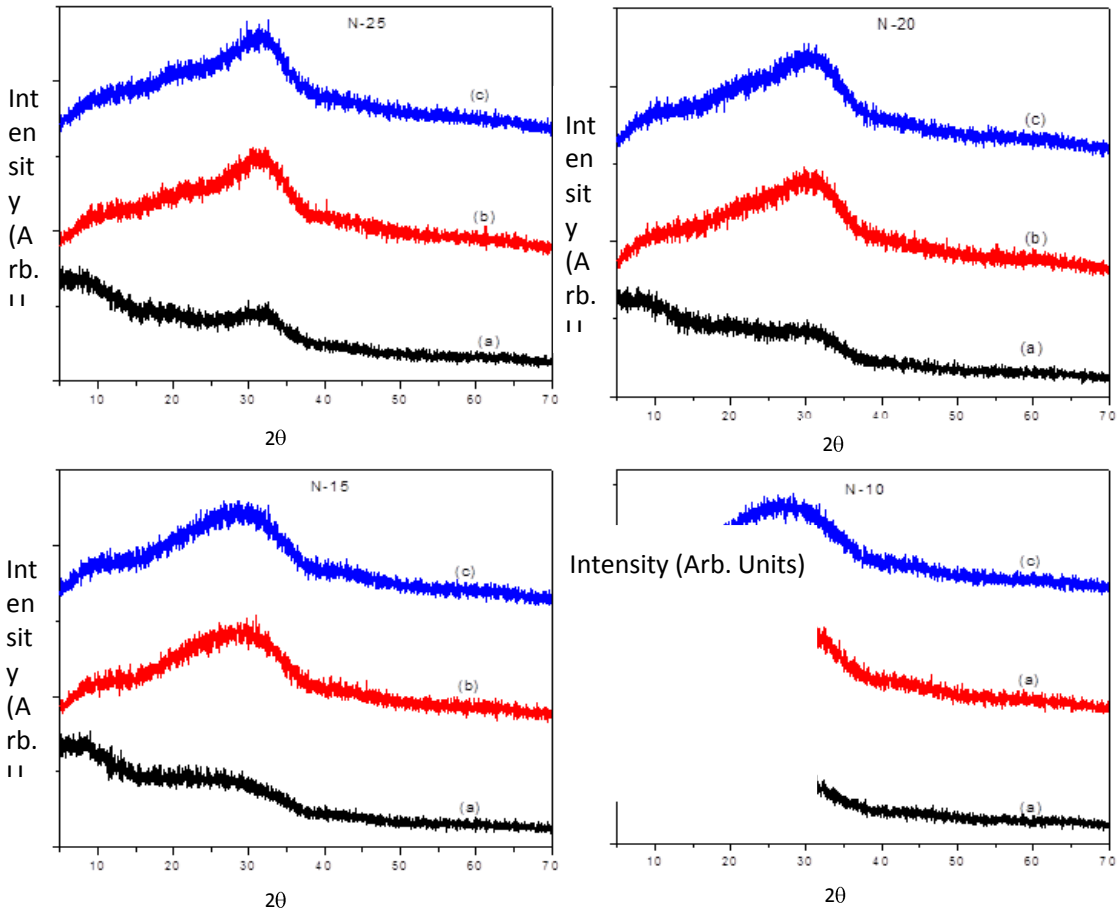

Fig. 4.131: XRD patterns of (a) pristine glass, (b) dipped in distilled water and (c) dipped in artificial seawater for 745 h.

The dissolution of sodium from the glass network has taken place which is indicated by absence of broad hump around 10 ° [82]. The hump around 30 ° is broad in distilled water as compared to

artificial seawater. This indicates that glass corrosion is controlled by a protective effect of the gel layer in distilled water [83]. Very small kinks are observed in the pattern of N-25 and N-20 glasses dipped in artificial seawater which indicates that the initiation of the crystallinity of glass due to corrosion may start. There is no crystalline peak observed in the patterns of N-15 and N-10 which indicates that the networks of these glasses are stable.

4.3.1.2. Investigation of FTIR

The powder of exposed glass kinks were analyzed using FTIR. It was observed that the spectrum as a whole is divided into two sections. The first one comprises of the sharp and distinct peaks showing characteristic absorption bands extending in the mid IR region from 400 to about 1400 cm^{-1} and the second part from 1400 and 4000 cm^{-1} reveals only small peaks, two peaks at about 1450 and 1640 cm^{-1} and two other small peaks at about 2840 and 2950 cm^{-1} followed by a broad band within the far IR region centered at about 3480 cm^{-1}. Some of the spectra show an additional small band around 2400 cm^{-1} [84-88]. The principle absorption frequencies usually observed in soda lime silicate glasses are identified as follows [84, 85, 89-93]:

1. Bands at 400–505 and 600 cm^{-1} are generally correlated with Si–O–Si and O–Si–O bending modes (Designated as 'A_1 and A_2').
2. Bands around 770–820 cm^{-1}, are attributed to Si–O–Si symmetric stretching of bridging oxygen between tetrahedra (Designated as 'B').
3. Bands around 970–1095 cm^{-1}, are related to Si–O–Si anti-symmetric stretching of bridging oxygen within the tetrahedra (Designated as 'C').

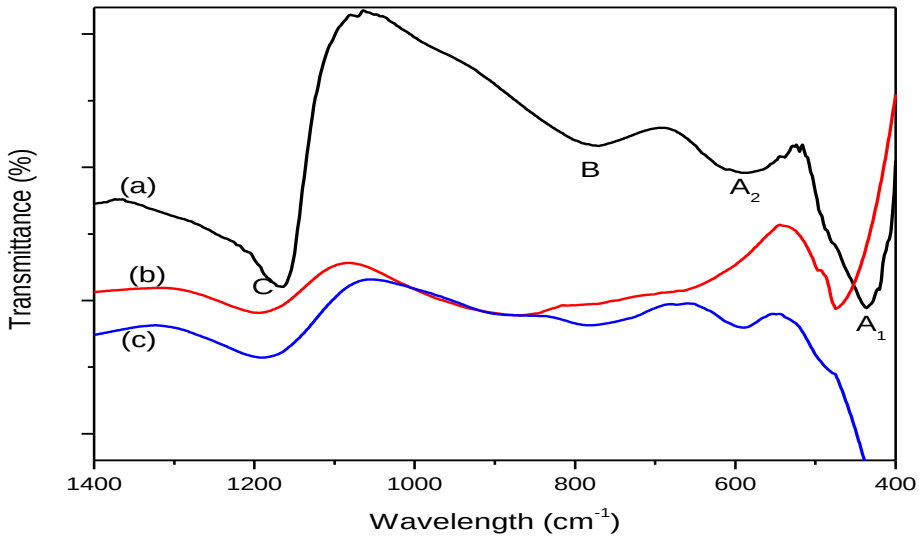

Fig. 4.132: FTIR spectra of (a) N-25 glass, (b) N-25 in distilled water and (c) N-25 in artificial seawater for 745 h.

In Fig. 4.132, the transmittance of C band decreases more in artificial seawater as compared to distilled water which indicates the leaching of silica content from the N-25 glass sample. Concurrently, the transmittance of B band also decreases in both solutions. These results state that corrosion of N-25 glass occurs in both solutions but it is maximum in artificial seawater.

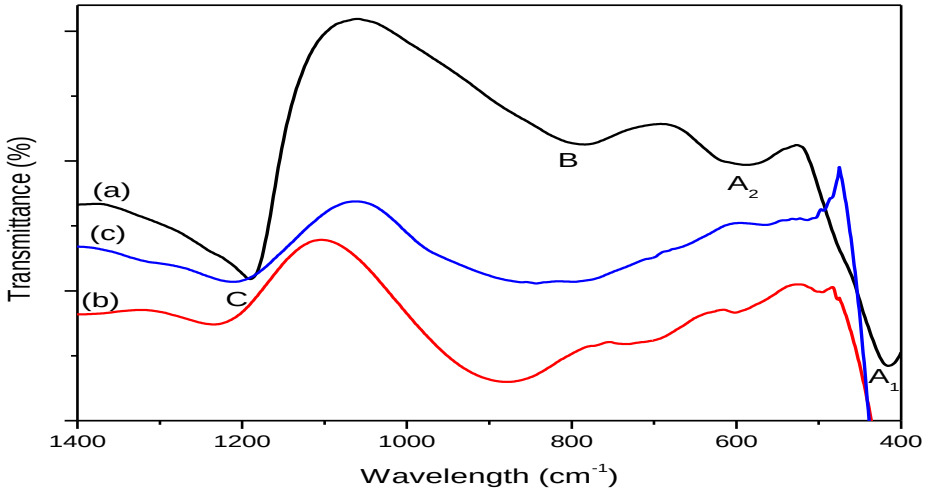

Fig. 4.133: FTIR spectra of (a) N-20 glass, (b) N-20 in distilled water and (c) N-20 in artificial seawater for 745 h.

In Fig. 4.133, the transmittance of B and C bands decrease more in distilled water as compared to artificial seawater. The C band shows almost same transmittance in the seawater. These results indicate that N-20 glass undergoes less corrosion in the artificial seawater as compared to distilled water.

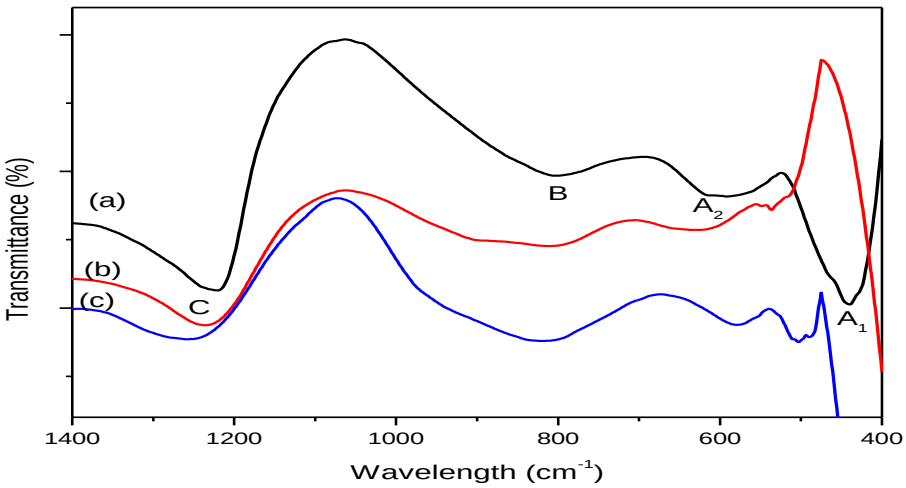

Fig. 4.134: FTIR spectra of (a) N-15 glass, (b) N-15 in distilled water and (c) N-15 in artificial seawater for 745 h.

In Fig. 4.134, the transmittance of C band is almost same in both artificial seawater and distilled water. However, the transmittance of other bands decreases in artificial seawater. It indicates that leaching of alkali ions are more prominent phenomenon than the dissolution of silica network in the N-15 glass network.

In Fig. 4.135, the transmittance of C band decreases from the spectrum of the pristine glass in distilled water. But the transmittance of C band increases from the spectrum of the pristine glass in artificial seawater. This change can be attributed to the formation of protective gel layer consisting of silanol group in the artificial seawater.

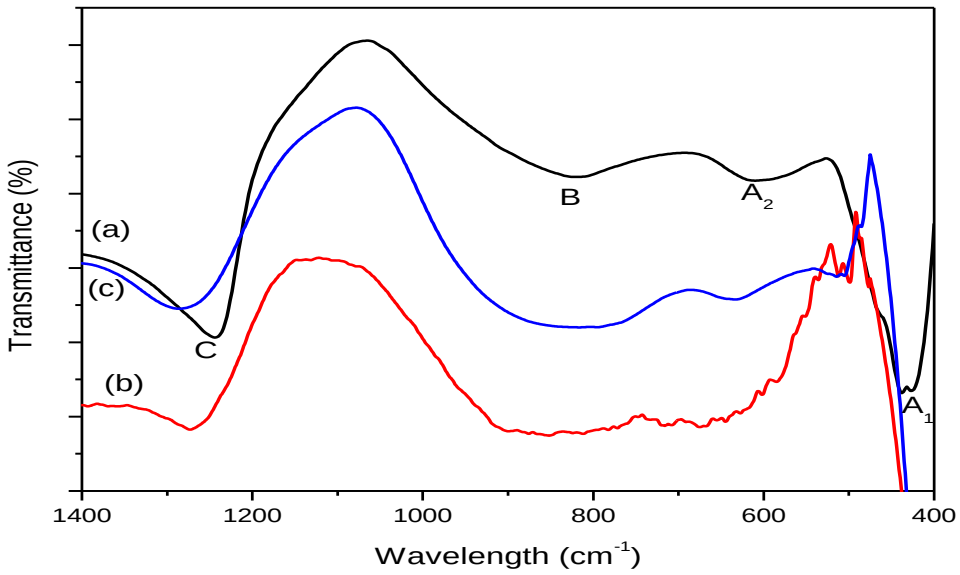

Fig. 4.135: FTIR spectra of (a) N-10 glass, (b) N-10 in distilled water and (c) N-10 in artificial seawater for 745 h.

The non-bridging silicon-oxygen associated with alkali ions namely A_1 and A_2 bands is observed to decrease in all glasses. Appearance of peak at around 900 cm^{-1} in N-15 and N-10 glasses was due to the silicon non-bridging oxygen vibration associated with bonded hydrogen ions in a polymerized gel structure [94]. All of the above changes are expected due to the leaching of alkali ions and increasing the concentration of silica content [95]. The transmittance of A_1 and A_2 band are large in the N-15 glass which leads to the result that N-15 glass is most corrosion resistive glass.

Regarding the other absorption bands in the region 1400–4000 cm^{-1} shown in Fig. 4.136, different authors have correlated the observed bands as follows [96-98]:

1. Band at 1460 cm^{-1}, is related to carbonate groups.
2. Band at 1640 cm^{-1}, can be related to molecular water or hydroxyl related band.
3. Bands around 2800–2980 cm^{-1}, are attributed to asymmetric and symmetric stretching modes of interstitial H_2O molecules.
4. Bands around 3400–3500 cm^{-1}, are due to molecular water.
5. Bands around 3600–3950 cm^{-1}, are attributed to different stretching modes of silanol Si(OH) groups.

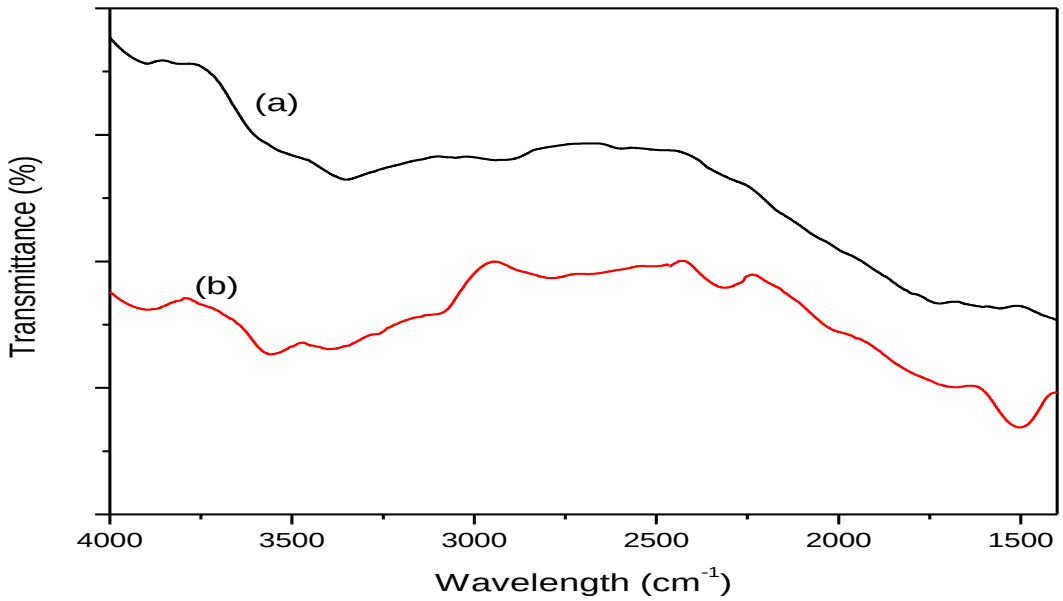

Fig. 4.136: FTIR spectra of (a) N-15 in distilled water and (b) N-15 in artificial seawater for 745 h from 1400-4000 cm^{-1}.

4.3.1.3. ICPS analysis

Changes in the concentration of Si, Al, Ca, Na and Cl were measured by inductively coupled plasma after the removal of the glass samples from solutions. The obtained results of concentration of Si, Al, Ca, Na and Cl in distilled water after 745 h are given in Fig. 4.137 and Fig. 4.138 for all glasses.

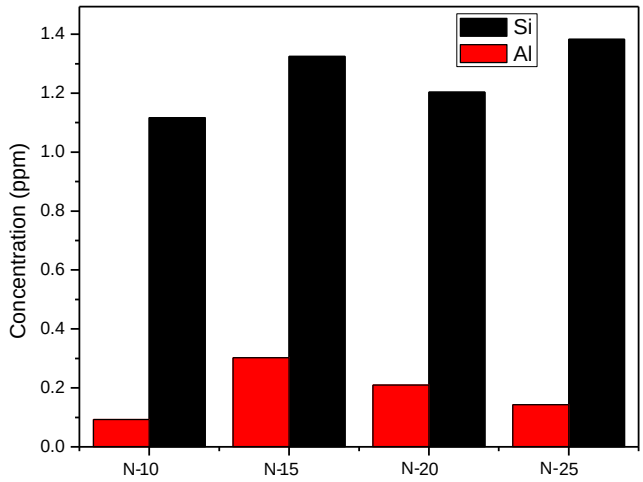

Fig. 4.137: The graphical representation of concentration of Si and Al with respect to glasses in distilled water after 745 h.

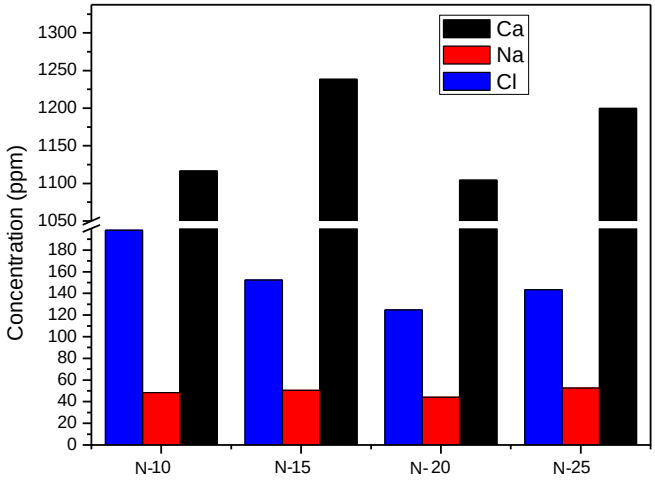

Fig. 4.138: The graphical representation of concentration of Ca, Na and Cl with respect to glasses in distilled water after 745 h.

From the above bar graphs, we can say that Si dissolved maximum in the case of N-25 glass. Al and Ca dissolved maximum from N-15 glass. Na concentration seems to be of similar level in all solutions. Concentration of Cl is maximum in the glass of N-10 solution that means Cl ions penetrate minimum in the N-10 glass network. Hench [99] reported the time-dependent changes of a single-phase amorphous or glassy material which involve the release of alkali ions in the surrounding fluid and the loss of soluble silica to the solution, resulting from the breaking of Si-

O-Si bonds and the formation of Si-OH (silanols) at the glassy solution interface. Overall analysis reveals that N-10 glass seems to be most stable as compared to other compositions due to less alkali ion concentration. In another set of experiment, the glass pieces were kept for 745 h in artificial seawater. Fig. 4.139 and Fig. 4.140 show the results of ions concentration in the solution for all glasses.

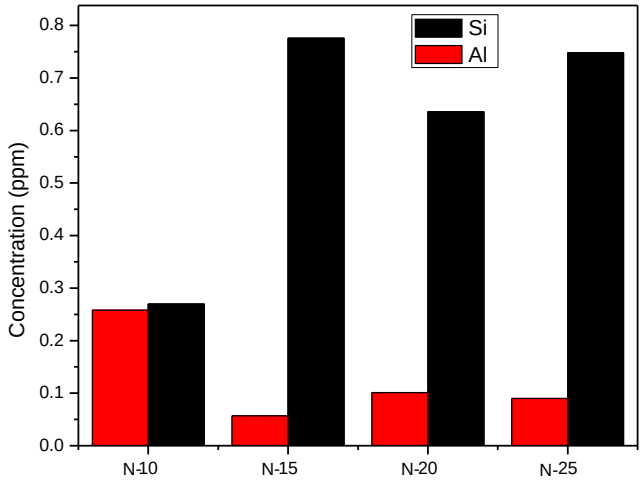

Fig. 4.139: The graphical representation of concentration of Si and Al with respect to glasses in artificial seawater after 745 h.

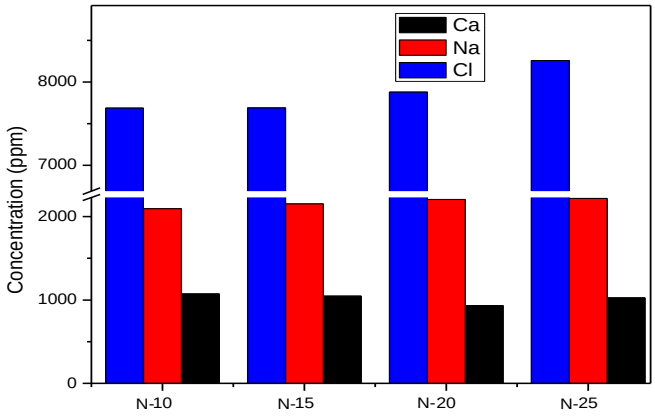

Fig. 4.140: The graphical representation of concentration of Ca, Na and Cl with respect to glasses in artificial seawater after 745 h.

From Fig. 4.139, we observed that Si ions from N-15 and N-25 glasses dissolved faster as compared to other compositions. Al ions showed opposite trend in seawater i.e. Al ions dissolved maximum from N-10 glass network. Ca ions concentration is minimum in N-20 glass solution as shown in Fig. 4.140. Na ions concentration is almost same in all cases. Cl ions concentration is

maximum N-25 glass. Again N-10 glass shows opposite results to distilled water i.e. Cl ions concentration is minimum in N-10 glass solution. These results of N-10 glass are not to the tune of observed behavior as it has strongest network. In order to confirm the results further for the stability of glass network, each glass pieces were dipped for 1490 h in artificial seawater. The results of 1490 h study are given in the Fig. 4.141 and Fig. 4.142.

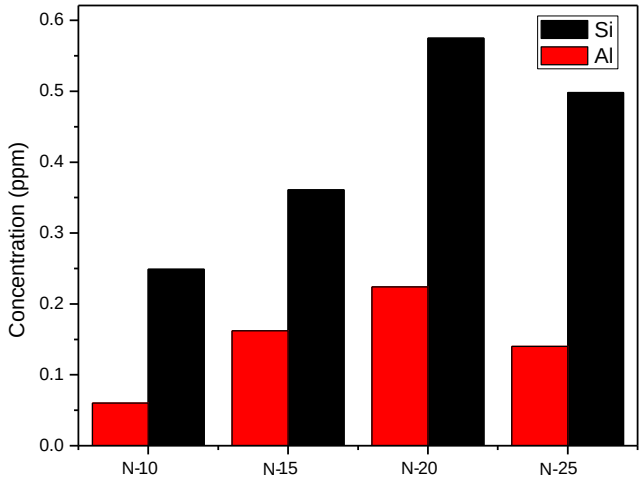

Fig. 4.141: The graphical representation of concentration of Si and Al with respect to glasses in artificial seawater after 1490 h.

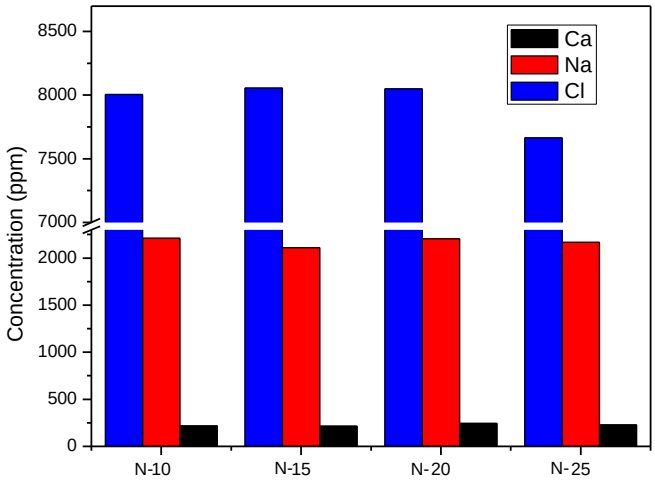

Fig. 4.142: The graphical representation of concentration of Ca, Na and Cl with respect to glasses in artificial seawater after 1490 h.

Silicon ions concentration shows drastic change in the N-15 glass solution and becomes maximum in the N-20 glass solution as shown in the Fig. 4.141. Also Al ions concentration is maximum in the N-20 glass solution. Dissolved ion concentrations of Na and Ca ions are minimum in the N-15 glass solution as presented in Fig. 4.142. Also the concentration of Cl ions is maximum in the N-15 glass solution. Thus, we can say that N-15 glass is most stable in the artificial seawater as compared to other glasses.

4.3.1.4. Electrochemical tests of N-series glasses

In order to confirm the corrosion resistant nature of glasses, pieces of glasses have been tested for electrochemical measurements by taking artificial seawater as electrolyte. From open circuit potential (OCP) measurements, the following data could be obtained in 3.5 % NaCl solution. The OCP values of N-25, N-20, N-15 and N-10 glasses are -0.361 ± 0.002, -0.243 ± 0.0005, -0.675 ± 0.005 and -0.16 ± 0.001 V, respectively for the same time period under similar conditions.

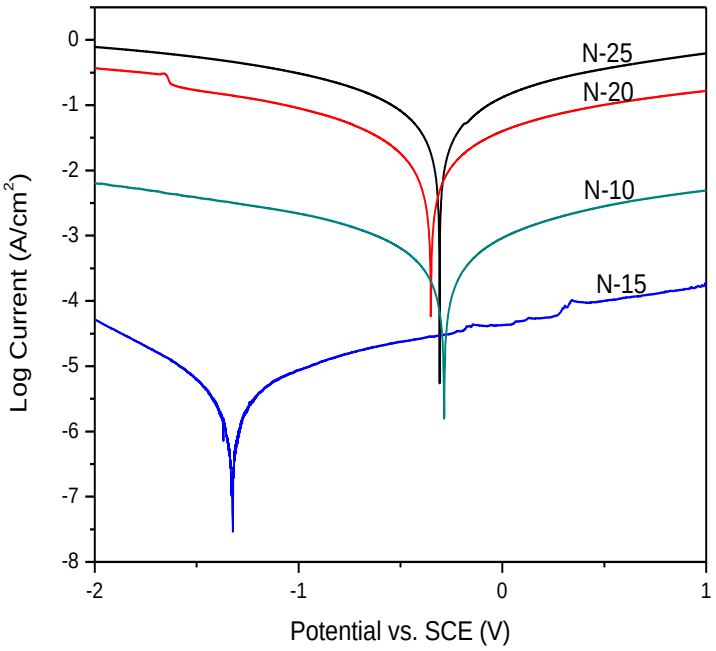

Fig. 4.143: Potentiodynamic polarization curves of N-10, N-15, N-20 and N-25 glasses in artificial seawater.

Table 4.11: Results of potentiodynamic polarization in glass samples.

Specimen	E_{corr} (mV)	I_{corr} (μA cm^{-2})	β_c (mV/decade)	β_a (mV/decade)	R_p (Ω cm^2)	Corrosion rate (mm/year)
N-25	-312.3	20.8	307.3	334.1	0.23×10^4	0.136
N-20	-347.7	5.5	298.7	308.2	0.86×10^4	0.036
N-15	-1329.1	0.001	269.1	335.8	31.4×10^6	6.54×10^{-6}
N-10	-286.3	0.147	313.5	304	0.46×10^6	0.48×10^{-3}

Fig. 4.143 presents the polarization curves for N-10, N-15, N-20 and N-25 glasses in artificial seawater. Using the Tafel extrapolation method, the corrosion potential E_{corr}, corrosion current density I_{corr}, anodic/cathodic Tafel slopes β_a and β_c and polarization resistance R_p values are calculated from polarization curves and are given in Table 4.11.

The value of I_{corr} and the corrosion rate is less for N-15 glass which suggests that N-15 glass is most stable glass as compared to other compositions. Thus the results of electrochemical tests again confirm the obtained results from FTIR and ICP. The impedance spectra of N-25, N-20, N-15 and N-10 glasses are presented in Fig. 4.144.

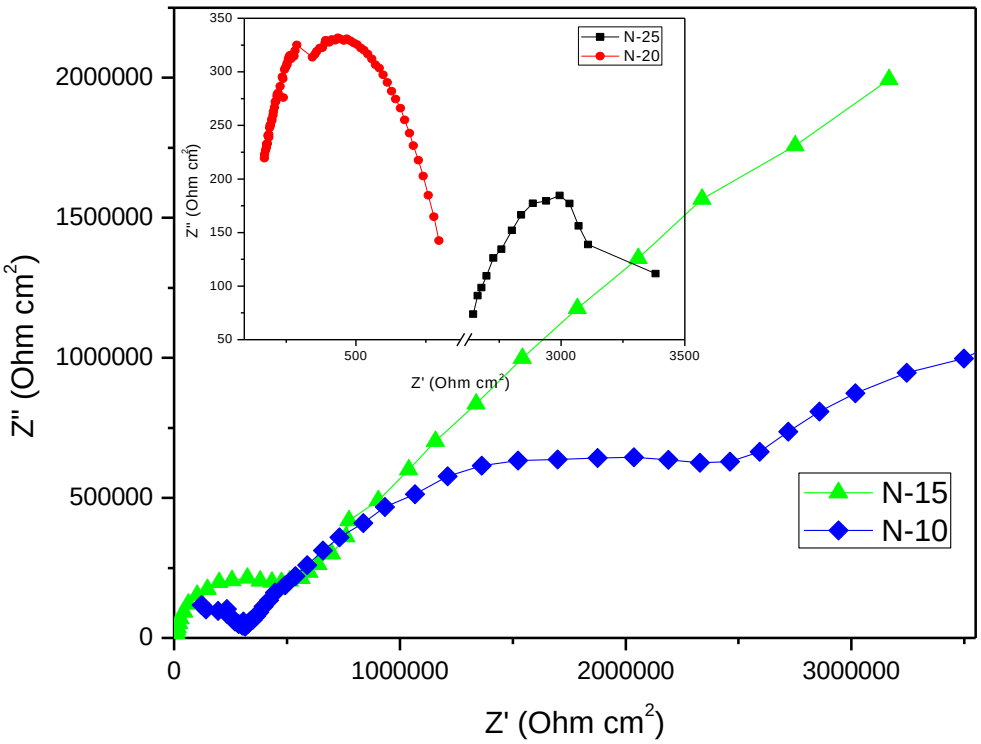

Fig. 4.144: Nyquist plots of N-25, N-20, N-15 and N-10 glasses in artificial seawater.

From Nyquist plots, the diameter of the semicircle for N-15 glass is largest than other glasses which indicates the better suitability of N-15 glass for corrosion resistant coating [100]. The bode phase plots are shown in Fig. 4.145. All glasses showed capacitive behavior at high frequency region except N-15 glass. N-15 glass showed capacitive behavior at middle frequency region and its phase angle value is less as compared to others.

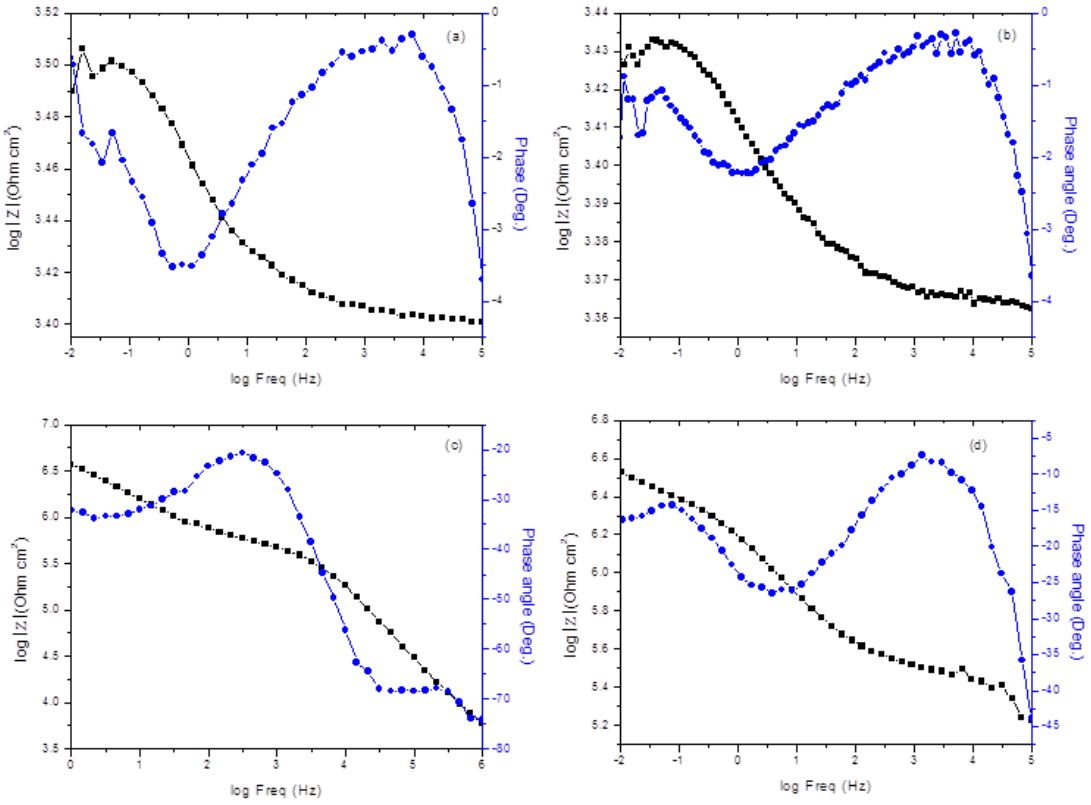

Fig. 4.145: Log Z versus log Freq. plots and phase angle (Z) versus log Freq. plots of (a) N-25 glass, (b) N-20 glass, (c) N-15 glass and (d) N-10 glass in artificial seawater respectively.

The fitting of electrochemical impedance data of the glass is obtained by using the $R_s(CPE_{dl}R_{ct})$ model [101], with one time constant as shown in Fig. 4.146. R_s is solution resistance, R_{ct} and CPE_{dl} are associated with the charge transfer process that occurs on the surface of the glass sample in the sea water.

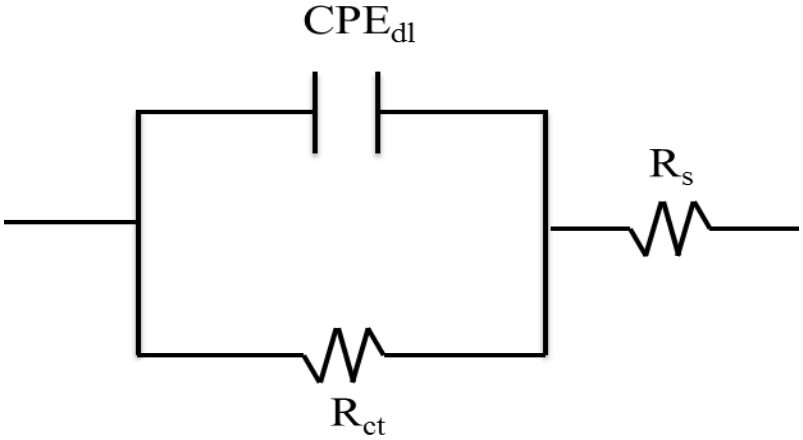

Fig. 4.146: Equivalent circuit for glass in artificial seawater.

The obtained impedance spectrum was analysed using a non-linear regression method, and the values of circuit parameters were estimated as given in Table 4.12.

Table 4.12: Electrochemical measurements of samples obtained by equivalent circuit.

Specimen	R_s (Ω cm^2)	R_{ct} (Ω cm^2)	CPE_{dl} (μF cm^{-2})	n_{dl}
N-25	23.16	360.9	0.47×10^{-3}	0.5
N-20	16.67	869.2	1.37×10^{-9}	0.83
N-15	15.51	9.51×10^{6}	42.5×10^{-9}	0.49
N-10	12.23	8.59×10^{6}	3.99×10^{-6}	0.27

R_{ct} values of N-10 and N-15 glasses show remarkable difference compared with N-20 and N-25 glasses. The second parameter CPE_{dl} is very less in case of N-15 glass which gives the proof of very low charge accumulation on the surface of the N-15 glass. The increase in R_{ct} value and the decrease in CPE_{dl} value of N-15 glasses indicate that N-15 glass is more corrosion resistive as compared to other compositions.

4.3.2. Corrosion study of steels

Steels are the most dependable structural materials under dynamic or flow conditions and virtually shows no corrosion even after very long exposures in different atmosphere. A diagrammatic representation of the processes involved in the corrosion of iron or steel under aqueous conditions is illustrated in Fig. 4.147. The region on the metal surface where ferrous ions are released by corrosion is called the anode. Electrons flow in the metal from these anodic sites to regions on the metal surface where reduction reactions take place. These sites are known as cathodes. The energy for this spontaneous corrosion reaction comes from the difference in potential between the anodic and cathodic reactions. The circuit is completed by ion movement in the electrolyte.

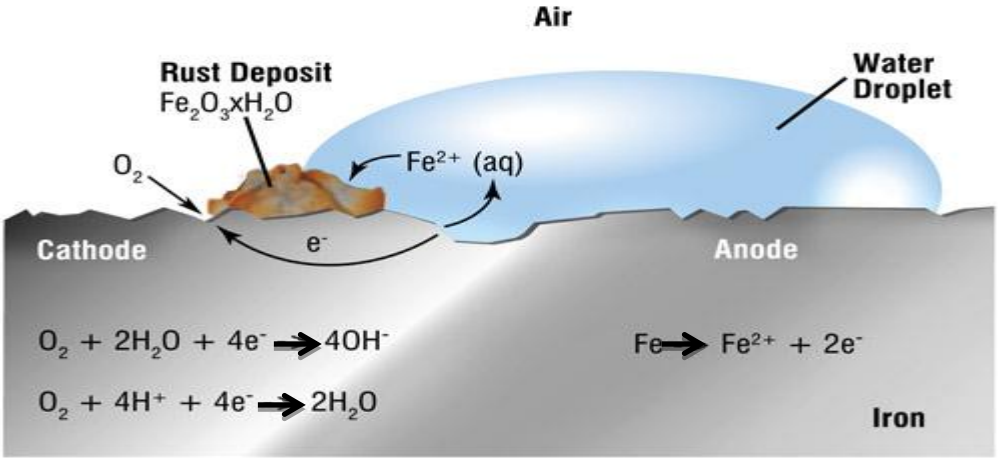

Fig. 4.147: Diagram illustrating the mechanism of corrosion in aqueous systems [102].

In the case of iron or steel the anodic reaction will be:

$$Fe \rightarrow Fe^{2+} + 2e^{-} \quad (4.22)$$

The cathodic reaction is a reduction process. There are two main reactions that may occur at the cathode during aqueous corrosion. Firstly, a process that consumes dissolved oxygen and generates hydroxyl ions,

$$O_2 + 2\,H_2O + 4e^{-} \rightarrow 4\,OH^{-} \quad (4.23)$$

and secondly; a process in which hydrogen gas is generated by the reduction of water when the potential becomes more negative:

$$2H_2O + 2e^{-} \rightarrow H_2 + 2\,OH^{-} \quad (4.24)$$

Corrosion products may appear in the form of deposits when the compounds that comprise these anodic and cathodic products react with each other, and this leads to the formation of ferrous hydroxide; given by the reaction:

$$Fe^{2+} + 2\,OH^{-} \rightarrow 2Fe\,(OH)_2 \quad (4.25)$$

The ferrous hydroxide may subsequently by oxidized to ferric oxide [Iron (III) oxide], which is the very familiar yellow-brown compound commonly known as rust. This reaction is as follows:

$$4Fe\,(OH)_2 + 2O_2 \rightarrow 2H_2O + 2Fe_2O_3.H_2O \quad (4.26)$$

However, these are subjected to localized corrosion in the presence of chloride ions and also under static or stagnant conditions. The pits also provide active crevices for a formidable corrosion attack [103].

4.3.2.1. Electrochemical tests

Electrochemical techniques are the principal tool for characterizing pitting corrosion. The pitting potential is a fundamental parameter in evaluating the susceptibility of different materials in different environment to localized corrosion [104].

An open circuit potential (OCP) measurement was done for samples in 3.5% NaCl solution, immediately after immersion. The sample's potential was recorded using a SP300 Electrochemical Interface controlled by a desk-top computer over an initial time period of 2 hours after immersion. Fig. 4.148 shows the variation of potential data recorded for two hours for all the steels used in present work. The results indicate that the curve is showing positive potential with variation in time.

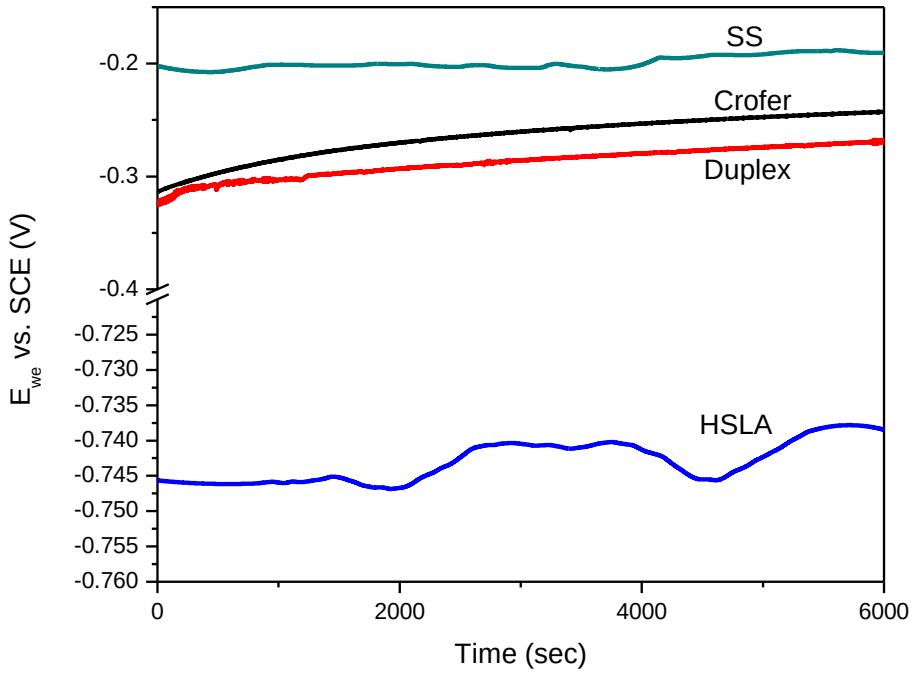

Fig. 4.148: Plots of potential/time measurements for various steels in 3.5% NaCl solution.

From Fig. 4.148, it is clear that crofer, duplex and SS showed more positive potential as compared to HSLA steel. Chlorination of seawater is the normal practice to destroy microorganism or microbiological growth, the residual chlorine influences significantly on the corrosion behavior of materials. SS containing high alloy appears to have good resistance to residual chlorine as compared to HSLA steel [105]. Fig. 4.149 presents the polarization curves for crofer, duplex, HSLA and SS in artificial seawater. Using the Tafel extrapolation method, the corrosion potential E_{corr}, corrosion current density I_{corr}, anodic/cathodic Tafel slopes β_a and β_c and polarization resistance R_p values are calculated from polarization curves and are given in Table 4.13.

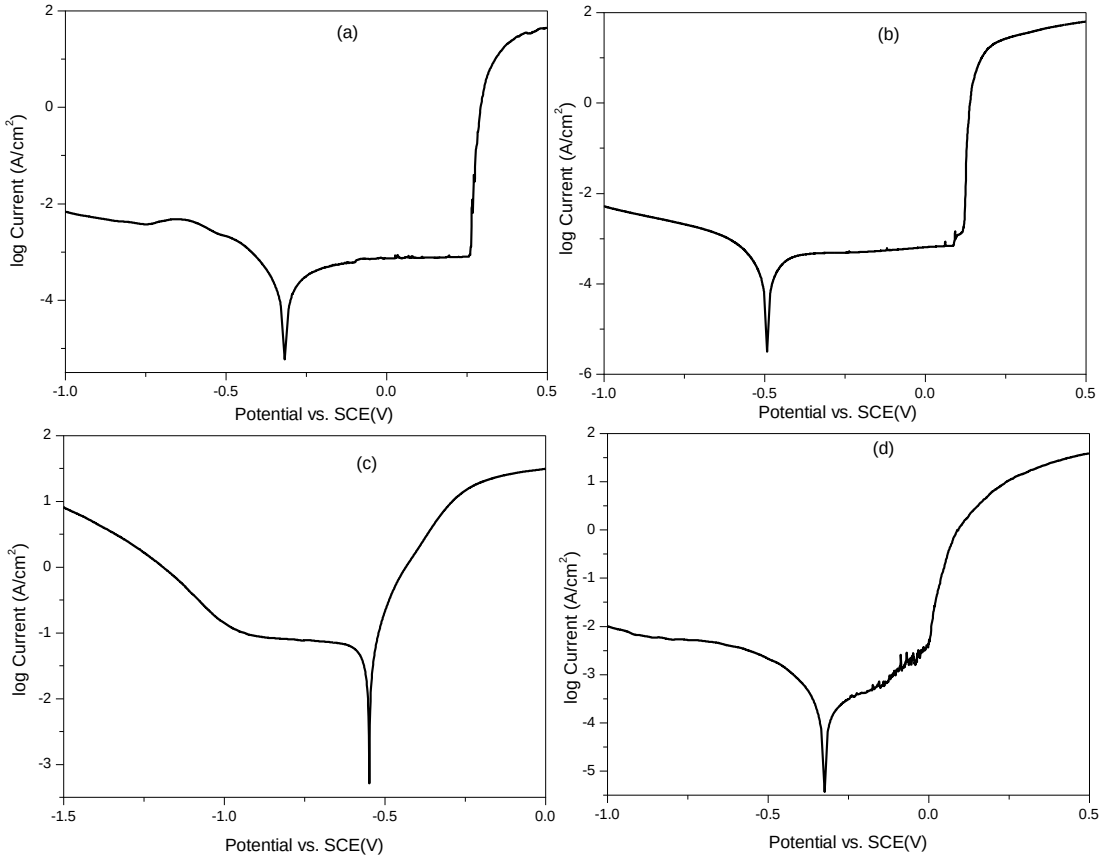

Fig. 4.149: Potentiodynamic polarization curves of (a) crofer, (b) duplex, (c) HSLA and (d) SS in artificial seawater.

Table 4.13: Results of potentiodynamic polarization in steel samples.

Specimen	E_{corr} (mV)	I_{corr} (μA cm^{-2})	β_c (mV/decade)	β_a (mV/decade)	R_p (Ω cm^2)	Corrosion rate (mm/year)
Crofer	-315.7	0.306	206.3	466.0	0.17×10^6	0.89×10^{-3}
Duplex	-491.1	0.232	211.4	371.0	0.19×10^6	0.47×10^{-3}
HSLA	-548.6	41.07	790.0	94.3	0.41×10^3	0.103
SS	-322.3	0.186	171.0	271.0	0.15×10^6	0.54×10^{-3}

The value of I_{corr} and the corrosion rate is less for duplex steel which suggests that duplex is less corroded in artificial seawater as compared to other steels.

The impedance spectra of crofer, duplex, HSLA and SS are presented in Fig. 4.150.

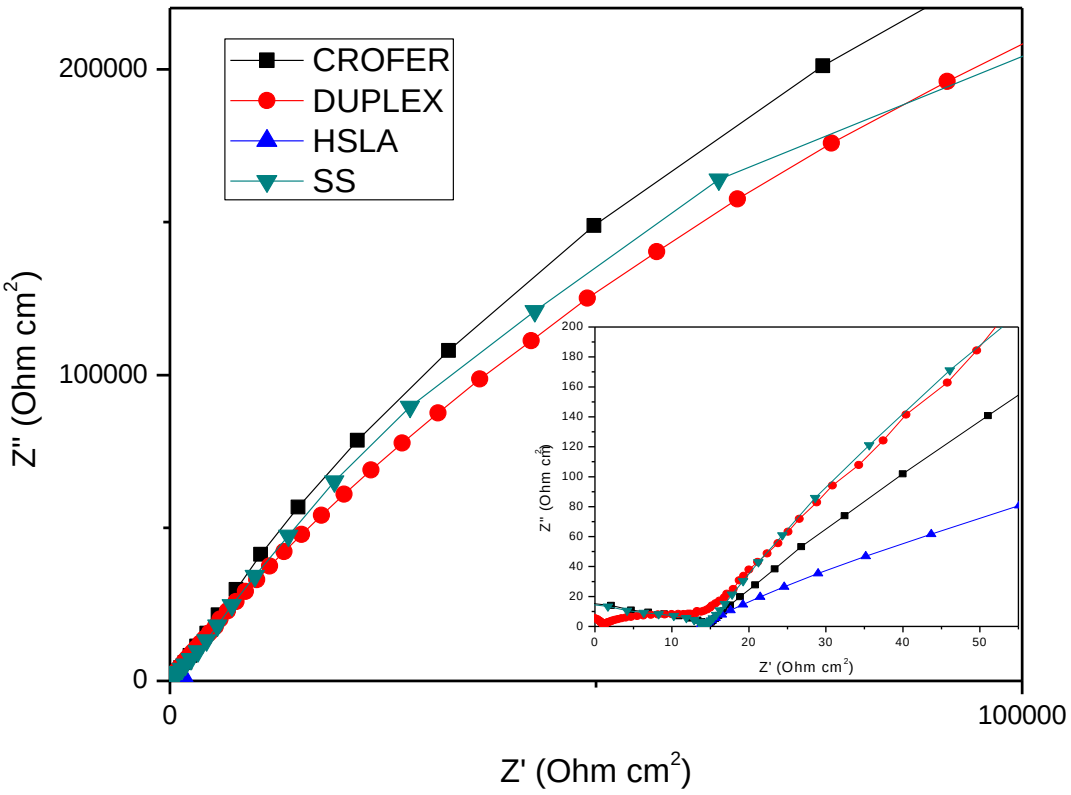

Fig. 4.150: Nyquist plots of crofer, duplex, HSLA and SS in artificial seawater.

From Nyquist plot (Fig. 4.150), the diameter of the semicircle for duplex steel is largest and for HSLA is lowest which indicates that duplex steel has lower corrosion rate as compared to others. The bode phase plots of steel samples are shown in Fig. 4.151. All steels showed capacitive behavior at higher frequency region [106]. HSLA steel showed less value of impedance and its phase angle value is highest among the steel samples which were again confirming the corrosive nature of this steel [107, 108].

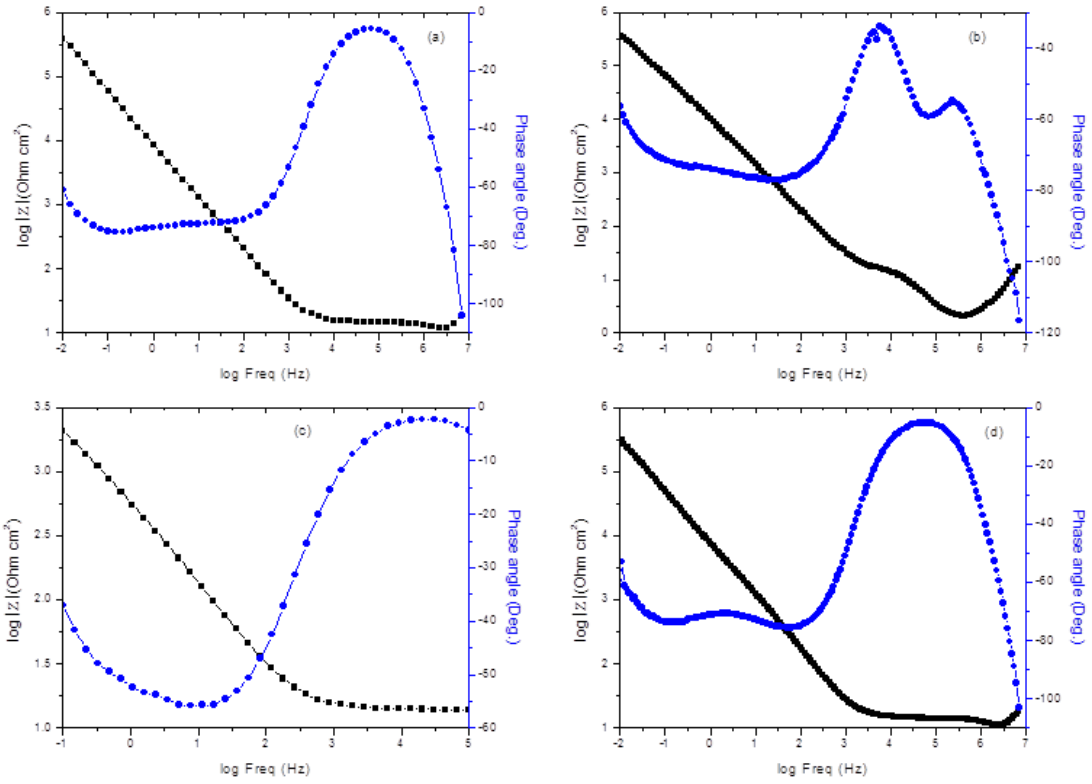

Fig. 4.151: Log Z versus log Freq. plots and phase angle (Z) versus log Freq. plots of (a) crofer steel, (b) duplex steel, (c) HSLA steel and (d) SS in artificial seawater respectively.

The fitting of electrochemical impedance data of the steels is obtained using the $R_s(CPE_{dl}R_{ct})$ model [99], with one time constant as shown in Fig. 4.146. The obtained impedance spectrum were analysed using a non-linear regression method, and the values of circuit parameters were estimated as given in Table 4.14.

Table 4.14: Electrochemical measurements of samples obtained by equivalent circuit.

Specimen	R_s (Ω cm^2)	R_{ct} (Ω cm^2)	CPE_{dl} (μF cm^{-2})	n_{dl}
Crofer	11.21	1.35×10^6	23.9×10^{-6}	0.83
Duplex	10.2	1.18×10^6	21.7×10^{-6}	0.84
HSLA	13.24	3723	0.44×10^{-3}	0.71
SS	10.86	1.39×10^6	28.5×10^{-6}	0.83

R_{ct} values of crofer, duplex and SS show remarkable difference from HSLA steel. The second parameter CPE_{dl} is very less in case of duplex steel which gives the proof of very low charge accumulation on the surface of the steel substrate. The R_{ct} and CPE_{dl} values of duplex steel again indicate that duplex steel is more corrosion resistive as compared to other steels. When n is close to 1, the CPE resembles a capacitor [109].

4.3.2.2. Microstructural analysis of exposed surface of steels

4.3.2.2.1. Surface analysis of crofer steel

All samples were scanned using a flatbed scanner at the end of 24 h corrosion testing. The photographic image of crofer steel is presented in Fig. 4.152.

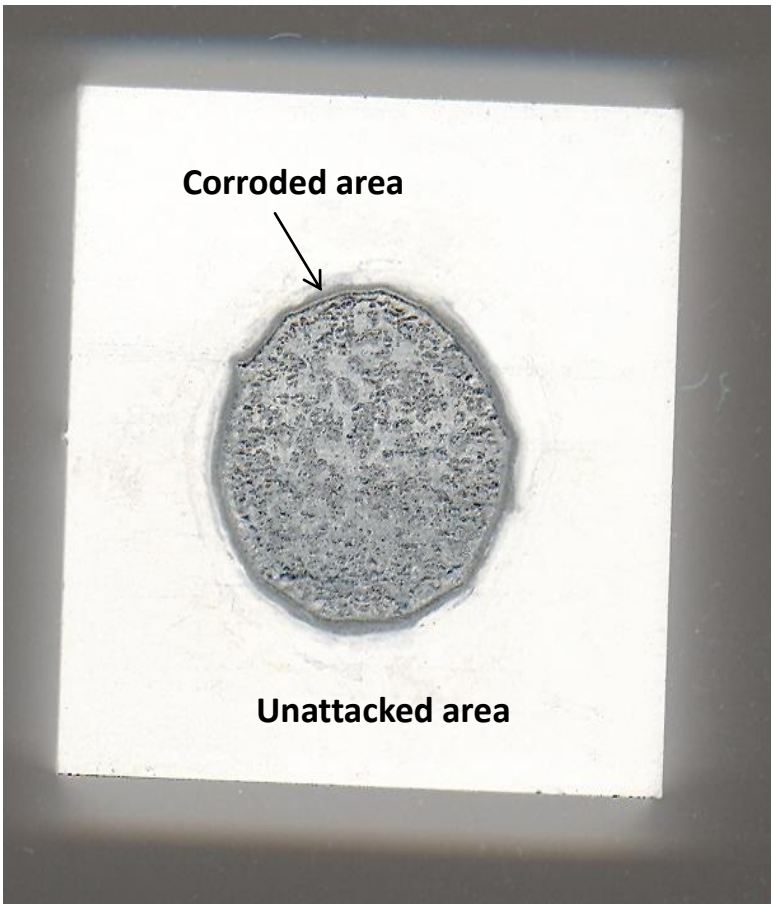

Fig. 4.152: Photograph of surface of crofer steel sample after corrosion testing for 24 h in 3.5% NaCl solution.

There is remarkable difference in structure of the steel. It indicates that 3.5% NaCl solution is highly corrosive medium for crofer steel. Fig. 4.153 (a) shows the micrograph of the crofer steel sample in the as received state, so that a comparison can be drawn with the morphology after exposure to the artificial seawater. Fig. 4.153 (b) presents the micrograph of the corroded portions which exhibits the formation of grooves. The higher magnification micrographs of the grooves (Fig. 4.153, c) indicate the corrosion along the grain boundary is more as grains are seen individual patches. The presence of small size pits in Fig. 4.153 (d) clearly indicates that the steel undergoes pitting corrosion in the seawater. However, the degree of susceptibility to pit is high as compared to HSLA steel [110].

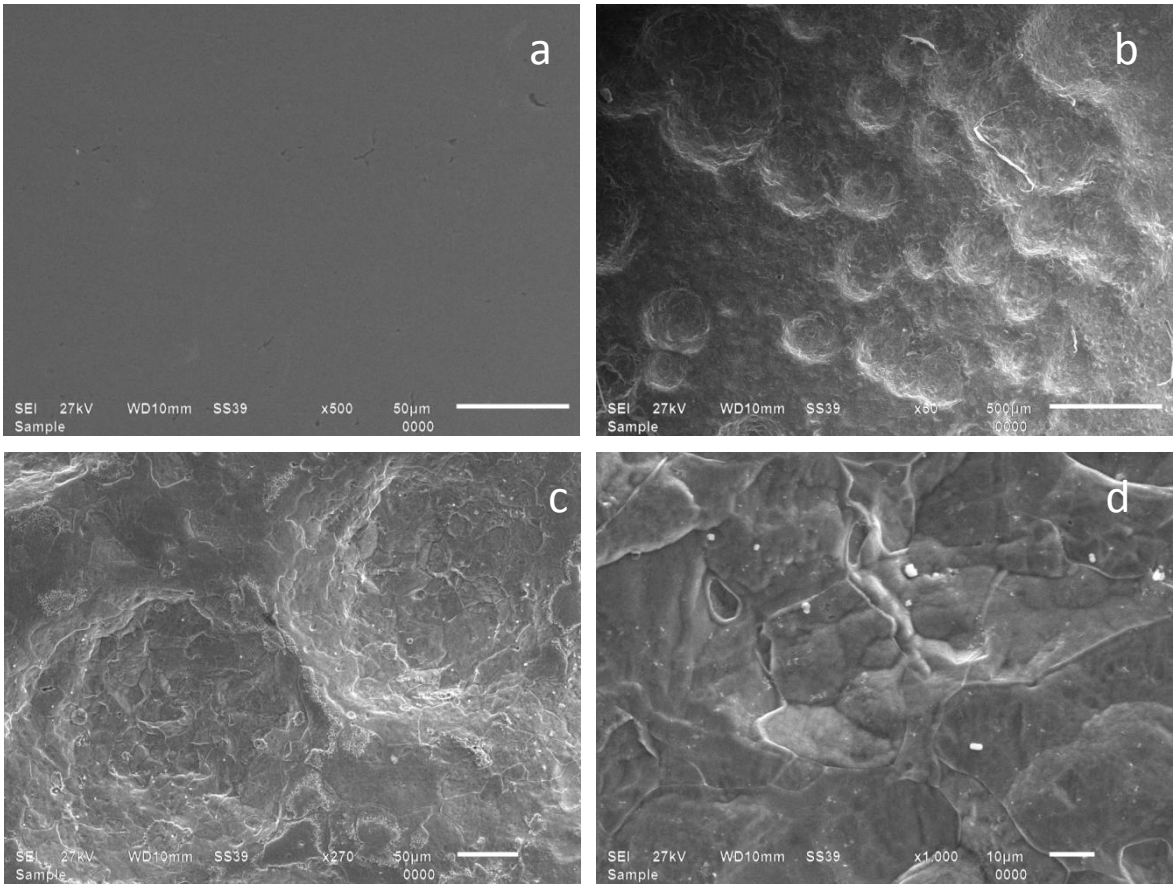

Fig. 4.153: Scanning electron micrographs of the crofer steel before and after corrosion testing for 24 h in 3.5% NaCl solution.

Fig. 4.154 shows the EDS spectrum of the unattacked crofer steel sample with the elemental analysis. As expected, there is Fe Kα and Cr Kα peaks as the main constituents [111].

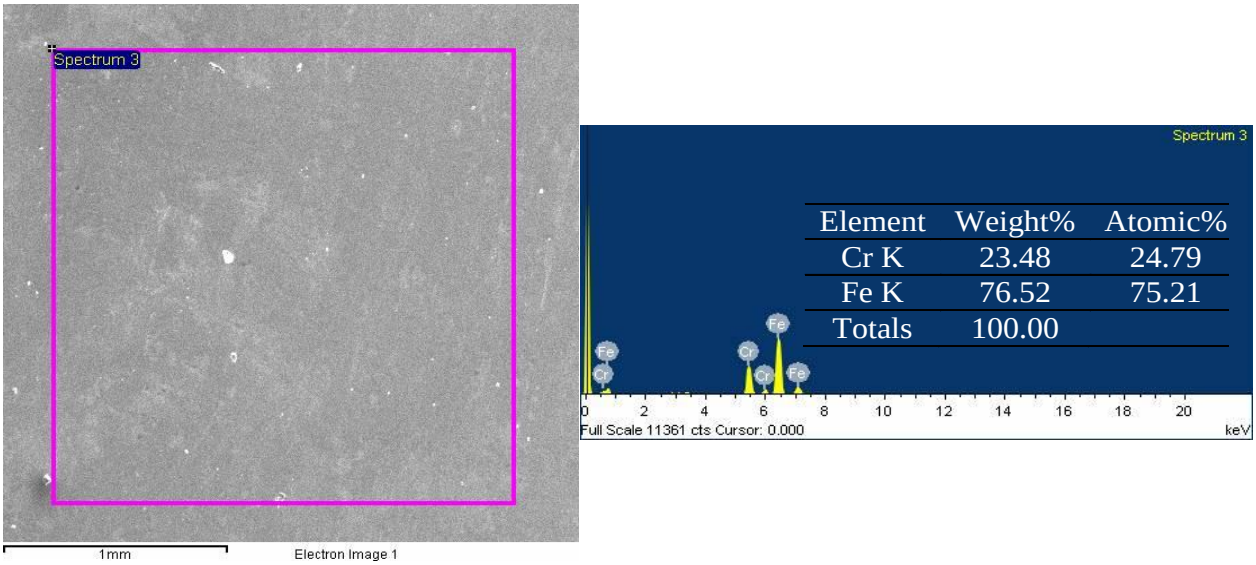

Fig. 4.154: EDS spectrum with elemental analysis of the crofer steel.

In the corroded portion two types of areas are formed. One is uniformly corroded and other is grooves type. In order to confirm the composition of these areas, EDS analysis of these phases has also been done as shown in Fig. 4.155.

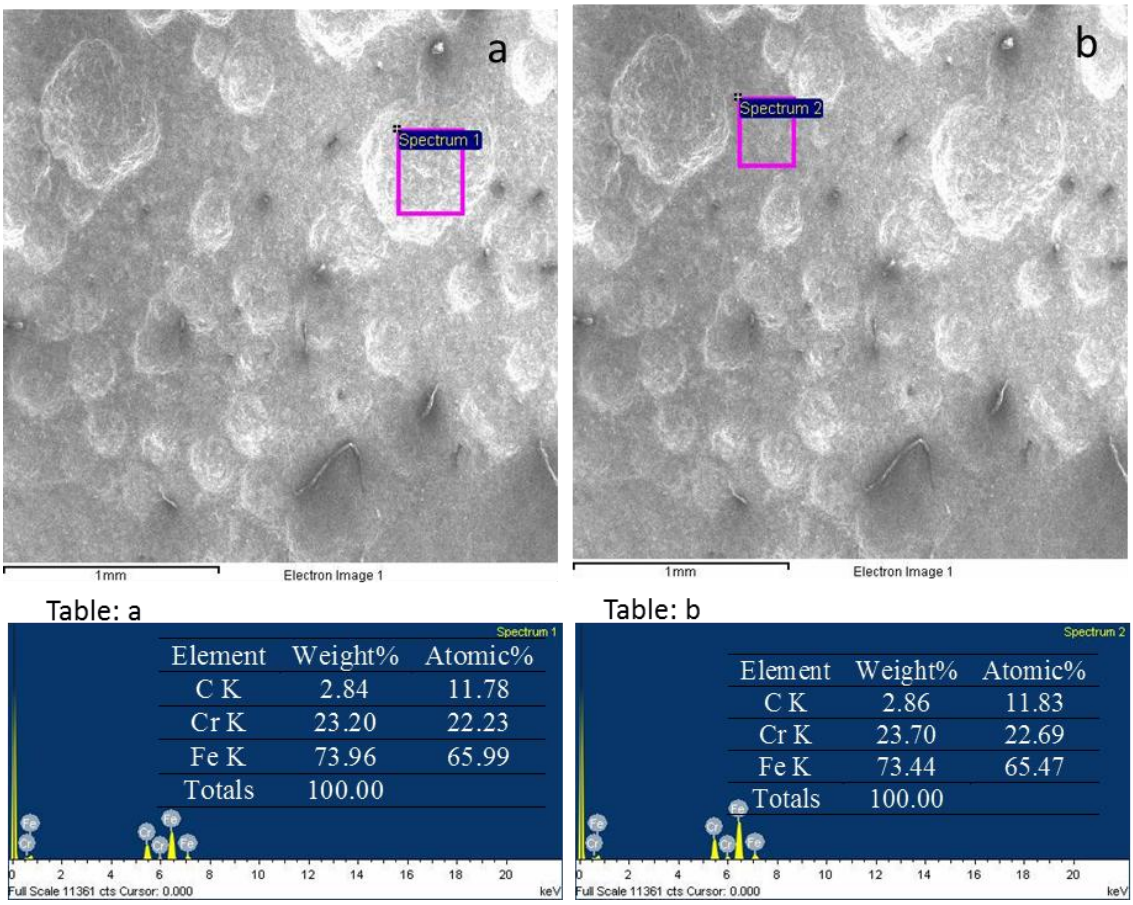

Fig. 4.155: SEM of the corroded crofer steel and correspondingly EDS analyses of the corroded region marked in the micrograph.

The analysis indicates that there is not much difference of elements present in these areas. However, slight variation in iron content is observed. The X-ray dot mapping of C, O, Ti, Cr, Mn and Fe taken from area shown in Fig. 4.156 (a) are also shown in Fig. 4.156 (b-g) respectively. These results further confirmed that the Fe and Cr are the main constituents along with small amount of Mn and Ti elements.

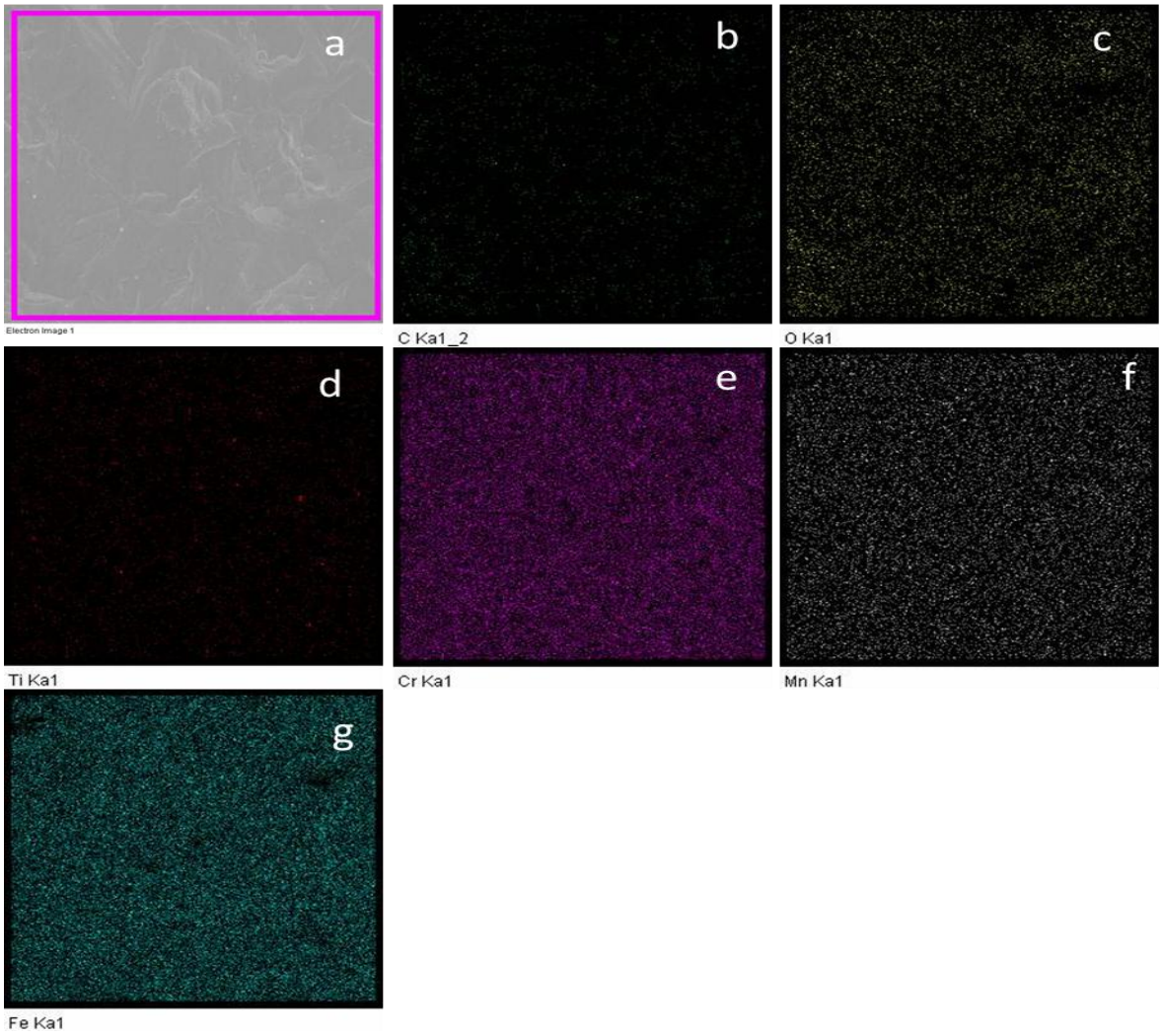

Fig. 4.156: X-ray dot mapping of C, O, Ti, Cr, Mn and Fe on crofer steel.

4.3.2.2.2. Duplex steel surface analysis

The photographic image of duplex steel is presented in Fig. 4.157.

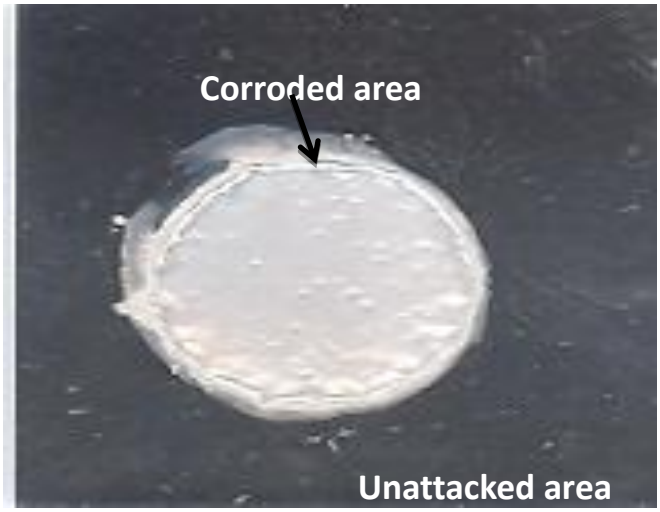

Fig. 4.157: Photographs of surfaces of duplex steel samples before and after corrosion testing for 24 h in 3.5% NaCl solution.

There is remarkable difference in structure of the steel. It indicates that 3.5% NaCl solution is highly corrosive medium for duplex steel as shown in Fig. 4.157. Uniform corrosion tends to proceed evenly over the entire exposed surface of any uncoated part and eventually causes a general thinning of the metal [112].

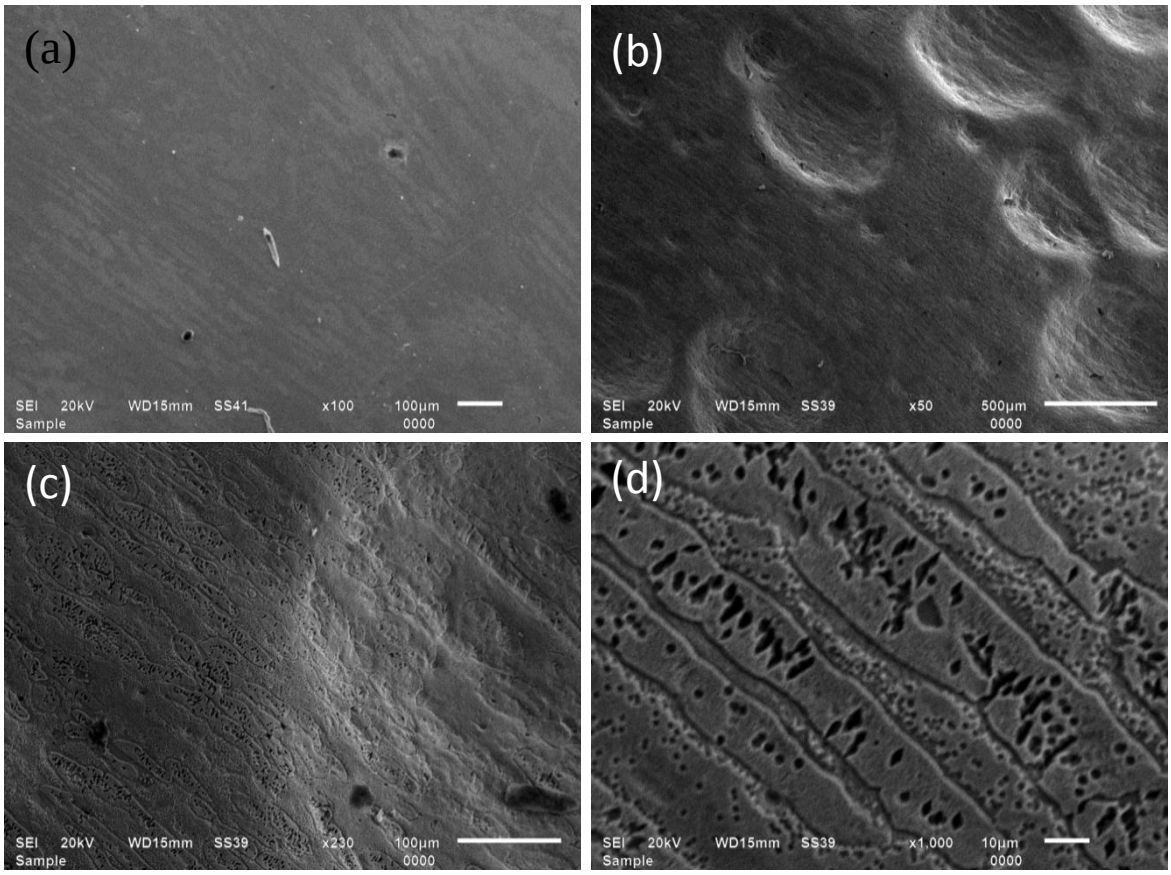

Fig. 4.158: Scanning electron micrographs of the duplex steel before and after corrosion testing for 24 h in 3.5% NaCl solution.

Fig. 4.158 (a) shows the micrograph of the unattacked duplex steel sample. Fig. 4.158 (b) presents the micrograph of the corroded portions which are look like the layers of the riverbed. The higher magnification micrographs of the layers (Fig. 4.158, c, d) indicate the corrosion of the different phases of steel. This steel has Cr, Ni and Mo elements which increase the resistance to pitting corrosion of steels [113]. Chloride is the most common element for initiation of pitting. Once a pit is formed, it in effect becomes a crevice; the local chemical environment is substantially more aggressive than the bulk environment. Further, the area of pit becomes considerably small when compared to other area, thereby the pit growth is very fast and the ultimate result is the formation of holes in the steel within short time of exposure to the marine environment. The stability of passive film with respect to resistance to pitting initiation is

controlled primarily by chromium and molybdenum. Minor alloying elements can also have an important effect by influencing the amount and type of inclusions in the steel that can act as pitting sites. Although the effect of P is still ambiguous, it is suggested that H_2PO_4 accelerates the oxidation of Fe^{2+} to Fe^{3+} and prevents the growth of the corrosion products. Thus these elements are responsible for its lower corrosion rate as compared to other steels. Fig. 4.159 shows the EDS spectrum of the plane duplex steel sample with the elemental analysis. The analysis indicates that iron and chromium are the main constituents and Cu and Mn are also present in this steel.

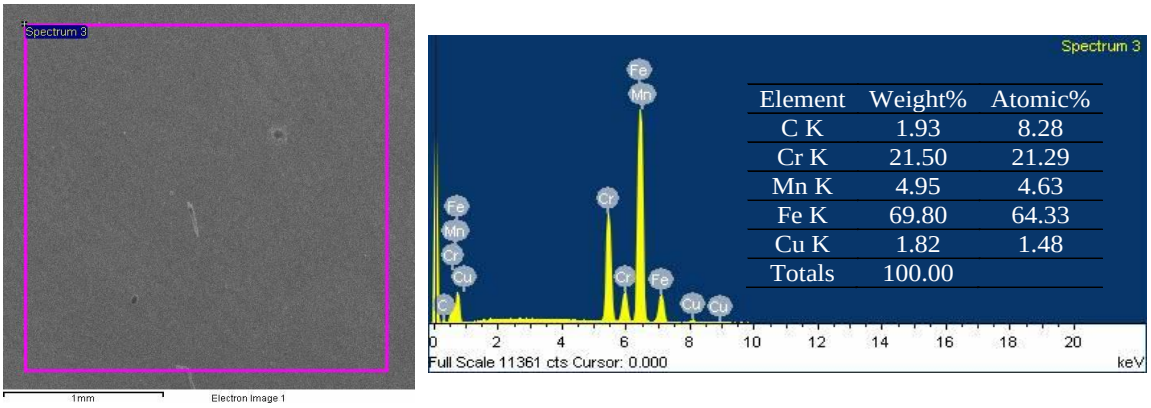

Fig. 4.159: EDS spectrum with elemental analysis of the duplex steel.

In the corroded potion two types of layers formed. One layer contains pits and other one contains small holes in uniform area.

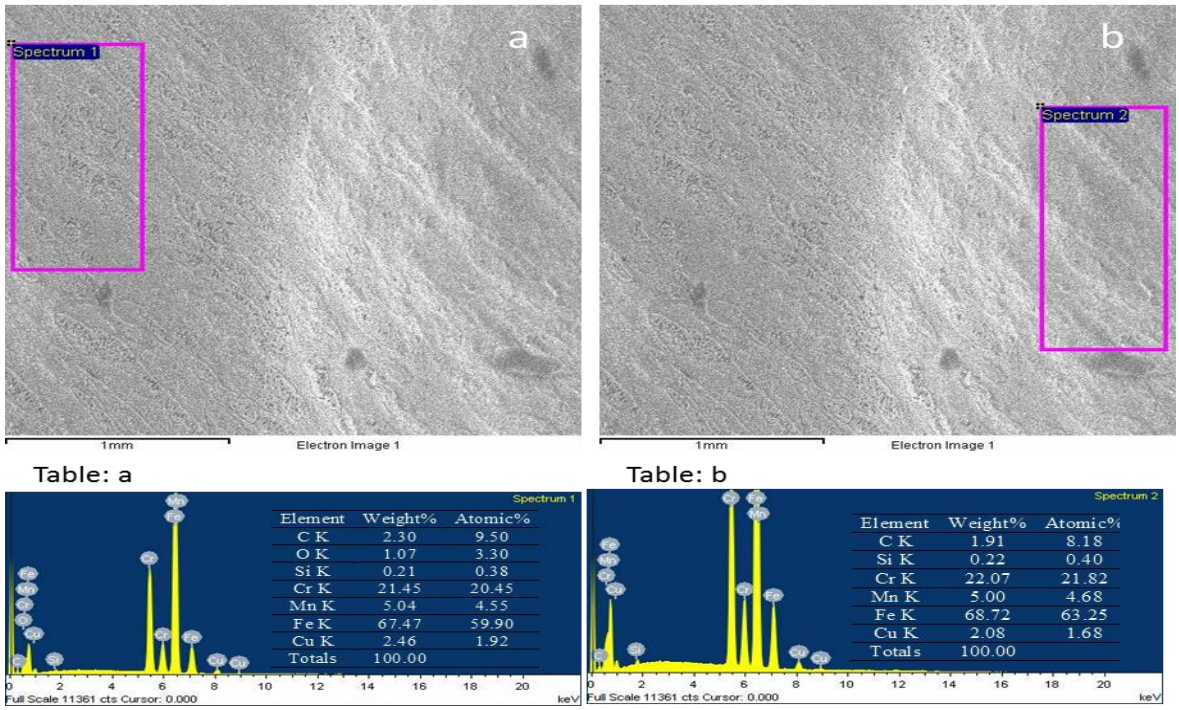

Fig. 4.160: SEM of the corroded duplex steel and correspondingly EDS analyses of the corroded region marked in the micrograph.

In order to confirm the composition of these areas, EDS analysis of these layers has also been done as shown in Fig. 4.160. The weight percentage of O is missing in the pits as compared to uniformly corroded area. Thus EDS analysis confirmed the variation in the constituents of different areas. The X-ray dot mapping of C, Cr, Mn, Fe and Cu taken from area shown in Fig. 4.161 (a) are also shown in Fig. 4.161 (b-f) respectively. These results further confirmed that the Fe and Cr are the main constituents along with small amounts of Mn and Cu elements in the duplex steel.

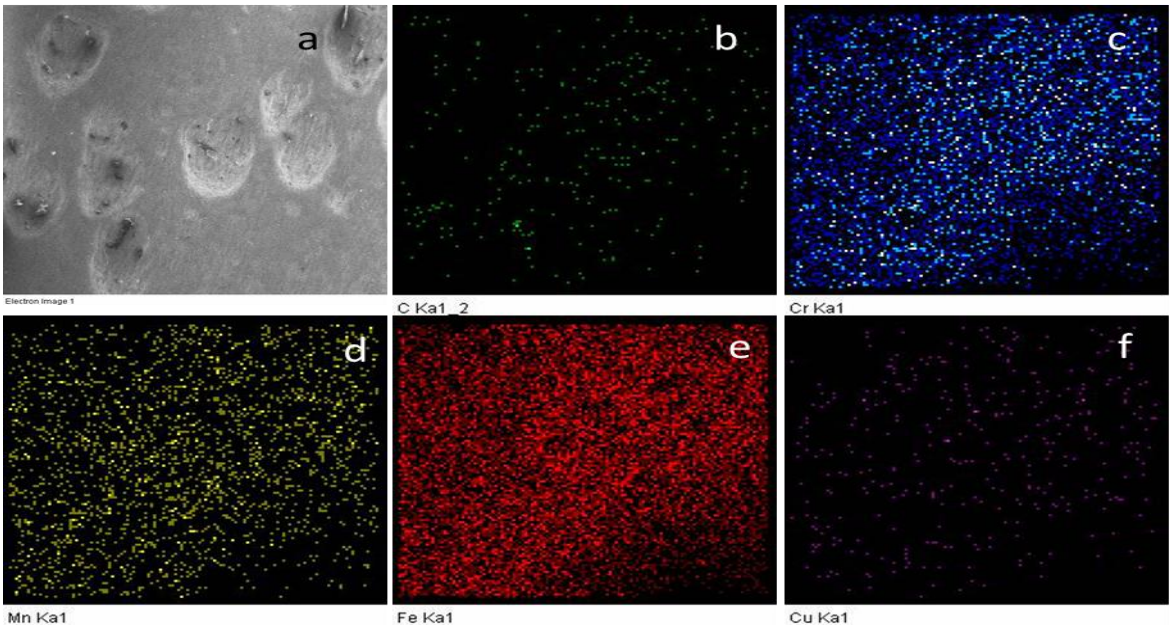

Fig. 4.161: X-ray dot mapping of C, Cr, Mn, Fe and Cu on duplex steel.

4.3.2.2.3. HSLA steel surface analysis

The photographic images of plane and corroded HSLA steel are presented in Fig. 4.162.

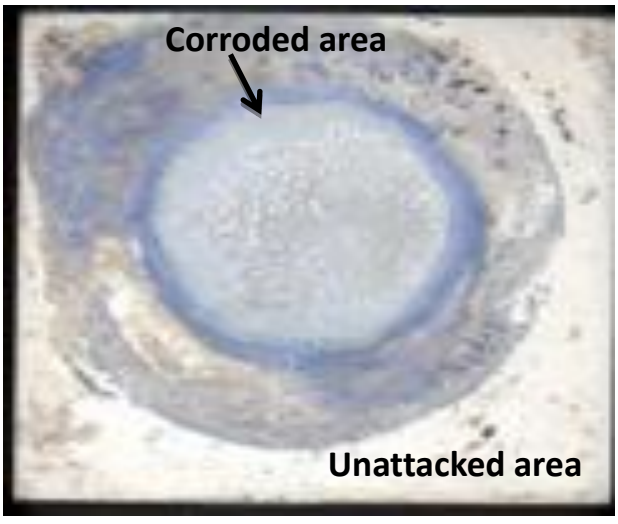

Fig. 4.162: Photographs of surfaces of HSLA steel samples before and after corrosion testing for 24 h in 3.5% NaCl solution.

The surface appearance of HSLA steel specimen exposed for 745 h in the artificial seawater was grey-brown. Examination of the surface after exposure to the 3.5% NaCl solution shows that the rust layers to be very porous. Rust particles were not completely removed from the corroded area [114].

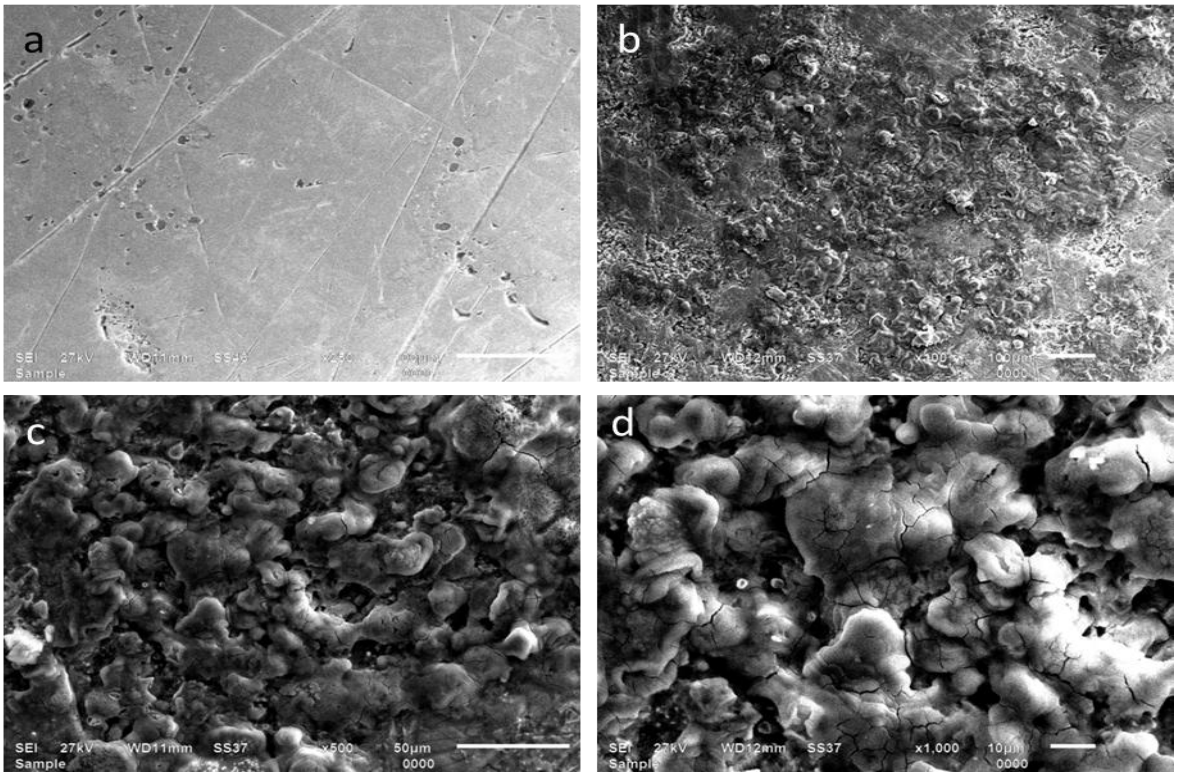

Fig. 4.163: Scanning electron micrographs of the HSLA steel before and after corrosion testing for 24 h in 3.5% NaCl solution.

Fig. 4.163 (a) shows the micrograph of the plane HSLA steel sample. Fig. 4.163 (b) presents the micrograph of the corroded portions which are globular structures [115]. The higher magnification micrographs of the layers (Fig. 4.163, c, d) appears like dried corrosion products from cracking of corrosion layers. Rust layers mainly consists of globular structures known as cotton balls. Fig. 4.163 (d) shows an irregular, cracked and non-protective oxide layer (open structure) which allows the easy access of corrosive species to the metallic substrate [116].

Fig. 4.164 shows the EDS spectrum of the plane HSLA steel sample with the elemental analysis. The analysis indicates that iron is the main constituent and small amount of Cr, Al, Si, Ni, Cu and Mn are also present in this steel.

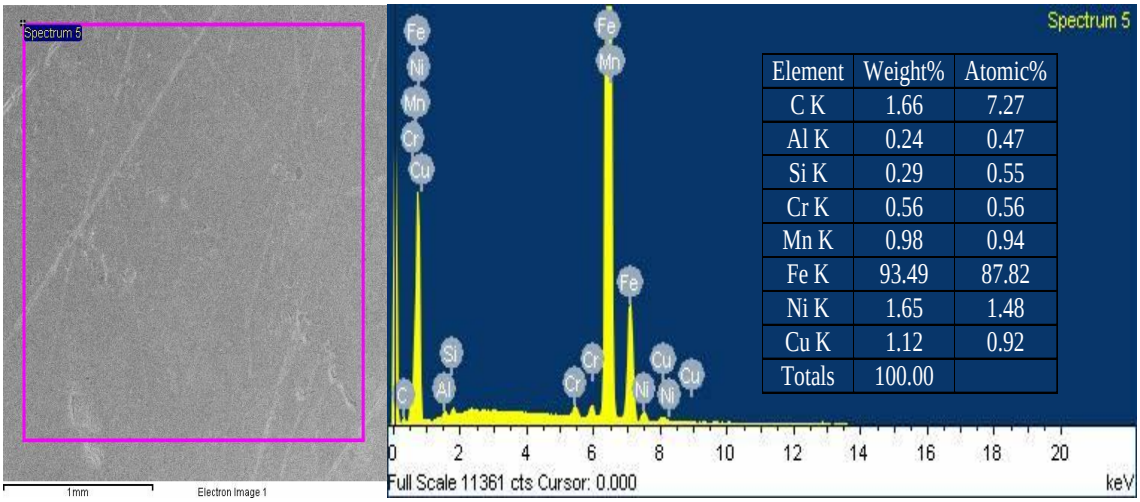

Fig. 4.164: EDS spectrum with elemental analysis of the HSLA steel.

Corrosion products are uniformly deposited on the corroded area. In order to confirm the composition of these products, EDS analysis of these has also been done as shown in Fig. 4.165.

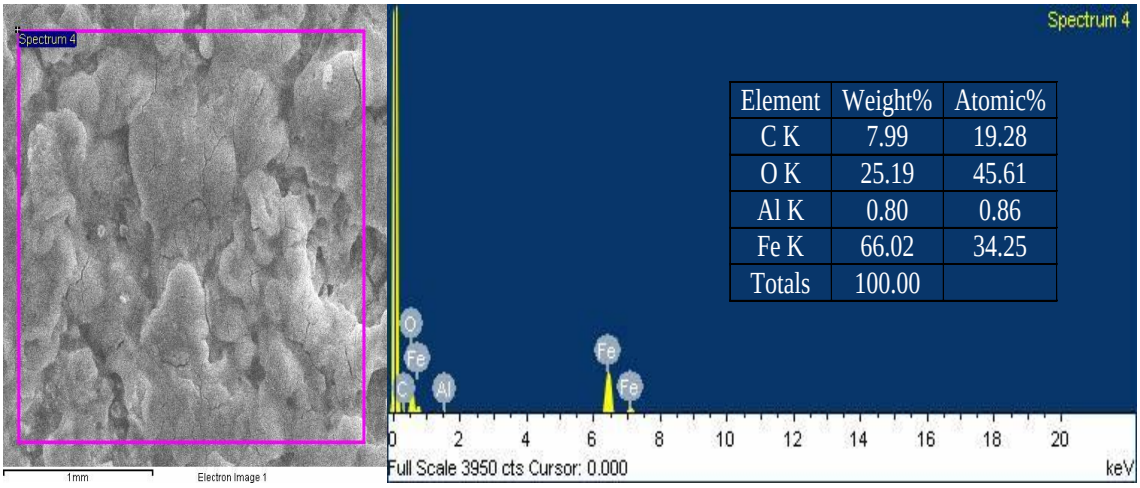

Fig. 4.165: EDS spectrum with elemental analysis of the corroded HSLA steel.

The weight percentages of Fe and O elements are higher among the all elements i.e iron oxide and are mainly present as corrosive layer. On comparison before and after corrosion testing, we find the Cu element is absent after corrosion. Cu precipitates and covers the steel surface during corrosion. Cu retards the crystallization of rust and contributes to a uniform dissolution of the steel and the formation of a rust layer at the initial stage [117].

The X-ray dot mapping of C, O, Ti, Cr, Mn and Fe taken from area shown in Fig. 4.166 (a) are also shown in Fig. 4.166 (b-e), respectively. These results further confirmed that the Fe and O are the main constituents along with small amounts of Ti, Cr and Mn elements in the corroded HSLA steel.

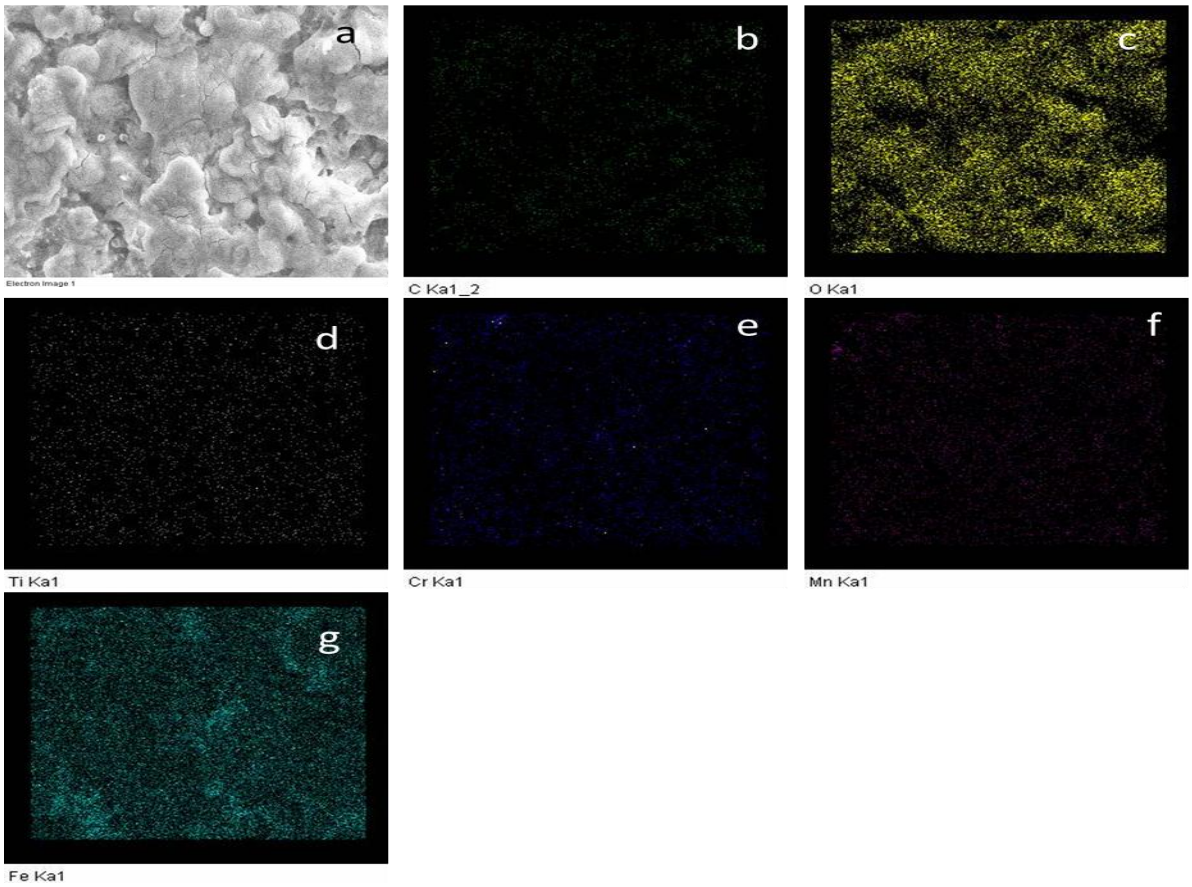

Fig. 4.166: X-ray dot mapping of C, O, Ti, Cr, Mn and Fe on corroded HSLA steel.

4.3.2.2.4. Stainless steel surface analysis

The visual observations of the corroded steel sample is shown in the photograph in Fig. 4.167. After 24 h testing, the blank sample was corroded and large numbers of pits are formed.

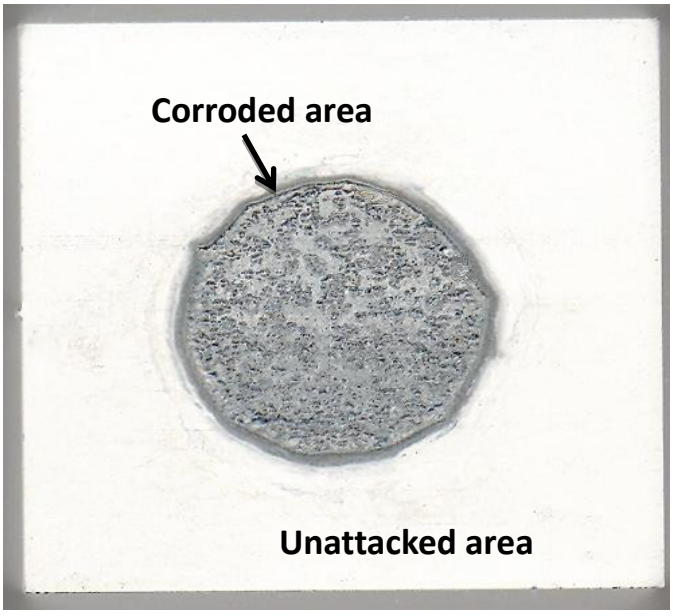

Fig. 4.167: Photographs of surfaces of stainless steel samples before and after corrosion testing for 24 h in 3.5% NaCl solution.

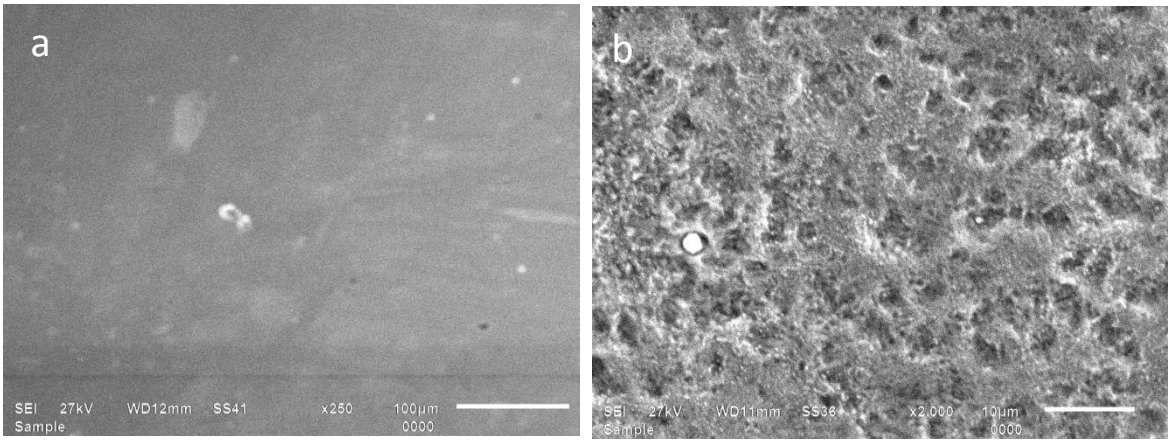

Fig. 4.168: Scanning electron micrographs of the stainless steel before and after corrosion testing for 24 h in 3.5% NaCl solution.

Fig. 4.168 (a) shows the micrograph of the plane SS sample. Fig. 4.168 (b) presents the micrograph of the corroded portions which indicates the formation of small pits due to corrosion. Fig. 4.169 shows the EDS spectrum of the plane SS sample with the elemental analysis. The analysis indicates that iron and Cr are the main constituents and small amount of Al, Ni and Mn are also present in this steel.

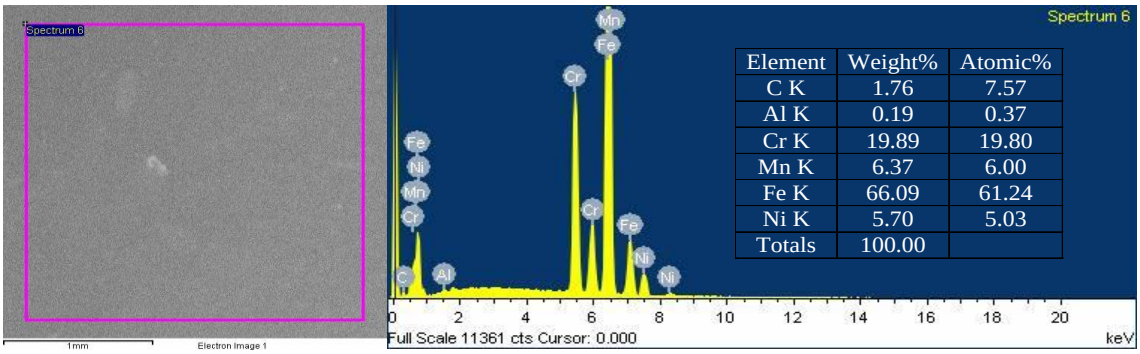

Element	Weight%	Atomic%
C K	1.76	7.57
Al K	0.19	0.37
Cr K	19.89	19.80
Mn K	6.37	6.00
Fe K	66.09	61.24
Ni K	5.70	5.03
Totals	100.00	

Fig. 4.169: EDS spectrum with elemental analysis of the SS steel.

Corrosion occurred uniformly throughout the area. In order to confirm the composition of this area, EDS analysis of these has also been done as shown in Fig. 4.170.

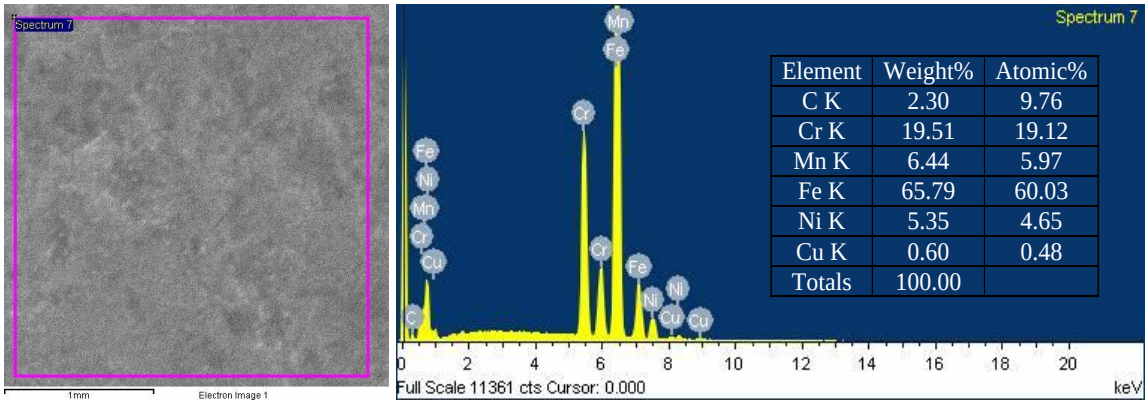

Element	Weight%	Atomic%
C K	2.30	9.76
Cr K	19.51	19.12
Mn K	6.44	5.97
Fe K	65.79	60.03
Ni K	5.35	4.65
Cu K	0.60	0.48
Totals	100.00	

Fig. 4.170: EDS spectrum with elemental analysis of the corroded SS steel.

The weight percentages of Fe and Cr elements are higher among the all elements in corrosive region. The X-ray dot mapping of C, Si, Cr, Mn, Fe, Ni, Cu, O, Ti, Cr, Mn and Fe taken from area shown in Fig. 4.171 (a) are also shown in Fig. 4.171 (b-g), respectively. These results further confirmed that the Fe and Cr are the main constituents along with small amounts of C, Si, Ti, Cr and Mn elements in the corroded SS steel.

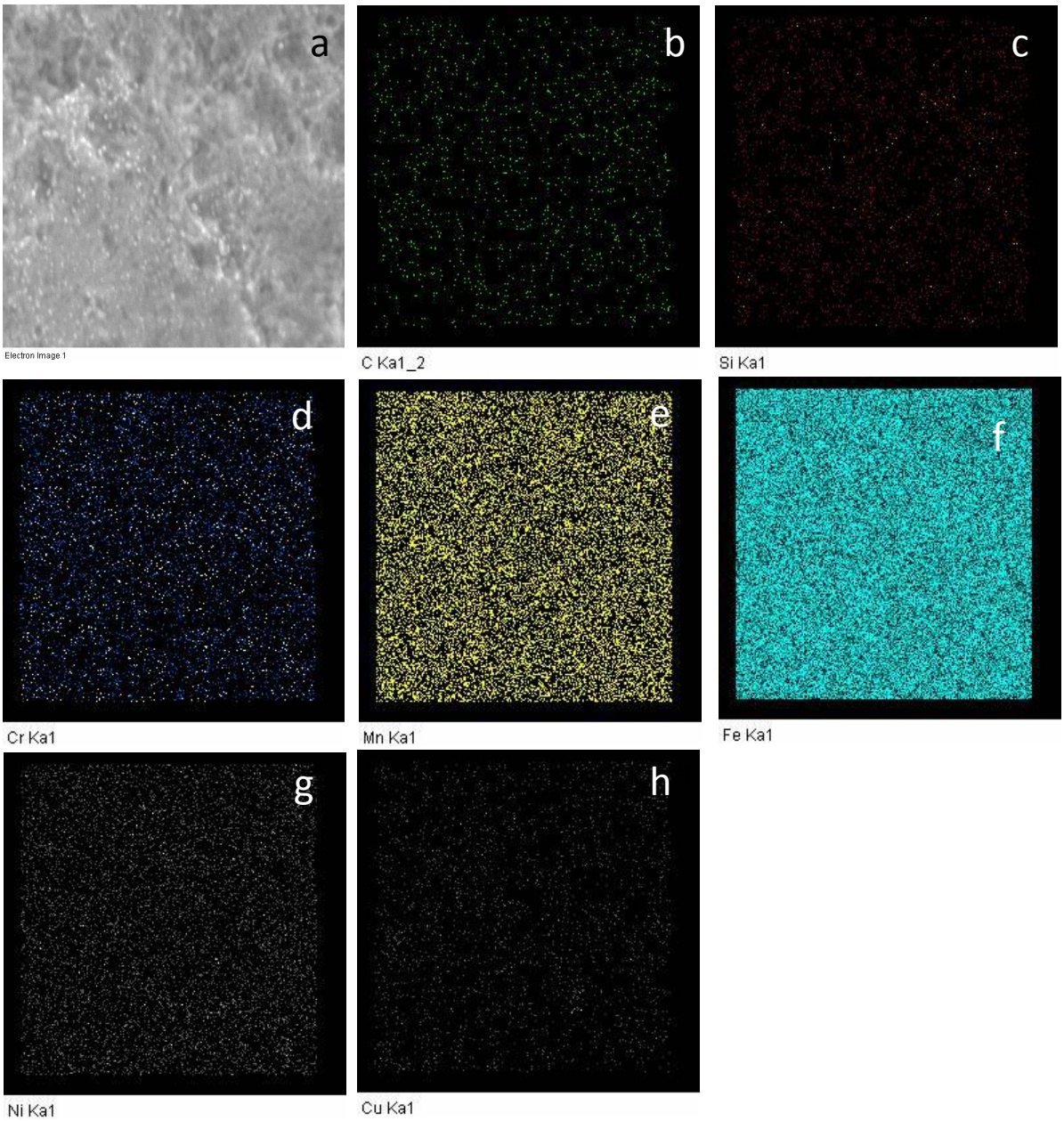

Fig. 4.171: X-ray dot mapping of C, Si, Cr, Mn, Fe, Ni and Cu on corroded SS steel.

From electrochemical analysis for different steels in marine environment revealed that the crofer, duplex, HSLA and SS steel may not be able to form protective oxide scale over their surfaces. The results also suggest that HSLA steel is more susceptible to corrosion as compared to other steels. Thus corrosion rate depends upon the composition of the steels. It is known that

chromium is essential element in forming the passive film on the steels and helps to lower down the corrosion rate [118]. Other elements can influence the effectiveness of chromium in forming or maintaining the film, but no other element can, by itself create the properties of stainless steel. The present results suggest that chromium alone is not helpful in minimizing corrosion because crofer steel contains 22% chromium but the corrosion rate is greater than duplex which contains 16% chromium. It indicates that the combination of alloying elements particularly Cr, Ni, and Mo decide the corrosion behaviour of crofer, duplex and SS. On the other hand, the low alloy steel exhibits high corrosion rate as expected due to the fact that it contains very low amounts of Cr, Ni, and Mo.

4.3.3. Corrosion analysis of diffusion couples

The amorphous coating which shows promising applications in marine environments, container for the nuclear fuel, oil and gas industries, power station, have attracted much attention in recent years [119]. Glass coatings were applied to steel substrates to inhibit corrosion and provide a decorative finish. The choice of a glass as a coating material was due to the harshness of the corrosive marine environment. Selected diffusion couples were studied for 745 h corrosion study and their results are presented below:

4.3.3.1. N-15 glass and crofer steel

The studies presented in previous chapters show that N-15 glass is most stable among the N-series glasses, so diffusion couple of N-15 glass with crofer steel was tested for 745 h in 3.5% NaCl solution.

4.3.3.1.1. Electrochemical testing

An open circuit potential (OCP) measurement for sample was done in 3.5% NaCl solution for 2 h. The average value of OCP measurements are given in Table 4.15.

Table 4.15: Results of OCP measurement of diffusion couple of N-15 glass with crofer steel.

Testing time (h)	OCP value (± 0.002V)
24	-0.491
265	-0.447
505	-0.444
745	-0.441

The OCP values shows the trend to noble potential and becomes stable at -0.44 ± 0.004 V. Fig. 4.172 presents the polarization curves of 24 h, 265 h, 505 h and 745 h testing for diffusion couple of N-15 glass and crofer steel in artificial seawater. Some important electrochemical parameters, such as the corrosion potential (E_{corr}), corrosion current density (i_{corr}) and the

polarization resistance (R_p) of the coating tested are summarized in Table 4.16. It is noted that the polarization resistance (R_p) is derived from the Stern-Geary Equation by fitting their Tafel polarization curves [120]. The corrosion rate is fast after 24 h of the testing which further decreases in subsequent hours. At the end its variation is less and is of the order of $\times 10^{-6}$. It can be seen that the value of R_p is of order $\times 10^{6}$ which is much higher than Fe based amorphous coatings [121].

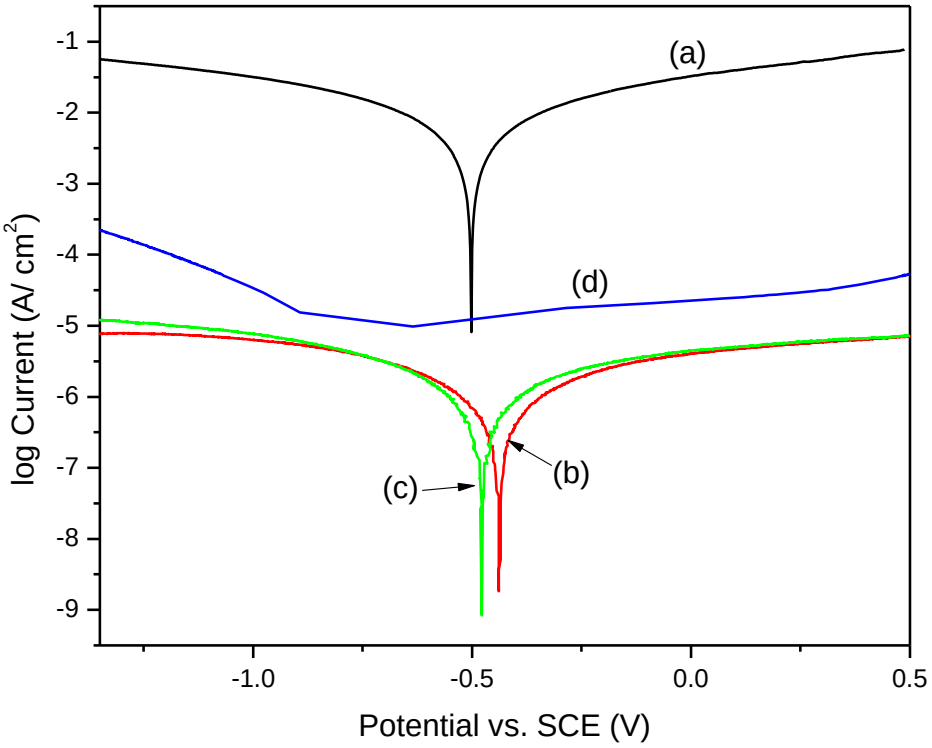

Fig. 4.172: Potentiodynamic polarization curves of (a) 24 h, (b) 265 h, (c) 505 h and (d) 745 h testing of diffusion couple of N-15 glass and crofer steel in artificial seawater.

Table 4.16: Results of potentiodynamic polarization in diffusion couple of N-15 glass with crofer steel.

Testing time (h)	E_{corr} (mV)	I_{corr} (μA cm^{-2})	β_c (mV/decade)	β_a (mV/decade)	R_p (Ω cm^2)	Corrosion rate (mm/year)
24	-500.28	2.441	308.0	308.6	0.16×10^{5}	8.968×10^{-3}
265	-435.66	0.0005	291.6	316.5	88.4×10^{6}	1.489×10^{-6}
505	-473.53	0.0006	295.5	336.5	82.5×10^{6}	1.775×10^{-6}
745	-322.3	0.0006	341.4	504.7	----	1.859×10^{-6}

In order to evaluate the variation in the electrochemical reaction of the coating, electrochemical impedance spectroscopy (EIS) was measured at different interval of time period in 3.5% NaCl

solution. The Nyquist plots of diffusion couple of N-15 glass and crofer steel are presented in Fig. 4.173.

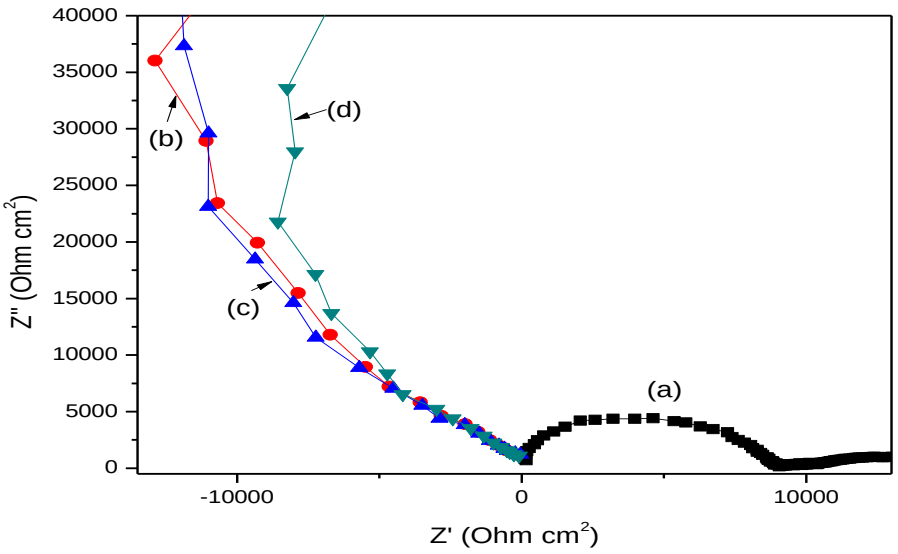

Fig. 4.173: Nyquist plots of diffusion couple of N-15 glass and crofer steel in artificial seawater.

From Nyquist plots (Fig. 4.173), the diameter of the semicircle of 360 h is biggest as compared to others which indicate that the corrosion of glass coating decreases upto 360 h. The Nyquist plots for the coating exhibit two continuous semicircles reflecting two time-constants. This behavior implies that two reaction mechanisms are operative on the coating surface i.e. diffusion and dissolution of the surface.

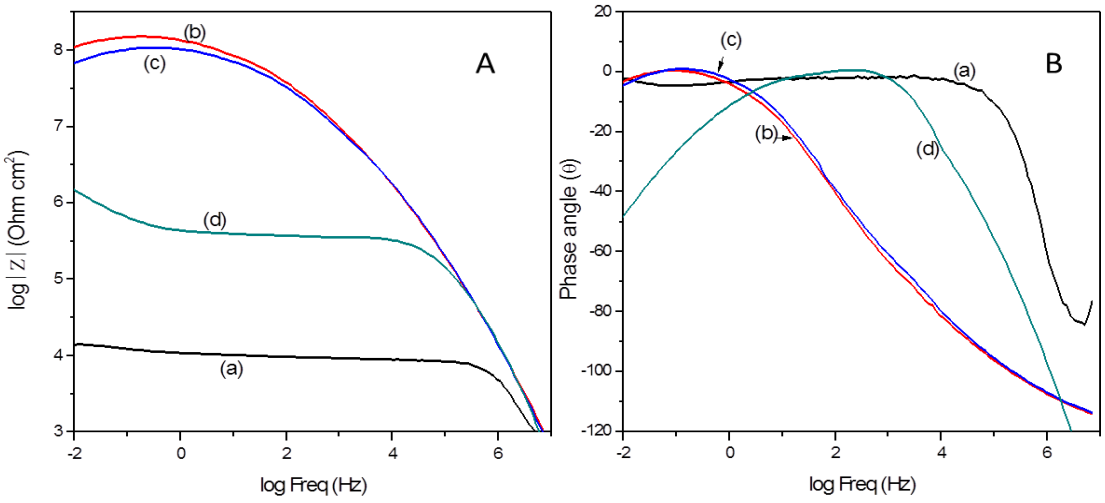

Fig. 4.174: (A) Log Z versus log Freq. plots and (B) phase angle (Z) versus log Freq. plots of (a) 24 h, (b) 265 h, (c) 505 h and (d) 745 h for diffusion couple of N-15 glass and crofer steel in artificial seawater.

In the Bode–log |Z| plots shown in Fig. 4.174 (A), the log |Z| value for the coated system for 265 and 505 h is approximately four orders of magnitude higher than that for the 24 h, which demonstrates a better corrosion performance of the coated sample. The Bode phase plots are shown in Fig. 4.174 (B). The phase angle of the coated sample on 745 h shows capacitive behaviour in the middle frequency region due to the dissolution of the glass coating. While the coated steel sample shows the linear behaviour in the high frequency range, which confirms the occurrence of two time constants due to glass coating.

Based on the above analysis, the fitting for the coated steel sample was obtained by using the $R_s(CPE_{dl}R_{ct} + CPE_cR_c)$ model [122], which includes two time constants as shown in Fig. 4.175. R_s is solution resistance, R_{ct} and CPE_{dl} are associated with the charge transfer process that occurs on the surface of the substrate, R_c is resistance of the coating and CPE_c is the constant phase element related to the coating.

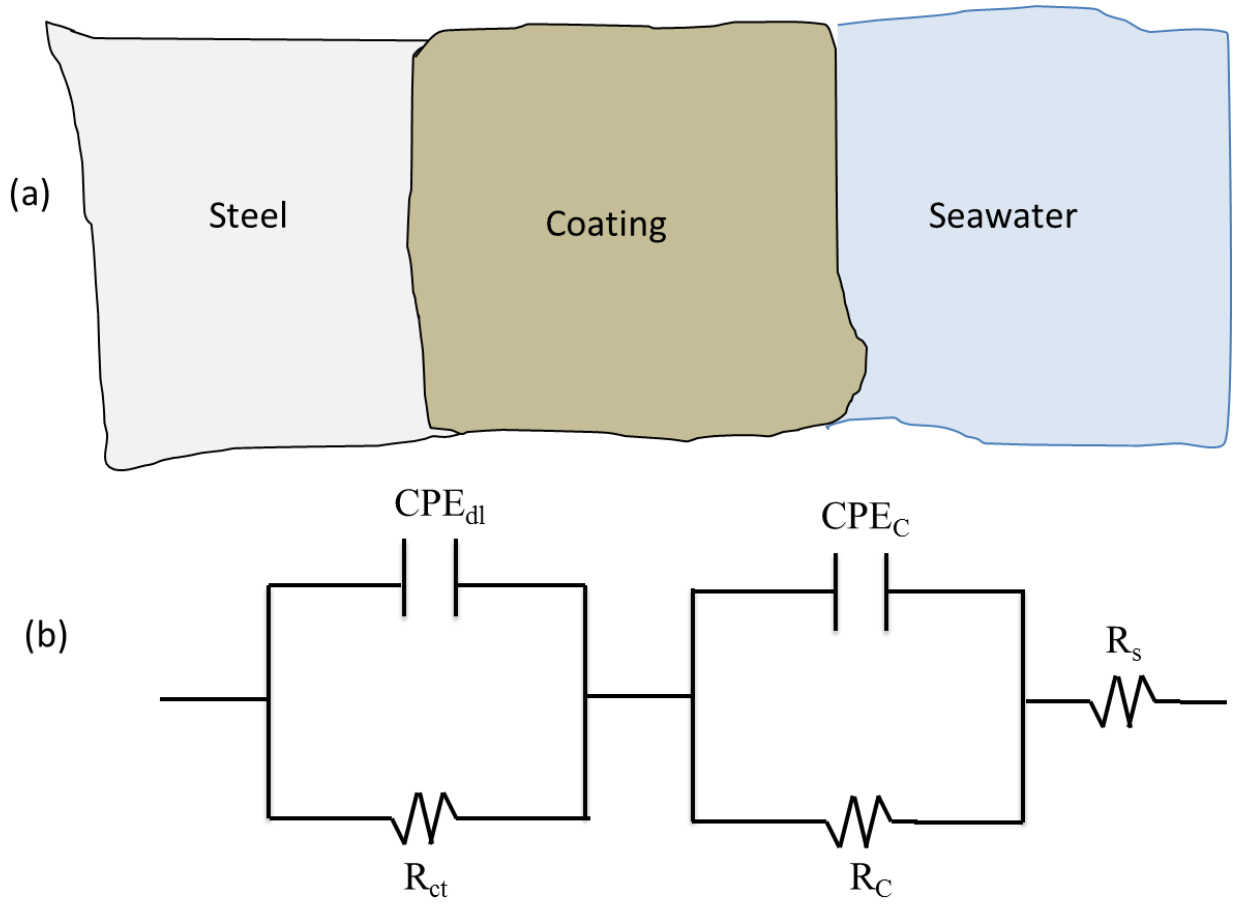

Fig. 4.175: (a) Schematic diagram of test conditions and **(b)** Equivalent circuits of glass coating on steel in artificial seawater [123].

The obtained impedance spectrum was analyzed using a non-linear regression method, and the values of circuit parameters were calculated as given in Table 4.17.

Table 4.17: Electrochemical measurements of diffusion couple of N-15 glass and crofer steel obtained by equivalent circuit.

Testing time (h)	R_s (Ω cm^2)	R_{ct} (Ω cm^2)	CPE_{dl} (μF cm^{-2})	n_{dl}	R_c (Ω cm^2)	CPE_c (μF cm^{-2})	n_c
24	6.2	17223	0.22×10^{-3}	0.19	8548	30.55×10^{-12}	1
265	10	0.12×10^{9}	0.46×10^{-9}	1	14.3×10^{6}	13.1×10^{-12}	1
505	10	77.7×10^{6}	0.65×10^{-9}	1	9.8×10^{6}	13.6×10^{-12}	1
745	15.9	0.35×10^{6}	0.68×10^{-9}	0.06	1349	35.77×10^{-12}	0.9

The values of R_{ct} of the coated steel have increased remarkably as compared to bare steel, which clearly indicates the formation of the compact interface layer on the coated steel. The second parameter CPE_{dl} is less as compared to bare steel which gives the proof of very low charge accumulation on the surface of the N-15 glass coated sample. The increase in R_{ct} value and the decrease in CPE_{dl} value of N-15 glass coated on crofer steel indicate that the transfer of charge is hindered and the diffusion of the solution in the pores of the coating is blocked to a greater extent by glass ceramic coating in comparison to bare steel. Moreover, the dissolution of iron from steel side is also suppressed by silicate glass ceramic coating.

4.3.3.1.2. Structural analysis

The nature of the corrosion of the coating, the surface morphology of the coating after polarization test in 3.5% NaCl solution was examined. The photograph of the couple after corrosion test is shown in Fig. 4.176.

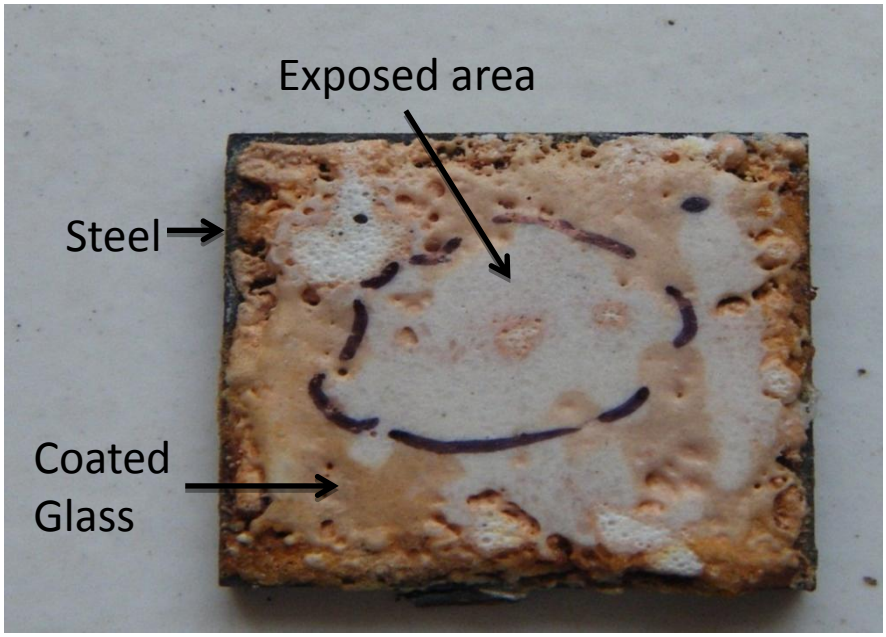

Fig. 4.176: Photograph of N-15 glass coated on crofer steel after corrosion testing for 745 h in 3.5% NaCl solution.

As shown in Fig. 4.176, the circular marked area is exposed for corrosion testing. There is no remarkable difference between exposed and non-exposed areas by visual observation. Coated glass is stable after 745 h exposure. In order to see microscopic level changes, scanning electron micrographs of this area was taken as shown in Fig. 4.177. The surface morphology of the corroded area exhibits few pits as can be seen in Fig. 4.177 (a). However, there are some corrosion products which is visible in Fig. 4.177 (a & b). On analyzing the structure of frits, one could see the presence of faceted crystals inside the pits which can be seen in Fig. 4.177 (c & d). The morphological features of these crystals indicate that these are some crystalline silicate products of glass. During corrosion, the glass matrix dissolves from those areas where the internal stress due to precipitation of crystalline phase during heating of glass is more and leads to formation of pits leaving behind unreacted crystalline silicate phase [124]. However, very few amounts of pits are visible on the surface indicating the uniform dissolution of glass during testing. Such nature of surface clearly indicates the good corrosion resistance property of the glass coating.

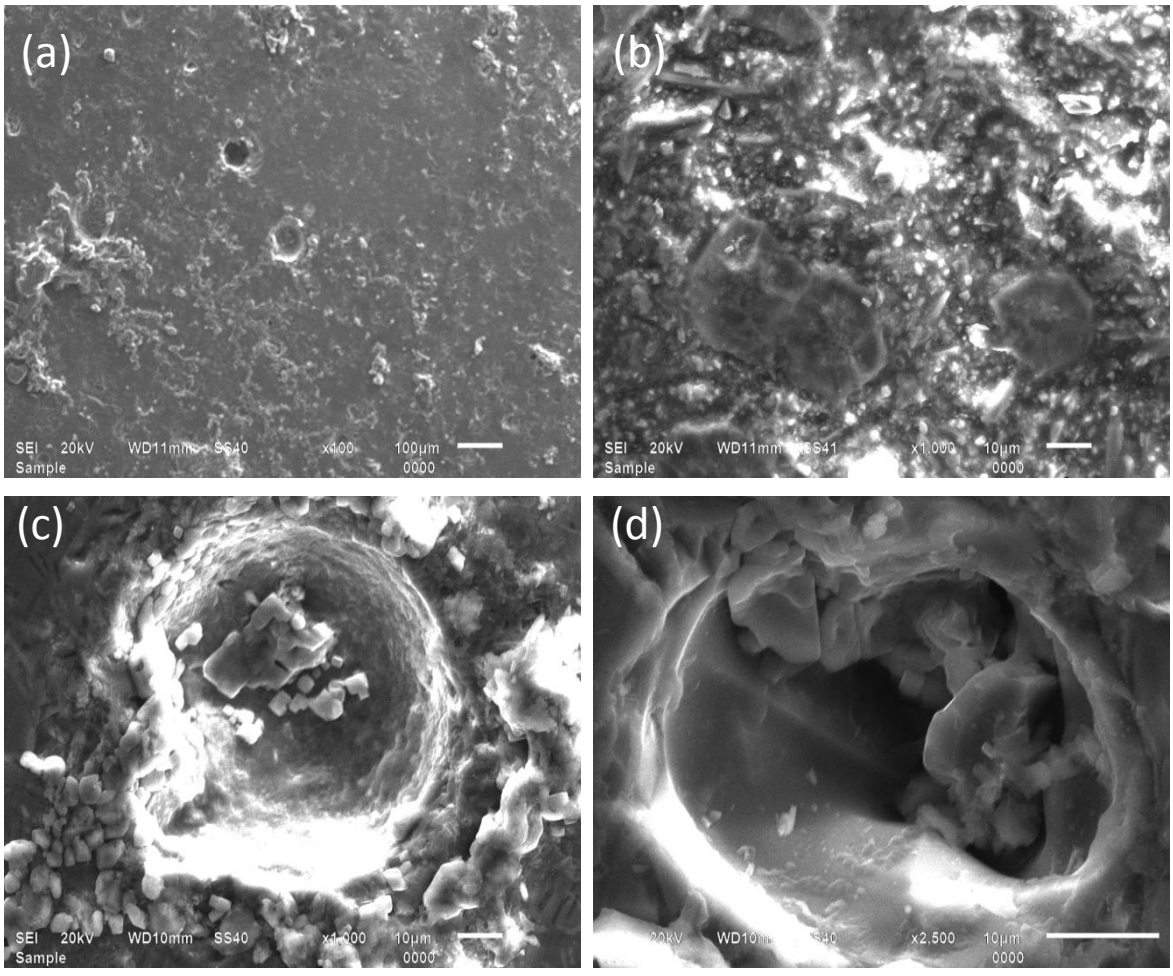

Fig. 4.177: Scanning electron micrographs of the corroded diffusion couple of N-15 glass coated on crofer steel.

It is generally accepted that the long term mechanisms of glass corrosion is a combination of matrix dissolution followed by incongruent dissolution and solution/precipitation reactions [125]. EDS analysis of incongruent dissolution and precipitation reactions of corroded glass is given in Fig. 4.178. EDS analysis of marked area in Fig. 4.178 (a) revealed that the corroded glass surfaces are enriched in multivalent elements such as Fe, Al and alkali. The precipitated products in hole are enriched in Ca and Ti and depleted in Fe and Si and other constituents of the glass as shown in Fig. 4.178 (b). The presence of higher amount of Ti indicates that these areas have higher concentration of the crystalline phases as Ti facilitates the nucleation of crystalline phases. These precipitates are not tightly bound to the glass surface and are easily removed by rinsing with water [126].

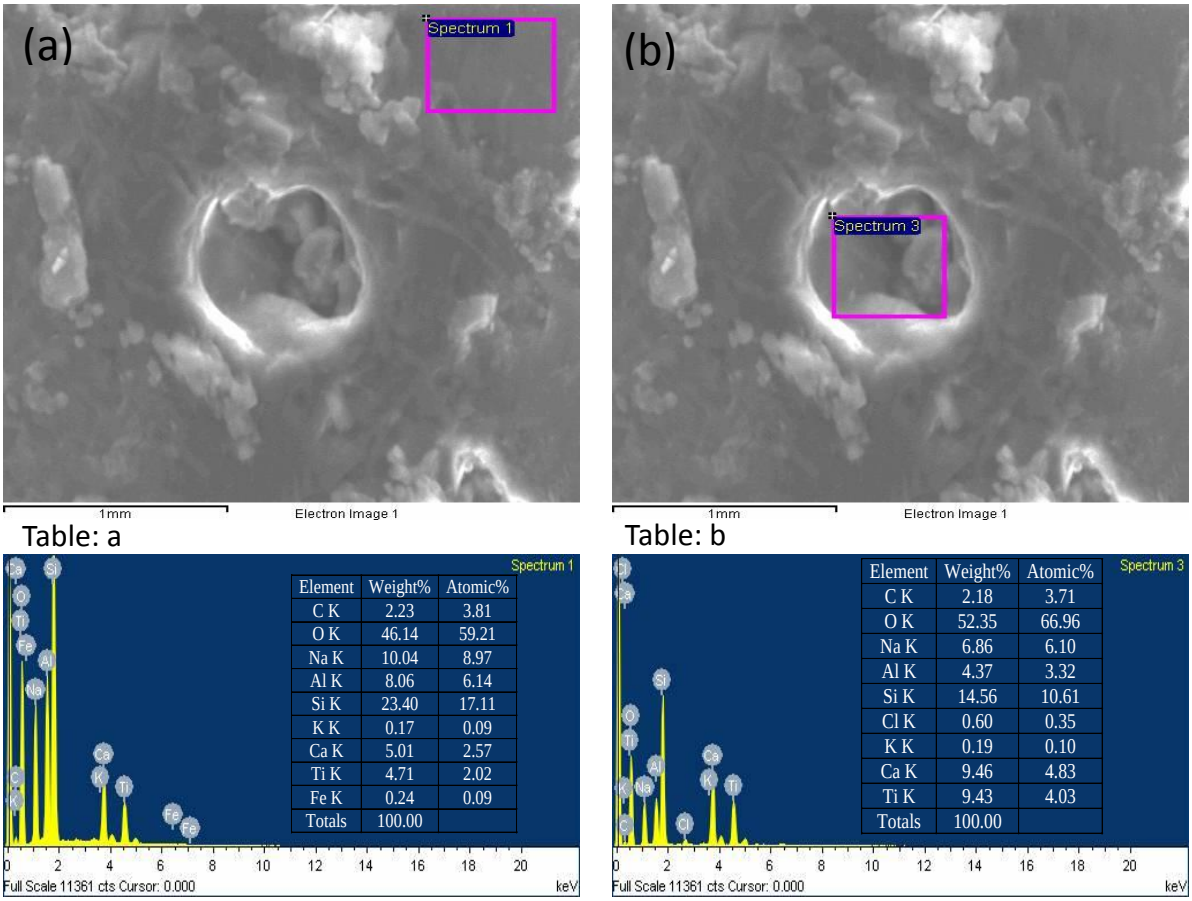

Fig. 4.178: SEM of the corroded diffusion couple of N-15 glass and crofer steel and correspondingly EDS analyses of the corroded region marked in the micrograph.

4.3.3.2. X glass and crofer steel

4.3.3.2.1. Electrochemical testing

An open circuit potential (OCP) measurement was taken for sample in 3.5% NaCl solution for two hours before measurement. The average value of OCP measurements are given in Table 4.18.

Table 4.18: Results of OCP measurement of diffusion couple of X glass with crofer steel.

Testing time (h)	OCP value (± 0.002V)
24	-0.468
265	-0.396
505	-0.381
745	-0.461

The OCP values show that glass coating goes under dissolution process in the starting. After that oxide layer is formed on the surface of glass which again dissolved after 745 h. Fig. 4.179 presents the polarization curves of 24 h, 265 h, 505 h and 745 h testing for diffusion couple of X glass and crofer steel in artificial seawater. Using the Tafel extrapolation method, the corrosion potential E_{corr}, corrosion current density I_{corr}, anodic/cathodic Tafel slopes β_a and β_c and polarization resistance R_p values are calculated from polarization curves and are given in Table 4.19.

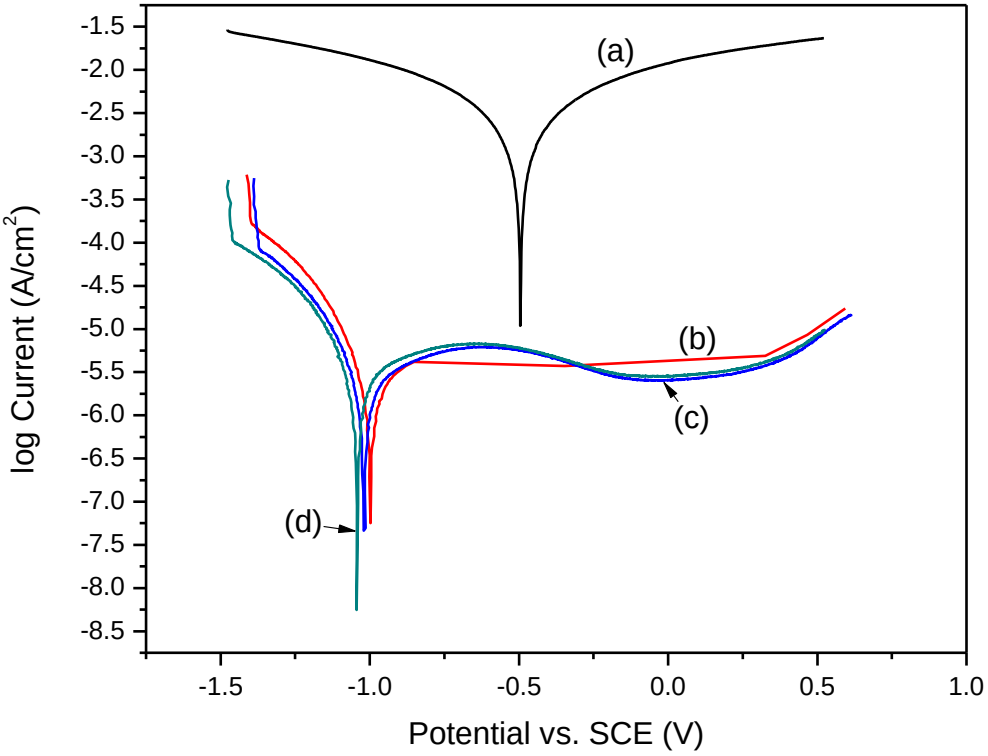

Fig. 4.179: Potentiodynamic polarization curves of (a) 24 h, (b) 265 h, (c) 544 h and (d) 745 h testing of diffusion couple for X glass and crofer steel in artificial seawater.

Table 4.19: Results of potentiodynamic polarization in diffusion couple of X glass with crofer steel.

Testing time (h)	E_{corr} (mV)	I_{corr} (μA cm^{-2})	β_c (mV/decade)	β_a (mV/decade)	R_p (Ω cm^2)	Corrosion rate (mm/year)
24	-494.81	1.18	305.0	311.1	0.39×10^5	3.44×10^{-3}
265	-978.73	0.002	170.0	422.5	15.6×10^6	5.82×10^{-6}
505	-1021.5	0.002	151.9	529.3	18.6×10^6	5.83×10^{-6}
745	-1044.7	0.003	175.6	602.2	16.5×10^6	8.74×10^{-6}

The corrosion rate is fast after 24 h of the testing. After that it decreases continuously and finally falls to the order × 10^{-6}. The Nyquist plots of diffusion couple of X glass and crofer steel are presented in Fig. 4.180. The diameter of the semicircle of 24 h is very less as compared to other measurements. Thus the corrosion resistant property of the coating is improved after 745 h due to the formation of passive film on the surface [127].

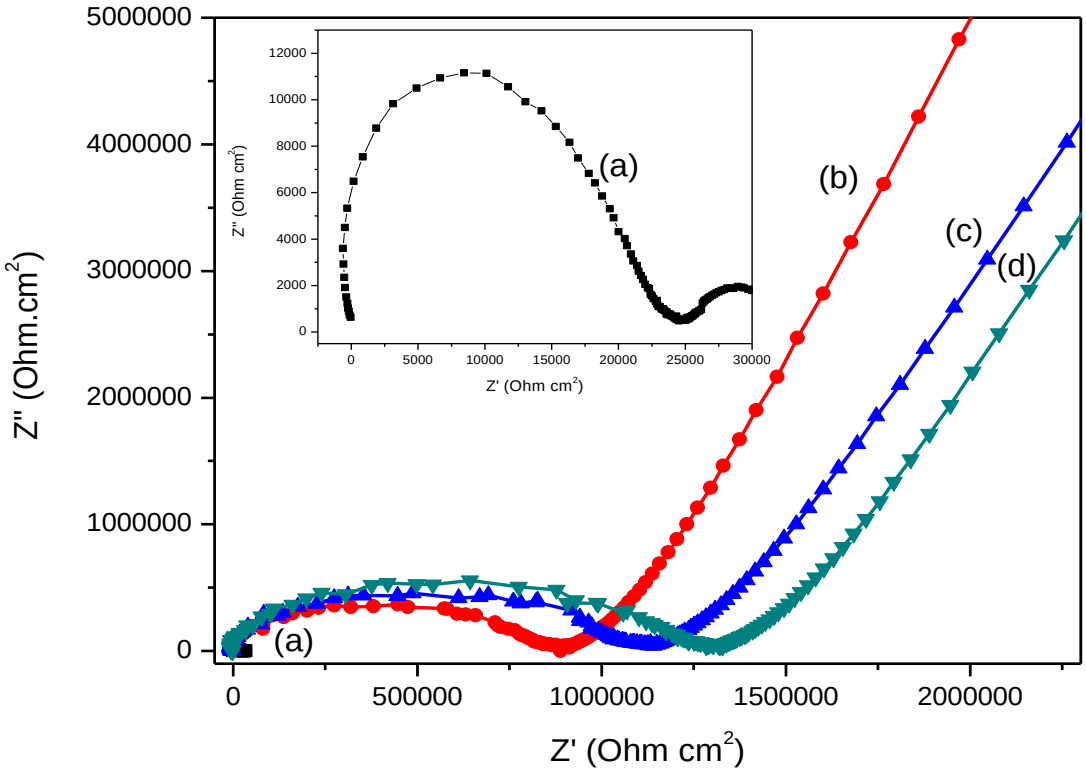

Fig. 4.180: Nyquist plots of (a) 24 h, (b) 265 h, (c) 505 h and (d) 745 h for diffusion couple of X glass and crofer steel in artificial seawater.

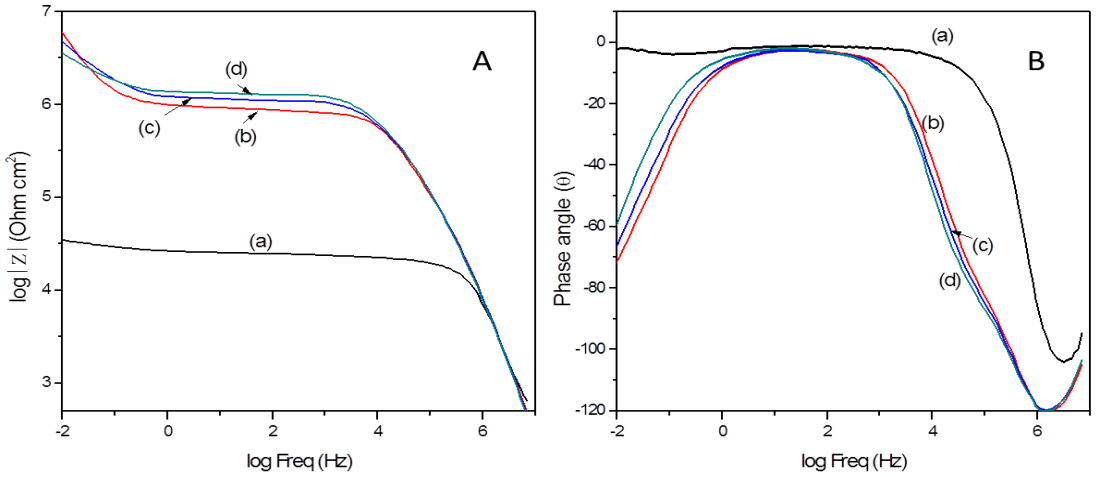

Fig. 4.181: (A) Log Z versus log Freq. plots and (B) Phase angle (Z) versus log Freq. plots of (a) 24 h, (b) 265 h, (c) 505 h and (d) 745 h for diffusion couple of X glass and crofer steel in artificial seawater.

From Fig. 4.181 (A), it can be observed that values of impedance of 265 h, 505 h and 745 h are very large as compared to 24 h measurement. Phase angle measurements again confirmed the presence of two time constants as shown in Fig. 4.181 (B). The fitting of electrochemical impedance data of the diffusion couple was obtained by using the $R_s(CPE_{dl}R_{ct} + CPE_cR_c)$ model [122], with two time constants as shown in Fig. 4.175. The obtained impedance spectrum was analyzed using a non-linear regression method, and the values of circuit parameters were estimated as given in Table 4.20.

Table 4.20: Electrochemical measurements of diffusion couple of X glass and crofer steel obtained by equivalent circuit.

Testing time (h)	R_s (Ω cm^2)	R_{ct} (Ω cm^2)	CPE_{dl} (μF cm^{-2})	n_{dl}	R_c (Ω cm^2)	CPE_c (μF cm^{-2})	n_c
24	10.5	0.23×10^5	14.9×10^{-12}	1	2885	40.1×10^{-12}	1
265	10	15.1×10^6	2.35×10^{-6}	1	0.9×10^6	24.9×10^{-12}	1
505	11	12.4×10^6	2.39×10^{-6}	1	1.2×10^6	24.8×10^{-12}	1
745	16	1.31×10^{12}	2.06×10^{-6}	0.74	1.3×10^6	25.6×10^{-12}	1

R_{ct} values of the X glass coating show remarkable difference as compared to N-15 glass coated on crofer steel. The increase in R_{ct} value of X glass coating on crofer steel indicate that X glass is more corrosion resistive as compared to N-15 glass.

4.3.3.2.2. Structural analysis

Photograph of diffusion couple of X glass with crofer steel after corrosion testing for 745 h in 3.5% NaCl is shown in Fig. 4.182.

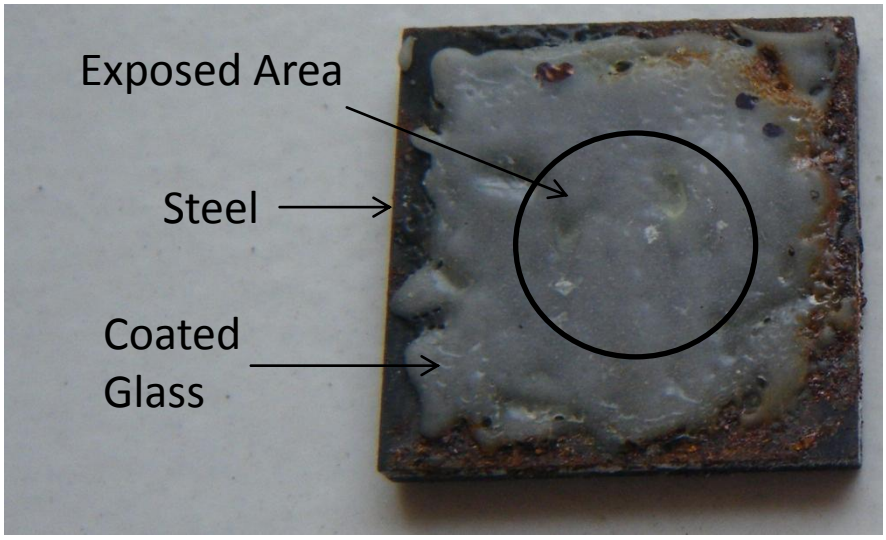

Fig. 4.182: Photograph of X glass coated on crofer steel after corrosion testing for 745 h in 3.5% NaCl solution.

The circular marked area shown in Fig. 4.182 is exposed for corrosion testing. Apparently, there is no difference between exposed and non-exposed areas. Coated glass is stable even after 745 h exposure. However, glass coating got shrinked during heat treatment. The glass layer becomes denser and form to white film at 700 °C. This change is observed due to the transformation of the glass into glass ceramic [128]. In order to see microscopic level changes, scanning electron micrographs of this area was taken as shown in Fig. 4.183. Surface of glass coating appeared to be smooth at low magnification as shown in Fig. 4.183 (a). At higher magnification, small pits were observed as shown in Fig. 4.183 (b & c). The agglomeration of particles was detected on the surface of the coating (Fig. 4.183 (d)). EDS analysis of the dissolved surface and the precipitates on the corroded glass is given in Fig. 4.184. Fig. 4.184 (a) shows that the corroded glass surface is enriched in multivalent elements such as Si, O and alkali and depleted in Fe. The precipitated products are enriched in S, Cl, Fe and O and depleted in Si as shown in Fig. 4.184 (b) indicating the formation of corrosion product on the surface of the glass.

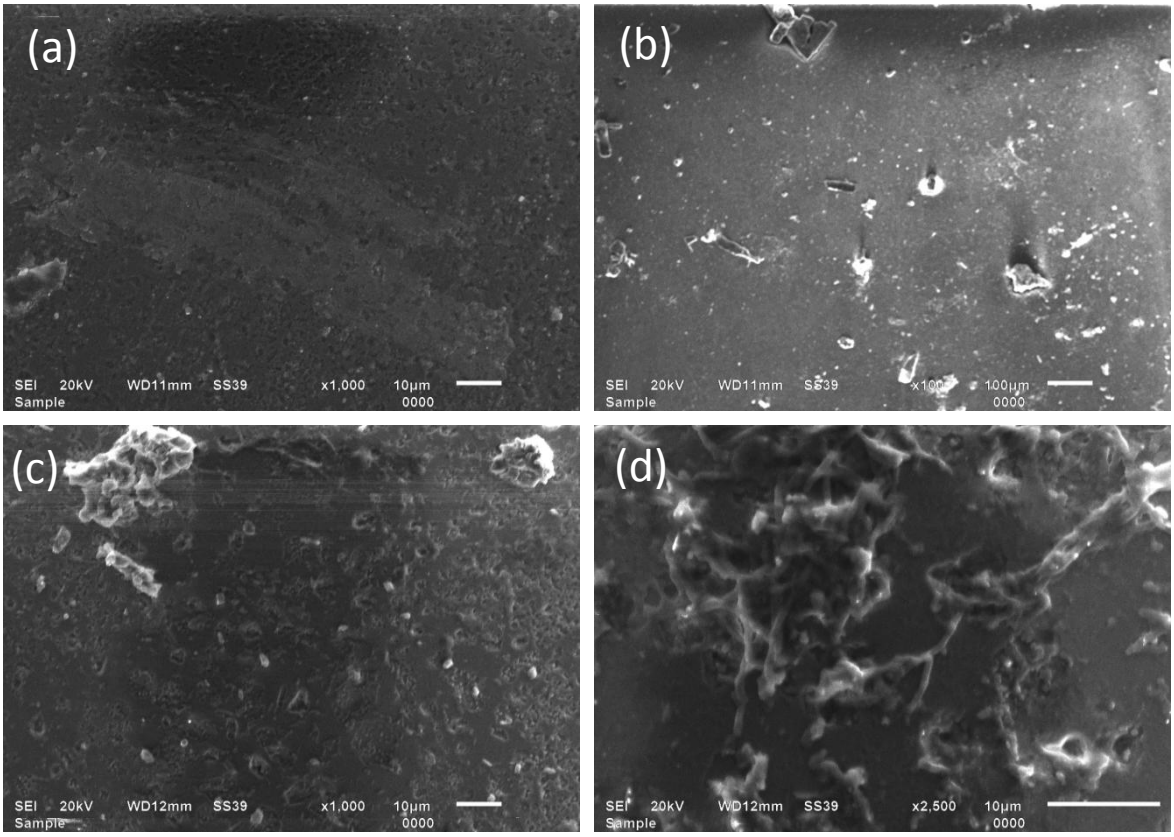

Fig. 4.183: Scanning electron micrographs of the corroded diffusion couple of X glass coated on crofer steel.

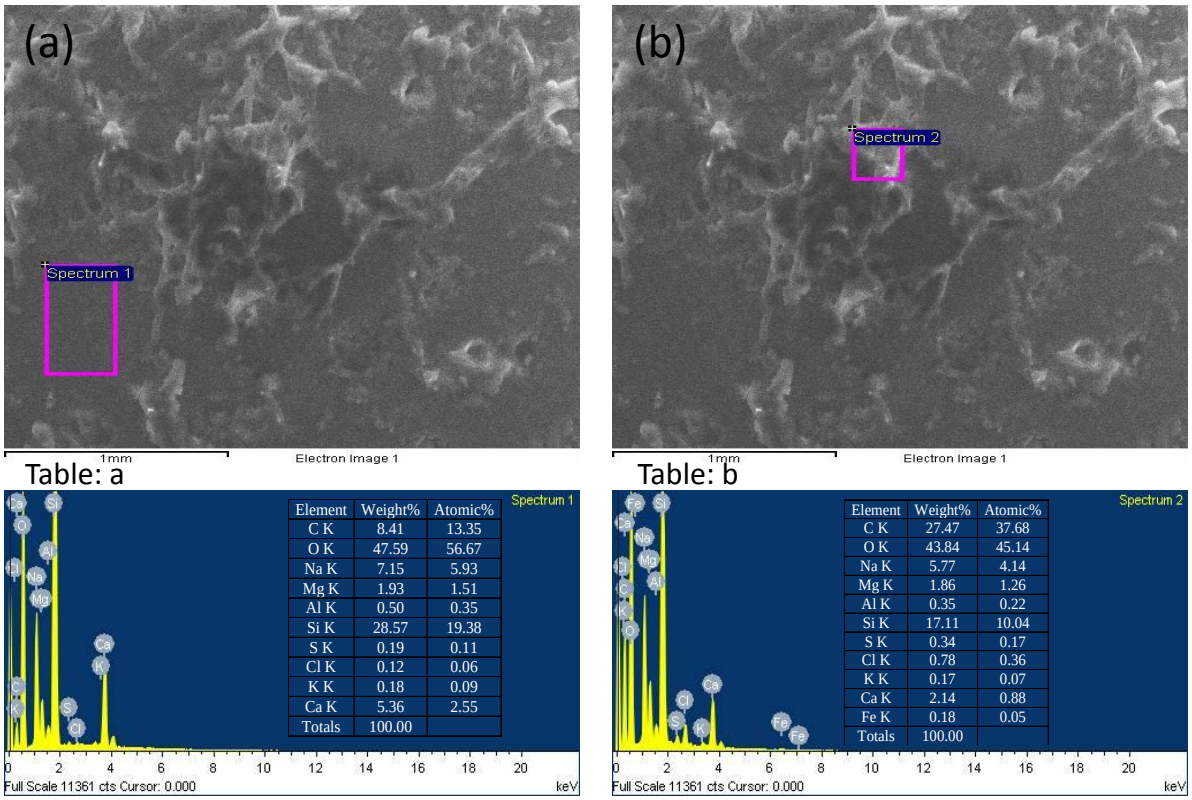

Table: a

Element	Weight%	Atomic%
C K	8.41	13.35
O K	47.59	56.67
Na K	7.15	5.93
Mg K	1.93	1.51
Al K	0.50	0.35
Si K	28.57	19.38
S K	0.19	0.11
Cl K	0.12	0.06
K K	0.18	0.09
Ca K	5.36	2.55
Totals	100.00	

Table: b

Element	Weight%	Atomic%
C K	27.47	37.68
O K	43.84	45.14
Na K	5.77	4.14
Mg K	1.86	1.26
Al K	0.35	0.22
Si K	17.11	10.04
S K	0.34	0.17
Cl K	0.78	0.36
K K	0.17	0.07
Ca K	2.14	0.88
Fe K	0.18	0.05
Totals	100.00	

Fig. 4.184: SEM of the corroded diffusion couple of X glass and crofer steel and correspondingly EDS analyses of the corroded region marked in the micrograph.

4.3.3.3. S glass and crofer steel

The high corrosion resistance of glass leads to outstanding application potentials in marine environment in place of traditional crystalline materials [129]. The testing of commercial grade S glass coated on crofer steel is presented here.

4.3.3.3.1. Electrochemical testing

The average value of OCP measurements are given in Table 4.21.

Table 4.21: Results of OCP measurement of diffusion couple of S glass with crofer steel.

Testing time (h)	OCP value (± 0.002V)
24	0.014
265	0.128
505	0.134
745	-0.144

The OCP values show that glass coating goes under dissolution process in the starting. After that oxide layer formed on the surface of glass which again dissolved after 745 h. Fig. 4.185 presents the polarization curves of 24 h, 505 h and 745 h testing for diffusion couple of S glass and crofer steel in artificial seawater. The calculated values of different variables are calculated using polarization curves and summarized in Table 4.22.

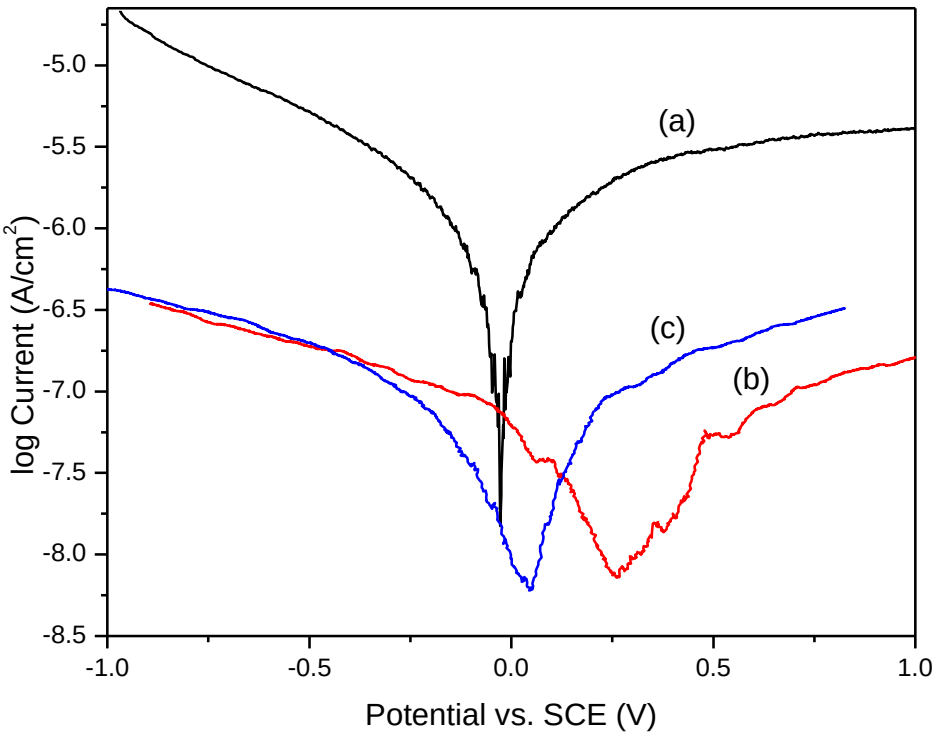

Fig. 4.185: Potentiodynamic polarization curves of (a) 24 h, (b) 505 h and (c) 745 h testing of diffusion couple for S glass and crofer steel in artificial seawater.

Table 4.22: Results of potentiodynamic polarization in diffusion couple of S glass with crofer steel.

Testing time (h)	E_{corr} (mV)	I_{corr} (μA cm^{-2})	β_c (mV/decade)	β_a (mV/decade)	R_p (Ω cm^2)	Corrosion rate (mm/year)
24	-31.2	0.0004	290.7	361.0	0.14×10^9	1.19×10^{-6}
505	298.2	0.000005	212.2	182.2	8.98×10^9	14.57×10^{-9}
745	11.76	0.000008	187.8	212.0	19.8×10^9	23.3×10^{-9}

The corrosion rate of S glass on crofer steel is very less. The 745 h result exhibits corrosion rate of 23.3×10^{-9} mm per year. Also the value of R_p is very high as compared to N-15 and X glass coatings. These facts clearly indicate the superiority of the S glass coating on crofer steel. The impedance spectra of diffusion couple of X glass and crofer steel are presented in Fig. 4.186.

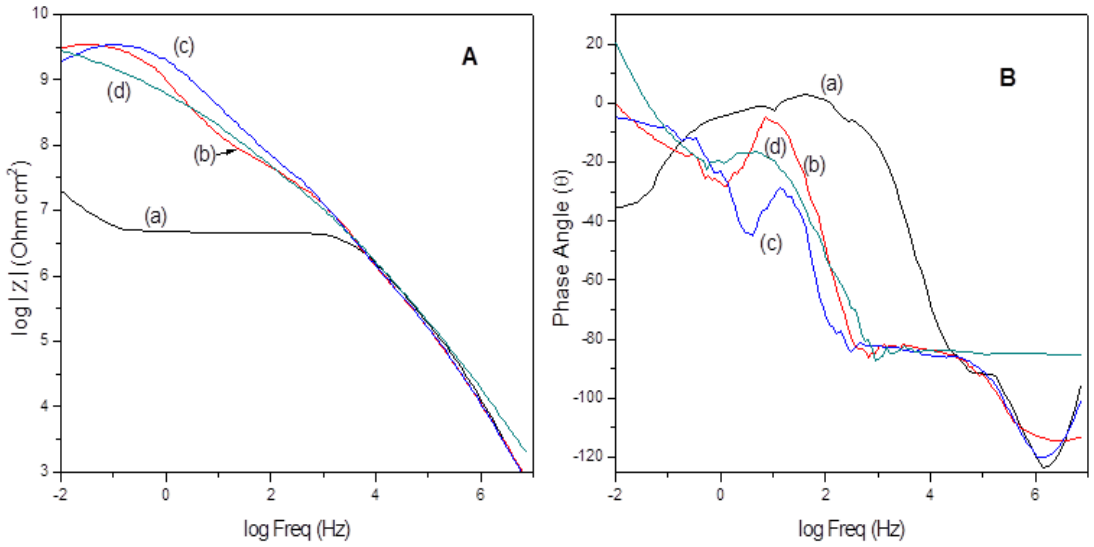

Fig. 4.186: (A) Log Z versus log Freq. plots and (B) Phase angle (Z) versus log Freq. plots of (a) 24 h, (b) 265 h, (c) 505 h and (d) 745 h for diffusion couple of S glass and crofer steel in artificial seawater.

The fitted values of circuit parameters were estimated and is given in Table 4.23.

Table 4.23: Electrochemical measurements of diffusion couple of S glass and crofer steel obtained by equivalent circuit.

Testing time (h)	R_s (Ω cm^2)	R_{ct} (Ω cm^2)	CPE_{dl} (μF cm^{-2})	n_{dl}	R_c (Ω cm^2)	CPE_c (μF cm^{-2})	n_c
24	11	4.34×10^6	0.56×10^{-6}	0.66	3.3×10^9	15.6×10^{-12}	1
265	11.3	1.9×10^6	2.3×10^{-9}	0.06	3.2×10^7	27.1×10^{-12}	0.9
505	13	53.6×10^6	0.12×10^{-6}	0.47	2.7×10^9	76.7×10^{-12}	0.9
745	15	1.42×10^9	0.36×10^{-9}	1	13.6×10^6	22.7×10^{-12}	0.9

The increased R_{ct} value and decreased CPE_{dl} value after 745 h measurement proved that the S glass coating improve the corrosion resistance of the steel and best suitable as compared to N-15 and X glass coating.

4.3.3.3.2. Structural analysis

Photographic image of diffusion couple of S glass with crofer steel after corrosion testing for 745 h in 3.5% NaCl is shown in Fig. 4.187.

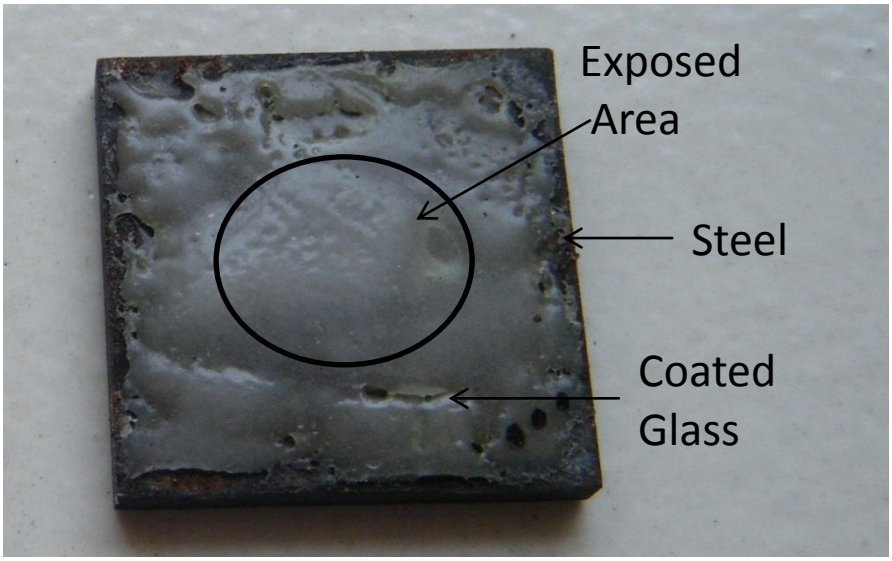

Fig. 4.187: Photograph of S glass coated on crofer steel after corrosion testing for 745 h in 3.5% NaCl solution.

The circular marked area was exposed for corrosion testing. Visual examination shows that there is no remarkable difference between exposed and un-exposed areas. Coated glass is stable even after 745 h exposure. In order to see microscopic level changes, scanning electron micrographs of this area was taken as shown in Fig. 4.188. Surface of glass coating appeared to be smooth at low magnification as shown in Fig. 4.188 (a). At higher magnification, formation of oxide layer was observed as shown in Fig. 4.188 (b). The crystals of NaCl were identified from mirror like transparency. The pits were also observed in another area as shown in Fig. 4.188 (c). The agglomeration of particles was detected on the surface of the coating (Fig. 4.188 (d)). EDS analysis was done on the surface of glass and also on the corrosion product as shown in Fig. 4.189. The corroded glass surface was enriched in the constituents of the glass and depleted in Fe as shown in Fig. 4.189 (a). The presence of Fe, Ca and Mg with O in the analysis indicates the formation of oxide layer on the glass surface as shown in Fig. 4.189 (b) [130].

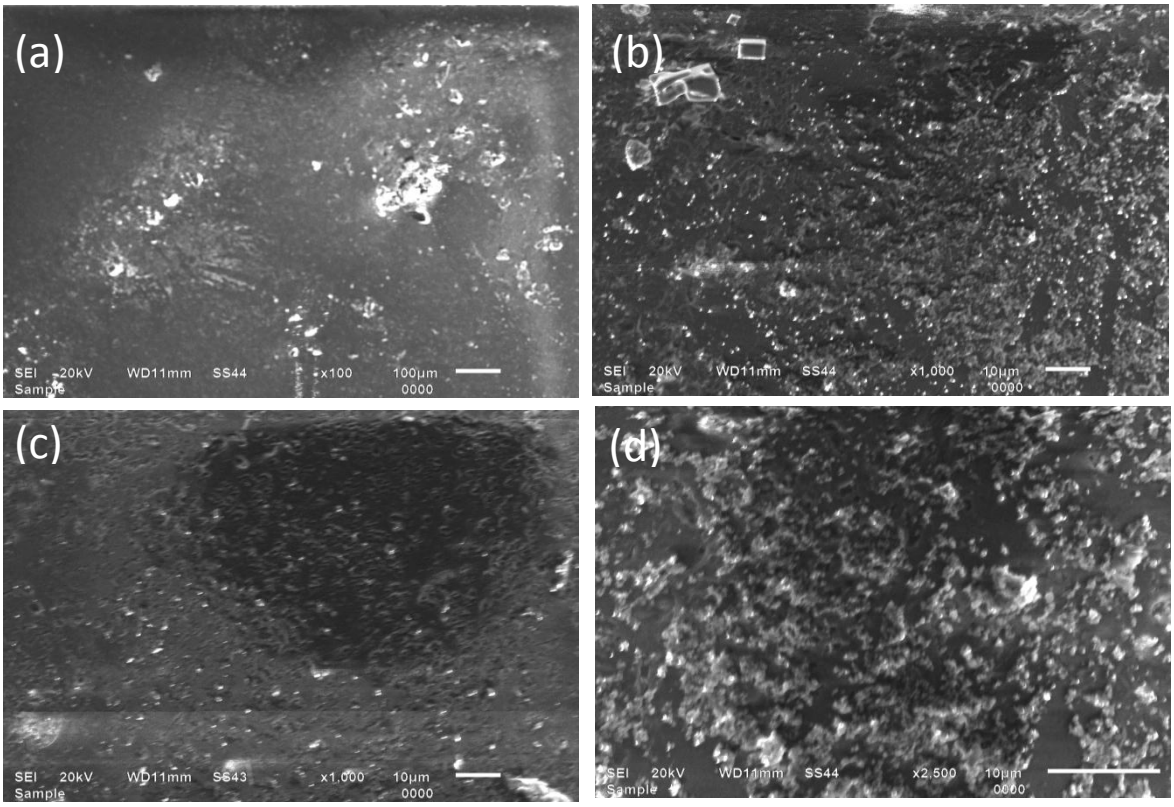

Fig. 4.188: SEM of the corroded diffusion couple of S glass coated on crofer steel.

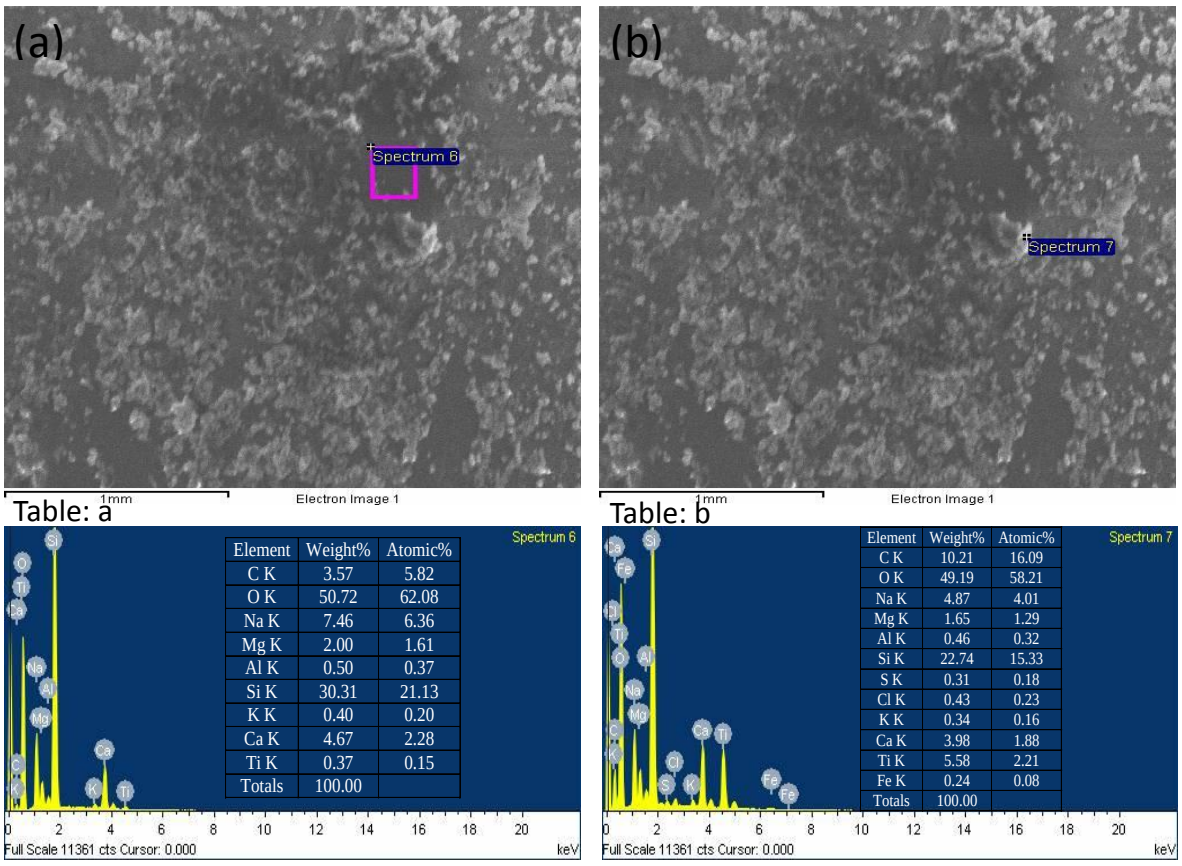

Fig. 4.189: SEM of the corroded diffusion couple of S glass and crofer steel and correspondingly EDS analyses of the corroded region marked in the micrograph.

4.3.3.4. X glass and duplex steel

4.3.3.4.1. Electrochemical testing

The average value of OCP measurements are given in Table 4.24.

Table 4.24: Results of OCP measurement of diffusion couple of X glass with duplex steel.

Testing time (h)	OCP value (± 0.002V)
24	-0.416
360	-0.406
745	-0.422

The OCP values show that glass coating goes under dissolution process in the starting. After that oxide layer formed on the surface of glass. Fig. 4.190 presents the polarization curves of 24 h, 360 h and 745 h testing for diffusion couple of X glass and duplex steel in artificial seawater. The results are given in Table 4.25.

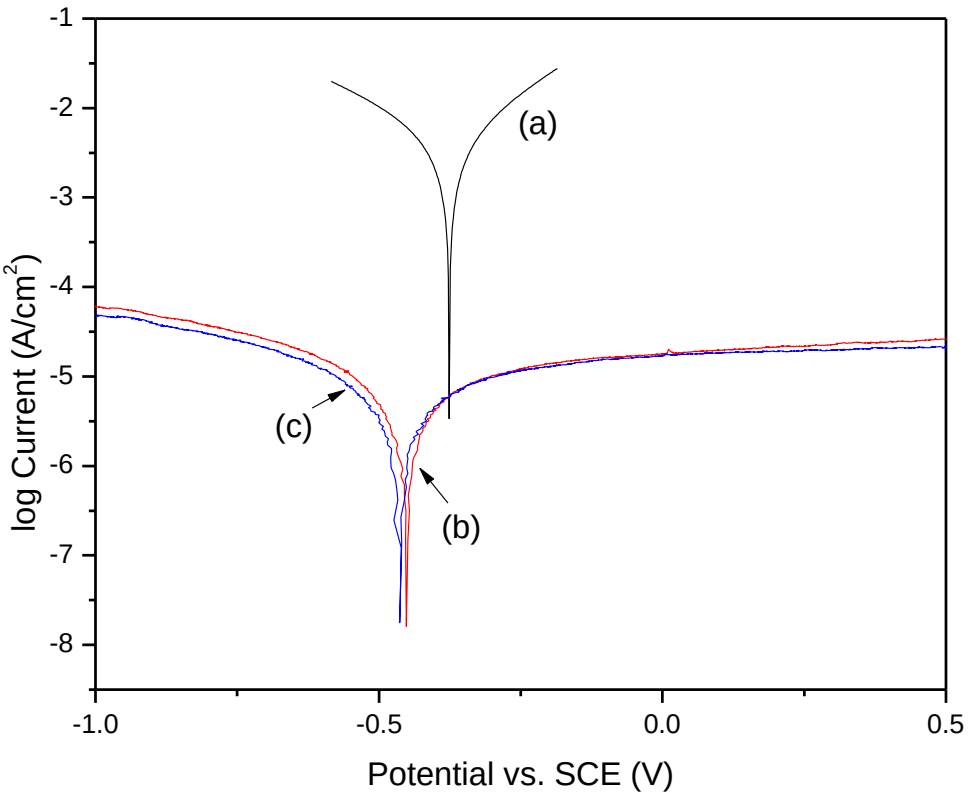

Fig. 4.190: Potentiodynamic polarization curves of (a) 24 h, (b) 360 h and (c) 745 h testing of diffusion couple for X glass and duplex steel in artificial seawater.

Table 4.25: Results of potentiodynamic polarization in diffusion couple of X glass with duplex steel.

Testing time (h)	E_{corr} (mV)	I_{corr} (μA cm^{-2})	β_c (mV/decade)	β_a (mV/decade)	R_p (Ω cm^2)	Corrosion rate (mm/year)
24	-374.9	3.4	266.3	205.5	0.11×10^5	8.0×10^{-3}
360	-445.9	0.005	304.3	459.9	11×10^6	11.7×10^{-6}
745	-458.1	0.004	310.3	420.3	12.1×10^6	8.3×10^{-6}

The corrosion rate is fast after 24 h testing which further decreases and fall in order $\times 10^{-6}$. The Nyquist plots of diffusion couple of X glass and duplex steel are presented in Fig. 4.191. The diameter of the semicircle of the 745 h measurement is large as compared to 24 h measurement which proves the improvement of the corrosion resistance of the glass coating.

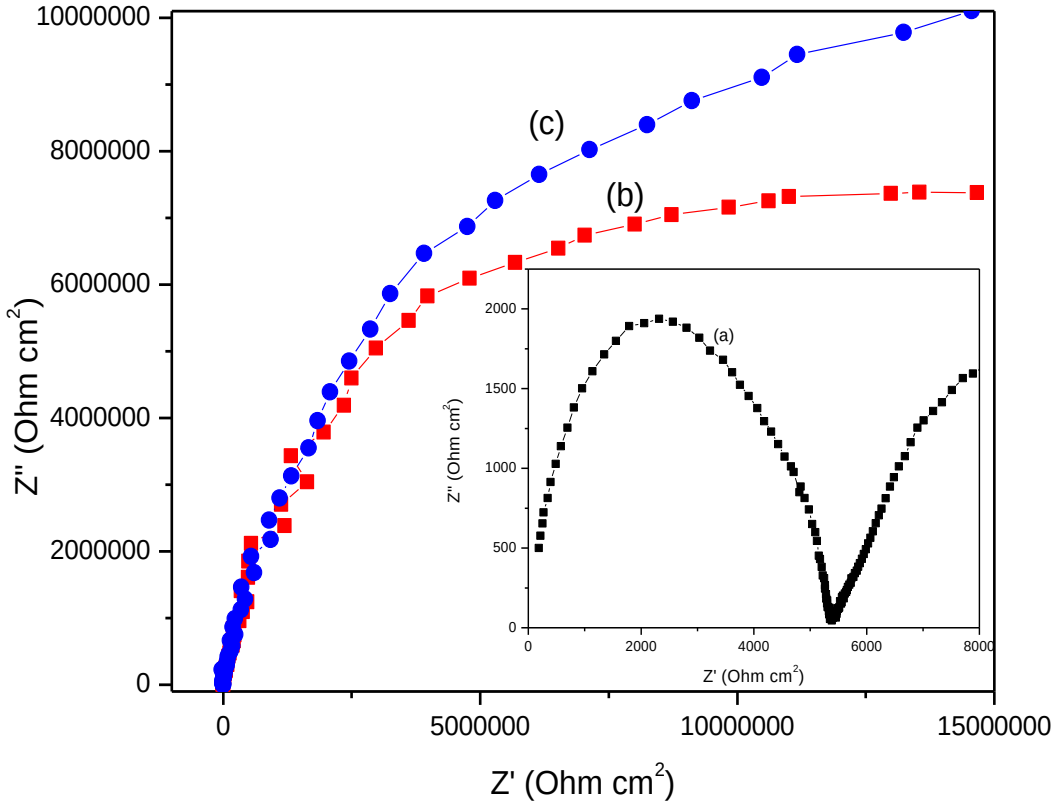

Fig. 4.191: Nyquist plots of (a) 24 h, (b) 360 h and (c) 745 h for diffusion couple of X glass and duplex steel in artificial seawater.

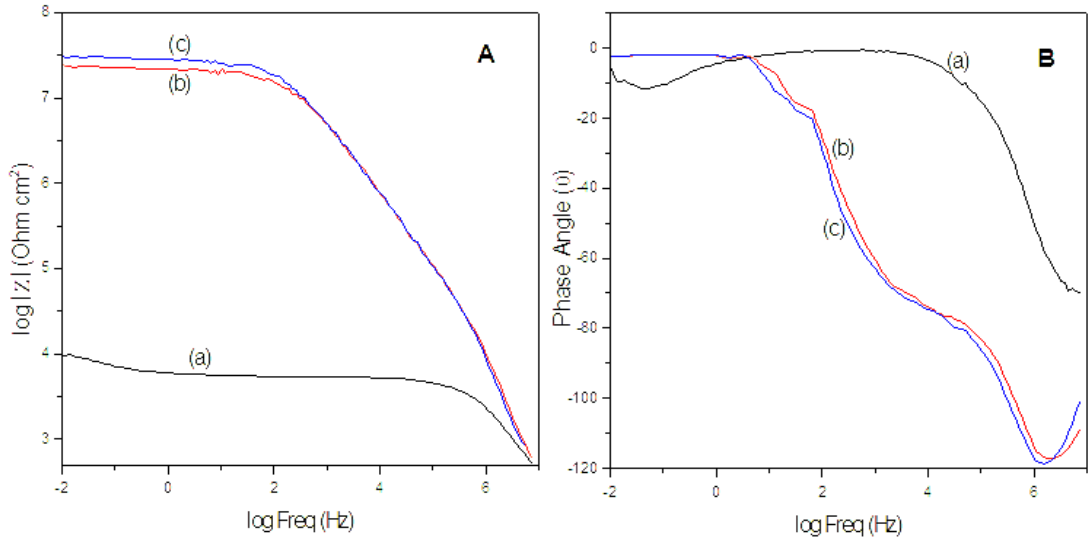

Fig. 4.192: (A) Log Z versus log Freq. plots and (B) Phase angle (Z) versus log Freq. plots of (a) 24 h, (b) 360 h and (d) 745 h for diffusion couple of X glass and duplex steel in artificial seawater.

The impedance value after 745 h is maximum and phase angle values become linear at lower frequency range as shown in Fig. 4.192. The fitted values of circuit parameters were estimated as given in Table 4.26.

Table 4.26: Electrochemical measurements of diffusion couple of X glass and duplex steel obtained by equivalent circuit.

Testing time (h)	R_s (Ω cm^2)	R_{ct} (Ω cm^2)	CPE_{dl} (μF cm^{-2})	n_{dl}	R_c (Ω cm^2)	CPE_c (μF cm^{-2})	n_c
24	15.15	0.36×10^5	0.51×10^{-3}	0.37	5190	0.55×10^{-9}	0.85
360	14	21.9×10^6	0.17×10^{-9}	0.42	3687	0.11×10^{-9}	0.84
745	12	32.2×10^6	52.6×10^{-12}	0.74	0.46×10^6	82.9×10^{-12}	0.86

The lowest value of CPE_{dl} after 745 h again confirmed the corrosion resistive nature of the coating.

4.3.3.4.2. Structural analysis

Photograph of diffusion couple of X glass with duplex steel after corrosion testing for 745 h in 3.5% NaCl is shown in Fig. 4.193.

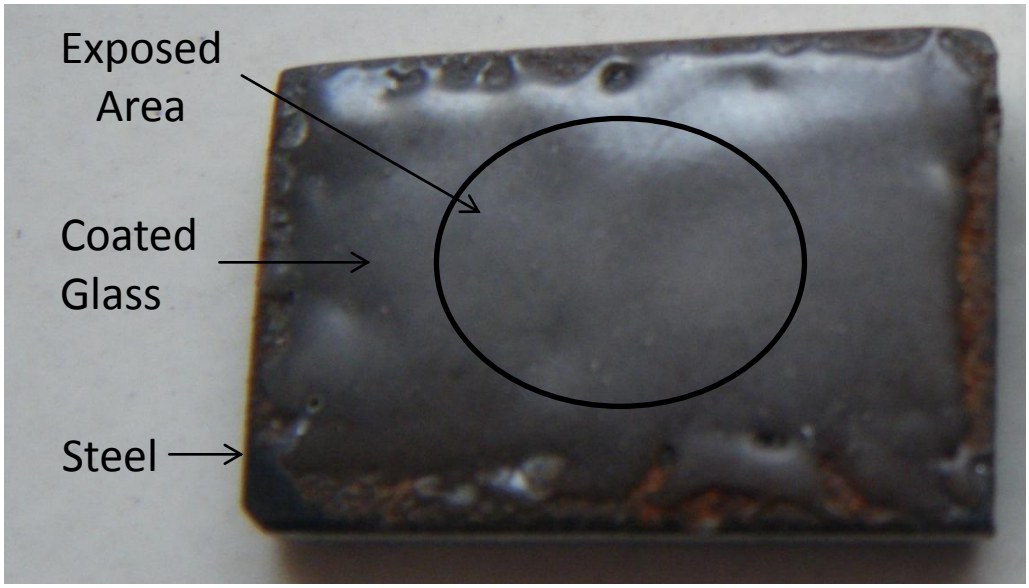

Fig. 4.193: Photograph of X glass coated on duplex steel after corrosion testing for 745 h in 3.5% NaCl solution.

Corrosive products at the periphery of the sample were due to atmospheric moisture. In order to see microscopic level changes, SEM of this area was done as shown in Fig. 4.194. Surface of glass coating appeared to corrode as shown in Fig. 4.194 (a). There were two types of area found on the surface of the glass. One exhibiting pits because of dissolution of glass and other was accumulation of corrosive products [131]. The corrosive precipitates on the surface of the coated glass have faceted structure (Fig. 4.194 (b)).

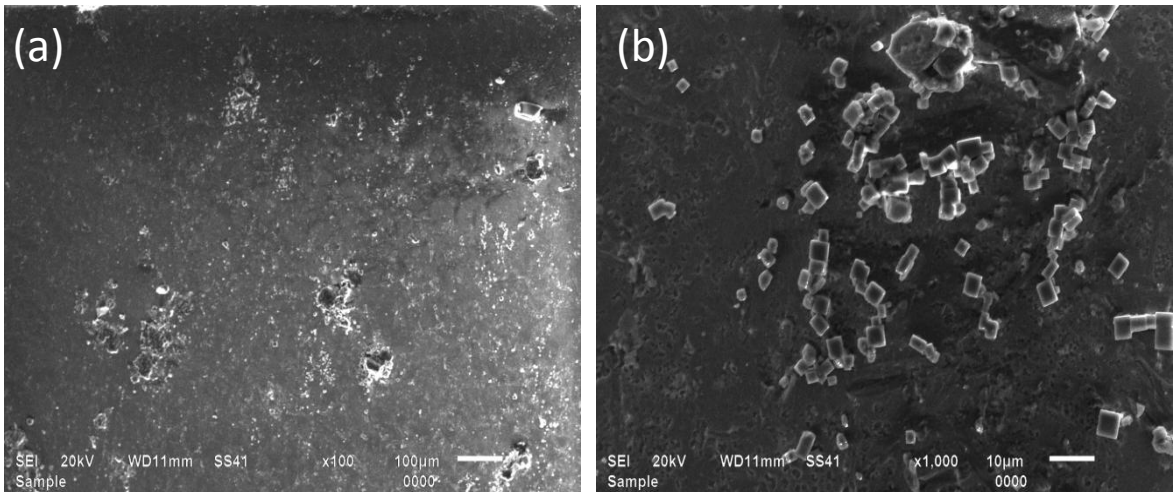

Fig. 4.194: SEM of the corroded diffusion couple of X glass coated on duplex steel.

In order to quantify the nature of the surface, EDS analysis was done on the surface of glass and on the precipitates as shown in Fig. 4.195. The corroded glass surface was enriched in the oxygen and Fe as shown in Fig. 4.195 (a). The presence of Fe, Ca and Mg with O in the analysis indicates the formation of corrosion product on the surface of glass as shown in Fig. 4.195 (b).

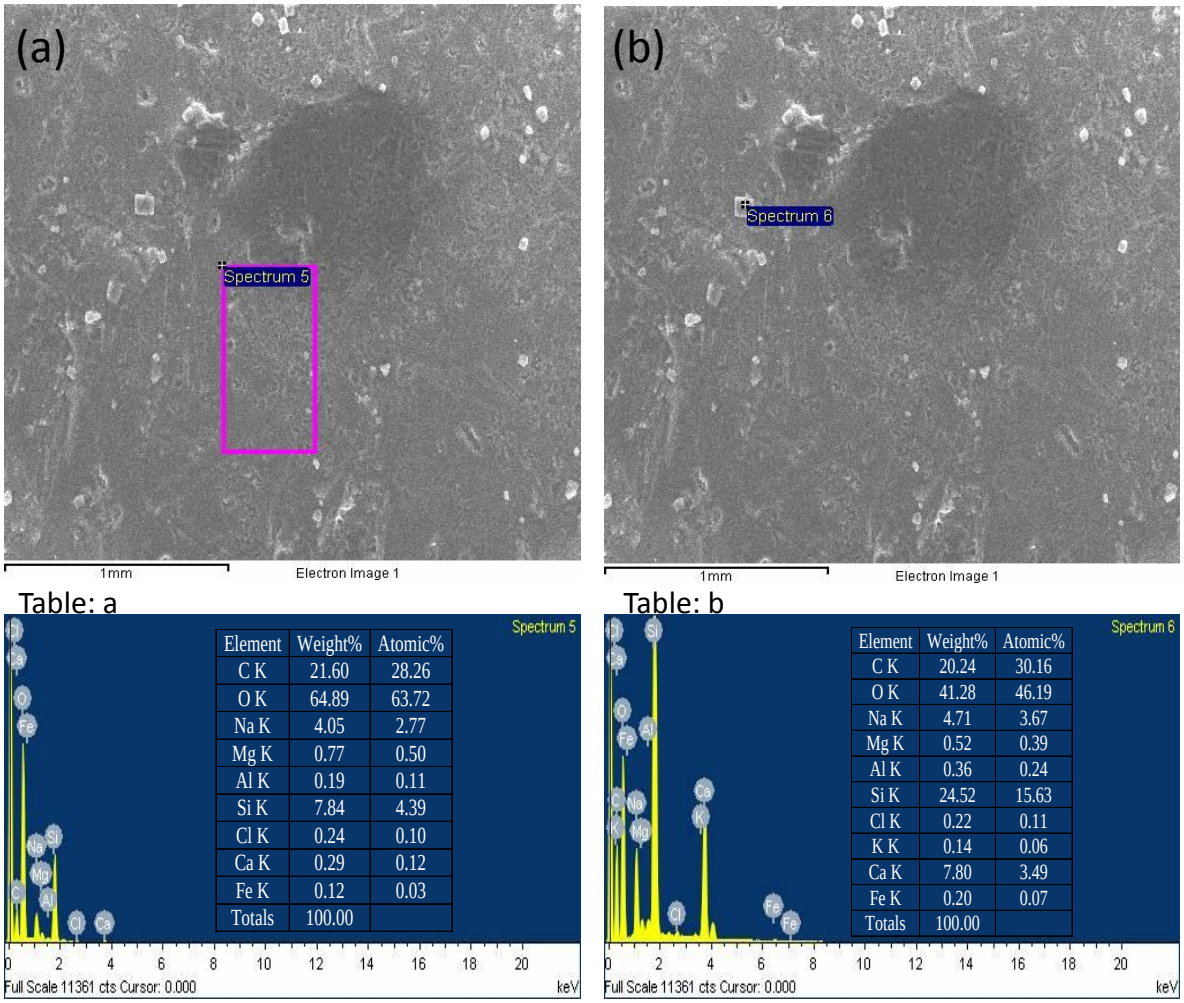

Fig. 4.195: SEM of the corroded diffusion couple of X glass and duplex steel and correspondingly EDS analyses of the corroded region marked in the micrograph.

4.3.3.5. S glass and duplex steel

4.3.3.5.1 Electrochemical testing

The average value of OCP measurements are given in Table 4.27.

Table 4.27: Results of OCP measurement of diffusion couple of S glass with duplex steel.

Testing time (h)	OCP value (± 0.002V)
24	0.151
360	0.049
745	0.041

The OCP values of S glass coating shows downward trend which indicates that the glass undergoes dissolution process and does not form oxide layer. Fig. 4.196 presents the polarization curves of 24 h, 360 h and 745 h testing for diffusion couple of S glass and duplex steel in artificial seawater. Using the Tafel extrapolation method, the corrosion potential E_{corr}, corrosion

current density I_{corr}, anodic/cathodic Tafel slopes β_a and β_c and polarization resistance R_p values were calculated from polarization curves and are given in Table 4.28.

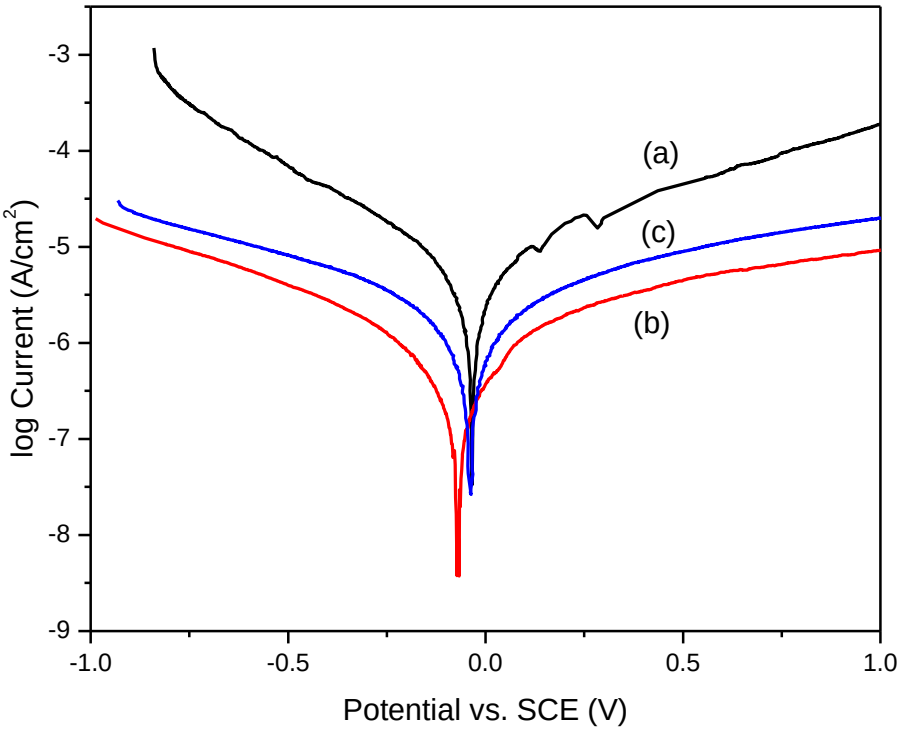

Fig. 4.196: Potentiodynamic polarization curves of (a) 24 h, (b) 360 h and (c) 745 h testing of diffusion couple for S glass and duplex steel in artificial seawater.

Table 4.28: Results of potentiodynamic polarization in diffusion couple of S glass with duplex steel.

Testing time (h)	E_{corr} (mV)	I_{corr} (μA cm^{-2})	β_c (mV/decade)	β_a (mV/decade)	R_p (Ω cm^2)	Corrosion rate (mm/year)
24	-36.0	0.003	278.7	353.2	14.5×10^6	6.24×10^{-6}
360	-57.7	0.0002	250.4	221.4	0.71×10^9	0.45×10^{-6}
745	-40.1	0.0007	301.1	318.6	0.06×10^9	1.6×10^{-6}

The corrosion rate of S glass coating is more as compared to X glass coated on crofer steel which is considerably less than that of the siloxane hybrid and sodium silicate conversion coating [132-134]. The Nyquist plots of diffusion couple of S glass and duplex steel are presented in Fig. 4.197. The diameter of the semicircle after 745 h measurement is large as compared to 24 h measurement which proves the improvement of the corrosion resistance of the glass coating.

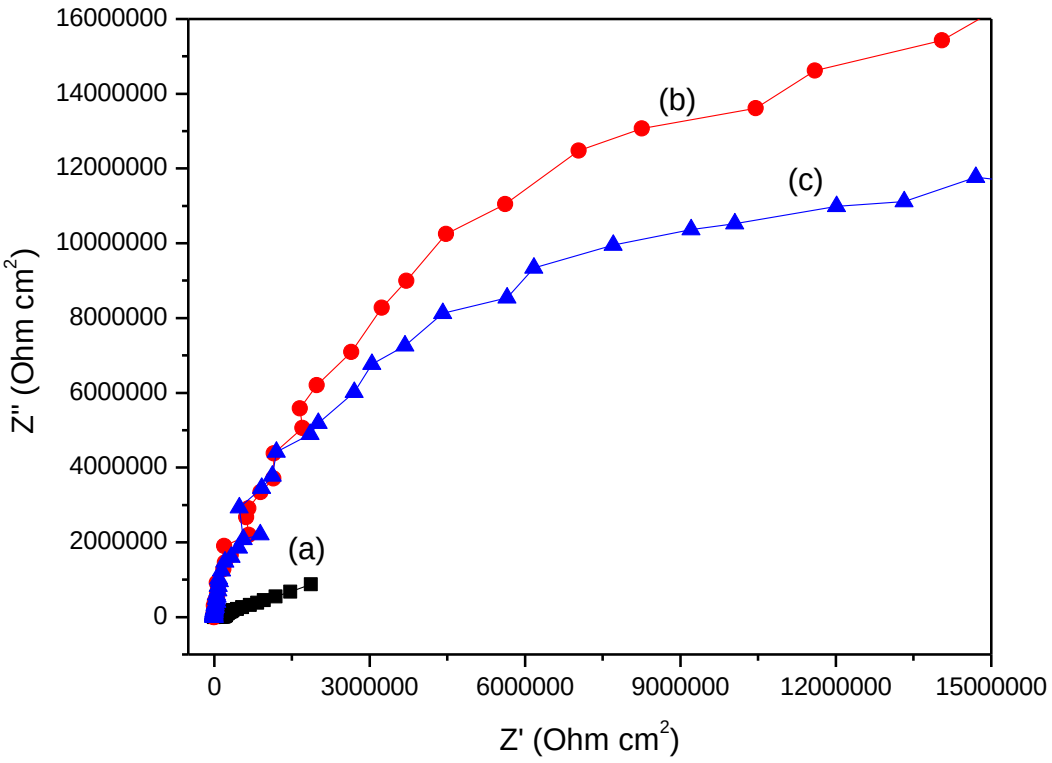

Fig. 4.197: Nyquist plots of (a) 24 h, (b) 360 h and (c) 745 h for diffusion couple of S glass and duplex steel in artificial seawater.

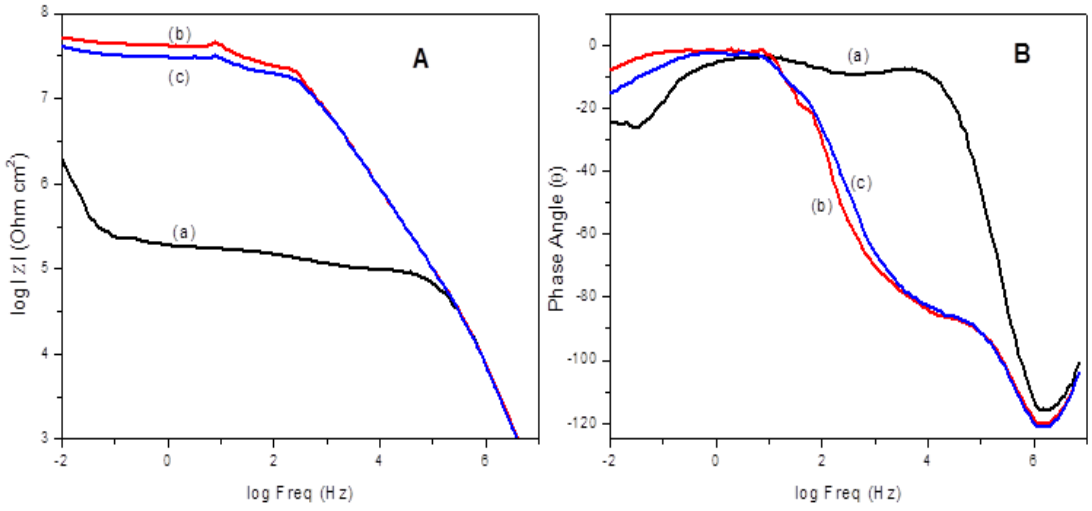

Fig. 4.198: (A) Log Z versus log Freq. plots and (B) Phase angle (Z) versus log Freq. plots of (a) 24 h, (b) 360 h and (d) 745 h for diffusion couple of S glass and duplex steel in artificial seawater.

The impedance value after 745 h is maximum as compared to 24 h measurement and phase angle values confirmed the presence of two time constants as shown in Fig. 4.198. The fitted values of circuit parameters were estimated as given in Table 4.29.

Table 4.29: Electrochemical measurements of diffusion couple of S glass and duplex steel obtained by equivalent circuit.

Testing time (h)	R_s (Ω cm^2)	R_{ct} (Ω cm^2)	CPE_{dl} (μF cm^{-2})	n_{dl}	R_c (Ω cm^2)	CPE_c (μF cm^{-2})	n_c
24	10.3	0.21×10^6	3.4×10^{-6}	0.2	97503	4.7×10^{-9}	0.6
360	14.4	28.1×10^6	5.87×10^{-12}	0.02	5625	25.5×10^{-12}	1
745	12	0.42×10^6	6.6×10^{-12}	0.9	19.0×10^6	51.5×10^{-12}	0.9

The value of R_{ct} after 745 h of S glass coating is less as compared to X glass coating on the duplex steel. Thus X glass coating is more suitable for duplex steel.

4.3.3.5.2. Structural analysis

Photograph of diffusion couple of S glass with duplex steel after corrosion testing for 745 h in 3.5% NaCl is shown in Fig. 4.199.

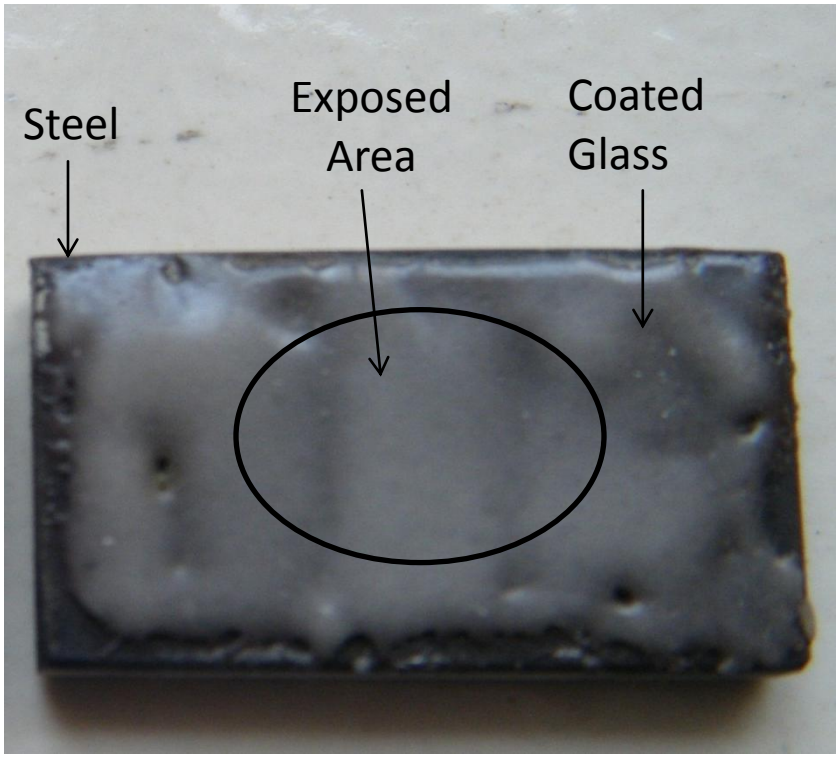

Fig. 4.199: Photograph of S glass coated on duplex steel after corrosion testing for 745 h in 3.5% NaCl solution.

Fig. 4.199 shows that there is no remarkable difference between exposed and unexposed areas by visual observation. Coated glass is stable even after 745 h exposure. In order to see the microscopic level changes, SEM of this area was done as shown in Fig. 4.207. Surface of glass

coating appeared to corrode as shown in Fig. 4.200 (a). There were two types of area found on the surface of the glass. One was of dissolved glass and other was accumulation of corrosive products [131]. The corrosive precipitates on the surface of the coated glass have faceted structure (Fig. 4.200 (b)). At higher magnification, dissolution of glass was clearly observed as shown in Fig. 4.200 (c).

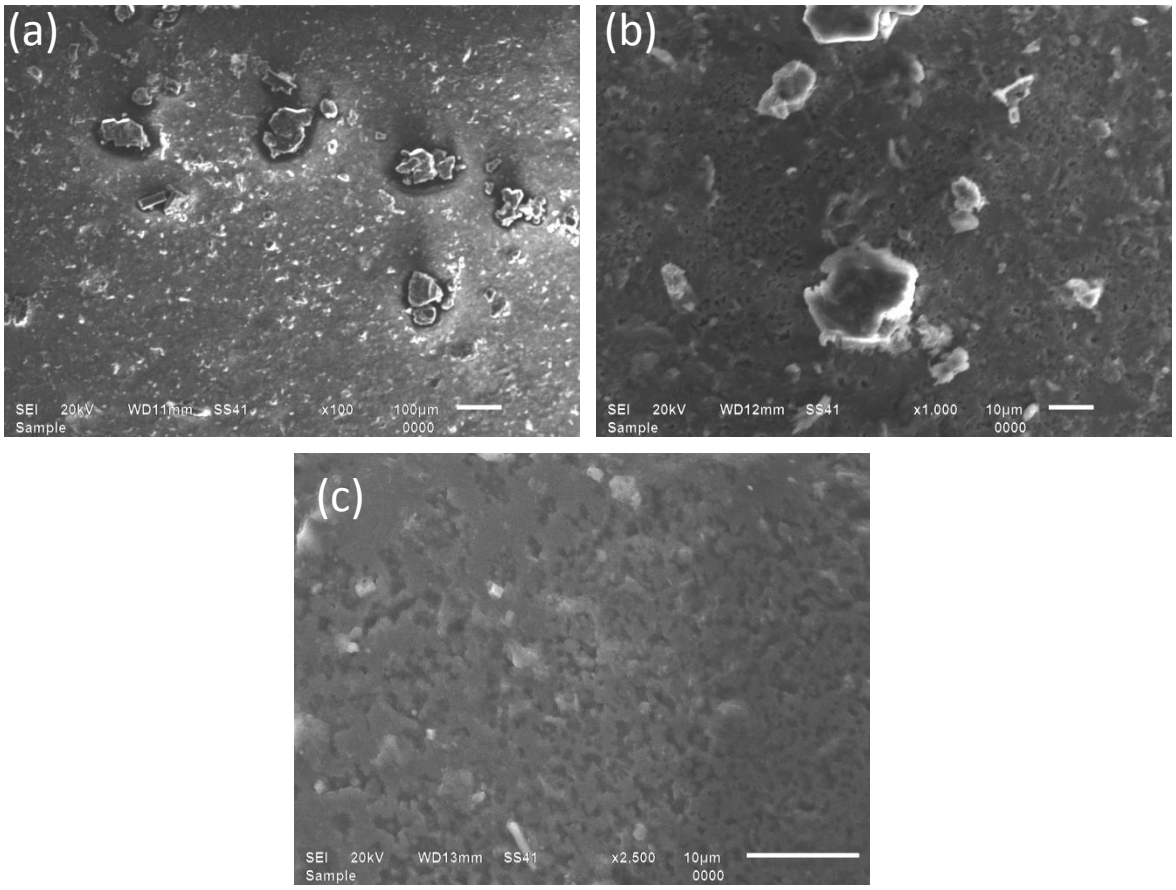

Fig. 4.200: Scanning electron micrographs of the corroded diffusion couple of S glass coated on duplex steel.

In order to quantify the nature of the surface, EDS analysis was done on the surface of glass and on the precipitates as shown in Fig. 4.201. The corroded glass surface was enriched in the oxygen and Fe as shown in Fig. 4.201 (a). The presence of Cl in the analysis indicates the penetration of chloride ions through the glass coating and susceptibility of the base to chloride attack as shown in Fig. 4.201 (b) [135].

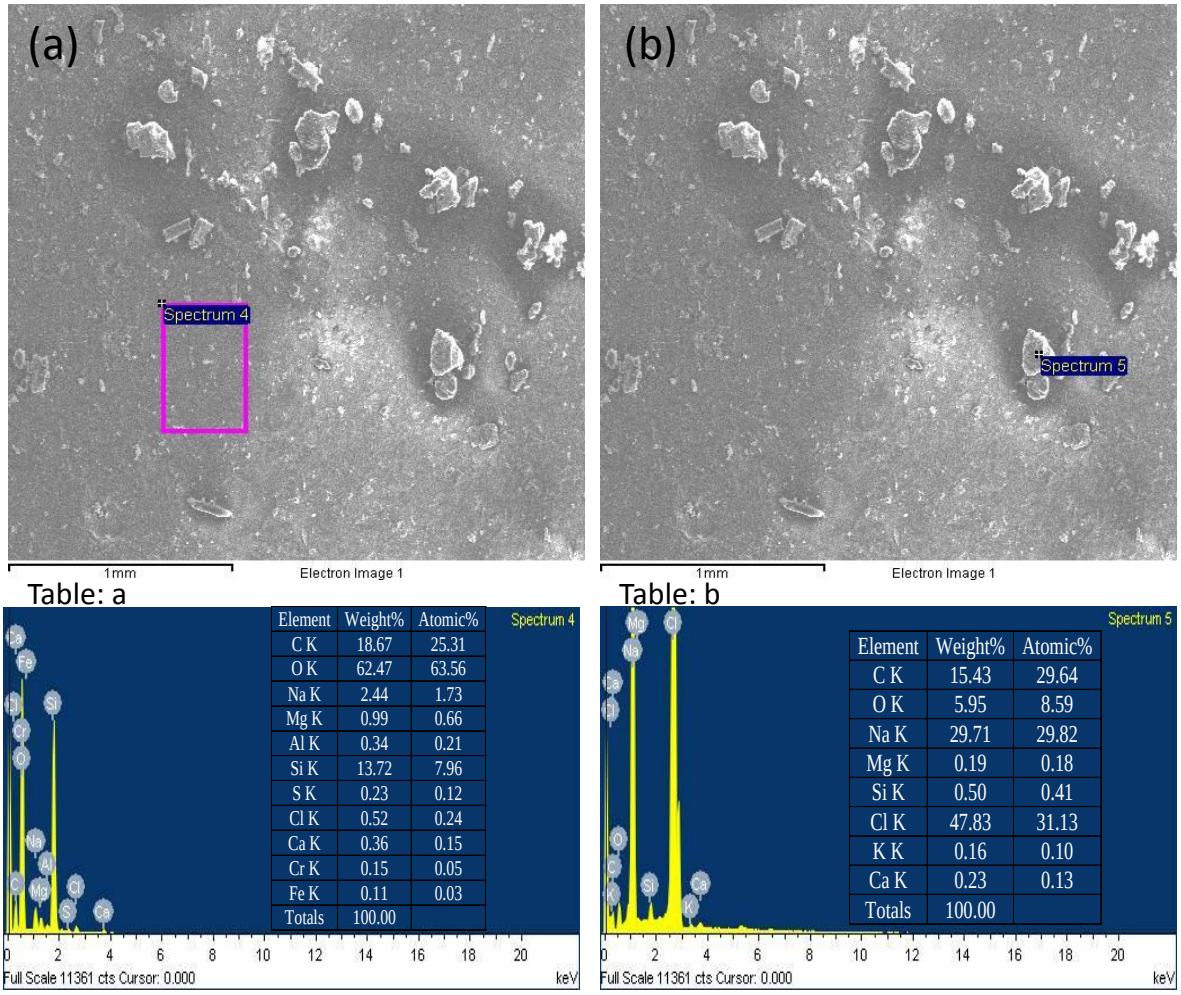

Fig. 4.201: SEM of the corroded diffusion couple of S glass and duplex steel and correspondingly EDS analyses of the corroded region marked in the micrograph.

4.3.3.6. Diffusion couple of X glass with HSLA steel

4.3.3.6.1. Electrochemical testing

The average value of OCP measurements are given in Table 4.30.

Table 4.30: Results of OCP measurement of diffusion couple of X glass with HSLA steel.

Testing time (h)	OCP value (± 0.002V)
24	-0.462
265	-0.457
505	-0.524
745	-0.524

The OCP values of S glass coating shows downward trend which indicates the glass undergoes dissolution process and does not form oxide layer. Fig. 4.202 presents the polarization curves of 24 h, 265 h, 505 h and 745 h testing for diffusion couple of X glass and HSLA steel in artificial seawater. The summarized results are incorporated in Table 4.31.

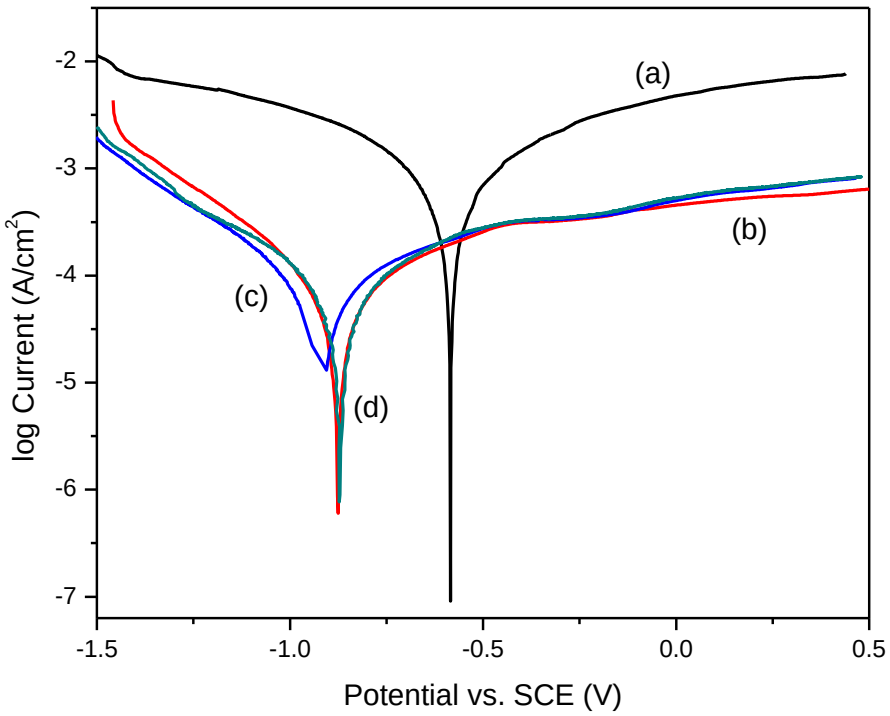

Fig. 4.202: Potentiodynamic polarization curves of (a) 24 h, (b) 265 h, (c) 505 h and (d) 745 h testing of diffusion couple for X glass and HSLA steel in artificial seawater.

Table 4.31: Results of potentiodynamic polarization in diffusion couple of X glass with HSLA steel.

Testing time (h)	E_{corr} (mV)	I_{corr} (μA cm^{-2})	β_c (mV/decade)	β_a (mV/decade)	R_p (Ω cm^2)	Corrosion rate (mm/year)
24	-580.9	0.398	301.1	312.0	0.12×10^6	0.99×10^{-3}
265	-877.7	0.04	346.9	356.0	1.2×10^6	99.9×10^{-6}
505	-917.7	0.036	241.3	309.9	1.08×10^6	89.9×10^{-6}
745	-869.9	0.044	286.0	342.4	1.07×10^6	0.109×10^{-3}

The corrosion rate of X glass coating on HSLA steel firstly decreases upto 505 h. After 745 h, it again increases and fall to order 10^{-3} mm per year which is less as compared to corrosion rate of HSLA steel but large as compared to other diffusion couples. The Nyquist plots of diffusion couple of X glass and HSLA steel are presented in Fig. 4.203. The decrease in diameter of the semicircle after 745 h measurement was also confirmed the results obtained from polarization.

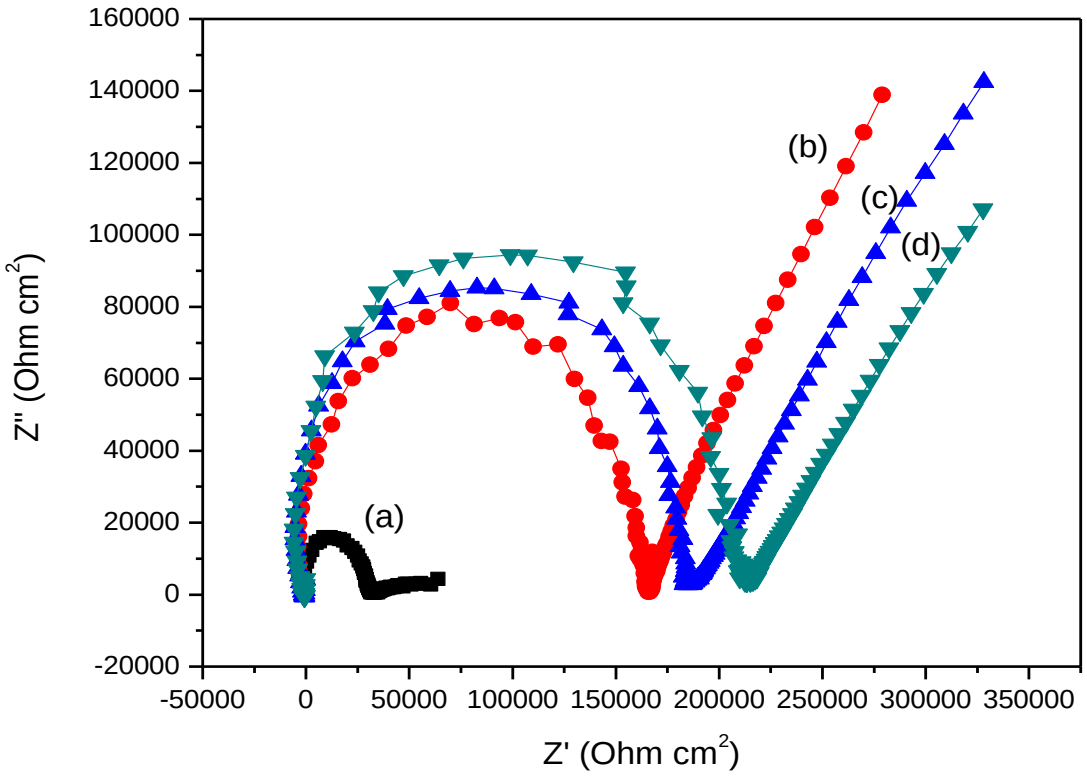

Fig. 4.203: Nyquist plots of (a) 24 h, (b) 265 h, (c) 505 h and (d) 745 h for diffusion couple of X glass and HSLA steel in artificial seawater.

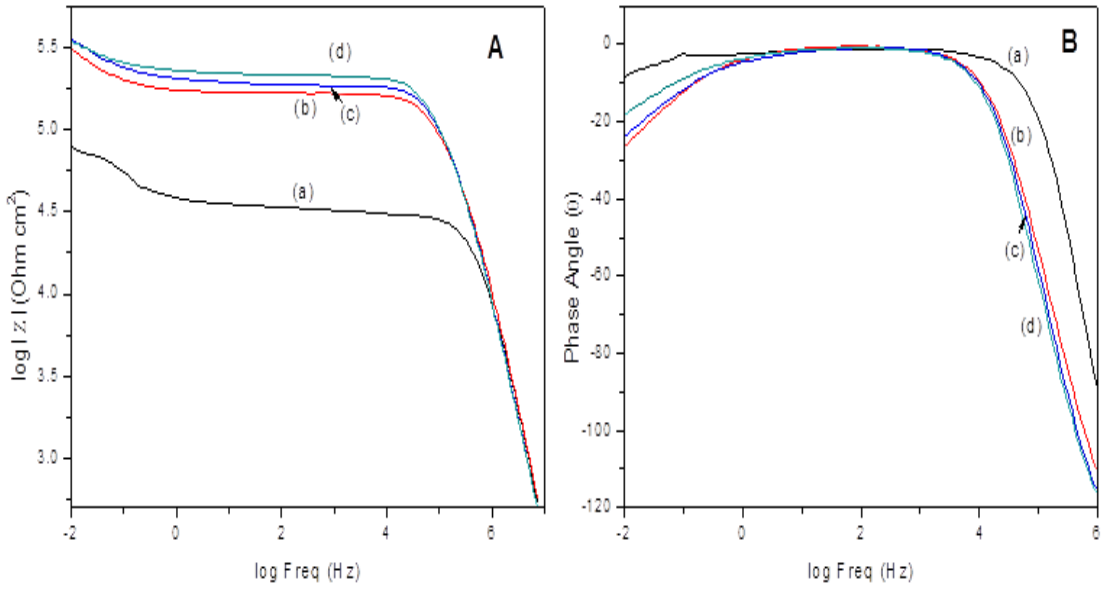

Fig. 4.204: (A) Log Z versus log Freq. plots and (B) Phase angle (Z) versus log Freq. plots of (a) 24 h, (b) 265 h, (c) 505 h and (d) 745 h for diffusion couple of X glass and HSLA steel in artificial seawater.

The impedance value after 745 h is maximum as compared to 24 h measurement and phase angle values confirmed the presence of two time constants as shown in Fig. 4.204. The fitted values of circuit parameters were estimated as given in Table 4.32.

Table 4.32: Electrochemical measurements of diffusion couple of X glass and HSLA steel obtained by equivalent circuit.

Testing time (h)	R_s (Ω cm^2)	R_{ct} (Ω cm^2)	CPE_{dl} (μF cm^{-2})	n_{dl}	R_c (Ω cm^2)	CPE_c (μF cm^{-2})	n_c
24	13.4	0.4×10^5	43.8×10^{-6}	0.35	30946	25.2×10^{-12}	1
265	11	0.21×10^6	47.5×10^{-6}	1	0.16×10^6	17.1×10^{-12}	0.98
504	11.2	0.21×10^6	36.6×10^{-6}	1	0.19×10^6	14×10^{-12}	1
745	13.5	0.15×10^6	42.2×10^{-6}	1	0.22×10^6	14.2×10^{-12}	1

The value of R_{ct} after 745 h of X glass coating got decreased but more than steel. Thus it proves good corrosion resistance of the coating.

4.3.3.6.2. Structural analysis

Photograph of diffusion couple of X glass with HSLA steel after corrosion testing for 745 h in 3.5% NaCl is shown in Fig. 4.205.

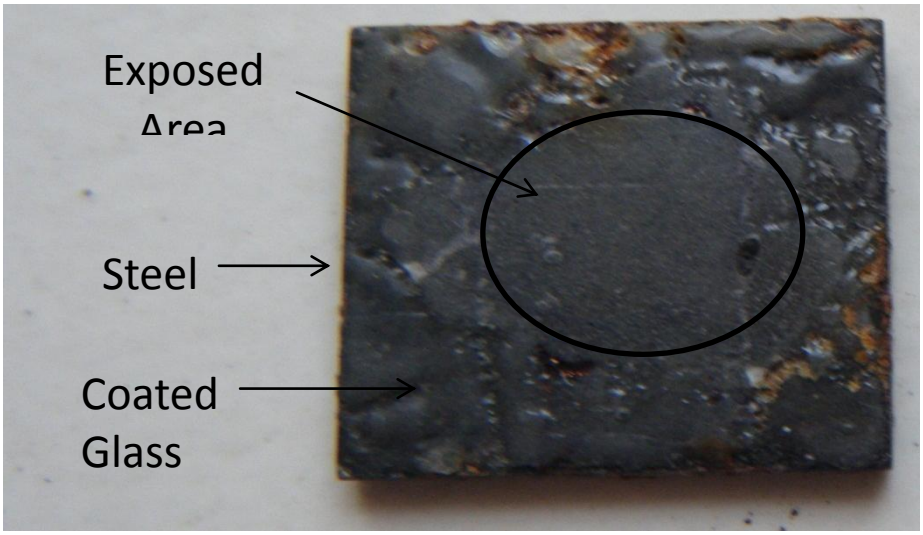

Fig. 4.205: Photograph of X glass coated on HSLA steel after corrosion testing for 745 h in 3.5% NaCl solution.

The circular marked area is exposed for corrosion testing. There is no remarkable difference between exposed and non-exposed areas by visual observation. Corrosive products at the periphery of the sample were due to atmospheric moisture. In order to see microscopic level changes, scanning electron micrographs of this area was taken as shown in Fig. 4.206. Surface of glass coating appeared to corrode as shown in Fig. 4.206 (a). The glass was dissolved. Formation of pits holes and accumulation of corrosive products in the holes can be seen as shown in Fig. 4.206 (b). In order to quantify the nature of the surface, EDS analysis was done on the surface of

glass coating and on the precipitates as shown in Fig. 4.207. The corroded glass surface was enriched in the oxygen and Fe was also present as shown in Fig. 4.207 (a). The presence of Fe, Ca and Mg with O in the analysis indicates the precipitation of corrosion product on the glass surface as shown in Fig. 4.207 (b).

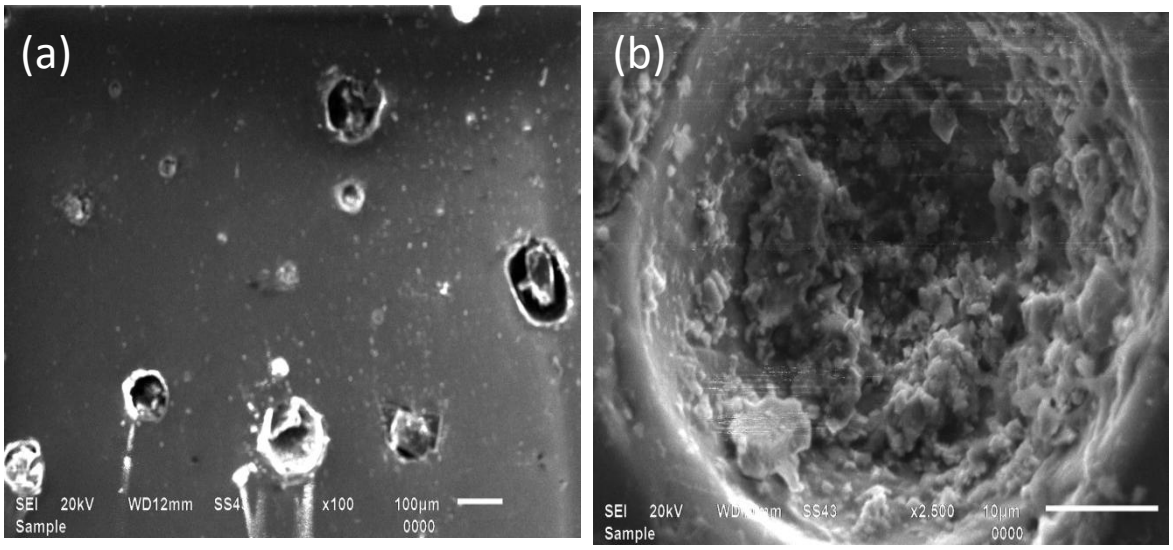

Fig. 4.206: Scanning electron micrographs of the corroded diffusion couple of X glass coated on HSLA steel.

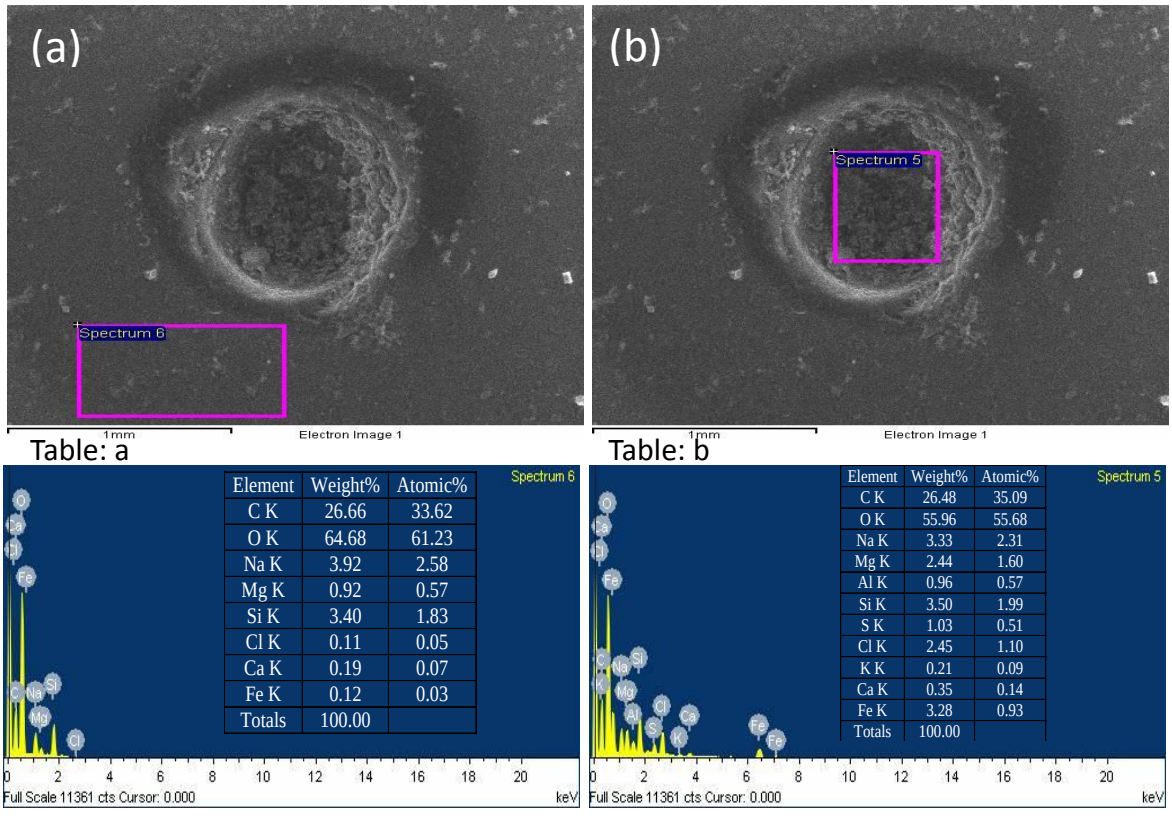

Element	Weight%	Atomic%
C K	26.66	33.62
O K	64.68	61.23
Na K	3.92	2.58
Mg K	0.92	0.57
Si K	3.40	1.83
Cl K	0.11	0.05
Ca K	0.19	0.07
Fe K	0.12	0.03
Totals	100.00	

Element	Weight%	Atomic%
C K	26.48	35.09
O K	55.96	55.68
Na K	3.33	2.31
Mg K	2.44	1.60
Al K	0.96	0.57
Si K	3.50	1.99
S K	1.03	0.51
Cl K	2.45	1.10
K K	0.21	0.09
Ca K	0.35	0.14
Fe K	3.28	0.93
Totals	100.00	

Fig. 4.207: SEM of the corroded diffusion couple of X glass and HSLA steel and correspondingly EDS analyses of the corroded region marked in the micrograph.

4.3.3.7. S glass and HSLA steel

4.3.3.7.1. Electrochemical testing

The average value of OCP measurements are given in Table 4.33.

Table 4.33: Results of OCP measurement of diffusion couple of S glass with HSLA steel.

Testing time (h)	OCP value (± 0.002V)
24	-0.497
265	-0.169
504	-0.202
745	-0.291

The OCP values of S glass coating shows upward trend towards positive potential which indicates the formation of oxide layer. Fig. 4.208 presents the polarization curves of 24 h, 265 h, 505 h and 745 h testing for diffusion couple of S glass and HSLA steel in artificial seawater. Using the Tafel extrapolation method, the corrosion potential E_{corr}, corrosion current density I_{corr}, anodic/cathodic Tafel slopes β_a and β_c and polarization resistance R_p values are calculated from polarization curves and are given in Table 4.34.

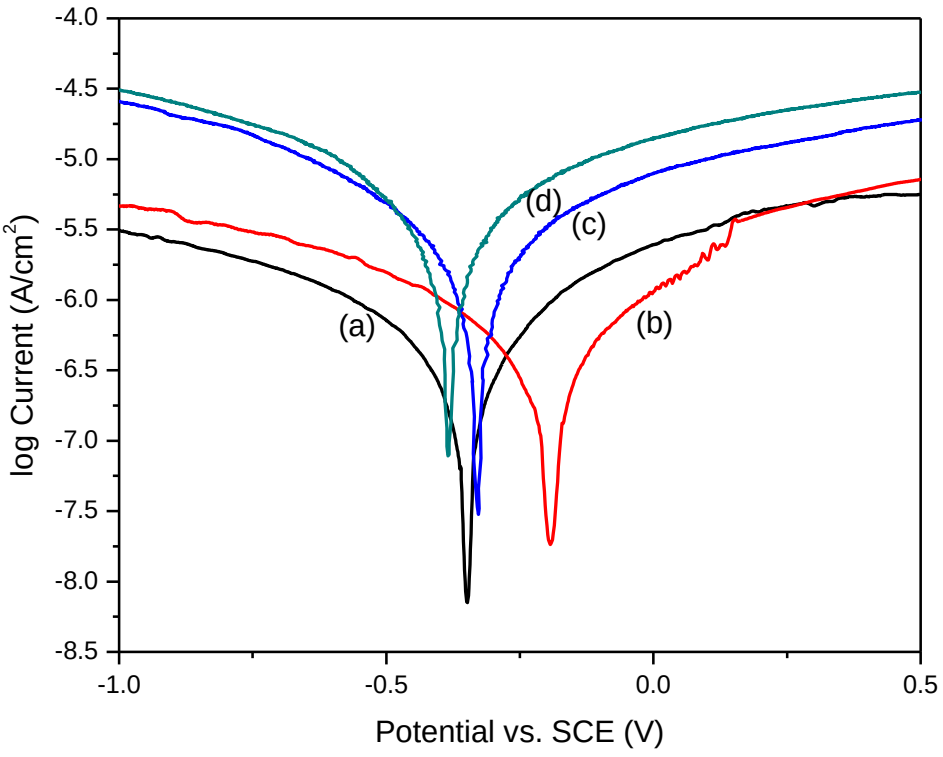

Fig. 4.208: Potentiodynamic polarization curves of (a) 24 h, (b) 265 h, (c) 505 h and (d) 745 h testing of diffusion couple for S glass and HSLA steel in artificial seawater.

Table 4.34: Results of potentiodynamic polarization in diffusion couple of S glass with HSLA steel.

Testing time (h)	E_{corr} (mV)	I_{corr} (μA cm^{-2})	β_c (mV/decade)	β_a (mV/decade)	R_p (Ω cm^2)	Corrosion rate (mm/year)
24	-348.2	0.0002	315.1	255.5	0.19×10^9	0.57×10^{-6}
265	-188.9	0.0002	302.4	248.5	0.18×10^9	0.64×10^{-6}
504	-330.1	0.001	293.3	328.9	39.8×10^6	2.91×10^{-6}
745	-386.4	0.002	278.7	335.0	23.7×10^6	5.83×10^{-6}

The decreasing trend in corrosion rate supported the OCP results. The corrosion rate per year value of S glass coating after 745 h measurement is less as compared to X glass coated on HSLA steel. Thus S glass coating is more suitable than X glass coating for HSLA steel. The Nyquist plots of diffusion couple of S glass and HSLA steel are presented in Fig. 4.209.

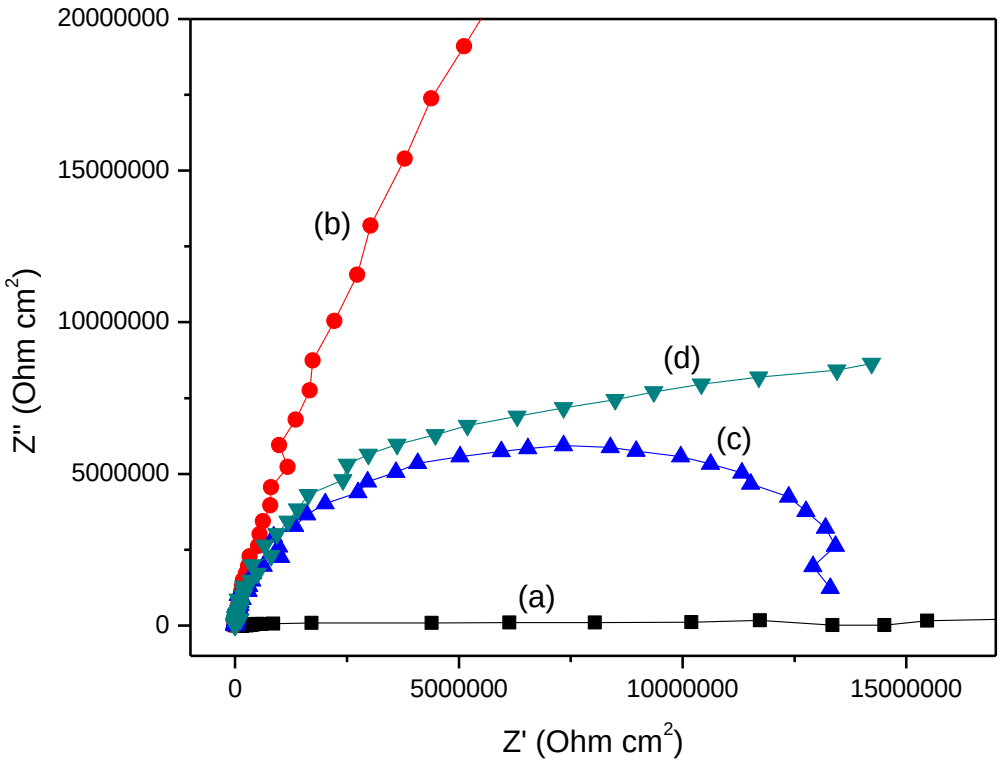

Fig. 4.209: Nyquist plots of (a) 24 h, (b) 265 h, (c) 505 h and (d) 745 h for diffusion couple of S glass and HSLA steel in artificial seawater.

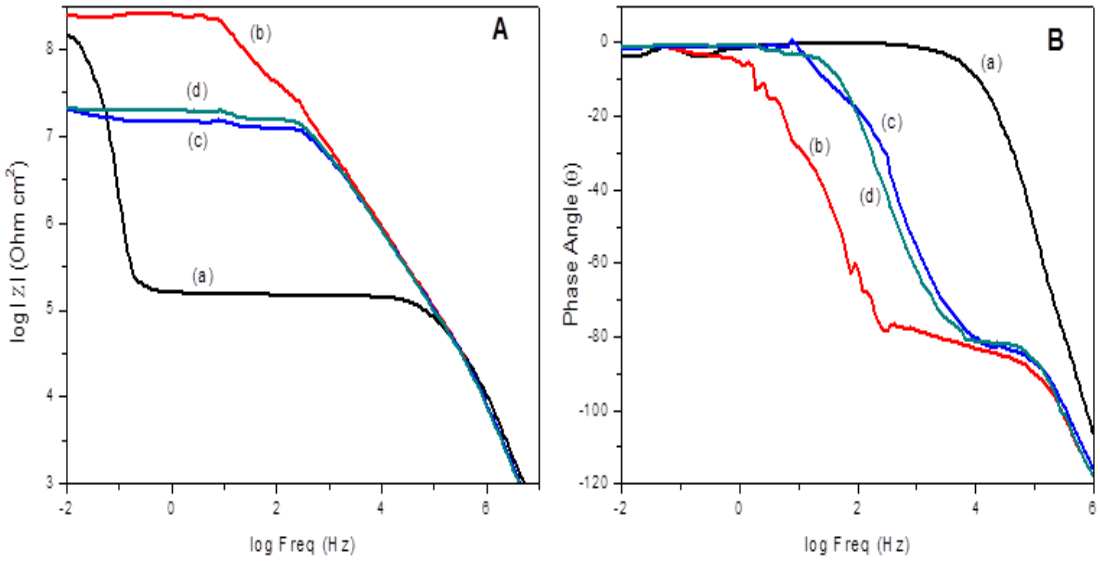

Fig. 4.210: (A) Log Z versus log Freq. plots and (B) Phase angle (Z) versus log Freq. plots of (a) 24 h, (b) 265 h, (c) 505 h and (d) 745 h for diffusion couple of S glass and HSLA steel in artificial seawater.

The impedance value after 745 h is maximum as compared to 24 h measurement and phase angle values confirmed the presence of two time constants as shown in Fig. 4.210. The fitted values of circuit parameters were estimated as given in Table 4.35.

Table 4.35: Electrochemical measurements of diffusion couple of S glass and HSLA steel obtained by equivalent circuit.

Testing time (h)	R_s (Ω cm^2)	R_{ct} (Ω cm^2)	CPE_{dl} (μF cm^{-2})	n_{dl}	R_c (Ω cm^2)	CPE_c (μF cm^{-2})	n_c
24	17	0.28×10^5	6.13×10^{-6}	1	0.15×10^6	21.5×10^{-12}	0.97
265	15.3	0.17×10^9	8.1×10^{-12}	0.29	2058	30.8×10^{-12}	0.98
505	11.9	5.12×10^6	22.8×10^{-12}	1	8.6×10^6	34.6×10^{-12}	0.94
745	10.6	23.6×10^6	0.12×10^{-9}	0.37	0.83×10^6	0.11×10^{-9}	0.83

The increase in R_{ct} value and the decrease in CPE_{dl} value after 745 h proved that the S glass coating is more corrosion resistive as compared to X glass coating.

4.3.3.7.2. Structural analysis

Photograph of diffusion couple of S glass with HSLA steel after corrosion testing for 745 h in 3.5% NaCl is shown in Fig. 4.211.

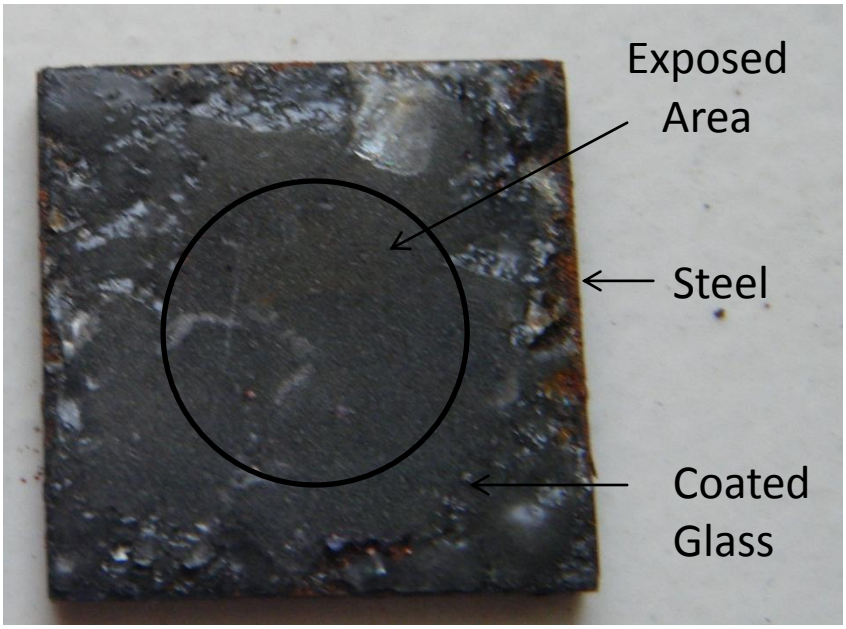

Fig. 4.211: Photograph of S glass coated on HSLA steel after corrosion testing for 745 h in 3.5% NaCl solution.

In Fig. 4.211, the circular marked area is exposed for corrosion testing. There is no remarkable difference between exposed and un-exposed areas which shows its stability. In order to see the microscopic level changes, SEM of this area was done as shown in Fig. 4.212. Surface of glass coating appeared to corrode as shown in Fig. 4.212 (a-b). The glass was dissolved which is apparent the presence of pits and accumulation of corrosive products in the holes. At higher magnification, formation of open pores was clearly observed as shown in Fig. 4.212 (c). In order to quantify the nature of the surface, EDS analysis was done on the surface of glass coating and also on the precipitates as shown in Fig. 4.213. The corroded glass surface was enriched in the oxygen and Fe as shown in Fig. 4.213 (a). The presence of Fe, Ca and Mg with O in the analysis indicates the precipitation phenomenon on the glass surface as shown in Fig. 4.213 (b).

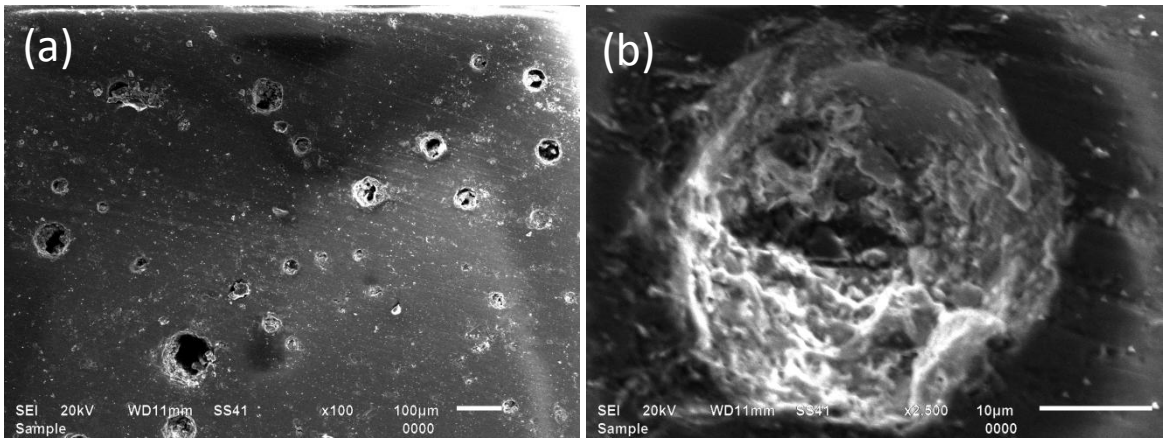

Fig. 4.212: Scanning electron micrographs of the corroded diffusion couple of S glass coated on HSLA steel.

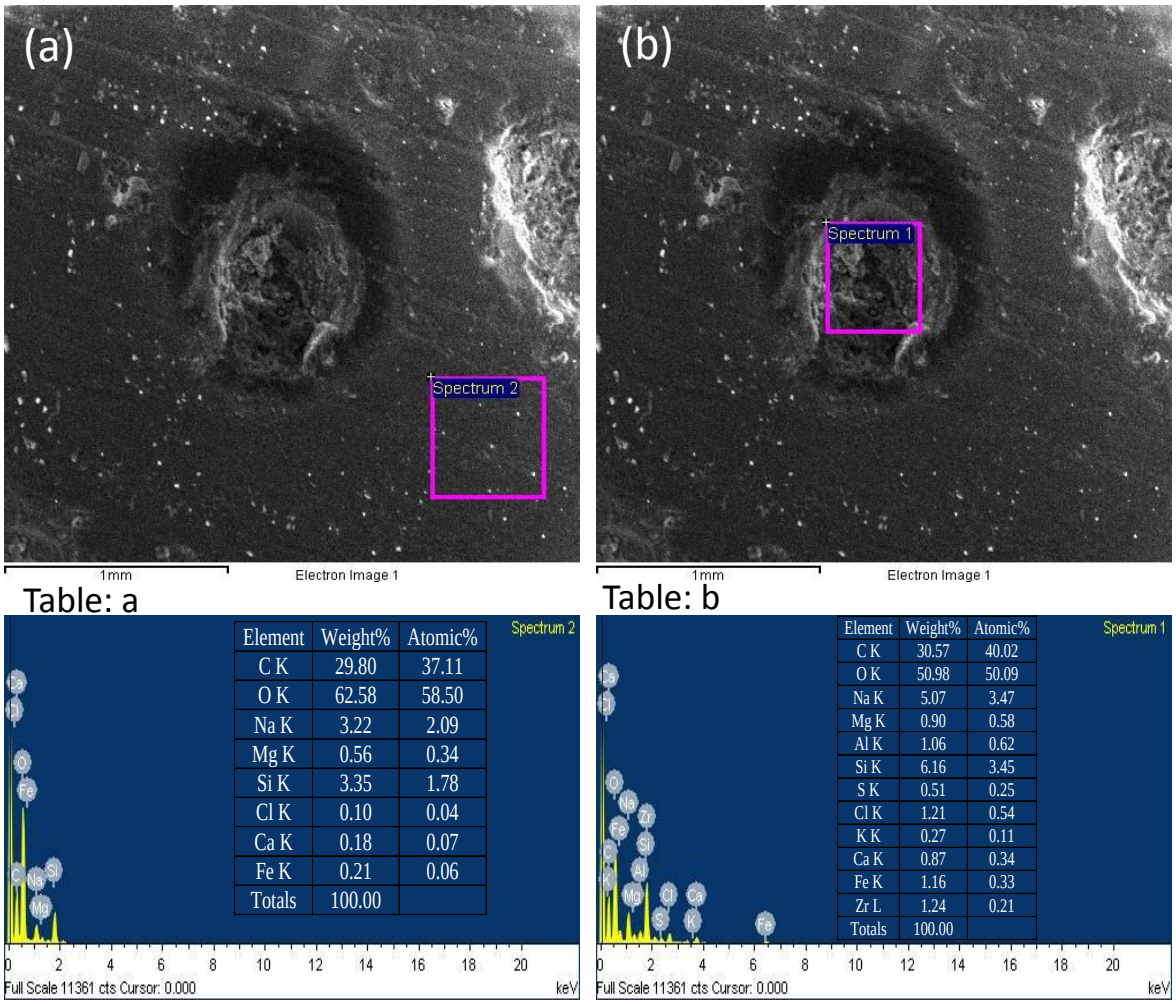

Fig. 4.213: SEM of the corroded diffusion couple of S glass and HSLA steel and correspondingly EDS analyses of the corroded region marked in the micrograph.

The corrosion tests performed on glasses, steels and glass coated steels (diffusion couple) indicate that glass coating on steel prevents corrosion to greater extent as compared to individual glasses and steels.

References

1. N. Lahl, K. Singh, L. Singheiser, K. Hilpert, J. Mater. Sci. 35 (2000) 3089 – 3096.
2. H. Ruzha, V. Gunter, R. Christian, Mater. Res. Bull. 46 (2011) 81-86.
3. M. Younesi, M.E. Bahrololoom, Mater. Des. 31 (2010) 234-243.
4. Samia N. Salama, Saad M. Salman, Hussein Darwish, Ceramics− Silikáty 46 (2002) 15-23.
5. Shouguo Huang, Qiliang Lu, Chunchang Wang, J. Alloys Comp. 509 (2011) 4348–4351.
6. S. Mahadevan, A. Giridhar, A.K. Singh, J. Non-Cryst. Solids 88 (1986) 11-34.
7. H.E. Kissinger, Anal. Chem. 29 (1957) 1702-1706.
8. J.A. Augis, J.E. Bennett, J. Therm. Anal. 13 (1978) 283-292.
9. A. Arora, K. Singh, O.P. Pandey, Int. J. Hydrogen Energy 36 (2011) 14948-14955.
10. M. Saad, M. Poulin, Mater. Sci. Forum 19-20 (1987) 11-18.
11. A. Hruby, Czech. J. Phys. B 22 (1972) 1187-1193.
12. M. Mingsheng, N. Wen, W. Yali, W. Zhongjie, L. Fengmei, J. Non-Cryst. Solids 354 (2008) 5395–5401.
13. V. Raghavan, Materials Science and Engineering: A First Course, 5th Ed.
14. C. Lara, M. J. Pascual, M.O. Prado, A. Duran, J. Solid State Ionics 170 (2004) 201-208.
15. T. Kitamura, Physics Letters A 235 (1997) 515-524.
16. J.E. Shelby, J. Non-Cryst. Solids 349 (2004) 331-336.
17. H. Vogel, Phys. Zeitschrift. 22 (1921) 645–646.
18. G.S. Fulcher, J. Am. Ceram. Soc. 8 (1925) 339–355.
19. G. Tammann, W. Hesse, Z. Anorg. Chem. 156 (1926) 245–257.
20. J.E. Shelby, Viscosity of glass forming melts, Introduction to Glass Science and Technology, The Royal Society of Chemistry, Cambridge, 2005.
21. C.H. Gur, A. Ozturk, J. Non-Cryst. Solids 351 (2005) 3655-3662.
22. Hsiu-Tao Chang, Chih-Kuang Lin, Chien-Kuo Liu, J. Power Sources 189 (2009) 1093–1099.
23. J. Park, A. Ozturk, Thermochim. Acta 470 (2008) 60–66.
24. M. Criado, A. Fernández-Jiménez, A.G. de la Torre, M.A.G. Aranda, A. Palomo, Cement Concrete Res. 37 (2007) 671–679.
25. Amitava Majumdar, Sunirmal Jana, Bull. Mater. Sci. 24 (2001) 69-77.
26. G. Lusvardi, G. Malavasi, L. Menabue, M.C. Menziani, A. Pedone, U. Segre, J. Phys. Chem. B 109 (2005) 21587- 21592.
27. I. Simon, Modern Aspects of the Vitreous State, Butterworth, London, 1960.
28. S.L. Lin, C.S. Hwang, J. Non-Cryst. Solids 202 (1996) 61-67.
29. H. Rawson, Inorganic Glass-forming Systems, Academic Press, New York, 1967.
30. E.M.A. Khalil, F.H. ElBatal, Y.M. Hamdy, H.M. Zidan, M.S. Aziz, A.M. Abdelghany, Physica B 405 (2010) 1294-1300.
31. D.R. Neuville, L. Cormier, A.M. Flank, V. Briois, D. Massiot, Chem. Geol. 213 (2004) 153-163.
32. L. Cormier, D.R. Neuville, G. Calas, J. Non-Cryst. Solids 274 (2000) 110-114.
33. A. Novatski, A. Steimacher, A.N. Medina, A.C. Bento, M.L. Baesso, L.H.C. Andrade, S.M. Lima, Y. Guyot, G. Boulon, J. Appl. Phys. 104 (2008) 094910-094917.
34. J.A. Duffy, J. Solid State Chem. 62 (1986) 145-147.
35. F. Urbach, Phys. Rev. 92 (1953) 1324-1324.
36. S. Sebastian, M.A. Khadar, Bull. Mater. Sci. 27 (2004) 207-212.
37. N.F. Mott, E.A. Davis, Electronic Process in Non-Crystalline Materials, Clarendon Press, Oxford, 1971.
38. S. Yusub, Ch. Rajyasree, A.R. Babu, P.M.V. Teja, D. Krishna Rao, J. Non-Cryst. Solids 364 (2013) 62–68.
39. S.K. Lee, J. F. Stebbins, J. Phys. Chem. B. 107 (2003) 3141-3148.

40. S.K. Lee, S. Sung, Chem. Geol. 256 (2008) 326-333.
41. L. Cormier, D.R. Neuville, Chem. Geol. 213 (2004) 103-113.
42. J. Kalužný, M. Kubliha, V. Labaš, T. Djouama, M. Poulain, J. Non-Cryst. Solids 355 (2009) 2003–2005.
43. G.N. Greaves, K.L. Ngai, Phys. Rev. B 52 (1995) 6358-6380.
44. F.A.A. Wahab, M. Abdel-Baki, J. Non-Cryst. Solids 355 (2009) 2239-2249.
45. Alo Dutta, T.P. Sinha, P. Jena, S. Adak, J. Non-Cryst. Solids 354 (2008) 3952-3857.
46. G. W. Bak, A. K. Jonscher, J. Mater. Sci. 34 (1999) 5505 – 5508.
47. S. Petrescu, M. Constantinescu, E.M. Anghel, I. Atkinson, M. Olteanu, M. Zaharescu, J. Non-Cryst. Solids 358 (2012) 3280–3288.
48. S. Duhan, S. Sanghi, A. Agarwal, A. Sheoran, S. Rani, Physica B 404 (2009) 1648–1654.
49. B. Ouni, M. Haj Lakhdar, R. Boughalmi, T. Larbi, A. Boukhachem, A. Madani, K. Boubaker, M. Amlouk, J. Non-Cryst. Solids 367 (2013) 1–7.
50. A.S. Fawzi, A.D. Sheikh, V.L. Mathe, Mater. Res. Bull. 45 (2010) 1000-1007.
51. T. Srikumar, Ch. SrinvasaRao, Y. Gandhi, N. Venkatramaiah, V. Ravikumar, N. Veeraiah, J. Phys. Chem. Solids 72 (2011) 190-200.
52. G. Singla, K. Singh, Ceram. Int. 39 (2013) 1785- 1792.
53. M.P.F. Graç a, M.G. Ferreira da Silva, A.S.B. Sombra, M.A. Valente, Physica B 396 (2007) 62–69.
54. M.H. Shaaban, J. Mater Sci. 47 (2012) 5823-5832.
55. T. Yano, T. Nagano, J. Lee, S. Shibata, M. Yamane, Solid State Ionics 150 (2002) 281–290.
56. S. Ghosh, P. Kundu, A. Das Sharma, R.N. Basu, H.S. Maiti, J. European Ceramic Society 28 (2008) 69-76.
57. Z. Yang, J.W. Stevenson, K.D. Meinhardt, Solid State Ionics 160 (2003) 213-225.
58. S. Ghosh, A. Das Sharma, A.K. Mukhopadhyay, P. Kundu, R.N. Basu, Int. J. Hydrogen Energy 35 (2010) 272-283.
59. S. Ghosh, P. Kundu, A. Das Sharma, R.N. Basu, J. Electrochem. Soc. B473 (2008) 155.
60. V.A.C. Haanappel, V. Shemet, S.M. Gross, Th. Koppitz, N.H. Menzler, M. Zahid, W.J. Quadakkers, J. Power Sources 150 (2005) 86-100.
61. S. Song, Z. Wen, Y. Liu, J. Lin, X. Xu, Q. Zhang, J. Solid State Electrochem 14 (2010) 1735-1740.
62. J. Frenkel, J. Phys. 9 (1945) 385.
63. R. Harizanova, G. Völksch, C. Rüssel, Mater. Res. Bull. 46 (2011) 81-86.
64. W.J. Quadakkers, J. Piron-Abellan, V. Shemet, L. Singheiser, Mater. High temp. 20 (2003) 115-127.
65. J. Gallardo, A. Duran, I. Garcia, J.P. Celis, M.A. Arenas, A. Conde, J. Sol-Gel Sci. Tech. 27 (2003) 175–183.
66. J.E. Shelby: Handbook of Gas Diffusion in Solids and Melts, ASM International, Materials Park, OH, 1996.
67. G. Bolelli, V. Cannillo, L. Lusvarghi, T. Manfredini, Surf. Coat. Tech. 201 (2006) 458–473.
68. S. Das, A.K. Mukhopadhyay, S. Datta, G.C. Das, D. Basu, J. European Ceram. Soc. 28 (2008) 729–738.
69. Dennis Chilson, Glass coated high strength steel, United States Patent, 6087013, July 11, 2000.
70. J.W. Park, P.F. Mendez, T.W. Eagar, Acta Mater. 50 (2002) 883.
71. S. Ghosh, A. Das Sharma, P. Kundu, S. Mahanty, R.N. Basu, J. Non-Cryst. Solids 354 (2008) 4081.
72. K.A. Jackson, J. Cryst. Growth 24 (25) (1974) 130.

73. A. Arora, A. Goel, E.R. Shaaban, K. Singh, O.P. Pandey, J.M.F. Ferreira, Physica B 403 (2008) 1738.N.
74. Keyvani, V.K. Marghussian, H.R. Rezaei, M. Kord, Int. J. Appl. Ceram. Technol. 8 (2011) 203.
75. M. H. Lewis, J. Metcalf-Johansen, P. S. Bell, J. Amer. Ceram. Soc. 62 (1978) 278-288.
76. J. Pech, M. Braccini, A. Mortensen, N. Eustathopoulos, Mater. Sci. Eng. A 384 (2004) 117–128.
77. A. Iost, R. Bigot, F. Barbieux, P. Vast, J. Mater. Sci. 34 (1999) 3991 – 3996.
78. N. Laorodphan, P. Namwong, W. Thiemsorn, M. Jaimasith, A. Wannagon, T.Chairuangsri, J. Non-Cryst. Solids 355 (2009) 38–44.
79. F. Smeacetto, M. Salvo, M. Ferraris, J. Cho, A.R. Boccaccini, J. Eur. Ceram. Soc. 28 (2008) 611.
80. Yung-Jen Lin, Shin-Hua Tu, Ceram. Int. 35 (2009) 1311–1315.
81. Xiaodong Qi, Gang Song, Mater. Desig. 31 (2010) 605–609.
82. B.P. McGrail, J.P. Icenhower, D.K. Shuh, P. Liu, J.G. Darab, D.R. Baer, S. Thevuthasen, V. Shutthanandan, M.H. Engelhard, C.H. Booth, P. Nachimuthu, J. Non-Cryt. Solids 296 (2001) 10.
83. C. Cailleteau, Nat. Mater. 7 (2008) 978.
84. J. Wong, C.A. Angell, Glass Structure by Spectroscopy, Marcel Dekker, New York, 1976.
85. A.M. Efimov, J. Non-Cryst. Solids 235 (1999) 95.
86. E.I. Kamitsos, C.P.E. Varsamis, A. Vegeri, in: Proceedings of the Inter- national Glass, congress, vol. I, Edimbargh, Scotland, Invited paper, July 2001, pp. 234–246.
87. E.I. Kamitsos, Phys. Chem. Glasses 44 (2003) 79. B.B. Wilson, J.C. Decius, P.C. Cross, Molecular vibrations, McGraw-Hill, NewYork, 1955.
88. G.J. Exarhos, in: G.E. Walrafen, A.G. Revesz (Eds.), Structure and Bonding in Non-Crystalline Solids, Plenum, New York, 1986, p. 203.
89. C.I. Merzbacher, W.B. White, J. Non-Cryst. Solids 130 (1991) 18.
90. F.H. ElBatal, M.M.I. Khalil, N. Nada, S.A. Desouky, Mater. Chem. Phys. 82 (2003) 375.
91. R.D. Husung, R.H. Doremus, J. Mater. Res. 5 (10) (1990) 2209.
92. Kh.M. ElBadry, F.A. Moustaffa, M.A. Azooz, F.H. ElBatal, Indian J. Pure Appl. Phys. 38 (2000) 741.
93. H. Dunken, R.H. Doremus, J. Non-Cryst. Solids 92 (1987) 61.
94. A.M. Efimov, J. Non Cryst. Solids 93 (2003) 334.
95. A.M. Efimov, Optical Constants of Inorganic Glasses, CRC, Boca Raton, FL, 1995.
96. A.M. Efimov, J. Non-Cryst. Solids 203 (1996) 1.
97. G. Navara, J. Non-Cryst. Solids 351 (2005) 1796.
98. G. Navara, J. Non-Cryst. Solids 353 (2007) 555.
99. L.L. Hench, J. Amer. Ceram. Soc. 74 (1991) 331-343.
100. D. Chaulet, S. Martemianov, J.H. Thomassin, P. Le Coustumer, J. Nucl. Mater. 298 (2001) 192-196.
101. J.R. Macdonald: Impedance spectroscopy emphasizing solid materials and systems, 1987, New York, John Wiley & Sons.
102. E. Malard, D. Kervadec, O. Gil, Y. Lefevre, S. Malard, Electrochim. Acta 54 (2008) 8–13.
103. A.U. Malik, S. Ahmad, I. Andijani, S. Al-Fouzan, Desalination 123 (1999) 205-213.
104. A.U. Malik, S. Al-Fouzan, Corr. Sci. 33 (1992) 51.
105. J.K. Boah, P. Frazer, Proc., 7th Middle East Corrosion Conference, Bahrain, 1996, p. 409.
106. J.E.G. Gonzalez, J.C. Mirza-Rosca, J. Electroanal. Cham. 471 (1999) 409.
107. A.K. Shukla, R. Balasubramaniam, S. Bhargava, Intermetallics 13 (2005) 631.
108. A.W.E. Hodgson, Y. Mueller, D.C. Forster, S. Virtanen, Electrochim. Acta 47 (2002) 1913.
109. S.S. Abdel Rehim, O.A. Hazzazi, M.A. Amin, K.F. Khaled, Corros. Sci. 50 (2008) 2258.

110. I. Gurrappa, G. Malakondaiah, Mater. Sci. Eng. A 391 (2005) 235-242.
111. Light Truck Frame Project Team, A guide to corrosion protection, Michigan, 1999.
112. R. Álvarez-Bustamante, G. Negrón-Silva, M. Abreu-Quijano, H. Herrera-Hernández, M. Romero-Romo, A. Cuán, M. Palomar-Pardavé, Electrochim. Acta 54 (2009) 5393-5399.
113. S.J. Green, Corrosion, Metals Hand Book, vol. 13, ninth ed., ASM International, Metals Park, OH, 1987, p. 550.
114. Advanced Mater. Processes, 162 (2004) 26, http://www.wlv.com.
115. S.W. Dean, D. Knotkova, K. Kreislova, ISOCORRAG. International Atmospheric Exposure Program: Summary of Results, ASTM Data Series 71, ASTM International, West Conshohocken, 2010.
116. D. de la Fuente, I. Díaz, J. Simancas, B. Chico, M. Morcillo, Corros. Sci. 53 (2011) 604–617.
117. Q.C. Zhang, J.S. Wu, J.J. Wang, W.L. Zheng, J.G. Chen, A.B. Li, Mater. Chem. Phys. 77 (2002) 603–608.
118. Y. Ma, Y. Li, F. Wang, Corros. Sci. 51 (2009) 997-1006.
119. J.C. Farmer, J.J. Haslam, S.D. Day, T. Lian, C.K. Saw, P.D. Hailey, J.S. Choi, R.B. Rebak, N. Yang, J.H. Payer, J.H. Perpezko, K. Hildal, E.J. Laverniu, J. Mater. Res. 22 (2007) 2297-2311.
120. ASTM Standard G59-97, 2009, Standard test method for conducting potentiodynamic polarization resistance measurements, ASTM International, West Conshohocken, PA, 2009, doi: 10.1520/G0059-97R09.
121. Y. Yang, C. Zhang, Y. Peng, Y. Yu, L. Liu, Corros. Sci. 59 (2012) 10-19.
122. J.R. Macdonald: Impedance spectroscopy emphasizing solid materials and systems, 1987, New York, John Wiley & Sons.
123. B. Kaur, K. Singh, O.P. Pandey, Surf. Eng. (2013).
124. A.J. López, C. Taltavull, B. Torres, E. Otero, J. Rams, Corrosion 69 (2013) 497- 508.
125. D.E. Clark and L.L. Hench. Scientific Basis for Nuclear Waste Management, VI Ed., D.G. Brookins (Elsevier, New York, 1983) pp. 113-24.
126. D.E. Clark, E. Lue Yen-Bower, Surf. Sci. 100 (1980) 53-70.
127. Y.B. Wang, H.F. Li, Y. Cheng, S.C. Wei, Y.F. Zheng, Electrochem. Communic. 11 (2009) 2187-2190.
128. J.N. Calata, G. Lu, T. Chuang, Surf. Interface Anal. 31 (2001), 673-681.
129. C. Qin, K. Asami, H. Kimura, W. Zhang, A. Inoue, Electrochem. Communic. 10 (2008) 1408-1410.
130. S. Frangini, F. Zaza, A. Masci, Corros. Sci. (2012).
131. S.R. Paital, N.B. Dahotre, Mater. Sci. Eng. R 66 (2009) 1-70.
132. V. H. V. Sarmento, M. G. Schiavetto, P. Hammer, A. V. Benedetti, C. S. Fugivara, P. H. Surf. Coat. Technol. 204 (2010) 2689–2701.
133. X. Zhang, C. van den Bos, W. G. Sloof, H. Terryn, A. Hovestad, J. H. W. de Wit, Surf. Eng. 20 (2004) 244– 250.
134. B. Subramanian, K. Ashok, K. Subramanian, D. Sastikumar, G. Selvan, M. Jayachandran, Surf. Eng. 25 (2009) 490– 495.
135. T.M. Sridhar, U. Kamachi Mudali, M. Subbaiyan, Corros. Sci. 45 (2003) 2337-2359.

Chapter 5

CONCLUSIONS AND FUTURE SCOPE

Overview

The present chapter summarizes the experimental results described in previous chapters. For the synthesis of glasses the constituents used were varied to get the desired properties of the glasses so that it can be used as glass coating material on different types of steels. These variations in glass constituents were done to have nucleation site (TiO_2) and NBO (Na_2O) in glass so that a wide spectrum in their properties can be achieved. In turn these constituents also influence the TEC value which is important to have better glass coating on steel surface. The glass adherence and the corrosion properties of the glasses with steels have been summarized in this work. At the end, suggestions for future work are given on the basis of results obtained in this work.

5.1. Conclusions

Glass coating on metallic substance is useful to industries as it may lead to development of heat and corrosion resistant material. In order to have strong bond between two materials compacting is required which depends on chemical and physical properties of the interface. The combination of transparency and hardness at room temperature along with sufficient strength and excellent corrosion resistant in different environments make glass indispensable. Its high chemical stability can provide good corrosion resistant on the surface of glass coated steel.

In the present work, four glasses of N-series which were synthesized in our laboratory and two commercial glasses procured from industry namely S and X glass were investigated in detail to use them as coating substances on steels. Four steels crofer, duplex, HSLA and stainless steels were used as substrate. The glass coating was applied onto the cleaned steel surface by slurry method using fine size glass. The glass powder is applied on the metal surface by preparing slurry of glass in different liquid followed by its drying and heating in a furnace at 900 °C in air for 1 h. During heat treatment some of the constituents of glass/steel diffuse and form an adherent bond of glass layer on the surface of steel whereas some other glasses do not show adherence property.

The composition of N-series glasses (60-x) SiO_2 -10 Al_2O_3-5 TiO_2-15 CaO- (10+x) Na_2O (x= 0, 5, 10 and 15) used in present study has been selected on the basis of properties exhibited by E-glass fabric used to make glass fibres. The glasses were characterized using various experimental techniques such as XRD, DTA/TGA, Dilatometer, SEM and dielectric measurement to check their suitability to be used as coating materials. Four glasses were prepared by conventional casting and splat quenching technique. With the increasing SiO_2 content, the color of glasses changes from transparent to dark yellow. All the glasses exhibit amorphous nature when characterized by XRD. In the present glasses, the amount of modifier used was on higher side as compared to conventional glasses which in turn owe to large number of non-bridging oxygen ions. Si^{4+} cations can attain a coordination number of 4, so non-bridging oxygen gets converted into bridging oxygen with the addition of SiO_4 by replacing Na_2O in these samples. Therefore the conversion of non-bridging oxygen to bridging oxygen leads to increase in T_g, T_c and T_m of these glasses. The crystallization peak maximum is observed to increase with increase in heating rate. Theoretical calculation done by taking DTA data for the calculation of thermals stability of glass samples shows that N-10 and N-15 glasses exhibit highest thermal stability as compared to other glass samples of the present series. Dilatometer data of present glass series indicate that the values of TEC obtained in this series are close to the specified range of those of steels which

makes the glass suitable for coating on steel. Dilatometer data showed that with the increase in SiO_2 content softening temperature (T_s) increases. This is because of decrease in Na_2O content that lead to formation of the Si-O network.

The XRD patterns of all pristine glasses showed two broad humps around 10° and 30°. The pattern of N-20 glass showed formation of three humps around 10°, 20° and 30°. These humps clearly indicate that the nucleation of crystalline phase in the glass matrix is by the process of the phase separation in glass system. Phase separation leads less activation energy for crystallization, which is essential for good adhesion with other metallic materials. From XRD results of heat treated N-series glasses, N-15 glass shows low crystallization even at higher temperature. This study indicates that among N-series glasses, N-15 glass is most suitable glass for coating on steels. However, other glasses where the nucleation of crystalline phase(s) leads to achieve the matching coefficient of thermal expansion also make them suitable for glass coating. EDS analysis gives approximate composition where the variation in composition observed is within the limit. The presence of non-bridging oxygen leads to a change in physical properties of glasses such as glass transformation temperature, electrical conductivity, density and refractive index. Dielectric studies and optical studies such as UV-visible and refractive index results confirmed that the N-15 glass is most suitable for coating.

Thermal studies of commercial S and X glasses showed that the melting temperature of glasses was near to 1000 °C. Both the glasses did not show any crystalline peak even when heat treated up to 600 °C. This analysis clearly indicates that there is no crystalline phase present in both the glasses indicating that these glasses exhibit amorphous nature even after heat treatment like conventional enamel. The thermal properties of the glasses is summarized in Table 5.1 which shows that N-series glasses exhibit two crystallization peaks and the second crystallization peak is around 900 °C. Moreover, the commercial glasses (S and X) exhibit single crystallization peak around 700 °C. On the basis of these thermal results, interaction temperature for obtaining good quality diffusion couple of glasses with steels were selected as 900 °C and 700 °C for N-series and commercial glasses S and X. The thermal expansion coefficients of these glasses were within the range of steel used in present investigation except stainless steel.

Table 5.1: Thermal properties of glasses and steels used in present study.

Sample Identity	**T_g (^{o}C)**	**T_c (^{o}C)**	**T_p (^{o}C)**	**T_m (^{o}C)**	**TEC (10^{-6}/K) (200-550 °C)**
N-25 glass	692	721, 826	741, 864	1037	8.88
N-20 glass	616	655, 837	705, 915	1097	8.31
N-15 glass	607	684, 795	711, 910	1127	8.34
N-10 glass	720	795, 910	815, 950	1130	8.19

X glass	555	680	710	880	8.02
S glass	545	630	680	820	8.22
Crofer steel	--	--	--	--	8.41
Duplex steel	--	--	--	--	8.34
HSLA steel	--	--	--	--	8.83
Stainless steel	--	--	--	--	9.22

Among all steels crofer shows better adherence property. However, N-15 glass-crofer coating was smooth and defect free as compared to other diffusion couples. During heat treatment, the nucleation of silica phase takes place initially in silica-rich glass matrix. At a later stage, other cations such as Na^{+} and Al^{3+} entered in SiO_2 matrix by diffusion. Owing to inter-diffusion of ions, the formation of other crystalline phases occurs. The presence of Fe_3O_4 in glassy side clearly indicates the diffusion of Fe^{3+} to glass side, which is responsible for binding the steel with glass.

The corrosion test results of N-series glasses shows that N-15 glass is most corrosion resistive and formed smooth coating layer on crofer. Thus diffusion couple of N-15 glass and crofer steel was selected for corrosion resistance property of coating. Interaction results of N-series glasses and SS showed that glass layer diffuses into the stainless steel but do not form stable coated layer. N-series glasses interacted with HSLA steel and formed a layer. However, the coating layer was detached from steel piece due to heavy oxidation of steel at 900 °C.

After analyzing corrosion studies of the four glass samples, it is concluded that N-15 sample of N-series shows better results. The corrosion study of all the four steel samples revealed that HSLA steel has higher corrosion rate as compared to other steel samples. Microstructural analysis of corroded steels showed that there is formation of pits on the surface of crofer, duplex and SS. The deposition of corrosion products on the corroded surface of HSLA steel were seen in the micrographs.

Glass coating of commercially procured S and X glasses used as a coating on steel for corrosion protection was achieved at 700 ° C which is less as compared to N-series glasses. S and X glasses formed smooth coating with crofer, duplex and HSLA steel. However, because of thermal mismatch, S and X glasses do not exhibit any appreciable interaction with SS.

Corrosion studies of selected diffusion couples were done with the help of electrochemical testing for one month in artificial seawater. The summarized parameters obtained from polarization results of 31st day for all samples are given below Table 5.2.

Table 5.2: Polarization properties of diffusion couples of 31st day.

Diffusion Couple	E_{corr} (mV)	I_{corr} (μA cm^{-2})	β_c (mV/decade)	β_a (mV/decade)	R_p (Ω cm^2)	Corrosion rate (mm/year)
N-15/crofer	-322.3	0.0006	341.4	504.7	82.5×10^6	1.859×10^{-6}
X/crofer	-1044.7	0.003	175.6	602.2	16.5×10^6	8.74×10^{-6}
S/crofer	11.76	0.000008	187.8	212.0	19.8×10^9	23.3×10^{-9}
X/duplex	-458.1	0.004	310.3	420.3	12.1×10^6	8.3×10^{-6}
S/duplex	-40.1	0.0007	301.1	318.6	0.06×10^9	1.6×10^{-6}
X/HSLA	-869.9	0.044	286.0	342.4	1.07×10^6	0.109×10^{-3}
S/HSLA	-386.4	0.002	278.7	335.0	23.7×10^6	5.83×10^{-6}

For crofer steel, all the three glass coatings showed better results as compared to other commercial coatings. S glass coating is most corrosion resistive as its corrosion rate falls in the order of 10^{-9}. Order of corrosion rate for S and X glass coating on duplex steel is same. But S glass coating showed slightly less value as compared to X glass coating. In case of HSLA steel, again S glass coating showed minimum corrosion rate. Values of corrosion current density (I_{corr}) and the polarization resistance (R_p) of the coatings also supported the results of corrosion rate. The estimated values of circuit parameters of impedance spectrum of 31st day for all samples were summarized using a non-linear regression method and is given in Table 5.3 below:

Table 5.3: Electrochemical measurements of diffusion couples of 31st day.

Diffusion Couple	R_s (Ω cm^2)	R_{ct} (Ω cm^2)	CPE_{dl} (μF cm^{-2})	n_{dl}	R_c (Ω cm^2)	CPE_c (μF cm^{-2})	n_c
N-15/crofer	15.9	0.35×10^6	0.68×10^{-9}	0.06	1349	35.77×10^{-12}	0.9
X/crofer	16	1.31×10^{12}	2.06×10^{-6}	0.74	1.3×10^6	25.6×10^{-12}	1
S/crofer	15	1.42×10^9	0.36×10^{-9}	1	13.6×10^6	22.7×10^{-12}	0.9
X/duplex	12	32.2×10^6	52.6×10^{-12}	0.74	0.46×10^6	82.9×10^{-12}	0.86
S/duplex	12	0.42×10^6	6.6×10^{-12}	0.9	19.0×10^6	51.5×10^{-12}	0.9
X/HSLA	13.5	0.15×10^6	42.2×10^{-6}	1	0.22×10^6	14.2×10^{-12}	1
S/HSLA	10.6	23.6×10^6	0.12×10^{-9}	0.37	0.83×10^6	0.11×10^{-9}	0.83

The values of R_{ct} of the coated steel have increased remarkably as compared to bare steel, which clearly indicates the formation of the compact interface layer on the coated steel. The second parameter CPE_{dl} is less as compared to bare steel which gives the proof of very low charge accumulation on the surface of the glass coated sample. The increase in R_{ct} value and the decrease in CPE_{dl} value of glass coated on steels indicate that the transfer of charge is hindered and the diffusion of the solution in the pores of the coating is blocked to a greater extent by glass ceramic coating in comparison to bare steel. Moreover, the dissolution of iron from steel side is also suppressed by silicate glass ceramic coating. Again the high values of resistance and low

values of capacitance for S glass coating on steels proved that the S glass coating is most corrosion resistive among all the glass compositions.

During corrosion, the glass matrix dissolves from those areas where the internal stresses due to precipitation of crystalline phase during heating of glass is more and leads to formation of pits leaving behind unreacted crystalline silicate phase. However, very few amounts of pits are visible on the surface N-15 glass coating on crofer steel indicating the uniform dissolution of glass during testing. Such nature of surface clearly indicates the good corrosion resistance property of the glass coating. Surface of X glass coating appeared to be smooth at low magnification. But at higher magnification, small pits were observed and the agglomeration of particles was detected on the surface of the coating. Microstructural studies after corrosion testing also supported the stability of S glass coating due to the formation of oxide layer on the coated surface.

5.2. Future Scope

Details in thermal and structural studies of all glass coatings on steels exhibit high stability even under corrosive conditions. These glass coatings are more stable as compared to other hybrid, organic coatings on steels. This work needs to be repeated in real seawater, under well-defined conditions of temperature, oxygen content and under fluid flow at least one year and on much larger exposed area for a much longer exposure conditions.